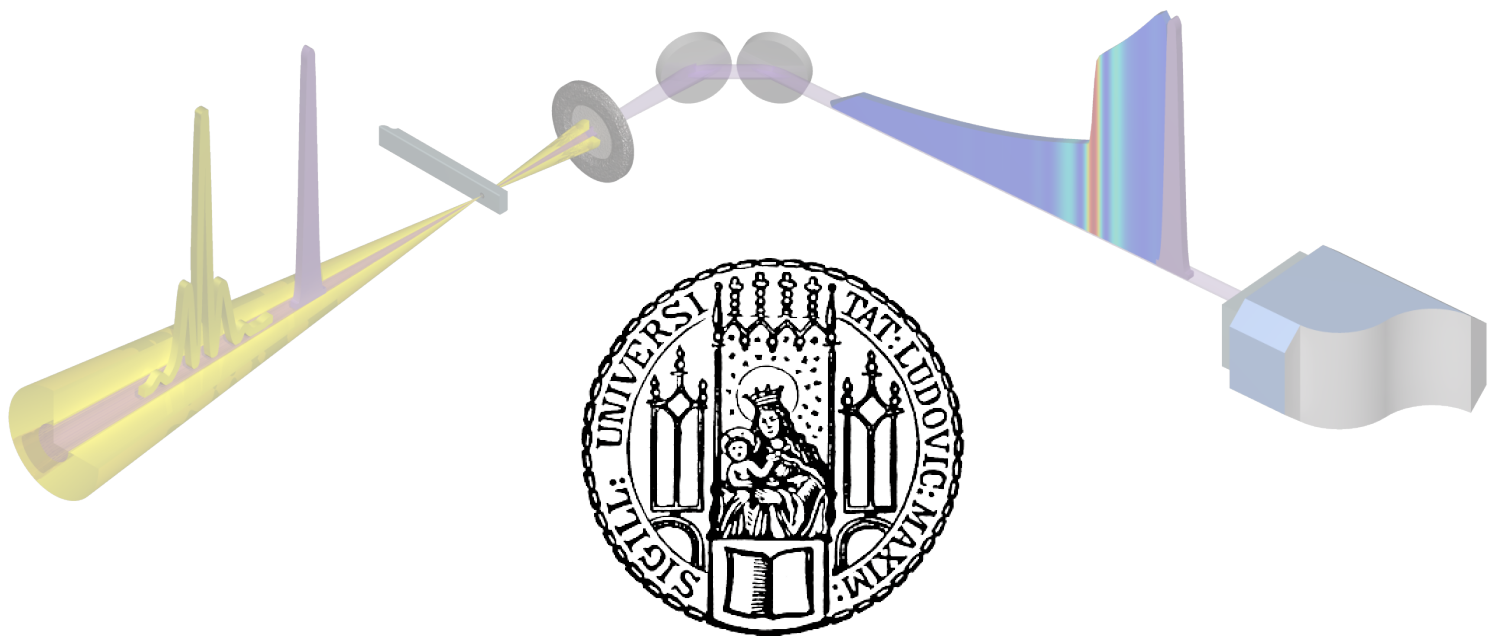

Attosecond Nonlinear Spectroscopy of Core-Shell Excitations in Atomic and Solid State Systems

Antoine Moulet



München 2015

Attosecond Nonlinear Spectroscopy of Core-Shell Excitations in Atomic and Solid State Systems

Antoine Moulet

Dissertation
an der Fakultät für Physik
der Ludwig-Maximilians-Universität
München

vorgelegt von
Antoine Moulet
aus Verdun (Frankreich)

München, den 16.03.2015

Erstgutachter: Prof. Dr. Ferenc Krausz
Zweitgutachter: Prof. Dr. Armin Scrinzi
Tag der mündlichen Prüfung: 27.04.2015

Zusammenfassung

Kernschalen Anregungen spielen eine Schlüsselrolle bei Röntgen Absorptions Strukturstudien. Da ihre Lebensdauer kürzer als 10 Femtosekunden ($1\text{fs} = 10^{-15}\text{s}$) ist, sind zeitaufgelöste Experimente an ihnen anspruchsvoll. Die Durchführung von solchen Studien in atomaren Gasen gelang erstmals Anfang dieses Jahrhunderts mittels Anrege-Abfrage Experimenten unter Einbindung von extrem ultravioletten (EUV) Attosekunden Pulsen ($1\text{as} = 10^{-18}\text{s}$) und nah-infraroten (NIR) Laser-Pulsen mit einer Pulslänge von wenigen optischen Zyklen [1]. Die Untersuchung von Festkörpersystemen ist mit dieser Methode nur sehr eingeschränkt möglich, da sie auf Photoelektronenspektroskopie basiert und daher für die Anwendung auf Volumenmaterial ungeeignet ist. Darüber hinaus zerfallen Lochzustände in Festkörpern schneller als in Gasen, da hier zahlreiche Dekohärenzkanäle existieren. Zusätzlich war die zeitliche Auflösung der Experimente bisher durch die Dauer des NIR Pulses limitiert, welche typischerweise einige Femtosekunden beträgt. So konnte die kurze Pulslänge im Attosekunden Bereich, die im EUV erreicht wurde, nicht voll ausgenutzt werden.

Allerdings wurde dieser Weg kürzlich dadurch geebnet, dass der Werkzeugkasten der Attosekunden-Physik um dynamische Absorptionsmessungen ergänzt wurde [2]. Darüber hinaus trugen Fortschritte in der kohärenten Lichtfeld-Synthese, die teilweise im Rahmen der vorliegenden Dissertation erreicht wurden [3], zur Generierung von multi-Microjoule optischen Attosekundentransienten bei [4]. In der vorliegenden Arbeit wird über ein Experiment mit EUV Attosekunden Anrege sowie sichtbaren Attosekunden Abfrage Pulsen berichtet. Es basiert auf der Störung des EUV Absorptionsprozesses durch den Abfrage Transienten. Diese Experimente stellen einen Machbarkeitsnachweis für die zeitliche Auflösung von sub-Femtosekunden Dekohärenz Phänomenen in Festkörpern dar.

Unsere Methode wurde zunächst in einem Experiment mit einem atomaren Gas (Krypton) angewendet um eine effiziente zeitliche Beschreibung des wenige Femtosekunden dauernden Zerfalls von Kernschalen Anregungen zu demonstrieren. Zur Untersuchung dieses Prozesses wurde ein phänomenologisches analytisches Modell erstellt. Bei diesem Ansatz wird beschrieben, wie die durch EUV Absorption erfassten elektronischen Zustände durch den NIR Transienten zu dressed states gekoppelt und depopuliert werden. Unser einfaches Model ermöglichte die Rekonstruktion von numerischen Daten aus komplexeren Simulationen sowie von experimentellen Daten zur Erkundung der in Frage stehenden Störungsmechanismen. Darüber hinaus ergaben sich numerische Werte für die Lebenszeiten sowie die Polarisierbarkeit der beteiligten Zustände.

Die entwickelten experimentellen Werkzeuge und Modelle wurden erfolgreich zur Untersuchung von Kernschalen Anregungen in dünnen SiO_2 Schichten eingesetzt. Unsere Experimente und intuitiven Modellierungen ermöglichen die Beschreibung der Dekohärenzzeit unserer Festkörperproben, die weniger als einer Femtosekunde beträgt. Weiterhin enthüllen sie neue spektroskopische Informationen über das Verhalten von Kernschalen Anregungen in kondensierter Materie.

Abstract

Core-shell excitations play a key-role in structural studies based on X-ray absorption. They decay faster than 10 femtoseconds ($1 \text{ fs} = 10^{-15}\text{s}$), which makes their investigation in the time domain challenging. The first demonstration of such studies in atomic gases has been made possible in the beginning of the 2000's by pump-probe schemes involving Extreme Ultraviolet (EUV) attosecond pulses ($1 \text{ as} = 10^{-18}\text{s}$) and few-cycle near infrared (NIR) laser pulses [1]. However, solid-state systems have stayed out of the scope of such methods. Indeed, based on photoelectron spectroscopy, they are ill-adapted to bulk materials. Moreover, hole states decay faster in solids than in gases, due to the ubiquity of decay channels. Furthermore, the duration of the NIR laser pulse, usually several femtoseconds, has prevented access to the ultimate temporal resolution allowed by the attosecond confinement of the EUV bursts.

The way has however recently opened, as the attosecond physics toolbox has been enriched with dynamical absorption measurements [2], and advances in coherent light field synthesis, partly realized in the framework of this thesis [3] have led to the generation of multi-microjoule optical attosecond transients [4]. This work thus presents an EUV attosecond pump - visible attosecond probe scheme. It is based on the perturbation of the EUV absorption process by the probing transient. Proof-of-principle experiments are presented, which allowed to temporally resolve subfemtosecond decoherence phenomena in solid state systems.

Our method has first been applied in a benchmarking experiment on an atomic gas (Krypton), to demonstrate the efficient temporal characterization of the few-femtosecond decay of a core-shell excitation. A phenomenological analytical model has been developed at this occasion, based on the sub-femtosecond dressing and depletion of the electronic states involved in EUV absorption. This simple man model has allowed the analytical reconstruction of state-of-the art numerical simulations, as well as experimental traces, shedding light on the perturbation mechanism at stake, and yielded numerical values for the lifetimes, as well as polarizabilities of the states involved.

The experimental tools and models developed have then been successfully applied to study core-shell excitations in SiO_2 thin films. Our experiments and intuitive modeling allowed the reconstruction of their decoherence time, which is below 1 fs. It also unveiled new spectroscopic information about the nonlinear behavior of core-shell excitations in a condensed matter system.

Contents

Zusammenfassung	v
Abstract	vi
Introduction	1
1 Optical Attosecond Transients	7
1.1 Subfemtosecond light pulses	7
1.2 PHz broad coherent optical continuum	11
1.3 Versatile multioctave spectral phase control: Light Field Synthesizer	15
1.4 Global phase control of an attotransient	19
1.5 Optical attosecond transients	21
2 Generation and manipulation of EUV pulses with light transients	25
2.1 EUV generation driven by attosecond light transients	25
2.2 Control of attosecond pulse birth by synthesized optical drivers	32
2.3 Generation of kilo-electronvolt photons with subcycle optical pulses	36
3 EUV-Visible attosecond pump- attosecond probe experimental setup	41
3.1 Overview of AS-1 beamline	41
3.2 Compatibility of the beamline with attosecond transients	44
3.3 80-120 eV central energy attosecond transient absorption capability	46
3.4 Synchronization issues in the attosecond regime	49
4 Polarization effects in Strong Field Ionization	57
4.1 Single and double field Ionization of atoms in a subcycle pulse	58
4.2 Real-time observation of strong-field ionization	63
4.3 A simple man's model of polarizability: the 3 levels system	66
4.4 Neutral induced polarizability of ionic Krypton	73
4.5 Addressing Double Ionization	74
5 Optical dipole gating of Auger decoherence process in Krypton	79
5.1 The dipole gating paradigm	79
5.2 Dipole gating measurement in Krypton	89
6 Attosecond nonlinear X-Ray Absorption Near-Edge Spectroscopy	101
6.1 The $L_{2,3}$ absorption edge of Silicon dioxide	101
6.2 Dipole gating measurement of the $L_{2,3}$ edge of SiO_2	108
6.3 Nonlinear spectroscopy of SiO_2 core-hole excitonic system	111

7	Conclusions and outlooks	119
A	Going further in exploiting the cross-correlation concept	123
A.1	Definitions	123
A.2	Principle	123
A.3	Influence of the transmission system	125
A.4	Spatio-temporal characterization	125
B	EUUV Dipole FROG	127
C	Linking polarizability and phase in the instantaneous gate model	129
D	Data Archiving	131
	Bibliography	143
	Acknowledgements	158
	Curriculum Vitae	161

Introduction

The interaction of light with matter has always been the tool of choice to investigate the properties of the microcosm. In return, the deeper understanding of the structure and rules governing these behaviors have allowed to advance technology for the realization of photon sources with ever more intricate properties. Spatial and temporal coherence, high spectral purity, attosecond duration, relativistic peak intensity or single, entangled or squeezed photonic states, diffraction limited size or intricate spatial properties are but few examples of the tools nowadays available to the curious experimentalist. They are still under continuous development, with various degrees of complexity in the different regions of the electromagnetic spectrum. The progress of the technology of light and the understanding of matter have therefore moved alongside, alternatively preceding or following, but always nourishing each other.

This work relies on the latest developments of the ability to confine coherent visible light in time, to durations below an optical cycle. It presents the first applications of the combination of an attosecond Extreme Ultraviolet (EUV) pulse and a visible attosecond pulse (attotransient) in a pump-probe scheme. The experiments and concepts developed in this thesis allowed to resolve subfemtosecond decoherence of core-shell excitations in the time domain, and to extract spectroscopic information about the coupling schemes within this class of excited states, living less than a handful of femtoseconds in condensed matter. Such states are largely addressed by X-Ray spectroscopies, but the lack of fitted tools has until now left the study of their nonlinear properties widely unexplored.

The first observation of the discrete nature of the quantum world has been realized by Wollaston, who used a prism to disperse the sunlight that had crossed a thin slit, and observed dark lines in the sun spectrum in 1802 [5]. In 1814, J. v. Fraunhofer was independently to rediscover and classify them and correlated the position of the so-called D line (due to sodium) with an emission line present in the spectrum of a flame he was using to shine his setup [6]. In 1849, L. Foucault demonstrated the correlation of absorption and emission phenomena by sending the sun light in a carbon arc producing the D emission line of sodium, and observing that the line stays at the same position but counter-intuitively switches to absorption [7]. It is however only in 1859, after the rediscovery of this fact that G. Kirchhoff and R. W. Bunsen really initiated absorption spectroscopy [8]. After running a thorough classification work, they produced a spectrochemical analysis of the sun spectrum and announced that sun contained iron, calcium, sodium, magnesium, nickel and chromium. Emission and absorption spectroscopies have since then been put to extensive use in a vast number of scientific fields for their element sensitive properties: astronomy, biology, chemistry, mineralogy, etc For physics, these phenomena have been cornerstones of the development of the successive theories describing the microcosm, from the classical elastically bound electron of Lorentz, which predicted the lorentzian absorption and emission

lineshape, to the establishment of quantum mechanics. The resulting invention of the laser and its first realization in 1960 [9] have brought a light source with unique properties of spectral purity and coherence to probe the absorption of matter.

Absorption of light by an atom is a process happening predominantly through dipolar interaction, and as such subject to selection rules. Therefore, direct linear absorption spectroscopy gives selective information (position, transition strength) about states that have a particular symmetry relationship with the ground state, and incoherent light sources are mostly limited to this class of experiments. Few years after the first demonstration of laser, Q-switching [10] and passive mode locking by saturable absorbers [11] have allowed the first demonstration of pulsed laser light, with the generation of pulses down to picosecond durations. The temporal confinement of the energy has allowed reaching field strengths comparable to the Coulomb fields holding nuclei and electrons together, and has brought the ability to drive matter in a nonlinear fashion. It opened a broad field of experiments, deepening our understanding of matter.

A most interesting example is the measurement of the most fundamental and theoretically known transition, the $1s - 2s$ transition in hydrogen. Two-photon absorption, which bypasses the selection rules, combined with another considerable breakthrough of nonlinear spectroscopy, Doppler-free techniques, [12], made the measurement of this most precise transition (1 Hz linewidth) possible [13]. The high coherence and energy density of light allowed driving the transition of selected speed atoms to saturation with a second pulsed laser, leading to the spectral resolution of the natural linewidth, which was hidden under Doppler broadening. Finally the frequency comb technology has brought another leap forward in performance for this frequency measurement [14].

But not only have nonlinear techniques improved our ability to resolve absorption spectra, they have also permitted the manipulation of these absorption spectra, following the precursor Autler-Townes experiments in the microwave range [15], in which the dressing of one of the states involved in a transition by a strong field on resonance with another excited state leads to the splitting of the absorption line in two. Control being always linked with knowledge, this type of experiments gives a way to access information about the presence and position of excited states non-trivially probed by absorption (because dipole forbidden), and the strength of the couplings involved.

All of the studies mentioned above address static (time-integrated) properties of matter. The temporal dynamics of quantum phenomena is also of prime interest, and the development of its study has also been accompanied by technological evolutions. It is indeed known to any photographer that taking a sharp picture of a moving object requires a shutter opening and closing on a timescale on which the object can be considered as motionless.

Translating this principle to the investigation of chemical dynamics, R. Norrish and G. Porter developed the technique of flash photolysis in the 1950s [16]. The technique consisted of generating free radicals (*e.g.* HO) with a photochemical reaction using a very intense 50 microsecond bunch of light from a flash lamp (obtained from photographic flashes of the

Navy). The reaction products, radicals, absorb light differently than the reactants, and they usually have a sub millisecond lifetime. Monitoring the time-dependent absorption of the sample therefore would give access to the radical recombination reaction kinetics. To this end they had the idea to send a second, as brief but less intense flash of light, delayed by the use of a rotating wheel, and measure its absorption by the sample as function of the delay [17]. This experiment, the first realization of a pump-probe scheme, gave access to the speed of these chemical reactions, unraveling on the sub-millisecond range. R. Norrish and G. Porter received the 1967 chemistry Nobel Prize for their work, together with M. Eigen who used a most interesting sound based method to determine the speed of chemical reactions [18].

The aforementioned pulsed lasers available from the late 1960s provided high energy densities in well confined picosecond time intervals, and they opened the way to the investigation of dynamics unraveling on these timescales, mainly intramolecular dynamics. As laser scientists continued to bring the laser pulse durations down, the femtosecond domain was reached. Thus, time-resolved tools were covering most of the molecular vibrational timescales, and transient absorption spectroscopy was applied to dynamics as fast as the breaking of a chemical bond in ICN and NaI [19, 20]. This led A.H. Zewail to the Nobel Prize for development of femtochemistry in 1999. The further development of femtosecond lasers in UV to IR regions of the spectrum, as well as different techniques and detection of other observables than absorption has allowed the investigation of a wide range of phenomena.

However, the electronic motion, unraveling on the few-femtosecond to attosecond scale stayed out of reach to experimentalists. EUV driven excitations of core electrons to outer shells is a class of phenomena of particular interest, because they form the basis of most of the EUV and X-ray spectroscopies, widely used tools in material and physical science. Realizing conventional laser type sources in spectral regimes deeper than the UV to study these transitions with nonlinear spectroscopy techniques is way more challenging than in longer wavelength domains. This is due to the large photon energy, together with excitation lifetimes in the femtosecond or sub-femtosecond range (we will come back to this fact), which require a very intense pumping to reach population inversion. Last but not least, the manipulation of such photons is extremely challenging, as they are absorbed by almost any material. This impeded the realization of EUV and X-ray lasers. As a consequence, although advanced in the linear regime by the development of synchrotron facilities from the 1950s, the nonlinear investigation of matter in this photon range remains largely unexplored.

As stated, the lifetime of EUV excitations is, in the 100 eV range which will be investigated in this work, mostly limited by Auger filling of the generated core hole to around 10 fs in atoms, or even less in solids, for which inhomogeneous broadening plays a big role. To draw an analogy with the previous discussion, exploring the dynamical behavior of these transitions in a time-resolved fashion requires coherent light sources of high intensity, and temporally confined to durations shorter than their decoherence time.

Two types of sources, both relatively new, are good candidates: the X-Ray free electron

laser (XFEL) and the High Harmonic Generation process.

XFELs are big facilities based on an electron accelerator. This technology uses the wiggling of relativistic electron bunches in an undulator as a gain medium to bypass the inversion population issue. It has been developed since the mid-1990s and has the advantage of producing very high photon fluxes, in the soft or hard X-ray domain depending on the facility [21]. This has allowed the observation of numerous nonlinear processes in the X-ray domain, such as the generation of Xe^{21+} ions by the absorption of more than 57 photons of 93 eV energy in a 10 fs pulse [22], the stripping of all the electrons of Neon [23] or 2 photon transitions at 46 eV [24]. However, XFELs are until now routinely operated in a stochastic mode, Self-Amplified Stimulated Emission (SASE), which leads to a very unstable temporal structure, ill-adapted to fine coherent studies [25].

In the beginning of the 2000s, subfemtosecond pulses centered in the EUV range have been generated for the first time, exploiting the high harmonic generation (HHG) process from newly available high power near infrared Carrier Envelope Phase (CEP) stable few-cycle pulses [26]. Pump-probe schemes involving two of these EUV attosecond pulses have so far remained elusive, mostly because of the low conversion efficiency of HHG, which low fluxes of light. Only at the expense of a low repetition rate, very low signal to noise ratio, and the use of a train of attosecond pulses have nonlinear processes (two-photon ionization of Helium) been observed with such radiation sources[27].

The use of high intensity few-cycle CEP stable pulses in combination with EUV attosecond pulses has however offered a way to significantly advance the resolution of time-resolved nonlinear spectroscopies. Experiments based on the streak camera technique have measured in the time domain the 7.9 fs decay time of a core-hole [1]. In this experiment, the EUV pulse ejects photoelectrons and creates a core hole vacancy which is filled while ejecting Auger electrons. The infrared field plays the role of probe pulse and brings Auger electrons to energetic sidebands by wiggling them in free space. The amplitude of these sidebands as a function of pump-probe delay therefore follows the decay of the hole. The temporal resolution of this technique is however limited by the duration of the infrared pulse. At that time a 7 fs driver was used. Pushing forward the technology of hollow-core fiber and chirped mirror compressor has brought the attainable duration in the 3 fs range, but this technology is ill-adapted to go further down. Such experiments were therefore far from exploiting the attosecond regime theoretically attainable with the HHG EUV pulses. Moreover, this photoelectron based technique is not adapted to study solid-state systems, in which the photoelectron is captured in the material.

Later on, in the first attosecond transient absorption study (ATAS), the EUV pulse has been used as a probe for the dynamics launched by the pump infrared 3.3 fs driver [28]. Thus, the coherent oscillation of a valence electronic wavepacket launched by strong field ionization has been demonstrated by exploiting the quantum beat encoded on absorption lines existing only in the strong field generated ion. The phenomenon probed there is the motion of valence electrons, with a coherence time virtually infinite for the pulse, and the EUV transition is merely a probe.

Efforts put through the years to bring the duration of light pulses down have taken a leap

forward around 2010, with the first generation of visible light field synthesized transients confined to an intensity envelope of 2 fs. With such a tool the first ATAS experiment has been revisited and confirmed and improved the previous findings [3]. As an extra result, the exponential nonlinearity of the strong field ionization process, together with the high energy confinement in a half-cycle of the visible driver has allowed to limit the rise of the ionic absorption to less than a femtosecond.

However, at this occasion, it has been noticed that during the overlap of the visible and EUV fields, *i.e.* during the ionization window, a modification of the EUV absorption process and spectral lineshape by the pump pulse, namely through the dephasing of the generated electronic coherence by polarization effects (Stark shift) of the EUV transition, blurring the neat picture of visible pump EUV probe which had been so successful elsewhere on the delay axis. This work began with the investigation of this behavior in the experiment, which will be presented in Chapter 4. Other teams around the world have since then investigated this class of phenomena, noticeably observing the effective transformation of a Fano absorption profiles into Lorentz lineshape [29]. They are however limited in their investigation of the delay-dependance of these effects by their relatively long IR driver duration.

In the following years, and in the framework of this dissertation, the light confinement ability of our team has on the other hand been risen even more, with the broadening of the synthesized spectrum, and visible light pulses have been virtually restricted to a single optical half-cycle, producing attosecond light transients [4]. From there on we had at hand two subfemtosecond pulses, which could nonlinearly interact via polarization effects detectable in the absorption spectrum, as learned from the previous experiment. In this scheme we would be able to drive time dependent nonlinear polarization effects after an EUV transition, but before the decoherence prevents this observation, *i.e.* on a subfemtosecond window. It has therefore the ability to trace such decoherences in the time domain, and to yield nonlinear information about EUV excitations. Such polarization effects having been observed in atoms [3, 29] and solids [30], the playground was quite open.

It is important to stress here that although using a similar setup and detection scheme, the technique presented here is NOT a transient absorption scheme, in the classical sense of the word. Indeed, the observable is the spectrum of the *pump pulse*, for which absorption is modulated by the optical transient. In that sense it is a time-resolved version of an Autler-Townes experiment with EUV transitions. The huge bandwidth to central frequency ratio characteristic of the attosecond transient however smears out the conventional photon formalism, due to the huge number of photonic paths involved in the nonlinear interaction. Approaches based in the time domain picture were therefore required to describe the interactions and exploit pump-probe traces.

This work presents experiments in which such traces were measured, in atoms as a benchmark of the technique, and in solid state. Phenomenological models were developed to reconstruct these experiments and extract physical constants. These simple models have been confronted with advanced atomic dynamics theory, yielding a very satisfactory agreement, and were then used on experimental data. They allowed the measurement of the decoherence time of core-shell transitions in the time domain, as well as nonlinear properties

of these excitations of atomic and solid state matter, lasting less than a femtosecond.

- Chapter 1 presents the principle of generation of attosecond optical transients, as well as its implementation on the AS-1 beamline.
- Chapter 2 revisits the principles of EUV pulse generation from High Harmonic processes in the context of the new object that is the synthesized light transient. It is shown that the precise manipulation of the waveform allows the manipulation of the EUV light, and a theoretical investigation of keV photon generation is presented.
- Chapter 3 describes the experimental setup used in the following experiments, and all the relevant modifications that have been made on the beamline to allow for the simultaneous use of an attosecond optical transient and a versatile EUV attosecond pulse in pump-probe experiments with subfemtosecond resolution.
- Chapter 4 describes the experiments that triggered the reflexion that led us to planning the following stages of this PhD, the observation of Stark-shift manifestations during Strong Field Ionization in the experiment of [3]
- Chapter 5 presents the benchmark of our technique and theoretical approaches to the probing of EUV transitions in the 3d-np absorption edge of Krypton. Resolution of a decay time of around 8 fs, and access to nonlinear properties of the excited state is demonstrated. A publication about this experiment is currently in preparation.
- Chapter 6 shows the application of our technique to the resolution of nonlinear behavior in the $L_{2,3}$ edge of SiO_2 , in which we were able to drive interactions of low order in an excited state which coherence survives less than a femtosecond. A publication about this experiment is currently in preparation.

1

Optical Attosecond Transients

Divide et impera - Divide and conquer

– Gaius Julius Caesar

Although electromagnetic radiation can be confined to subfemtosecond durations since the beginning of the 2000s in the extreme ultraviolet (EUV) range, with central photon energies since then moved from 50 to 150 eV, this regime has remained elusive in the optical domain until recently, and the efforts that opened up the era of light field synthesis [3]. This chapter aims at presenting the requirements and techniques implemented for the successful synthesis of a subfemtosecond optical pulse, hereafter named optical attosecond transient or in short attotransient.

1.1 Subfemtosecond light pulses

Definitions

Let us first introduce basic elements of the mathematical description of an ultrashort pulse. Given a real-valued electric field varying in time $E(t)$ (called waveform), the Fourier Transform allows its decomposition in a superposition of monochromatic waves of angular frequency ω . For reasons of clarity or comparison, this quantity will occasionally be referred to in units of frequency $\nu = \omega/2\pi$, photon energy $E = \hbar\omega$ (in eV), or translated into vacuum wavelength $\lambda = 2\pi c/\omega$ (in nm)

$$E(t) = \mathcal{F}[E(\omega)](t) = \frac{1}{2\pi} \int E(\omega) \exp(-i\omega t) d\omega \quad (1.1)$$

With $E(\omega)$ given by the Inverse Fourier Transform:

$$E(\omega) = \mathcal{F}^{-1}[E(t)](\omega) = \int E(t) \exp(i\omega t) dt \quad (1.2)$$

$E(\omega)$ being a complex valued quantity, it is usual to define its modulus $a(\omega) = |E(\omega)|$, and its phase $\phi(\omega) = \arg(E(\omega))$ being respectively the amplitude and phase at $t = 0$ of

the monochromatic wave of frequency ω entailed in the waveform.

We can define the central or carrier frequency ω_0 as the center of mass of the positive spectrum:

$$\omega_0 = \int_0^\infty \omega |E(\omega)|^2 d\omega \quad (1.3)$$

It is quite common to Taylor-expand the spectral phase around the central frequency:

$$\phi(\omega) \simeq \phi^{(0)} + \frac{\phi^{(1)}}{1!}(\omega - \omega_0) + \frac{\phi^{(2)}}{2!}(\omega - \omega_0)^2 + \frac{\phi^{(3)}}{3!}(\omega - \omega_0)^3 + \dots \quad (1.4)$$

- $\phi^{(0)}$ is the global or absolute phase, mostly referred to as Carrier-Envelope Phase (CEP), although as we shall see later, this term gets inaccurate in the case of subcycle pulses.
- $\phi^{(1)}$ corresponds to a group delay, it is expressed in fs
- $\phi^{(2)}$ is the second order phase (or linear chirp) expressed in fs²
- higher phase orders will distort the pulse temporal shape

A pulse with a linear spectral phase (only $\phi^{(0)}$ and $\phi^{(1)}$ differ from zero) is said to be Fourier Transform limited, if its group delay, the derivative of the phase, is constant, and therefore its duration is the shortest allowed by its spectral components.

It is useful to introduce the carrier-envelope decomposition of such a waveform. $E(t)$ being a real field, basic properties of the Fourier Transform impose that $E(\omega) = E(-\omega)^*$, the field has a positive and a negative frequency component which are related to each other. there is therefore enough information in the positive frequency part of the spectrum to describe the waveform. the Inverse Fourier Transform of this positive frequency part (times 2) is called the analytical field $\mathcal{E}(t)$:

$$\mathcal{E}(t) = \frac{2}{2\pi} \cdot \int_0^\infty E(\omega) \exp(-i\omega t) d\omega \quad (1.5)$$

the carrier envelope description of the field is then given by:

$$\mathcal{E}(t) = \mathbf{E}(t) \exp(i\phi(t)) \quad (1.6)$$

$\mathbf{E}(t) = |\mathcal{E}(t)|$ is the envelope, and $\phi(t)$ the temporal phase. In the case where the spectral phase is constant $\phi(\omega) = \phi(\omega_0) = \phi_0$, we can write:

$$\mathcal{E}(t) = \mathbf{E}(t) \exp(i\omega_0 t + i\phi_0) \quad (1.7)$$

This is the carrier-envelope decomposition of the waveform, and ϕ_0 is the global phase of the waveform.

Ingredients of an optical subfemtosecond pulse

Basic properties of the Fourier Transform include an uncertainty principle which links the width of the spectral amplitude, or bandwidth $\Delta\omega$, and the duration of the envelope of the pulse Δt (strictly speaking in the sense of the standard deviations of the spectral and temporal distributions):

$$\Delta t \cdot \Delta\omega \geq 2\pi \quad (1.8)$$

This inequality is saturated in the case of a Fourier limited pulse, *i.e.* a pulse with a linear spectral phase. It tells us that in order to generate a pulse with subfemtosecond duration:

- the spectral bandwidth has to be above 1 PHz, or 4.2 eV
- the nonlinear group delay has to be controlled

To be supported without negative frequencies, the central frequency must therefore be above 500 THz, or said otherwise the central wavelength lower than 600nm. In the case where the central frequency is still in the optical domain, the bandwidth will be superoctave, and the field subcycle, as can be seen on Figure 1.1. This is a remarkable feature in comparison with a more "conventional" subfemtosecond EUV pulse, which bandwidth will be considerably suboctave and will therefore comprise several cycles (see Figure 1.1). This calls for a very precise control of the absolute phase, as will be developed later on.

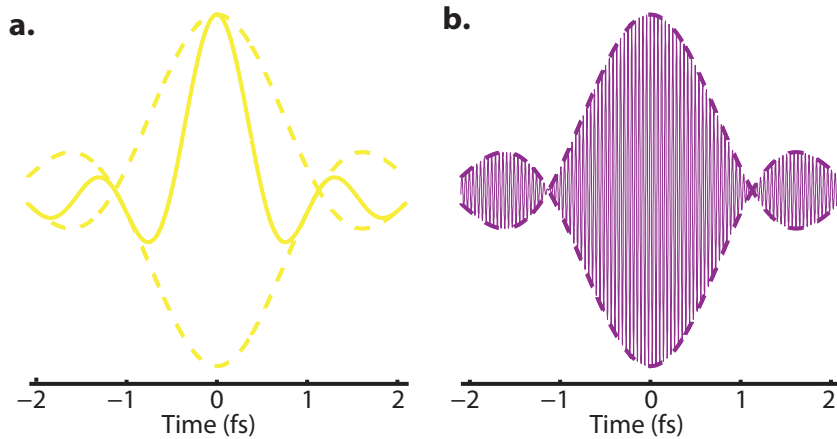


Figure 1.1: Electric field waveform of a 1 fs FWHM intensity duration pulse centered at **a.** 600 nm, and **b.** 12.4 nm or 100 eV

Another important aspect is the control of the spectral phase $\phi(\omega)$. To avoid any lengthening of the pulse compared to the capacity given by its spectrum, the quadratic and higher orders of spectral phase (Equation (1.4)) must be kept to 0. Figure 1.2 shows the effect of 10 cms of air (group delay has been removed) on an optical pulse centered at 530 nms. The distortion is quite dramatic as the radiation below 500 nm already undergoes

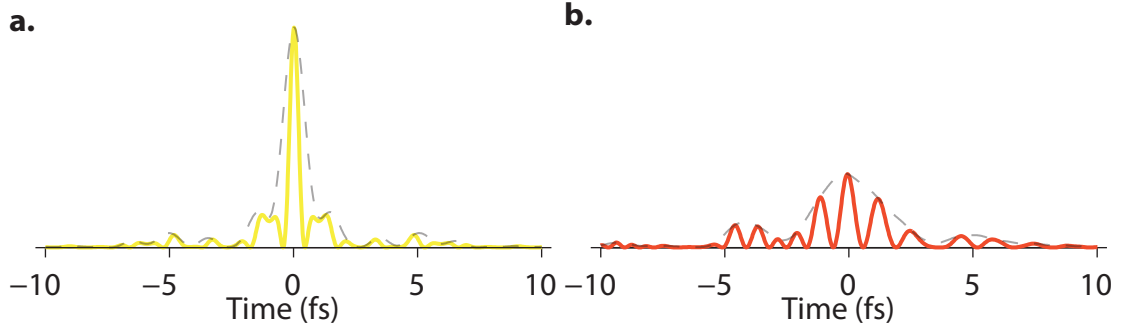


Figure 1.2: Waveforms deriving from the same optical subfemtosecond-able spectrum, with no chirp before (a.) and after (b.) propagation of 10 cms in air.

more than 5 fs of linear temporal chirp compared to the red part. 10 μm of glass have a similar effect. Special care should therefore be taken to manage the dispersion.

In the optical subfemtosecond regime, the carrier wave period is longer than the pulse duration: the waveform is subcycle. As such, it becomes critical to control the absolute phase of the wave, whose change would substantially alter the temporal profile of the waveform, as can be seen on Figure 1.3.

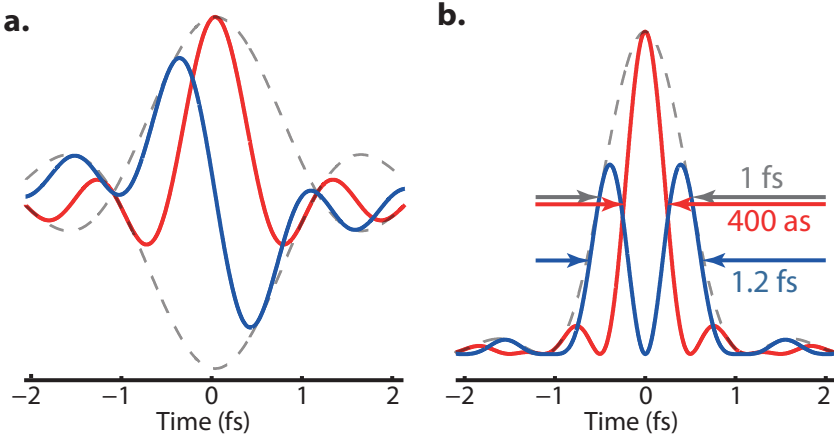


Figure 1.3: Two compressed square-spectrum, 1 fs intensity envelope FWHM waveforms with a constant spectral phase (no quadratic or higher order terms) of value 0 (blue) and $\pi/2$ (red) .

It is also worth noticing that for pulses with a contrast between the main and the adjacent half-cycles of more than 2, one can, following practices of the THz community [31], define an instantaneous intensity FWHM duration, which differs from the envelope intensity FWHM duration, and is dictated by the central wavelength, and not the spectral width. For our attotransients, the instantaneous intensity FWHM duration is 400 as at $\phi^{(0)} = 0$ and 1.2 fs at $\phi^{(0)} = \pi/2$ for an envelope intensity FWHM duration of 1 fs.

1.2 PHz broad coherent optical continuum

As seen in Section 1.1, the synthesis of subfemtosecond pulses requires the generation and control of a spectral bandwidth of close to 1 PHz. It has historically been achieved in the extreme ultraviolet (EUV) range, where the very high nonlinearity at play in the high harmonic generation process (see Chapter 2) causes a temporal confinement that leads to the generation of huge bandwidths [32]. In the optical domain, few approaches have been proposed and/or implemented for the generation of superoctave spectral sources, such as the use of Raman sidebands [33], or the generation and synchronization of harmonics 2 to 5 in bulk crystals [34]. These approaches however do not produce a continuum, but a discrete spectrum, which allows only multiple pulses generation. Recently also, the coherent superposition of Optical Parametric Chirped Pulse Amplifiers covering adjacent spectral ranges [35, 36] has been realized, but these methods have not yet managed to reach the PHz bandwidth associated with subfemtosecond duration.

The approach used in this work, supercontinuum generation by filament guiding in a hollow waveguide filled with high pressure gas, has been developed and optimized over the years [37]. The gas being free to flow in the setup, the nonlinear medium does not get damaged and this is therefore a widely used approach for the generation of few-cycle pulses. To extend this approach to the generation of PHz broad continua, we use a precisely dispersion controlled Chirped-pulse Amplifier (CPA) system and implement a relatively high pressure of gas.

1.2.1 23 fs dispersion controlled CPA system

The principle of Chirped Pulse Amplification, a prominent technique for the generation of high energy femtosecond pulses, has been widely described in numerous quality publications since its first demonstration in 1985 [38], as well as its particular implementation in similar systems to ours, and will therefore not be described in long details here. It is however useful to give an overview and point out where custom adaptations have been made to tailor the system to the needs of our attosecond precise experiments.

75 nm bandwidth multipass CPA

For all the experimental work presented in this thesis, a commercial femtosecond amplified system has been used as a front-end. We used a Titanium-doped sapphire (Ti:Sa) based ultrabroadband oscillator (RainbowTM from Femtolasers) pumped by a frequency doubled neodymium-doped yttrium aluminum garnet (Nd-YAG) continuous laser delivering 3 W at 532 nm (Verdi V6TM from Coherent) to seed the amplifier system. The oscillator delivers broadband (6 fs) pulses comprising around 5 nJ of energy at 78 MHz [39].

The pulse train coming from the oscillator is focused into a Periodically Poled Lithium Niobate crystal (PPLN) crystal, which broadens their spectrum and generates the nonlinear signals necessary for the global phase stabilization of the oscillator, as will be described further. The 78 MHz, 1 nJ pulse train is then stretched to around 15 ps in a heavy (SF57)

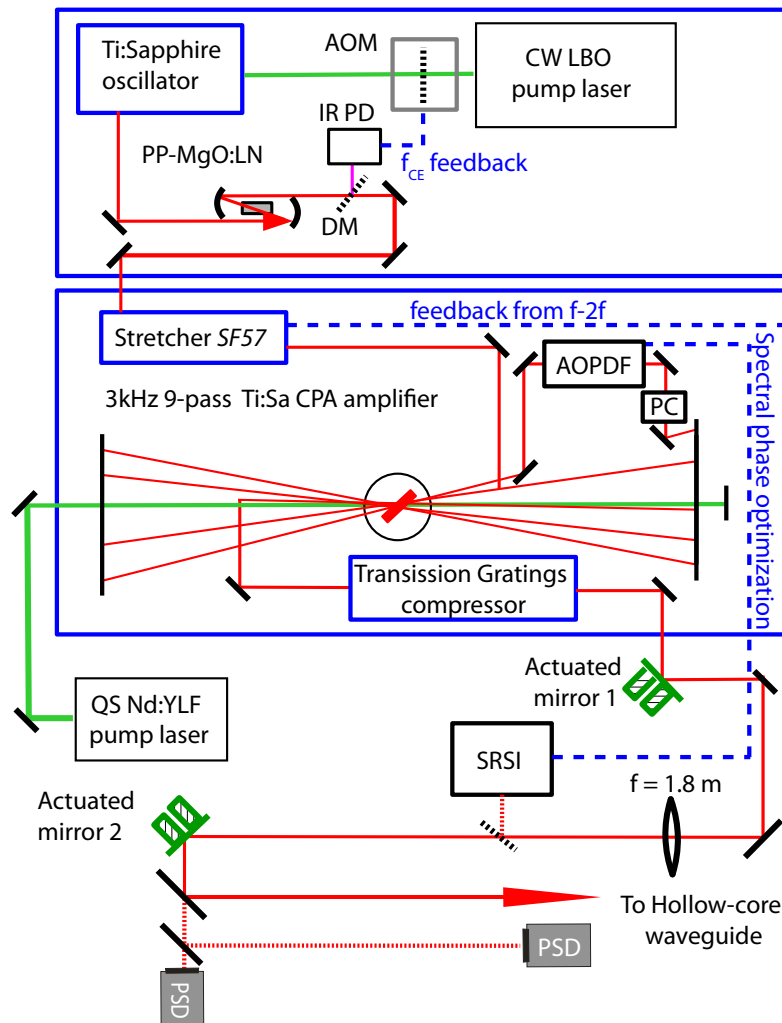


Figure 1.4: Overview of the front end 3 kHz, 1 mJ, 23 fs CPA system: a 78 MHz broadband oscillator seeds a 9 pass CPA system, with tailored spectral and amplitude shaping leading to the generation of a short and clean pulse. AOM: Acousto-optic modulator, IR PD: Infrared Photodiode, PC: Pockells Cell, AOPDF: Acousto Optic Programmable Dispersive Filter, SRSI: Self-Referenced Spectral Interferometry, PSD: Position Sensitive Detectors

glass stretcher, and seeded into the amplifier. The complete train is amplified during the first 4 passes, in the Ti:Sa crystal, pumped by a frequency doubled Q-switched neodymium-doped yttrium fluoride (Nd:YLF) delivering around 100 ns pulses (DM30TM from Photonics Industries). After the first 4 passes, a Pockells cell is used to slice the pulse train down to a 3kHz repetition rate. The pulse is then sent into an Acousto Optic Programmable Dispersive Filter [40, 41] (AOPDF: DazzlerTM from the company Fastlite). It is, in these conditions of use, an arbitrary spectral phase and amplitude shaper. It is used here to compensate for high orders of spectral phase coming from the stretching and compression scheme (mainly third order from the transmission grating compressor), but also as a way to fight the gain narrowing effect [42]. Indeed, a custom amplitude filter has been tailored to broaden the final bandwidth of the pulse from 40 nm up to 75 nm (see Figure 1.5).

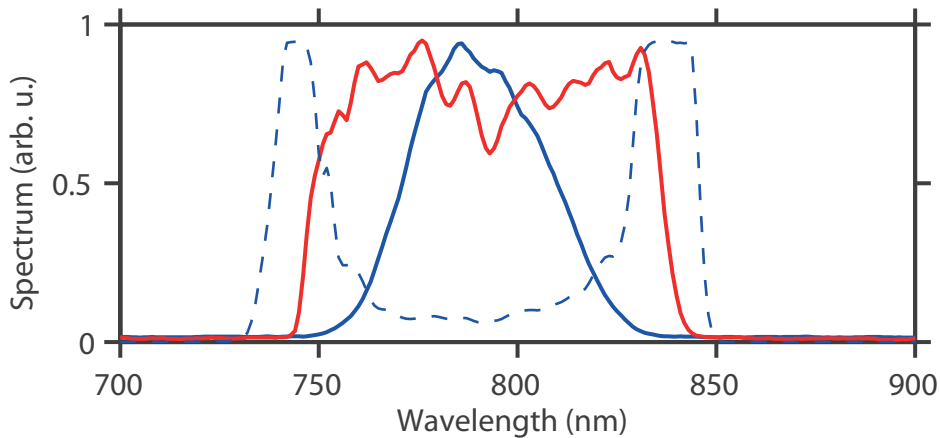


Figure 1.5: Spectrum without (blue plain line) and with (red plain line) the amplitude transmission hole dug in the AOPDF (dashed blue line)

As will be seen further on, the process governing the broadening of the spectrum of a femtosecond pulse in a hollow core waveguide is mainly Self-Phase Modulation (SPM) [43, 44, 45]. According to the principles of SPM broadening, the broader the starting bandwidth is, the more efficient the broadening will be and this bandwidth is therefore critical. Recent investigations have proven that the spectral width is now limited by the reflective optics, and can be further increased by the use of different mirrors in the amplifier system.

The last 5 passes allow the upscaling of the pulse energy to 1.3 mJ, *i.e.* 1 mJ after recompression in a transmission grating setup.

Self-Referenced Spectral Interferometry measurement and optimization

The use of a finely tailored amplitude filter as described in the previous section alters the spectral phase quite considerably, due to phase amplitude mapping phenomenon associated with Self-Phase Modulation. It is therefore required, to achieve an optimal compression, to compensate for the fine spectral phase features introduced by this phenomena, which effectively reduce the coherent contrast of the pulse, and decrease the energy it entails.

Indeed, if the second order phase is large for the bandwidth ($\phi^{(2)}\Delta\omega^2 \gg 1$), as it is the case in a CPA amplifier, each frequency of the spectrum has a group delay that is very different from the adjacent ones, and this group delay is linear. the complex spectrum of the pulse is then *mapped on the time axis* : $t \Leftrightarrow t_\omega = \phi^{(2)}(\omega - \omega_0)$.

Moreover, Self-Phase Modulation (SPM), a nonlinear phenomena at play in the CPA system, is characterized by an intensity dependent index of refraction $n(t) = n_0 + n_2\mathbf{E}(t)^2$, which adds a nonlinear temporal phase to the pulse, proportional to its intensity envelope $\phi_{NL}(t) \propto \mathbf{E}(t)^2$. With the time to spectrum mapping caused by high linear chirp, we can see that *the spectral amplitude will be imprinted on the spectral phase* after recompression:

$$\phi_{NL}(\omega) \propto \phi_{NL}(t_\omega) \propto \mathbf{E}(t_\omega)^2 \propto |E(\omega)|^2 \quad (1.9)$$

Since the spectral amplitude is strongly modulated by the AOPDF in the setup, the spectral phase will be modulated as well, and this needs to be measured and corrected. To this end, we use the Self-Referenced Spectral Interferometry (SRSI) technique [46] implemented in a commercial device (WizzlerTM by Fastlite). This technique, relying on the spectral interferometry of the pulse with a nonlinearly cleaned replica of itself, has the ability to resolve fine coherent contrast loss due to rapidly varying spectral phases [47]. We have used it to measure our pulses, and set up a feedback of the measured spectral phase on the AOPDF located inside of the CPA system. As can be seen on Figure 1.6, the spectral phase measurement before compensation displays quite heavy modulations, which are then completely removed from the pulse after a few iterations of the feedback to the pulse shaper.

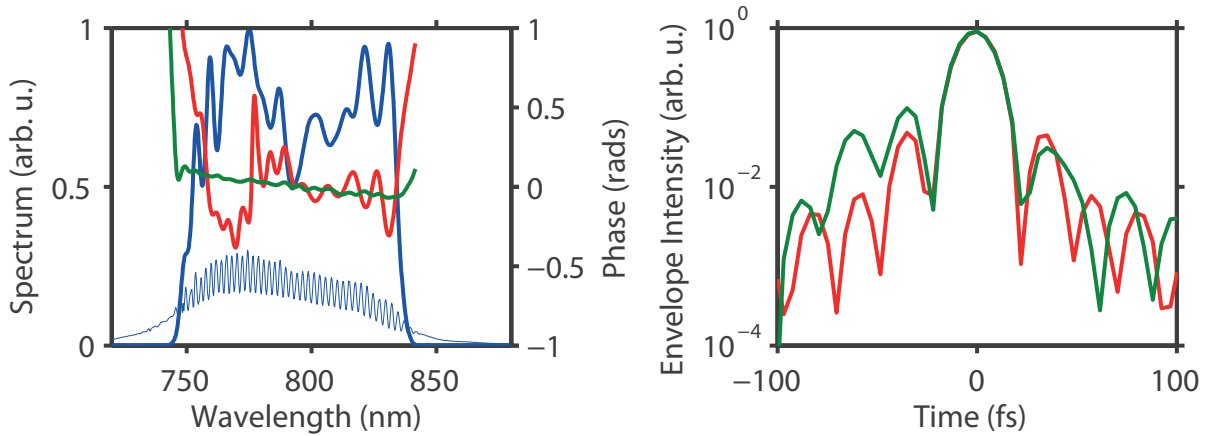


Figure 1.6: **a.** SRSI spectrogram (thin blue), Spectrum (blue) and spectral phase before (red) and after (green) the measurement and feedback loop with the Dazzler **b.** Associated temporal profiles, with gain of coherent contrast energy concentration

This fine compression increases the coherent contrast by one order of magnitude, which concentrates the energy in the main pulse. Also, as can be seen on Figure 1.6, the fast varying phase on the blue side of the spectrum before correction was responsible for the delaying of the blue components, and reduced the effectively available bandwidth for nonlinear mixing in the HCF. Thus, flattening this phase facilitates the broadening process

and its extension to the ultraviolet (UV) range, whose generation is highly sensitive to the original pulse spectral content. This optimization procedure can be realized in about five minutes every time it is needed, after amplifiers realignments for example.

1.2.2 PHz ranging supercontinuum generation

As stated in [45], the supercontinuum generation from high intensity femtosecond pulses in a hollow-core waveguide relies on an intricate interplay of various spatial and temporal linear and nonlinear phenomena (Self-phase modulation, self steepening, self-focusing, waveguide and plasma dispersion, ...). A common feature of all these processes is however that the newly generated frequencies come from a 4 wave-mixing process that mixes 3 frequencies $\omega_1, \omega_2, \omega_3$ to generate a fourth one $\omega_g = \omega_1 + \omega_2 - \omega_3$. From there, it is intuitive that the broader the initial spectrum and the available frequency set, the more effective the broadening will be, since the range of accessible ω_g will be larger.

In our setup, the 23 fs pulses are focused using a 1.8 m focal length anti-reflection coated lens in a 1.1 m long fused silica waveguide with a core hole diameter of 250 μm . To this end we use a 1.8 m focal length anti-reflection coated lens. The capillary is placed inside an airtight pressure chamber, pressurized with 2 to 2.5 bars of Neon gas (see Figure 1.7.a.). The pulses enter the gas chamber through a 0.5 mm thick anti-reflection coated glass window, and exit through a 0.5 mm UV graded fused silica window mounted at Brewster angle. The entrance and the exit windows are mounted respectively 0.8 m before and after the capillary in order to avoid spurious nonlinear effects in the windows.

As can be seen on Figure 1.7.b. the generated supercontinuum spans more than 1 PHz, and has therefore the potential to support the generation of subfemtosecond optical pulses. Indeed, if needed, the spectrum can be reshaped to be more even, at the price of pulse energy. This is what is implemented in our setup, and will be discussed in Chapter 3. The comparison is also shown with the input spectrum, which bandwidth has been increased by an order of magnitude.

1.3 Versatile multioctave spectral phase control: Light Field Synthesizer

As seen in Section 1.1, dispersion control is a critical parameter for the synthesis of attosecond transients. Many different ways to manage the dispersion of femtosecond pulses have been developed over the years. Since all the conventional materials have absorption peaks in the far infrared and the ultraviolet, respectively associated to vibrational and electronic transitions, the refractive index increases with frequency, which results in the addition of a dispersed group delay through propagation. In practice, ultraviolet transitions are usually the closest to the visible range, thus the dispersion is positive, meaning that the blue components are traveling slower than the red ones. Managing the dispersion of optical ultrashort pulses to compress them to their Fourier limit therefore boils down to finding

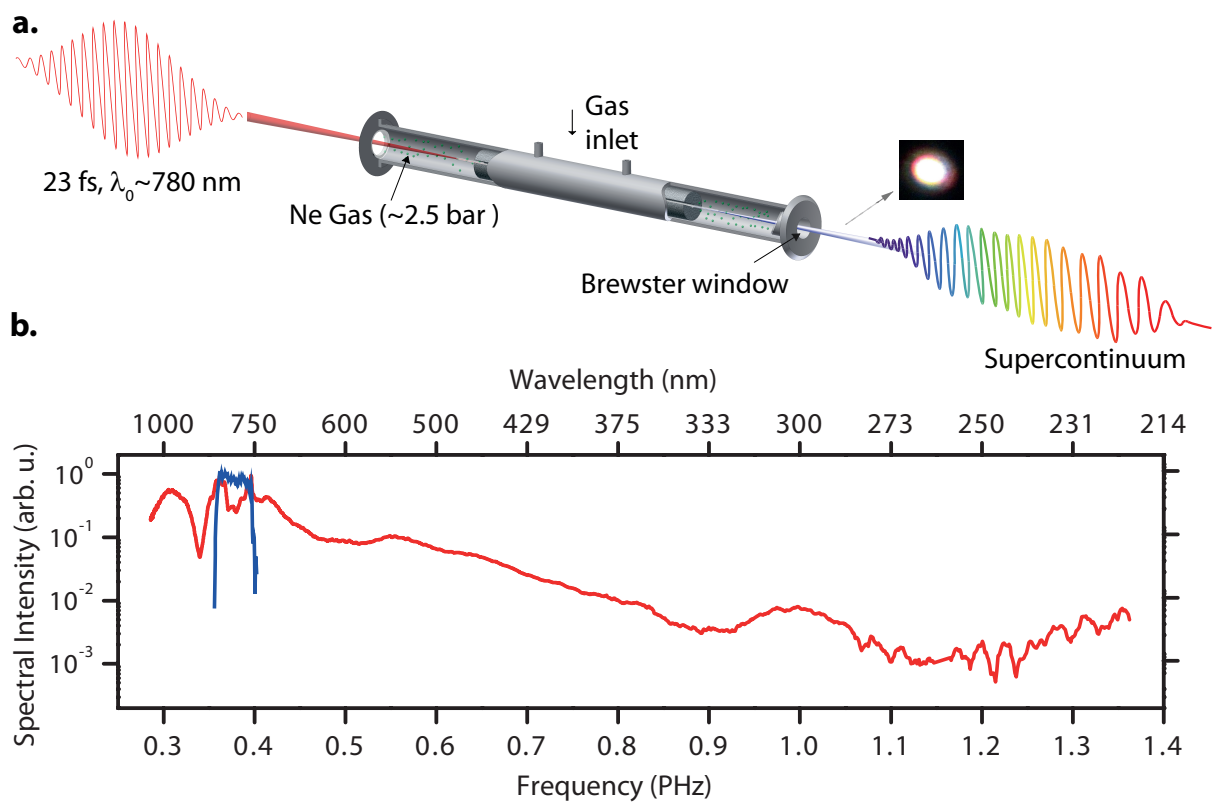


Figure 1.7: a. Hollow-core fiber setup. b. Spectra at the input (blue line) and at the exit of the fiber (red line). (adapted from [48])

ways of implementing controlled negative dispersion, and compensate for the propagation in materials.

Since the advent of femtosecond pulses a whole range of solutions have been demonstrated, such as the use of grating or prism based compressors, sometimes in combination with spatial light modulators (SLM), the AOPDF, or chirped mirrors [49]. Due to their ability to deal with broad bandwidths with a reasonably high efficiency, chirped mirrors have been the solution of choice to manage the dispersion of supercontinua produced by hollow-core fibers [50], giving access to a range of experiments requiring few-cycle high energy pulses, such as the generation of isolated attosecond pulses. It is however known that although this technology is continuously improved to further extend the bandwidth managed by a single chirped-mirror compressor, it is close to its limit. Indeed the broader the bandwidth handled, the lower the dispersion each mirror is able to imprint, and the lower and more spectrally modulated the reflectivity will be [49].

The development of the light field synthesizer has brought tools to overcome these obstacles.

The basic principles and first implementation of light field synthesis are exposed in Ref. [51]. This technique applies the famous "*divide et impera*", or "divide and conquer" adage. Since handling very broad bandwidths with a single multilayer mirror compressor has a limited potential, the supercontinuum is split into several sub-bands, using broadband, phase-controlled dichroic beamsplitters (DBS). In our setup, schematically depicted on Figure 1.8, four of these channels are implemented, the deep ultraviolet (DUV) channel, spanning from 270 to 350 nm, the ultraviolet visible (UV-Vis) channel from 350 to 500 nm, the visible (Vis) channel from 500 to 700 nm, and the near Infrared (NIR) channel from 700 to 1100 nm.

The dispersion of each of these narrower-band sub-spectra is independently characterized using a Transient Grating Frequency Resolved Optical Gating (TG-FROG) apparatus, and compensated with a combination of adapted chirped mirror and glass wedges (to confer some flexibility to the compression scheme). These four beams are then recombined using the same DBS units.

Spatial overlap is ensured by careful alignment on a CCD in the near and the far field. The temporal overlap is taken care of by small piezoelectric driven delay units placed in each channel except Vis, which serves as a reference. In a first place, a nonlinear effect, High Harmonic Generation (HHG) is optimized using the position of these delay units, achieving coarse (blind) temporal overlap. For precise synthesis, we rely on attosecond streaking [2] and field characterization, as presented in Section 1.5.

The overlap being critical, passive stability is ensured by the implementation of the setup on a monolithic Aluminium block thermally stabilized by water cooling, and active stability by the stabilization of spectral fringes produced at the overlap of the channels on the polarization orthogonal to the synthesis axis [51].

This setup, its development as well as details related to the coherent spatiotemporal superposition, locking and efficient transportation of the beams having been exposed in details in Refs. [3, 51, 48], they will not be discussed more here.

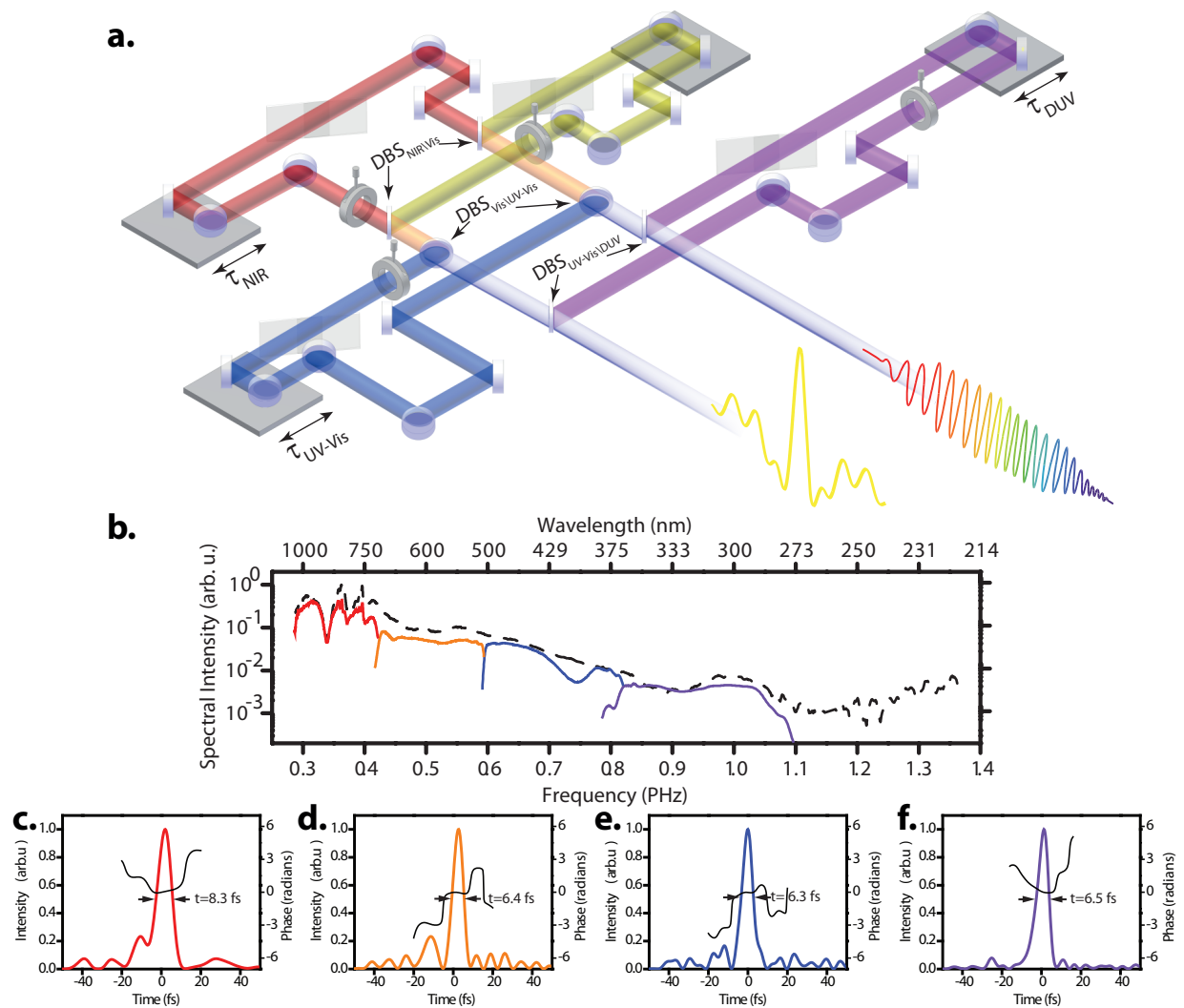


Figure 1.8: Implementation of Light Field Synthesis in our experimental apparatus: **a.** overview of the setup **b.** splitting of the supercontinuum from the HCF in four subchannels **c.-e.** FROG reconstruction of the pulses coming from the four individual channels. (adapted from [48])

1.4 Global phase control of an attotransient

1.4.1 Phase stable CPA system

Once the spectrum has been generated and the dispersion coming from the generation process and its transportation to the experiment has been accounted for and compensated with the light field synthesizer, the last degree of freedom that one has to fix is the absolute phase ϕ_0 presented in Section 1.1. Unlike the rest of the spectral phase and the spectral amplitude, this parameter is not deterministically fixed by the pulse train generation process of the femtosecond mode-locked oscillator. The technique of the f-0 measurement from the radiation generated in the PPLN crystal, as well as the feedback on the pumping intensity via an Acousto-Optic Modulator (AOM) allows the experimentalist to fix the *drift of absolute phase between two consecutive pulses of the train*. By choosing this drift carefully to be a divider of 2π (usually $\pi/2$, and setting the sampling rate of the Pockell's cell accordingly, it is possible to ensure that the absolute phase of two consecutive amplified pulses is constant [52].

This mechanism is the first building block of the absolute phase stabilization of the amplifier. Indeed, this parameter is very sensitive, and drifts constantly due to environmental variations, such as temperature or humidity, or slight beam pointing variations. It is therefore measured after the hollow-core fiber by means of an f-2f interferometer [52], and an active feedback is set up by varying the voltage of a piezoelectric unit on which one of the glass blocks composing the stretcher is mounted. The microscopic glass thickness variation changes the absolute phase of the pulse to bring it back to the desired "locking" value.

1.4.2 Global phase control of a PHz continuum

To change the absolute phase of a waveform, usually a very thin layer of thickness L of a dispersive material is added or removed. This principle applies to our CPA system, where the amount of glass in the stretcher is used a feedback mechanism to control the global phase. However, as we have seen, for potentially subfemtosecond optical transients, the accuracy of dispersion control is critical, and it is legitimate to ask the question of whether a thin layer of material will be able to change the absolute phase without impacting the pulse envelope with higher order dispersion.

When the absorption can be neglected, the change applied on the complex spectrum of a pulse is an addition of spectral phase. Considering this spectral phase variation in the frame moving at the group velocity of its central frequency, we obtain:

$$\Delta\phi(\omega) = \frac{\omega}{c} \left(n(\omega) - \left. \frac{d(n(\omega)\omega)}{d\omega} \right|_{\omega_0} \right) \Delta L \quad (1.10)$$

The added absolute phase $\Delta\phi_0$ is therefore

$$\phi_0 = \Delta\phi(\omega_0) = \frac{\omega_0}{c} \left(n(\omega_0) - \left. \frac{d(n(\omega)\omega)}{d\omega} \right|_{\omega_0} \right) \Delta L = -\frac{\omega_0^2}{c} \left. \frac{dn}{d\omega} \right|_{\omega_0} \Delta L \quad (1.11)$$

The first envelope distorting phase term, the second order phase added by the introduction of glass is:

$$\phi^{(2)} = \left. \frac{d^2\Delta\phi}{d\omega^2} \right|_{\omega_0} = \frac{1}{c} \left. \frac{d^2(n(\omega)\omega)}{d\omega^2} \right|_{\omega_0} \Delta L \quad (1.12)$$

For a pulse of bandwidth $\Delta\omega$, the condition on added second order for the envelope to stay constant is $\phi^{(2)}\Delta\omega^2 \ll 1$. This sets a limit on the amount of material ΔL that can be introduced, and therefore to the absolute phase change that can be realized:

$$\phi_0 < f(\omega_0) \frac{\omega_0^2}{\Delta\omega^2}, \text{ with } f(\omega_0) = \frac{\left. \frac{dn}{d\omega} \right|_{\omega_0}}{\left. \frac{d^2(n(\omega)\omega)}{d\omega^2} \right|_{\omega_0}} \quad (1.13)$$

The result takes a very simple form, where we see that the available absolute phase range depends on the central frequency via a material dependent function $f(\omega_0)$, and the square of the ratio between central frequency and bandwidth, or said otherwise the ratio between pulse duration and period.

For fused silica, at 600 nm, $f(\omega_0)$ equals 0.8. This means that for the user to be able to change the absolute phase by $\pi/2$ without deforming the pulse, the latter has to be longer than 1,4 cycles, i.e. 2 fs FWHM intensity duration. Other materials exhibit even a lower value of f at this wavelength. We see that for our double octave attotransients, inserting more or less glass in the beam is not a reasonable way of changing the global phase.

As a side remark, at 1,25 μm central wavelength, for fused silica f is 16, therefore even a pulse with 0.3 cycles, i.e 1 fs intensity duration, the phase can be harmlessly shifted.

How to change the global phase of our transients then? It is worth noticing that applying this technique on a 23 fs pulse centered at 800 nm is risk-free, since $\omega_0^2/\Delta\omega^2 = 100$, and the envelope will not be impacted by the phase change. Therefore the effect of such a change of material thickness results in the addition of a pure absolute phase offset ϕ_0 . If this pulse is further compressed by 4 wave mixing processes, as is the case in the HCF, this phase offset is imprinted as such on the nonlinear polarization. Indeed, since these effects involve the absorption of 2 photons ω_1 and ω_2 , and the emission of one photon ω_3 :

$$\omega_g = \omega_1 + \omega_2 - \omega_3 \Rightarrow \phi(\omega_g) = \phi(\omega_1) + \phi(\omega_2) - \phi(\omega_3) = \phi_0 + \phi_0 - \phi_0 = \phi_0 \quad (1.14)$$

Therefore, we can conclude that changing the global phase on the long pulse before its broadening in the HCF is an efficient way of controlling the global phase of the attotransient without chirping it. This has been checked by streaking measurements (see next section), validating the previous derivation experimentally.

1.5 Optical attosecond transients

1.5.1 Field characterization and optimization through streaking

The attentive reader will have noticed that while the compression of the pulses in each of the channels of the synthesizer can be evaluated and adjusted using FROG measurements, the exact temporal overlap between the channels, as well as the absolute phase of the waveform remains elusive. To resolve and set these last and essential degrees of freedom, extensive use is made of the attosecond streaking technique [53, 54, 2], which allows the direct characterization of the electric field. For this work, it is experimentally implemented using the setup which will be thoroughly described in Chapter 3.

This technique is a pump-probe scheme in which an isolated EUV attosecond pulse photoionizes the valence electron of an atom (from the $2p$ orbitals of Neon in our most common implementation) at the moment t_r , in the continuum dressed by the electric field of the waveform. The streaking spectrogram (see Figure 1.9 **a.** and **e.**) consists of the photoelectron energy spectra depending on the pump-probe delay $\Delta t = -t_r$. The presence of the minus sign reflects the experimental convention used: Δt is the delay of the EUV pulse compared to the visible pulse, considered as fixed in the streaking experiment.

The most complete and powerful way of treating this kind of spectrogram is the application of the FROG-CRAB algorithm [55, 56], which allows the complete reconstruction of the electric field of the waveform and the photoelectron wavepacket (and the EUV radiation wavepacket if the photoionization cross-section is known [57]). This is very powerful, as this formalism can be in principle applied for any arbitrary EUV and visible radiation shape, in particular in the case of EUV pulse trains where the streaking picture derives to RABITT type techniques [58, 59, 60]. It is however cumbersome and relatively slow to use, and much simpler numerical methods can be applied in the case of an isolated EUV pulse shorter than the fastest features of the waveform to resolve, when only the waveform characterization is sought [61], like in the experiments presented here. This ease of use is of particular interest in the lab for online waveform characterization and optimization required by light field synthesis.

A classical treatment of the electron motion in the field then shows that its momentum p after the end of the pulse will be, with A the vector potential, primitive of the electric field E , ω^{EUV} the ionizing photon frequency and I_p the ionization potential of the considered electron:

$$p(t = +\infty, \omega^{EUV}) = p(t_r) - eA(t_r) = \sqrt{\hbar\omega^{EUV} - I_p} - eA(t_r) \quad (1.15)$$

The hypotheses that the EUV pulse is isolated and much shorter than the fastest field features to resolve and that the photoionization cross-section is constant on the bandwidth of the pulse [57], then justify the approximation that the center of mass of the photoelectron wavepacket energy spectrum recorded at a delay t_r is:

$$E_K(t_r) = \frac{p(t = +\infty, \omega_0^{EUV})^2}{2m_e} = \frac{(\sqrt{\hbar\omega_0^{EUV} - I_p} - eA(t_r))^2}{2m_e} \quad (1.16)$$

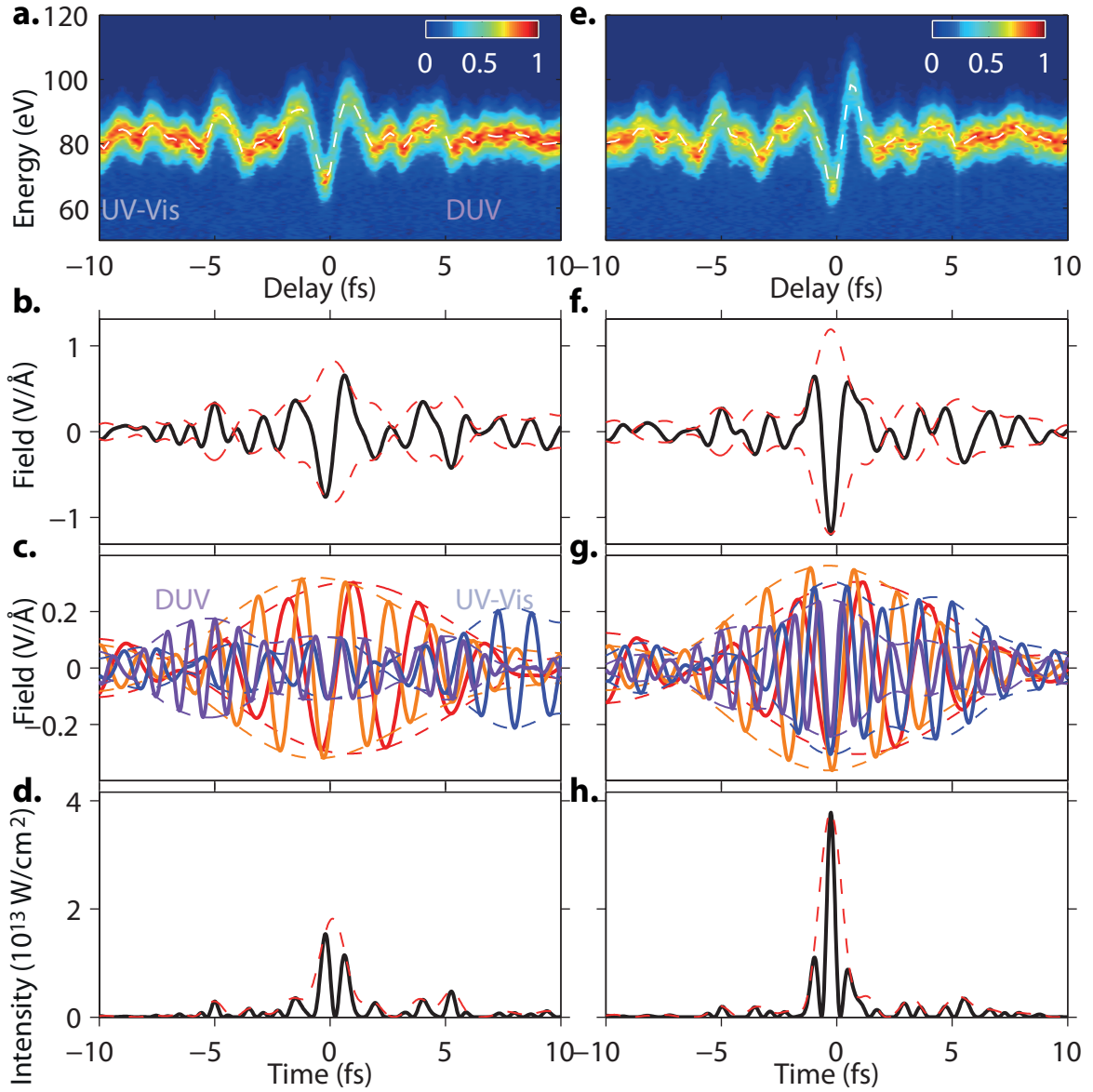


Figure 1.9: Finalizing the synthesis of Transients by streaking: **a.** Original streaking spectrogram, the DUV and UV-Vis channels are delayed (dashed line:center of mass) **b.** Extracted electric field **c.** Isolated channels after adequate Fourier filtering **d.** Resulting instantaneous intensity (black) and envelope (dashed red). **e.** Streaking spectrogram after optimization of delays (dashed line:center of mass). Less modulations out of the central feature. **f.** Extracted electric field **g.** Isolated channels after adequate Fourier filtering, the pulses are synchronized **h.** Instantaneous intensity (black) and envelope (dashed red).

Solving this straightforward second degree equation gives access to $A(t_r)$, which after numerical resampling and derivation, yields a measurement of the electric field of the waveform $E(t) = -dA/dt$ (see Figure 1.9 **b.** and **f.**).

This signal is then numerically Fourier filtered with hypergaussian filters corresponding

to the frequency borders of the synthesizer channels, which yields the fields of the pulses comprised in each of the channels, with their absolute timing with respect to each other. Thus for example, Figure 1.9 **c.** shows that the pulses of the DUV and the UV-Vis channels are desynchronized, respectively by -5.2 and +7.3 fs. These absolute timings are then compensated by the piezoelectric rods controlling the delay units of the synthesizer's channels, which then allows to converge towards the desired waveform (panels **e.-h.**), in which all the channels are correctly synchronized, and a high contrast attotransient is generated.

Figure 1.9 **e.-h.** shows a typical example of a well-synthesized attotransient with a 0 absolute phase. To sum up its characteristics, it is an almost isolated half-cycle of light with 1 fs FWHM envelope and 400 as field intensity duration, with an intensity contrast of more than 4:1 between the main crest and the adjacent half-cycles comprising several μJ on target.

This tool, as demonstrated in the following chapters, is able to drive and accurately control processes that have a response time faster than the field, like High Harmonic Generation (see Chapter 2), or the low-order nonresonant nonlinear response of bound electron systems (see [62, 4, 63]). In combination with a "more conventional" EUV attosecond pulse, in the pump-probe schemes developed in this work, the attotransient will also have the resolution needed to probe phenomena which are lasting down to few hundreds of attoseconds (see Chapter 4, Chapter 5 and Chapter 6).

2

Generation and manipulation of EUV pulses with light transients

If you can't control your peanut butter, you can't expect to control your life.
– Bill Watterson, *The Authoritative Calvin And Hobbes*

The synthesized optical transients presented in Chapter 1 have the particularity to exhibit significant contrast between successive half-cycles of light. Their waveform is also highly controllable, be it by use of the absolute phase or the interchannel delays. This chapter will first show that this high contrast naturally leads to the generation of EUV isolated attosecond pulses for a broad range of absolute phases. This will be one of the building blocks of the experiments presented in Chapter 4, 5 and 6. In a second section, an example of the control of EUV emission achieved by fine tuning of the generating waveform will be shown. To conclude, a theoretical study demonstrating how advantage of the high field contrast inherent to attosecond light transients could be taken to generate keV photons will be presented.

2.1 EUV generation driven by attosecond light transients

2.1.1 Basics of High Harmonic Generation

High harmonic Generation (HHG) has been first observed in the second half of the 1980s [64, 65]. By focusing a laser with sufficient intensity (10^{13} to 10^{16}W.cm^{-2}) in an atomic or molecular gas, its original frequency is upconverted to high odd multiples. In contradiction to what is known from perturbative nonlinear optics [66], the efficiency of generation does not drop continuously with harmonic order, it has a "plateau" behavior, meaning that the generation efficiency stays constant over an extended spectral range, and then exponentially drops at the so-called "cutoff frequency" (see Figure 2.1a.).

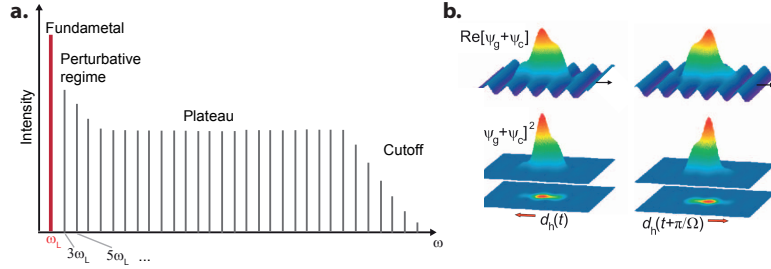


Figure 2.1: **a.** Typical High Harmonic Generation spectrum, with perturbative, plateau and cutoff region (from [67]). **b.** A spatially and temporally rapidly varying electron density is created by the interference of the returning continuum part of the electron wave function ψ_c with its bound part ψ_g shown for the two reversal points (illustration taken from [68])

First works described this phenomena theoretically shortly after [69]. In 1993, the so-called three-steps model, proposed by Prof. Paul Corkum [70] captured most of the observed features of HHG using a semi-classical description of the dynamics of an ionized electron in the field of the generating waveform on the cycle time scale. Its avatar in a quantum mechanical perspective, states the following [68]:

- The first step is the field ionization of a valence electron close to a peak of the electric field. There the field is intense enough to bend the atomic potential to the point where part of the electronic wavefunction can tunnel out of the Coulomb potential. A part of the wavefunction ψ_b stays bound, another part ψ_c is released in the continuum, in the presence of the strong time varying field.
- The second step is the acceleration of this part of the wavefunction of the electron by the varying field of the waveform, away and back to the parent atom. According to Ehrenfest theorem [71], the expectation value of the kinetic energy of ψ_c when it returns to the core is the kinetic energy E_k of a classical electron having been accelerated by the field until this point, which can be very easily calculated with Newton's second law of motion.
- The last step is the recombination of the electron and the parent ion, with the emission of a photon whose energy is the kinetic energy of the electron at recollision, plus the ionization potential I_p that the electron has to evacuate while falling in the ground state again. In quantum mechanical terms, the part of the electronic wavefunction which travelled in the continuum driven by the waveform, has accumulated a kinetic energy E_k , while the bound part has an energy $-I_p$. When these two coherent parts of the wavefunction overlap again, they interfere and produce a time-varying electronic density, with a characteristic frequency $(E_k - -I_p)/\hbar$, and therefore radiate at a photon energy $\hbar\omega = E_k + I_p$.

The full quantum mechanical description of this process, based on the Strong Field Approximation (SFA) has been introduced in [72], where an expression for the time dependent electronic dipole is given, the so-called Lewenstein integral. It has been completed in [73]

and [74], to take into account atom-specific ionization, Coulomb effects and recombination cross-sections. Such a calculation has been developed by Dr. Tosa, and interfaced with our Light Field Synthesis software for fast calculation for various waveforms, and has been used in this work to perform the single-atom calculations.

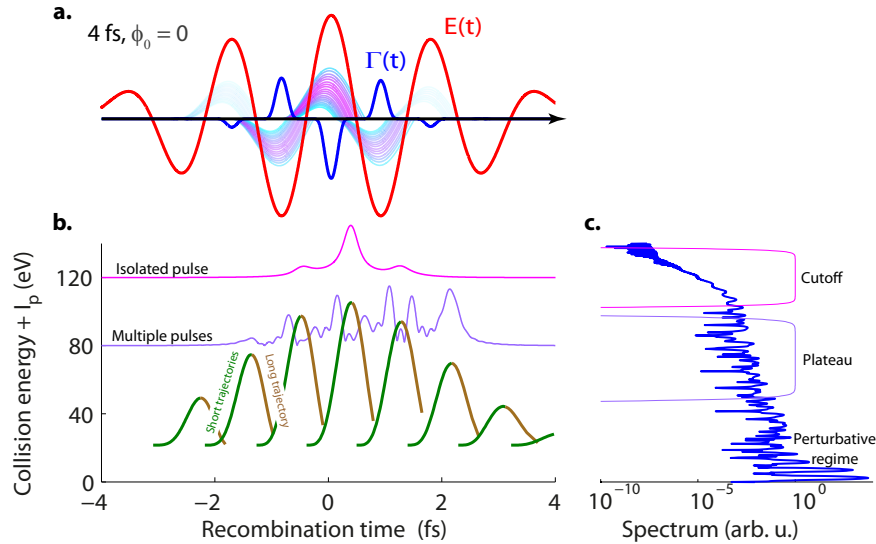


Figure 2.2: EUV generation by a 4 fs Intensity FWHM, 520 nm central wavelength, $2 \cdot 10^{15} W.cm^{-2}$ pulse in Neon. **a.** Trajectory representation: the electric field (red) ionizes an electron at a time t (blue line shows instantaneous ionization rate), and its trajectory in space is represented, color coded with the energy it has at recollision **b.** Green and brown curves show the energy of the electron recolliding at time t (translated vertically by the I_p), respectively for short and long trajectories. The pink and purple curves show the envelope of the radiation contained in the accordingly colored filters of **c.**, which itself displays the spectrum of the nonlinear polarization of a single atom of neon, calculated with this waveform using a Lewenstein integral [72].

Figure 2.2 illustrates these principles on the case of a 4 fs intensity FWHM pulse, with a peak intensity of $2 \cdot 10^{15} W.cm^{-2}$, in Neon atoms. The panel **a.** shows the waveform in red, with the electron trajectories returning to the parent ion, color coded by energy at recollision. As can be seen, in each subset of trajectories, there is one trajectory that leads to the highest attainable energy, while two trajectories, a short and a long one, lead to lower energies. The blue curve shows the ionization rate $\Gamma(t)$. It is based on the fitting of numbers calculated in a time-independent theory, similar to [75] for Helium [76]. Only the sets of trajectories emanating from the most probable ionization events will be well represented in the final nonlinear polarization.

Panel **b.** shows the energy of the recolliding electron as a function of recollision time. We see again for each of the bell like curves the two sets of trajectories, short (green) and long (brown). The emission of photons of different energies being spread in time, the EUV emission will be chirped, positively for short and negatively for long trajectories. The cutoff radiation will however be mainly free of chirp.

It is also to be noted that beyond this single emitter picture, propagation in the gener-

ating medium, then in free space, will lead to the separation of short and long trajectories due to differences of phase-matching [73].

Panel **c.** shows the power spectrum of the time-varying dipole in a single atom of neon, calculated with this waveform using a Lewenstein integral calculation. In the cutoff region, the spectrum has only weak modulations, indicating quasi single event in time, as shown by the pink curve on panel **b.**, frequency filtered dipole in the cutoff region, showing a quasi isolated pulse. The plateau region is very modulated, and indeed the violet curve on panel **b.** shows multiple pulses, generated in several cycles which have the ability to accelerate electrons to these energies. In the perturbative region (below I_p), the structure of harmonics is clearly visible.

2.1.2 Isolated EUV pulse generation with attotransients

The previous description shows that in the regime where ionization does not fully deplete the ground state (the total depletion in the previous example amounts to 20 %), the physics of the EUV generation in atoms is governed, on the cycle time scale, by the sequence of two half-cycles of light, *an ionizing and an accelerating half-cycle*. In the few-cycle pulses regime, the envelope of the pulse starts to constrain the carrier wave, and, as it has been demonstrated experimentally (see *e.g.* [32]), for certain global phase settings, and the appropriate spectral filtering, these pulses have the ability to generate isolated EUV pulses with durations down to few tens of attoseconds.

The degree of confinement to a single half-cycle, or two isolated half-cycles met by the attotransients suggests however that they could be a tool of choice for the precise control of the generation of EUV continua. This is explored in Figure 2.3, which applies the analysis developed on Figure 2.2 for the case of a (measured in the lab) 1fs FWHM attotransient of peak intensity $2 \cdot 10^{15} \text{ W.cm}^{-2}$, for two different values of the global phase $\phi_0 = 0$ (panels **a.-c.**) , and $\phi_0 = \pi/2$ (panels **d.-f.**).

In both cases presented in Figure 2.3, it is quite noticeable that the spectra are very modulation free, and this at almost any photon energies, as confirmed by the frequency filtered dipole envelopes in panels **b.** and **e.**, showing isolated pulses for all the cutoffs. This is due to the fact that in such a pulse, unlike in pulses with more than one cycle of duration, *each of the possible combinations of 2 half-cycles is, under any phase condition, extremely different from all the other ones*. Since the physics of EUV generation is governed by the combination of an ionizing and an accelerating half-cycle, this naturally leads to extremely different electronic dipoles for each of these "two half-cycles combinations". Therefore the EUV spectra generated by each of these combinations will have a very different cutoff energy and generate widely different number of photons. Thus, an isolated attosecond pulse will emerge quite naturally at any global phase setting, almost independently of spectral filtering and in particular for our implementation relying on a thin metallic filter and a multilayer XUV mirror. This is of course of strong interest for our experiments, relying on the presence of an isolated pulse. It is however not obvious that this isolated burst will carry a lot of photons, which sometimes leads to situations of low EUV counts, making measurements difficult.

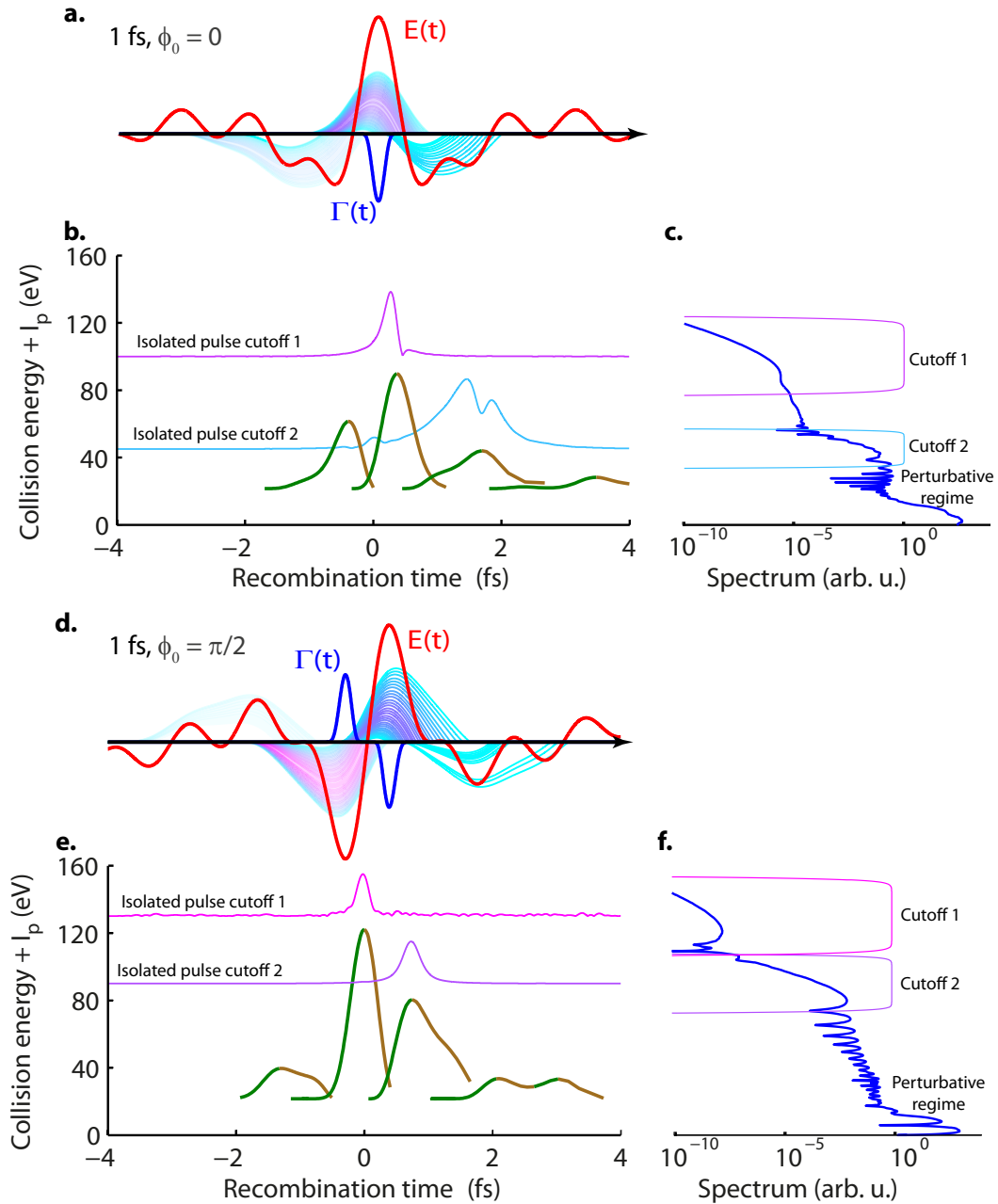


Figure 2.3: EUV generation by a 1 fs Intensity FWHM, $2.10^{15} \text{ W.cm}^{-2}$ pulse in Neon. **a.,d.** Trajectory representation: the electric field (red) ionizes an electron at a time t (blue line shows instantaneous ionization rate), and its trajectory in space is represented, color coded with the energy it has at recollision **b.,e.** Green and brown curves show the energy of the electron recolliding at time t (translated by the I_p), respectively for short and long trajectories. The pink and purple curves show the envelope of the radiation contained in the accordingly colored filters of **c.,f.** These last panels display the spectrum of the nonlinear polarization of a single atom of neon, calculated with a Lewenstein integral.

In the case of $\phi_0 = 0$, there is one dominant ionization event, which leads to a low cutoff of around 40 eV, due to the absence of a strong accelerating field (cutoff 2). The highest cutoff (cutoff 1) has much less photons, but is at much higher energy, because it comes from the ionization by a weak spike of field, but is accelerated by the first strong field crest. The plateau associated to this cutoff even lacks the modulation characteristic of the interference of short and long trajectories, quite seeable on the plateau of cutoff 2 in panel **f.** This is also seen on the purple curve of **b.**, which shows an envelope developed on the short trajectories side, but abruptly falling for the long trajectories side. This is due to two facts : first the short trajectories are less chirped than the long ones, as can be seen by the asymmetry of the corresponding collision energy bell, and the strong asymmetry of the ionizing spike considerably suppresses the ionization for long trajectories.

The second case, with $\phi_0 = \pi/2$, is more balanced, and corresponds to what one would intuitively think to use as a "perfect EUV generator": a first strong isolated field crest to ionize the medium efficiently, and a second one to accelerate the electron to high energies before recollision. This corresponds to the cutoff 2 of panel **f.**, which indeed shows a strong isolated plateau from 20 to 90 eV (the modulations are only due to interference of long and short trajectories), enough bandwidth to potentially generate a 50 as pulse. It is however to be noticed on the recollision energy curve (panel **e.**) that the second strong crest is not the most efficient for acceleration, since cutoff 1 extends even further. The first strong half-cycle is more efficient, due to an artificially long half-cycle created in front of it by the envelope of the field. Indeed the trajectories using this half-cycle as "accelerator" are longer, which leads to higher accelerations, since it is known [72] that the cutoff frequency scales with the square of the carrier period of the driver field.

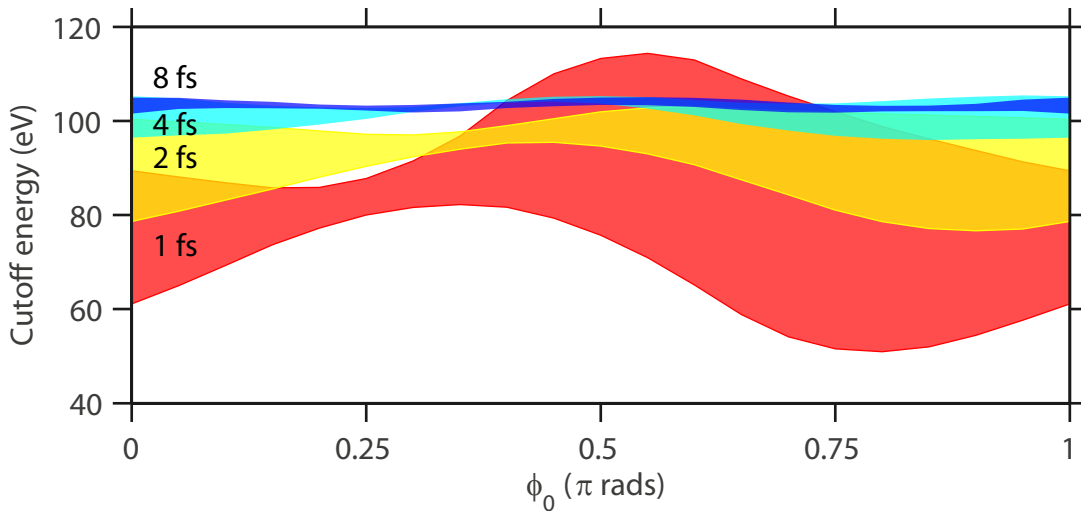


Figure 2.4: Cutoff variations with global phase for different durations. The colored band represents the region of cutoff 1 (see cutoff region 1 in Figure 2.3), for pulses with same peak intensity $2 \cdot 10^{15} \text{ W.cm}^{-2}$ and central wavelength 540 nm, but various intensity FWHM durations, 8, 4, 2 and 1 fs.

To illustrate these concepts, Figure 2.4 shows, as a function of global phase, the extent

of the first cutoff for pulses with various intensity FWHM durations, but similar cycle level structure to make the comparison fair (same envelope peak intensity $2 \cdot 10^{15} \text{ W.cm}^{-2}$ and central wavelength 540 nm, which is the central wavelength of our synthesized attotransients). It represents the extent of the spectral region where a single EUV generation event exists. It is clear that the longer the pulse, the smaller and the more stable with respect to phase this domain is.

An experimental verification of this fact is shown on Figure 2.5, displaying measurement taken with an EUV spectrometer only separated from the EUV source by reflections on a gold:Platin (Au:Pt) mirror, and an Au coated flat-field grating, as well as $1 \mu\text{m}$ of Zirconium (Zr) used to filter out the driver's radiation. The graph displays a broad (30 eV) spectrum, free of any spectral modulations (red curve), as well as a modulated spectrum coming from an imperfectly compressed pulse (blue curve). Both spectra are corrected for the Zr transmission (data from [77]). The resolution of this spectrometer, although limited to 1 eV, would be sufficient to resolve pulses separated by less than 3 fs, which would be the case with our driver wavelength, and we can therefore conclude on the single event character of HHG in the case of the red curve.

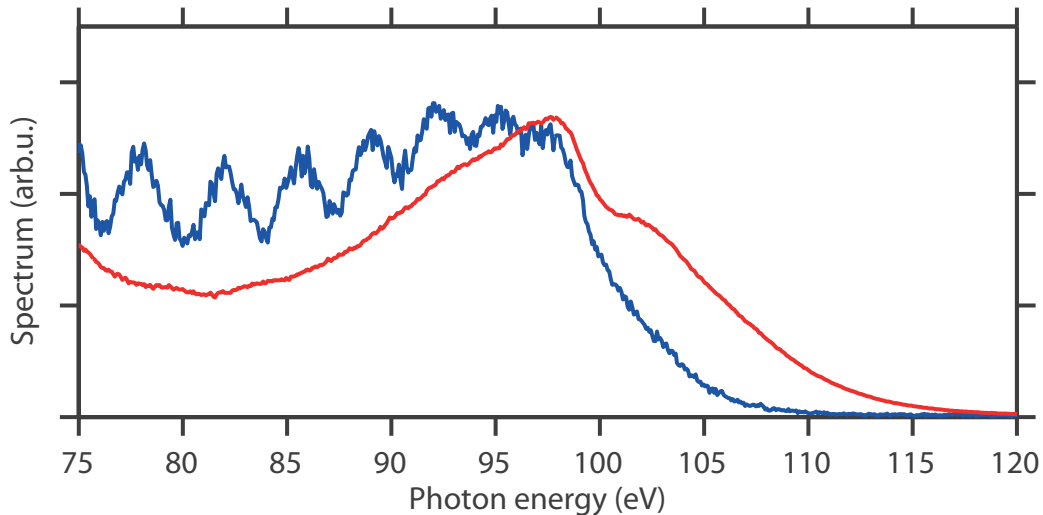


Figure 2.5: HHG spectra generated by a 1.8 fs Fourier limit FWHM intensity transient (with unknown absolute phase) in a case of good compression (red curve) and imperfect overlap between the channels (blue curve). The kink at 100 eV comes from the silicon coating of the EUV CCD used.

Thus, we have seen that the high temporal confinement characteristic of our attotransients (and to a smaller extent for single cycle, 2 fs FWHM pulses) leads to a situation for which most of the global phase settings, an isolated pulse is present in any energy range.

Other technologies have been developed to generate isolated attosecond pulses from longer driver fields, like polarization gating [78], in which the experimentalist imposes a time varying ellipticity to a long pulse. This prevents the recollision of the ionized electron during all of the half-cycles but one. It is now mature enough to enable the generation of isolated attosecond pulses from 25 fs FWHM pulses [79]. Ionization gating is also used

[80, 81]. In this method, the strength of the field is such that the atom is fully ionized after the first few half-cycles. Thus, only the first cycles of the pulse encounter a medium capable of generating EUV, leading to a single attosecond pulse.

2.2 Control of attosecond pulse birth by synthesized optical drivers

As mentioned in Chapter 1, and developed in [3, 51], the manipulation of the interchannel delays on a subcycle scale gives the ability to control the synthesized waveform. According to the ideas developed in the previous section, fine modifications of the waveform will impact the very nonlinear generation of EUV light in a significant way. The streaking metrology, allows the reconstruction of the synthesized waveform, but it also carries information about the generated EUV pulse. This section presents a way of using the streaking to study the control of the electron recollision time exerted by the synthesis of different waveforms.

Figure 2.6 shows the comparison between 2 consecutive streaking measurements taken with a 3 channels (NIR, Vis and Vis-UV) version of the synthesizer, their extracted waveforms and channels decomposition. The measurement of panel **a.** is the reference measurement. From there the NIR channel has been delayed by $\pi/2$ of its central wavelength (corresponding to 730 as) to lead to the waveform measured in panel **b.**. Panel **c.** shows the comparison between the extracted waveforms (reference in grey), and panels **d.** - **f.** between the extracted 3 channels.

Since the experimental pump-probe setup is externally stabilized (see Chapter 3), only the infrared channel is expected to show a different delay in the measurement of panel **a.** and **b.**. However, the analysis of panels **d.** - **f.** reveals that all of the 3 channels, including the UV-visible and the visible channels, supposed to have been left untouched, appear to have been delayed. To explain this fact, it has to be reminded that in streaking metrology, the optical waveform is sampled by the isolated EUV pulse. We then have to conclude that the absolute timing of this EUV pulse with respect to the visible channel has been changed between the two measurements. In our experimental implementation the EUV pulse is generated by the field that will be sampled. It therefore follows that the change applied to the waveform (shift of the IR channel) has led to a disturbance of the electron trajectories responsible for the EUV pulse generation, and hence an absolute change of the recollision, and radiation emission time.

To confirm this fact, a Lewenstein calculation is presented with the two sampled waveforms, for Neon and a peak intensity of $6 \cdot 10^{14} W.cm^{-2}$, corresponding to our experimental parameters. The results are displayed on Figure 2.7. They show, on panels **a.** and **b.** that the radiation filtered in the cutoff by a spectral filter mimicking the 150 nm of Zirconium and the multilayer refocusing the EUV beam on the streaking target has a clear isolated structure, centered at +0.6 fs for the reference waveform. For the waveform obtained after NIR channel delaying, the temporal structure is more disturbed, with the advent of a small

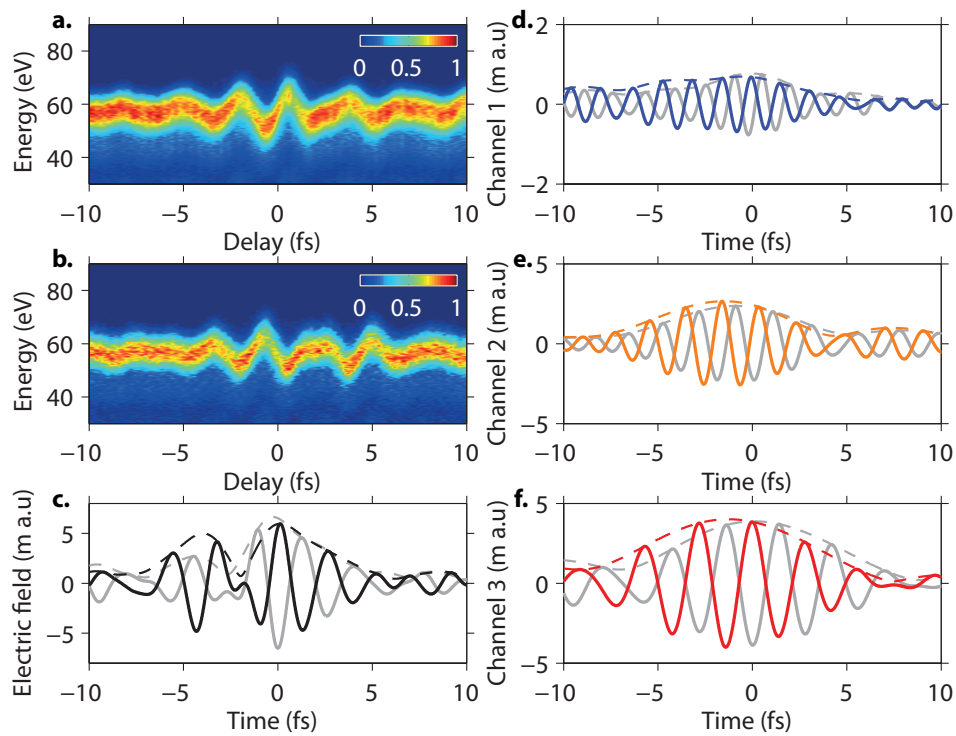


Figure 2.6: **a.** Streaking spectrogram of the original pulse **b.** Streaking spectrogram after delaying the visible channel by 730 as. **c.** original (grey) and modified (black) extracted waveforms **d.** original (grey) and modified (blue) extracted Vis-UV channel fields **e.** original (grey) and modified (yellow) extracted Vis channel fields **f.** original (grey) and modified (red) extracted NIR channel fields

pulse replica at +2 fs, but the main pulse is also centered at +0.6 fs. Hence, although the two waveforms are very different, the positioning of the generated EUV pulse on the time axis derived from the pump-probe delay axis is the same. It confirms the idea that the time axis extracted from a streaking measurement is relative.

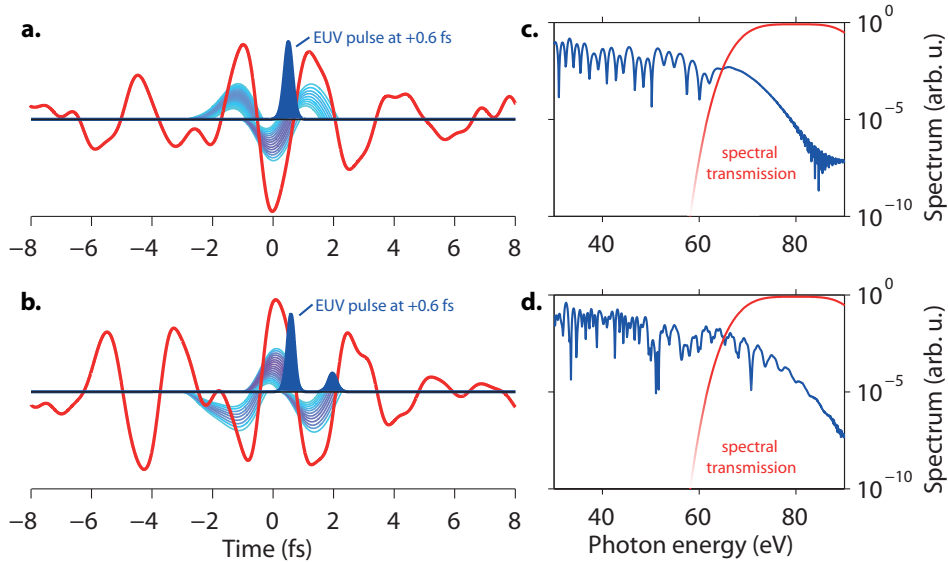


Figure 2.7: **a.**, **b.** Sampled waveforms of the original and modified pulses, with trajectories and envelope of the spectrally filtered EUV radiation **a.**, **b.** Single atom Lewenstein dipole spectrum for the the original and modified waveforms

Therefore, to compare the two waveforms on a common absolute time scale, one should find a way to measure the EUV pulse generation time shift, and take it into account. Since we know that the visible channel absolute timing is unchanged between the two measurements, this can directly be done by shifting the time axis of the second measurement until the reconstructions of the field of this channel match. This shift amounts to a delay of -700 as. The result, shown on Figure 2.8, then shows the correct synchronization of channels UV-Vis and Vis, and the imparted delay of $\pi/2$ on channel NIR. The 700 as delay applied here is a direct measurement of the shift of the absolute birth time of the EUV pulse imposed by the waveform change. This delay is, within measurement uncertainty, equal to the delay imposed on channel NIR between the two measurements, showing that this channel is the main driver of the EUV generation in our experimental conditions.

Other pairs of measurements have been investigated in a similar fashion and show that the delaying of the NIR channel is able to impose shifts of the attosecond birth time as big as 1.6 fs, when the effect of a shift of the UV-Vis channel is a driving on a smaller range of few hundreds of attoseconds.

As a final remark, the Lewenstein calculation presented as support for this interpretation may seem rather simplistic, as it represents only the single atom response and as such does not take propagation effects during the generation into account, and the waveforms have been sampled in a different place than the generation target. Yet, between

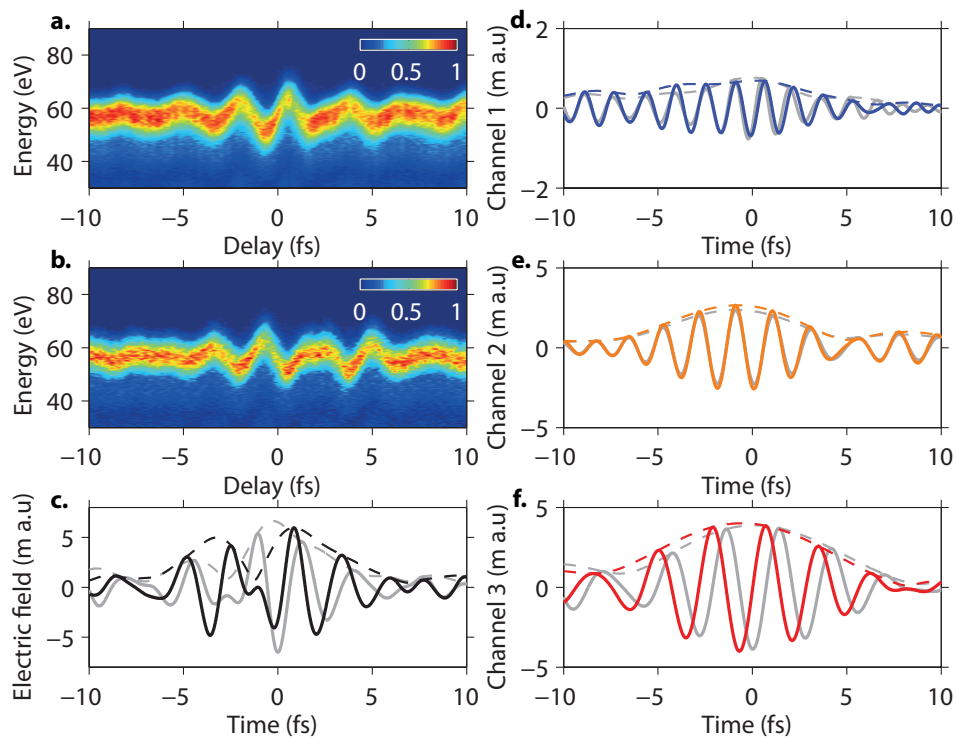


Figure 2.8: **a.** Streaking spectrogram of the original pulse **b.** Streaking spectrogram after delaying the visible channel by 730 as. **c.** original (grey) and modified and time shifted (black) extracted waveforms **d.** original (grey) and modified and time shifted (blue) extracted Vis-UV channel fields **e.** original (grey) and modified and time shifted (yellow) extracted Vis channel fields **f.** original (grey) and modified and time shifted (red) extracted NIR channel fields

the generation and the sampling, the field underwent only absolute phase shifts, through propagation in free space, leading to Gouy type phase shift, the crossing of 15 μm of nitrocellulose, which have been checked to have no differential effect on the phase of all the frequency components and a reflection on a silver (Ag) mirror, which on the considered bandwidth has a flat reflectivity, and therefore only adds π to the absolute phase. The waveform in the generation target and the sampled waveform should therefore be related by a given absolute phase shift, similar in both measurements, and it has been checked that the calculated EUV radiation from the cutoff are synchronized for both waveforms for 70% of the possible absolute phases.

2.3 Generation of kilo-electronvolt photons with sub-cycle optical pulses

It can be inferred from the physical picture of HHG presented in the previous sections, and it has long been well known [72] that for a monochromatic driver field, the cutoff energy is $I_p + 3.17U_p$, with U_p the ponderomotive energy, the average energy of a free electron in the driving field. Therefore this cutoff varies like $I\lambda^2$, with I the intensity of the field. To extend this cutoff to higher photon energies, two kinds of methods are therefore indicated: increasing the intensity, or increasing the carrier wavelength. Both have undesired side effects: with an intensity that is too high, the first weak-half cycles of even a few-cycle pulse have the occasion to completely deplete the ground state of even Helium, the most stable neutral atom ($I_p = 24.6 \text{ eV}$), and therefore suppress the EUV generation for the strongly accelerating half-cycles. By increasing the carrier wavelength, the electronic wavepacket travels longer in the continuum, quantum diffusion makes it transversally larger and the recombination efficiency with the ground state decreases, leading to lower efficiencies. It has however recently been demonstrated that phase matching could play in favor of higher wavelengths in high pressure gas cells [82]. In [83], it is suggested that the use of synthesized light pulses could overcome these limitations, by increasing the recollision energy without increasing the time spent in the continuum.

As seen in section 2.1.2, the attotransient with a phase of $\pi/2$ can be thought as a tool of choice to fulfill this purpose, since it possesses non standard trajectories with higher recollision energies, and lacks strong pre-structures which would ionize the atom completely, and cancel the HHG efficiency before the strong accelerating features come into play. We have investigated these behaviors by doing full (including propagation) calculations of the generated EUV fields, in He gas for a peak intensity of $10^{16} \text{ W.cm}^{-2}$, which ensures full ionization of the medium, even for the shortest pulse used, the attotransient (see Figure 2.9). For these calculation, we generated four waveforms (same as used in Figure 2.4) having the same peak intensity on axis ($10^{16} \text{ W.cm}^{-2}$), central wavelength (540 nm), absolute phase ($\pi/2$), and same beam waist in focus, but increasing time duration, with a FWHM intensity duration of 1, 2, 4 and 8 fs, as seen in the inset of Figure 2.10 a.

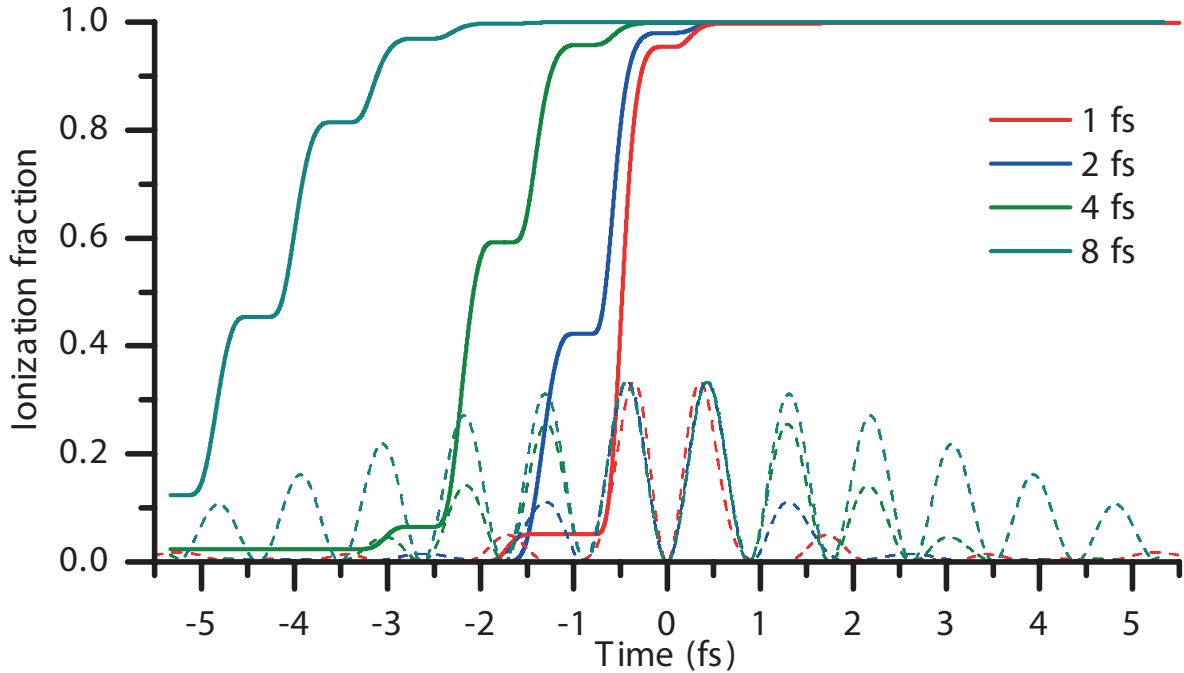


Figure 2.9: Fractional ionization of a single atom placed on axis in the first layer of gas, for waveforms of different durations

In collaboration with Dr. V. Tosa, numerical calculations were performed, extending a non-adiabatic three dimensional model describing HHG by a two-color field [84] to the case of the four coherently added arbitrary fields from our 4 channel synthesizer, propagating collinearly. In a first step the wave equation is solved for each field propagating in a space-time-dependent refractive index, accounting for dispersion from neutral atoms and from electron plasma as well as for optical Kerr effect. The total electric field given by the four channels superposition produces a plasma density which was calculated using the exact static ionization rates reported for He [75], the atom used in this study at a pressure of 50 Torr. Next we estimated, by using the strong field approximation [72], the single dipole response to the propagated field all over the interaction region. Finally the gas polarizability was used as a source term to solve the propagation equation for the harmonic field, taking again into account the frequency dependent absorption and dispersion. The result of the calculation is the harmonic field $H(r, z, t)$ in cylindrical coordinates.

In Figure 2.10.a., we show the single dipole response at the center of medium entrance for the four waveforms which can be seen in the inset (same CEP of $\pi/2$ was assumed for all). At this intensity we see a cutoff going beyond 1 keV for the 1 fs transient and multiple cutoffs of lower photon energies for the other waveforms. Intuitively, if earlier half-cycles are involved in ionization, then, corresponding dipoles develop at lower intensities. Here we can see the advantage of using shorter pulses: the shorter the pulse the higher the intensity at which a dipole develops. For longer pulses we see ionization at lower intensities in earlier cycles while at higher intensities the medium is already depleted and generates no more dipole (Figure 2.9).

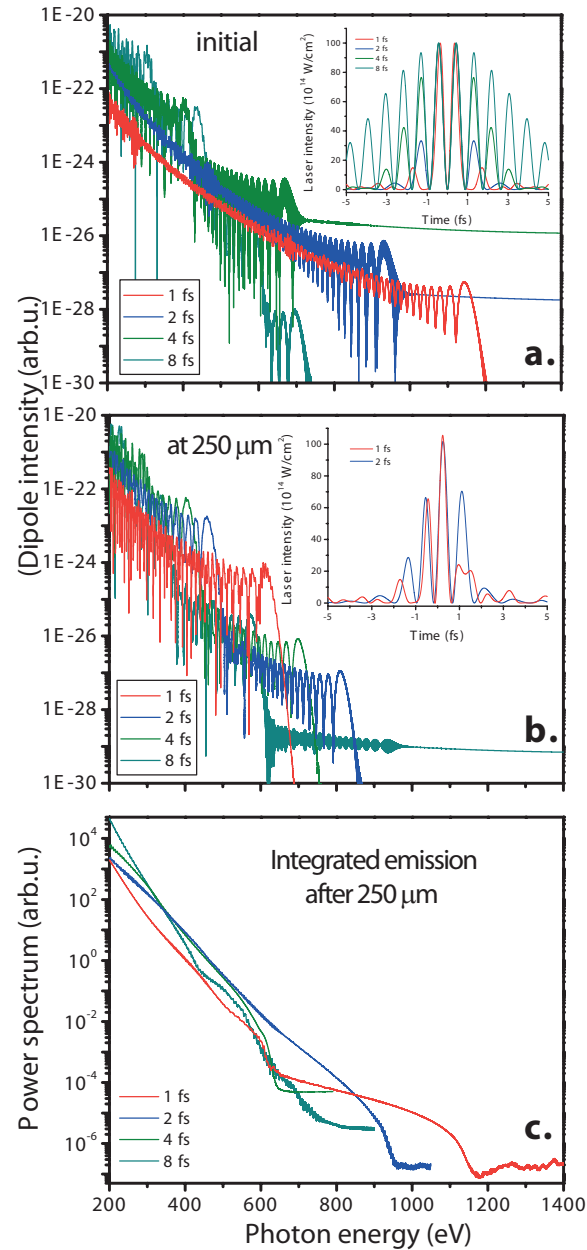


Figure 2.10: a. Single dipole response to the waveforms (shown in inset) at medium entrance; b. dipole response at medium exit (inset showing the 1 fs and 2 fs waveforms after 250 μm of propagation) c. Spatially integrated power spectrum at medium exit

After 250 μm of propagation the single dipole response (see Figure 2.10b.) has markedly changed, the main feature being the cutoff withdrawal, more marked for the 1 fs transient (from 600 to 1200 eV) and gradually less for the 3 other fields, so that we see almost no change for the dipole induced by the longest waveform. This withdrawal is directly connected with the modifications which each driving waveform suffers during propagation: the main changes, seen in the inset of Figure 2.10b. for the 1 fs and 2 fs cases, is a phase slippage and intensity modulation at the half-cycle level, due to defocusing and the self-phase modulation induced by the sharp variation of the refractive index. It is worth to note that both these changes contribute to the cutoff reduction during propagation, since they are modifying the structure of the ionization-acceleration half-cycle pairs.

The total harmonic emission, radially integrated at medium exit, is shown in Figure 2.10c. for the four cases. In the photon range from 200 to 1200 eV there is a ten order of magnitude span in the power emitted, reflecting the same order of magnitude variation of the single dipole. Around 1 keV only the shortest waveform builds-up a harmonic signal while going down to lower photon energies the dominant emission pass to longer fields so that at 200 eV the most intense harmonic signal is generated by the longest waveform.

To clarify the amount of phase-matching involved in the generation of the spectra of Figure 2.10, we represented in Figure 2.11 the dependence of the harmonic field on propagation distance for the attotransient, for different photon energies. For low photon energies up to 400 eV we see a quadratic dependence which denotes a standard phase-matched process [85]. For higher photon energies we see an initial increase and then no more harmonic field variation because the corresponding single dipole is zero, due to the driving field intensity decrease below the corresponding cutoff intensity. Obviously, the higher the photon energy, the shorter the distance over which the harmonic field builds-up before propagation destroys the ability of the waveform to generate the corresponding photons.

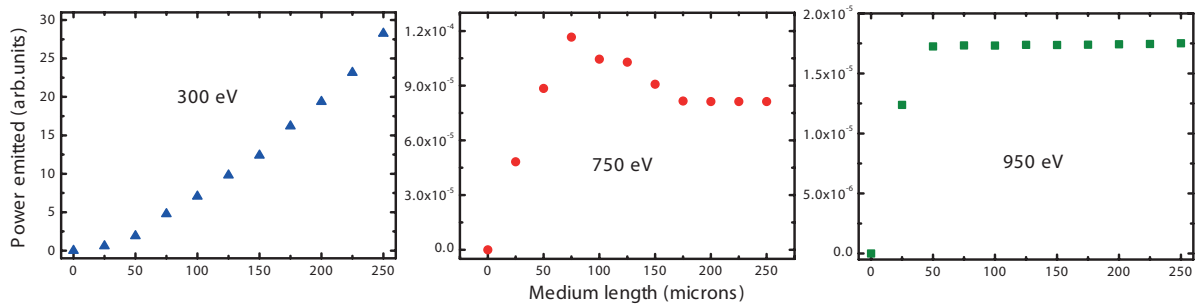


Figure 2.11: Build-up of harmonic field at different photon energies (left 300 eV, center 750 eV and right 950 eV) for the 1 fs waveform

To investigate the ability of the waveforms to produce short isolated pulses, we calculated the time structure of the total harmonic field emitted at medium exit when high-pass filtered from 80% of their respective highest cutoff energy. Plotted in Figure 2.12 are the normalized time-dependent fields when the EUV emission of Figure 2.10c. is filtered from 80% of their respective cutoffs. One can see, without any chirp compensation, single at-

to second pulses formed clearly for drivers of duration 1 fs FWHM (28 as), 2 fs FWHM (67 as) and 4 fs FWHM (195 as), while the longest one produces a train of pulses, clean in the early part of the pulse and more affected by ionization-induced distortions at later times. The peak intensity ratios for the four bursts is WF1:WF2:WF4:WF8 1:5:160:40, while the ratios of the areas under the peaks are 1:1.4:2250:4500.

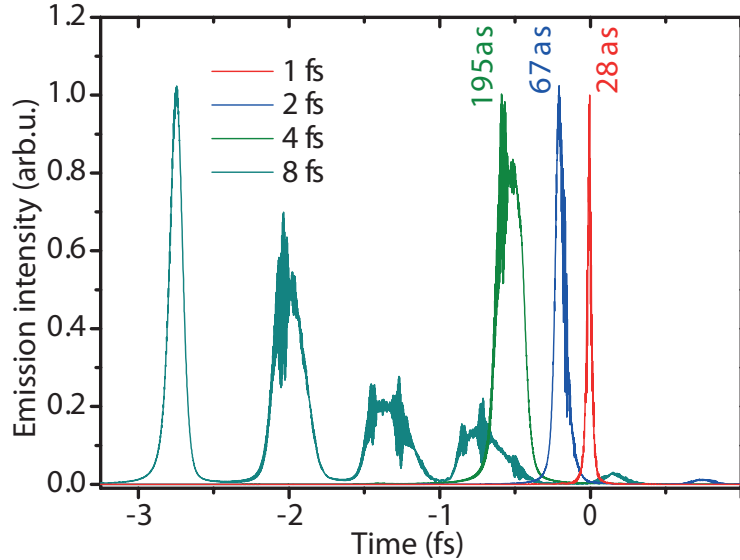


Figure 2.12: Temporal envelope of the cutoff radiation at the exit of the medium, obtained by Fourier filtering of the radiation of frequency above 80% of the respective cutoff energies.

This study shows that isolated attosecond pulses in the keV range could in principle be generated from high peak intensity synthesized attotransients, although with yields that would probably call for different phase matching schemes. Of big interest is also the fact that water window photons are present with a decent yield, and a spectrum lacking modulation indicating multiple recollision events and generated pulses. This indicates that high energy synthesized pulses could be a promising tool for generation of these higher energy photons, and their use in pump-probe experiments involving attosecond optical transients.

The current implementation of our direct EUV spectrometer does not allow the sampling of spectra much higher than 120 eV (see Figure 2.5), due to large angle (15 degrees) Au:Pt reflections. In the framework of this thesis an upgrade of this spectrometer based on multi grazing incidence reflections has been designed, to investigate multi-100 eV EUV generation by synthesized pulses. Together with a well-started major scheme and power upgrade of the synthesis concept [62]. It will, in the future, allow for experimental investigations of these phenomena.

3

EUV-Visible attosecond pump-attosecond probe experimental setup

In any statistics, the inaccuracy of the number is compensated by the precision of the decimals

– Alfred Sauvy

To probe phenomena in real time, pump probe schemes need at least two pulses shorter than the studied phenomenon, with a delay controlled accurately at a fraction of the desired resolution. To realize attosecond pump probe measurements implying one EUV and one visible attosecond pulses, some improvements to the beamline have been necessary. The first section will give an overview of the beamline, and will be followed by a presentation of the adaptations realized to conduct our experiments with the required precision.

3.1 Overview of AS-1 beamline

The AS-1 beamline has been commented in numerous PhD theses and publications (see *e.g.* [52]), we will not review its implementation in detail. An actualized version of its scheme can nevertheless be found on Figure 3.1. We will focus in this chapter on the relevant changes introduced in the course of this work.

3.1.1 Intensity control by closed loop iris, and scaling of the measured waveform.

We have implemented a closed loop-iris (from the company Smaract) controlled by our transient absorption software, which allowed us to do intensity-delay dependent measurements, as presented in Chapter 5 and Chapter 6. Importantly, it should be considered that opening the iris to increase the peak intensity both lets more energy though to the experimental target, and changes the size of the beam focus, due to diffraction effects. The streaking measurement gives an absolute value of the peak intensity of the waveform in

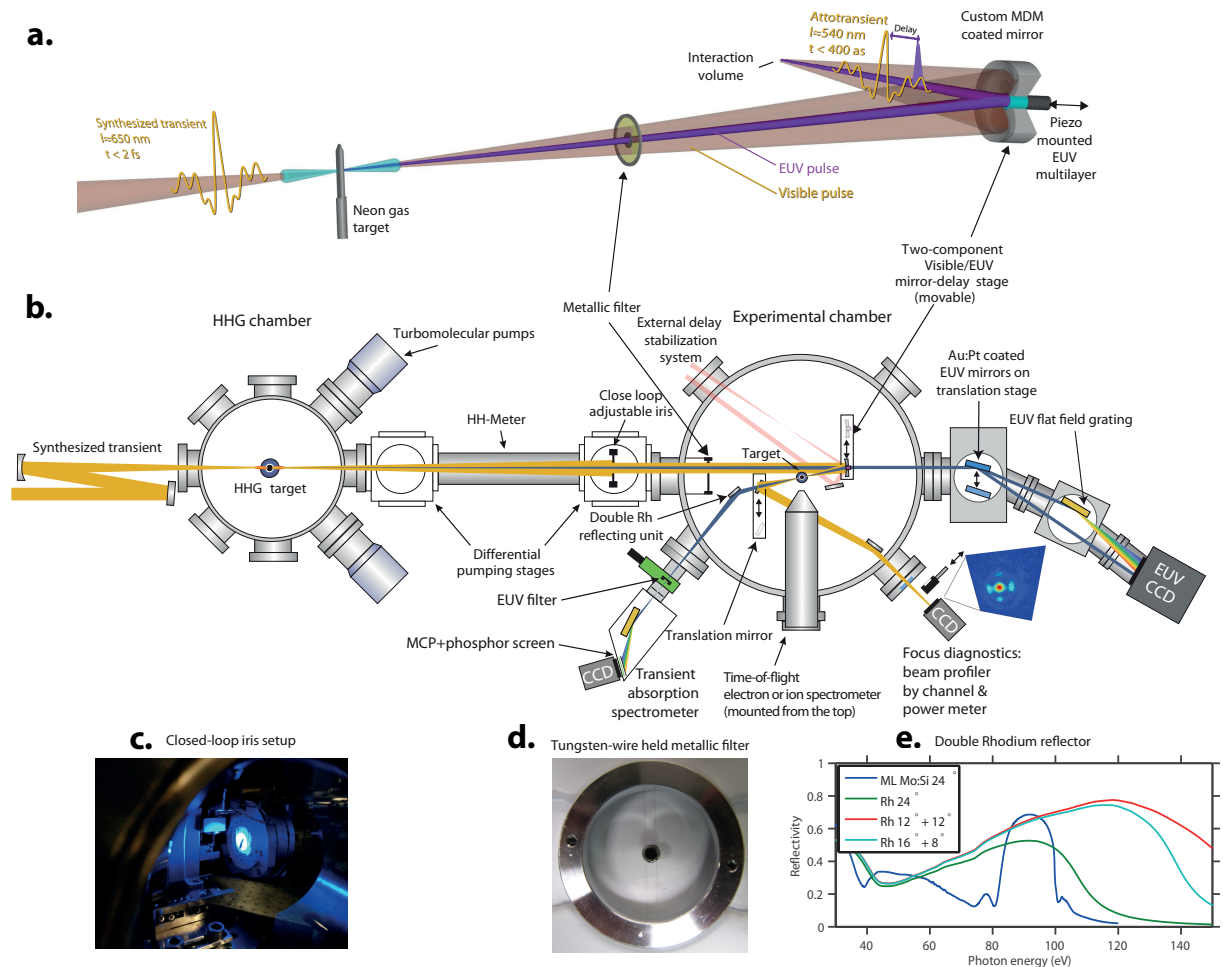


Figure 3.1: Overview of the AS-1 beamline. **a.** Is a schematics of the beam separations to the experimental target. A sub 2 fs pulse is focused in a Neon gas cell to generate EUV. A suspended metallic filter filters the visible radiation out of the beam central part, which carries the EUV radiation, more collimated. The visible beam is spectrally filtered by a MDM coated mirror which refocuses the final attotransient in the interaction region. The EUV radiation is refocused by a EUV multilayer mirror mounted on a piezoelectric unit used to introduce the attosecond controlled delay between pump and probe pulse. **b.** shows the experimental layout of the full beamline. **c.** shows the closed loop iris setup **d.** shows the tungsten-wire held metallic filter, **e.** the double Rhodium reflector used to refocus the beam in the spectrometer for transient absorption. Adapted from [67]

the interaction region, but when scaling this value to obtain the peak intensity attributed to a measurement point with a different iris opening, one has to use a scaling that takes into account this spatial effect, and not only the increase of total energy measured after the chamber by a powermeter. To do this, we always use the system imaging the profile in the interaction region, and record the scaling of the averaged peak value recorded by the CCD on a 3×3 pixels region (corresponding to $2.5 \times 2.5 \mu\text{m}^2$ in the focus) around the focus. Figure 3.2 presents a typical measurement of this value (blue curve), contrasted with the scaling extracted from the power measured in the powermeter (red curve), and integrating the intensity over the full CCD (green curve). As can be seen, considering only the latter gives an error of intensity scaling of a factor 2.

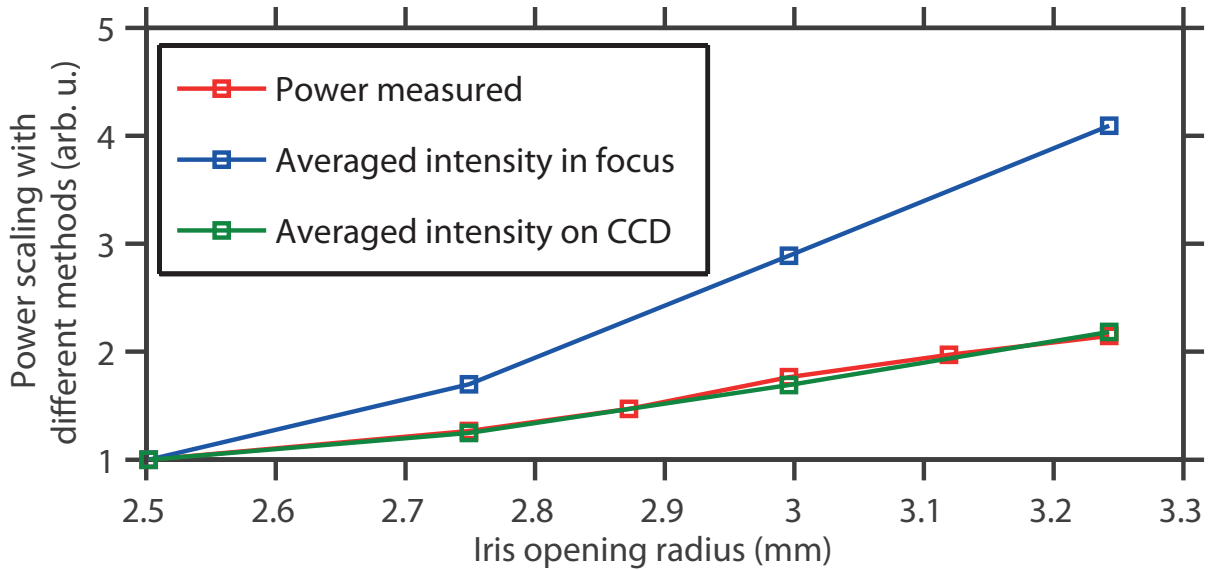


Figure 3.2: Intensity scaling with iris opening extracted by 3 different methods from the streaking iris opening (2.5 mm): total measured power (red), averaged measured intensity over the spatial profile (green) and averaged intensity in a $2.5 \times 2.5 \mu\text{m}^2$ area in the focus.

3.1.2 Using the exact waveform measurement to analyze the experiments

An important feature of our setup is the sub-micron precision of the motorized target holder, which allows a rapid switch between the streaking nozzle, used for the attotransients characterization and synthesis, and the experimental target, be it a gas cell or one of the $\simeq 100$ nm thick solid targets we have used.

This allows, for a visible-EUV experiment, to use the *exact waveform that has been characterized*, including its absolute intensity. Indeed, for streaking to happen, the EUV beam size, in the plane in which the streaking nozzle delivers atoms, is smaller than the visible beam. The opposite would prevent a good streaking and reconstruction quality by blurring the spectrogram, and a knife-edge measurement of the EUV beam yield a $10 \mu\text{m}$

beam diameter, when the focus spot diameter of the DUV channel, the smallest one, has a diameter of around $20 \mu m$ (measured by the CCD imaging the focus).

Cameras placed outside of the experimental chamber and imaging the interaction region from the side is used to ensure that the plane in which the experimental target is placed after the transient characterization is the same as the streaking plane, ensuring the waveform identity between the two experiments

3.2 Compatibility of the beamline with attosecond transients

The AS-1 beamline has not been conceived with light field synthesis in mind, several adjustments have therefore been necessary to make the attotransient technology reliable.

Tungsten wires have replaced the pellicle

To support the small metallic (Zr or Pd in our experiments) filters, a 5 or $15 \mu m$ thick nitrocellulose film was used. However this material undergoes photochemical reactions with photons from the DUV, and even the Vis-UV channel, which make it opaque in few minutes and prevent transmission of most of our supercontinuum spectrum.

To overcome this limitation, the small ring holding the metallic filter is now held in place by two $25 \mu m$ diameter tungsten wires, leaving most of the space around the filter free of obstacles for the field. This however reduced our ability to manipulate the phase of the waveform after the HHG target (*e.g.* for easier optimization of the counts in the EUV attosecond pulse while maintaining reasonable transients), and we tried without success to deposit and use few μm thick quartz films. Further attempts could take advantage of the MDM structure to manipulate this phase.

Reduction of the astigmatism of high photon energy channel

In the original design of the beamline, the angle of incidence on the double mirror unit was 6 degrees, with respect to the normal of the mirror. Having an off-axis spherical focusing unit, it is of course subject to astigmatism. The amount of astigmatism increases with the square of the size of the object, the square of the off-axis angle of the optics, and the considered optical frequency [86]. Therefore, as can be seen on the first row of Figure 3.3 showing the profiles of the focus of the channels UV-Vis, Vis, NIR before our modification (unfortunately no data for the DUV channel was taken before modification), our spectrum suffers more from astigmatism on the most blue side.

The annular beam causes the Bessel-type rings in the focus, but the astigmatism is responsible for the cross-like structure visible mostly on the UV-Vis channel, as has been confirmed by propagation calculations.

This of course prevents the coherent addition of all of our wavelengths for the build-up of the attotransient, and makes the synthesized pulse longer. This behavior gets even more

hindering at higher beam sizes needed for higher intensity experiments.

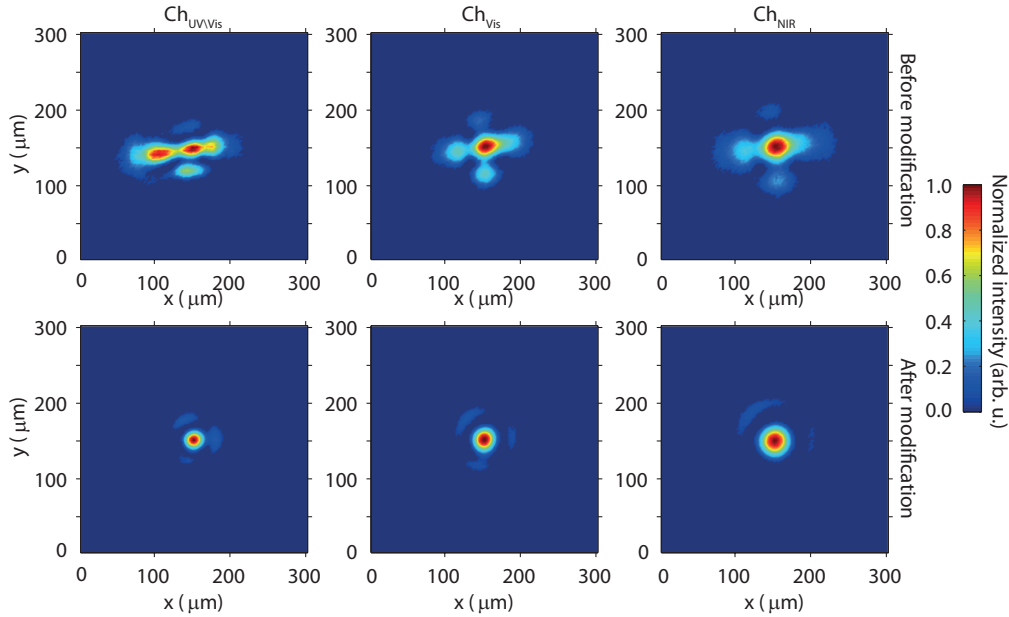


Figure 3.3: Channels profiles at experimental station before (upper row) and after (lower row) reduction of the focusing angle

To remedy this situation, we have reduced the angle of refocusing down to 2 degrees by displacing the electron Time-of-flight spectrometer by a few cms. Thanks to the scaling of astigmatism with the square of the angle [86], this has, for all beam configurations presented in this work, considerably suppressed the astigmatism issues even for the deepest UV photons of our attotransient spectra, as confirmed by the second row of Figure 3.3.

MDM

As seen in Chapter 1, a PHz broad spectrum is necessary for the generation of attotransients. However, although the spectrum at the output of the synthesizer and after transport to the experimental chamber (see Figure 1.8) comprises enough frequencies, it still has to be represented on a logarithmic scale to show the presence of UV photons, largely overcome by the visible ones. To remedy this situation, a custom-designed Metal-Dielectric Metal (MDM) coating is deposited on the refocusing unit of the broadband visible radiation (outer mirror). This type of coating, forming a Fabry-Perot type of cavity damping the visible radiation has been used as VUV reflector in the past [87, 88]. Here it has been designed to damp the red and yellow part of the spectrum while keeping the blue and UV side almost untouched, thus balancing the weight of all the spectral components at hand, *while keeping the spectral phase of the considered components almost constant*. This enables simultaneous synthesis of the attotransient and EUV generation.

3.3 80-120 eV central energy attosecond transient absorption capability

A relatively broad range of EUV photon energies has been used in the experiments presented in this work, to match the studied spectral features in the different samples considered, be it 80-85 eV for the $4p^{-1} - 3d^{-1}$ manifold of Kr^+ , and $4p^{-2} - 4p^{-1}3d^{-1}$ manifold of Kr^{++} in Chapter 4, 90-95 eV for the $3d^{10} - 3d^9np^1$ manifold of Kr neutral atoms in Chapter 5, or 100-115 eV for the Si:2p excitonic transitions in SiO_2 Chapter 6, as well as other tryouts in ZnO at 95 eV, and Si and Si_3N_4 around 110 eV. To this end, solutions have been developed to allow the proper spectral filtering and refocusing on the experimental target, as well as the most efficient collection of EUV photons in our McPherson EUV spectrometer.

3.3.1 Multilayer Mirrors

Alexander Guggenmos (PhD student in the group of U.Kleineberg) has been of great help to rapidly design, and coat on our inner mirror cores the numerous EUV multilayer reflectors needed in this thesis. Multilayers have been widely used to spectrally filter and compensate the so-called attochirp of HHG radiation since the beginnings of attosecond physics [89, 90, 91, 92]. Figure 3.4 shows the design of the relectivity (including relevant metallic filters), and spectra taken with the McPherson spectrometer of all the EUV mirrors relevant to this thesis. Below 100 eV, the technology used is a multilayer of Molybdenum and Silicon (Mo:Si). Above 100 eV, the multilayer stack is composed of Molybdenum and Lanthanum (Mo:La, [93] They have all been demonstrated to perform efficient streaking, *i.e.* to retain the attosecond confinement of the HHG radiation, and constitute a key capability of the AS-1 beamline. It is to be noted that future extensions up to 500 eV will find adapted multilayer designs to use [94].

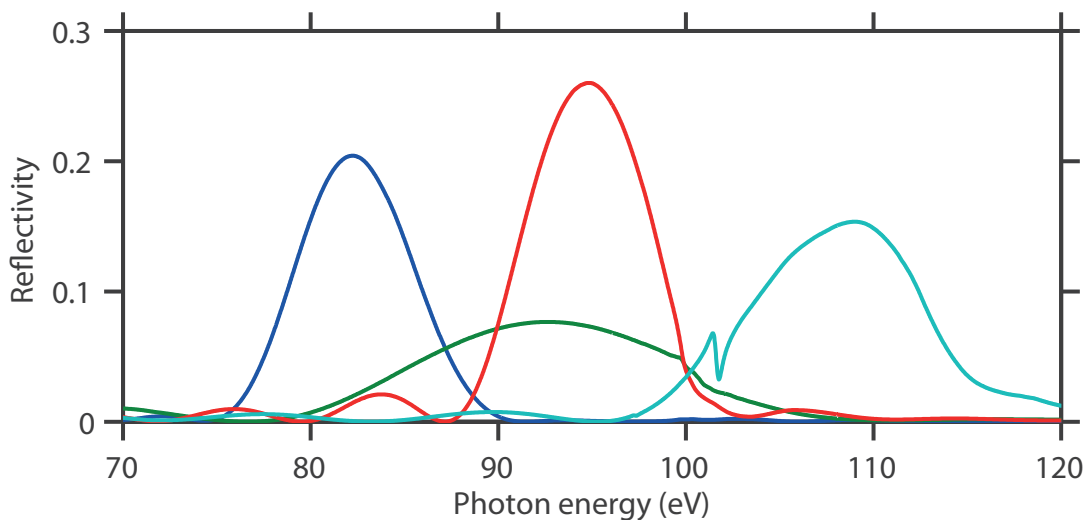


Figure 3.4: Design of the spectral filtering of EUV multilayers

3.3.2 Broadband EUV recollimation setup

The recollimation of the EUV radiation from the experimental target onto the entrance slit of the EUV McPherson spectrometer used for our transient absorption experiments is a rather intricate engineering challenge, and a quite challenging geometrical optics problem. It necessitates a compromise between two intertwined questions are the focusing geometry, and the spectral range intercepted.

Concerning the refocusing geometry, mirrors for the EUV range have to be superpolished, therefore it is extremely costly to get sufficient quality aspherical components (like toroidals, or elliptical mirrors which would be needed for perfect off-axis imaging). This can be avoided by relying on spherical optics in our case, since we do not need to image the experimental target onto a point object, but on a line, which will enter the spectrometer's slit. We can therefore tolerate some astigmatism, as long as the tangential size of the beam at the sagittal focus is not bigger than the slit, and counts do not get lost.

Concerning the spectral range accepted by the refocusing unit, for the efficient reflection of EUV from a bulk surface, grazing incidence reflections have to be used [86], since the index of refraction of usual materials in the EUV is smaller than one, and one must therefore rely on total *external* reflection. Therefore, the more grazing incidence the reflection is, the better the reflectivity will be. An alternative to the use of bulk reflection is the use of a multilayer (Bragg type) reflector, a technology similar to the one implemented in our inner mirrors, focusing the EUV on the experimental target (see Figure 3.1). However for these, a compromise has to be found between the reflectivity and the bandwidth of the recollimation setup. This is nevertheless a technology we have tried, and an example can be found on Figure 3.5. The ultimately chosen solution is the use of a double Rhodium (Rh) reflection, deriving from ideas developed for the AS-2 beamline [95]. The angle of deflection of the beam required by our experimental setup is 48 degrees, we could therefore have used 2 reflections at 12 degrees grazing incidence angle. One reflection will be on a spherical mirror for refocusing, and the second one on a plane mirror for beam steering. However, to prevent the tangential size of the beam to become too big, one should place the refocusing mirror as close to the experimental target as possible, and the slit of the spectrometer as close to the refocusing unit as possible. Due to the size of our chamber, the distance between the experimental target and the mirror cannot be smaller than $D_1 = 80\text{mm}$, and the distance between the mirror and the slit smaller than $D_2 = 500\text{mm}$. The sagittal focal length f_s should therefore be, according to the bent mirror reflection equations:

$$f_s = \frac{1}{\frac{1}{D_1} + \frac{1}{D_2}} = 69 \text{ mm}$$

The corresponding radius of curvature for a spherical mirror placed at a grazing incidence angle of $\theta = 12^\circ$ verifies the law for off-axis focusing:

$$f_s = \frac{R}{2} \sin(\theta) \Rightarrow R = 660 \text{ mm}$$

This is however rather a custom optical component, hence with a higher price, a reduced

availability and longer delivery times. It would be better to choose a standard optical component with $R = 500\text{mm}$ (available on the shelf in the desired polishing state). This will in turn fix the angle of grazing incidence to maintain the geometrical constraints to $\theta = 8^\circ$, and the second reflection angle (on the plane mirror) will therefore need to increase to 16° . As can be seen on Figure 3.5, this can be done at the expense of a decrease of reflectivity above 130 eV, and given our current photon energies it is the solution which has been chosen. This setup shall however be revisited when and if the need comes to increase the used photon energy.

As a conclusion point, with these geometrical characteristics, the tangential beam size on the slit is calculated (and measured) to have a spatial extension of around 10 mm. This is a bit more than the size of the slit. A further improvement of the setup could make use of a cylindrical mirror for the second reflection, focusing the beam a bit more in the tangential direction.

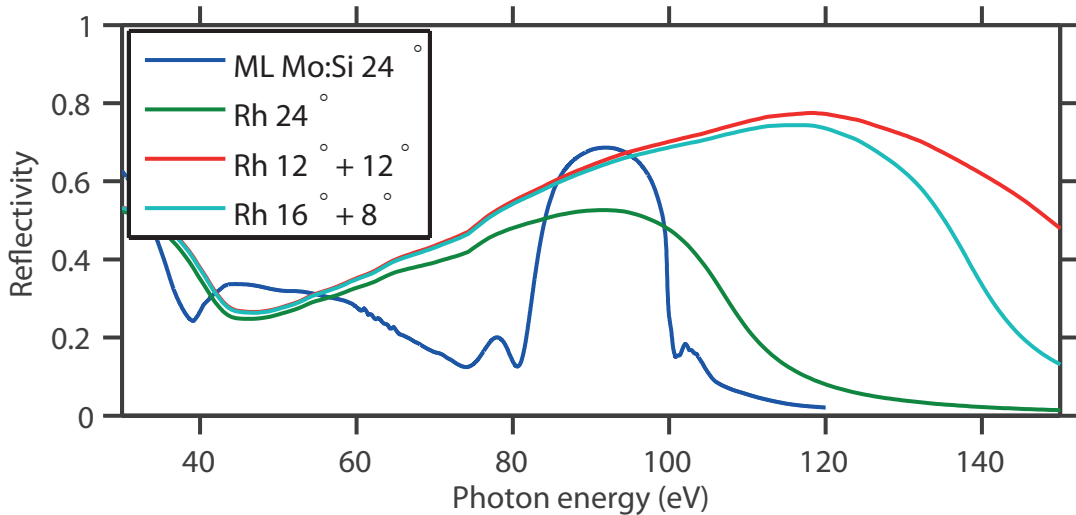


Figure 3.5: Reflectivities of the EUV refocusing unit, using a single reflection at 24° on a Mo:Si multilayer (blue, courtesy of A. Guggenmos) or a Rhodium mirror (green), or a double reflection on Rhodium, with balanced (red) and unbalanced angles (cyan).

On Figure 3.5, we can see that the double reflection on Rhodium has a high (> 0.6) reflectivity on all the 80-140 eV region, even if the angles are unbalanced to accommodate the use of standard optics. For comparison, using a Mo:Si Multilayer optimized for reflectivity at 92 eV results in performances which are not much higher, over a much narrower band.

3.3.3 Efficiency VS resolution in the detection system

The detection system used for the transient absorption experiments is a commercial blazed concave grating - Rowland circle based McPherson EUV spectrometer [96]. Based on the resolution needed for the experiments, we used various gratings of our collection (non grayed in Figure 3.6. With the highest available grooves/mm grating (2400 G/mm), we have achieved a resolution of 170 meV at 92 eV (see Chapter 5), and for the experiments

of Chapter 6, necessitating a higher level of signal, we used the 600 G/mm grating to have the best efficiency, by then lowering the resolution to 420 meV at 107 eV.

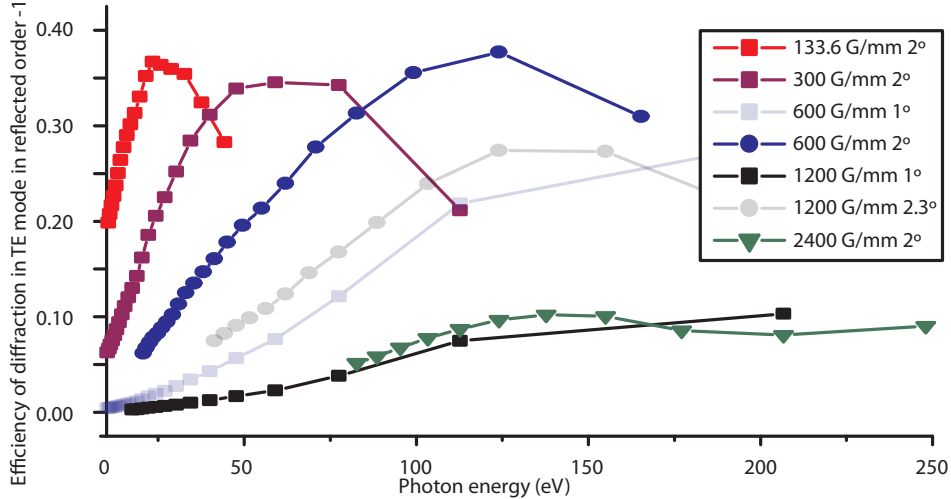


Figure 3.6: Efficiency of the EUV gratings used in the McPherson spectrometer (grayed out are available for sale, but not in our collection). Data: courtesy from McPherson, Inc

3.4 Synchronization issues in the attosecond regime

3.4.1 Interferometric stabilization for compensation of laser induced nanometric drifts and synchronization of different types of experiments

To resolve subfemtosecond features, the collinear optical pump probe setup displayed on Figure 3.1 must retain nanometric stability during the several hours of integration routinely required by such experiments. However, even for passively extremely stable collinear setups, the high optical power shone on the mirrors causes significant drifts of the introduced delay. Since in some of our experiments, this optical power even changes during the process (when sampling a streaking and then using higher intensity transients for example), special care must be taken to measure and account for these spurious delays.

Experimental setup

Figure 3.7 shows a zoom on the experimental implementation of the stabilization system. We shine a continuous Helium Neon laser ($\lambda_{\text{He-Ne}} = 633 \text{ nm}$, commercially available) on the double mirror setup, at an off-axis angle of 30° . Close to the focus, beams reflected from the inner and the outer mirrors overlap spatially and interfere. The fringes naturally arise from the relative tilts of their wavefronts.

To make the fringes pattern easier to treat numerically, it is made one dimensional: a mask is used in the far field to isolate a thin light band coming from each of the mirror

parts, and a lens images the resulting filtered interferogram with a magnification factor of 10 on a CCD sensor (FLEA 3, Pointgrey, 800 Mb/s).

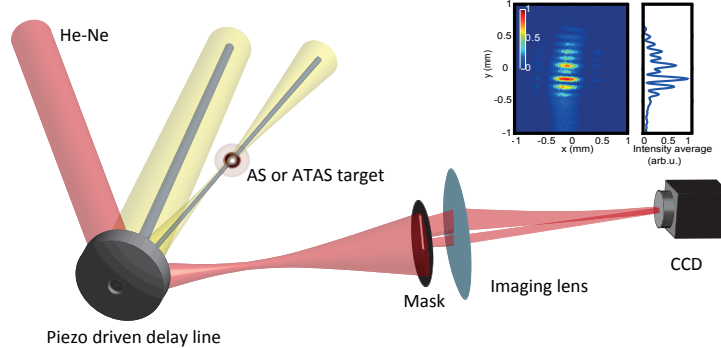


Figure 3.7: Experimental setup. Insert: typical fringe pattern and its 1D lineout (see text)

A good visibility of the interference pattern is ensured by the correct positioning of the CCD with respect to the focus. Placed too close, the two wavefronts are parallel: fringes disappear. Placed too far, the beams do not spatially overlap. A simple test to check the correctness of the alignment is to see the phase of the fringes responding to a movement of the PZT.

Numerical treatment

Once a satisfactory fringe pattern is obtained, a LABVIEW algorithm (running at 5 Hz) treats the image to yield the phase of these fringes, which is the relevant quantity related to the relative distance between the two mirrors, and therefore the pump-probe delay. The 1D fringe pattern $f(x)$ shown on Figure 3.8.a. (blue curve) is first extracted by averaging the 2D image on 100 horizontal pixels around the image intensity peak. Its Fast Fourier Transform (FFT) absolute value $|\tilde{f}(k_x)|$ yields three spikes at $0, \pm\Delta k$ (see figure 3.8.B), where Δk is the wavevector difference between the two interfering beams. The phase of the fringes is then extracted as the phase of the complex FFT of f at Δk : $\phi = \arg(\tilde{f}(\Delta k))$.

Fluctuations of the position of the pattern on the camera (due e.g. to air flows) are an important source of noise that has to be accounted for. Indeed, an average position difference Δx_0 immediately transfers to a phase difference $\Delta k \Delta x_0$ due to basic properties of the Fourier Transform. To compensate for this source of noise, Δx_0 is measured at each acquisition in a phase independent way, by measuring the center of mass of the DC component of $f(x)$ (green curve on Figure 3.8.a.), obtained by an adequate hypergaussian Fourier filtering between $-\Delta k/3$ and $\Delta k/3$ (green curve on figure 3.8.B). The quantity $\Delta k \Delta x_0$ is then removed from the phase.

This extraction procedure, is an improvement of other techniques [95] where the phase of interference fringes is derived from the intensity of the HeNe light on a single detector, and therefore subject to intensity and position fluctuations.

To link the phase variation to the introduced delay τ between the light transient and

the EUV attosecond pulse, we run a calibration of the interferometer by scanning the PZT position δ , and therefore the delay $\tau = 2\delta/c$, and recording ϕ . It is expected that $\phi = 2\pi c\tau \cos(30^\circ)/\lambda_{\text{He-Ne}} = 2.58\tau$. The results are presented on Figure 3.8c. The linearity is verified on a 50 fs range (the error bars derived from the averaging of 5 calibration runs are invisible), and a fit gives a proportionality relationship $\phi = 2.59\tau$, in excellent agreement with the expected value.

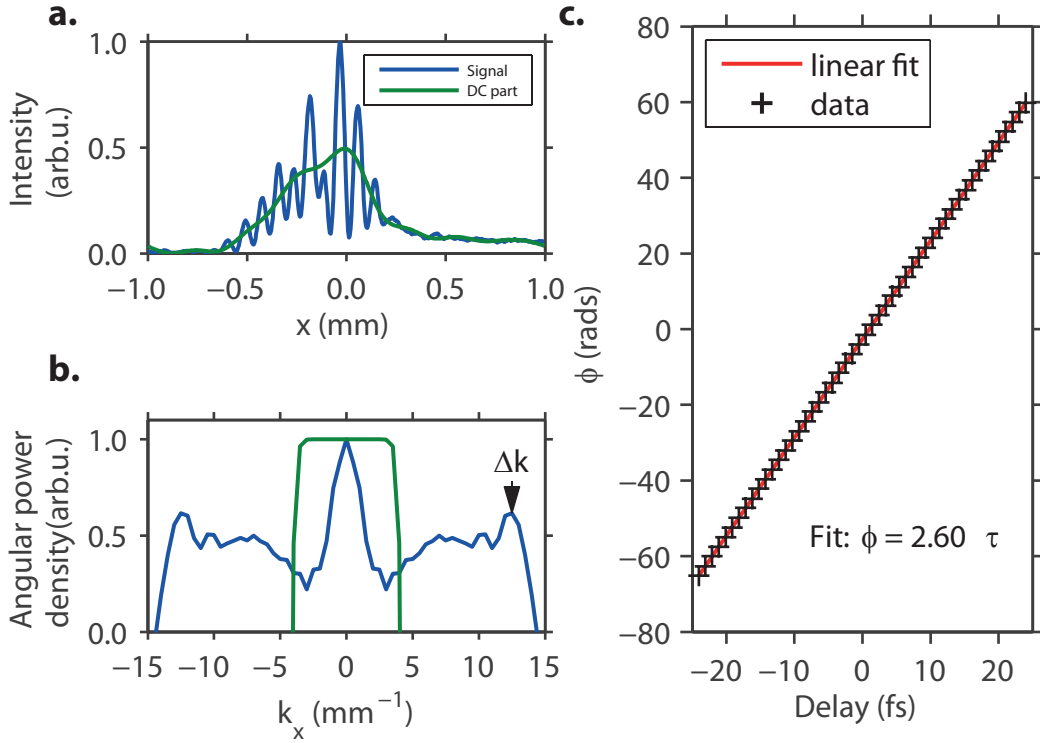


Figure 3.8: **a.** fringe pattern $f(x)$ (blue) and its DC component (green). **b.** FFT of the fringe pattern $|\tilde{f}(k_x)|$ (blue) and numerical filter applied for extraction of the DC component (green) **c.** Result of 5 interferometer calibration runs (error bars are plotted but invisible because too small)

Strategy for compensation of optical exposition induced thermal drifts

While the linear thermal expansion coefficient of optical glasses is usually low ($5 \cdot 10^{-7} \text{ K}^{-1}$ for fused silica), it is not the case of the materials (metals) used to mount optics, such as aluminum ($2.2 \cdot 10^{-5} \text{ K}^{-1}$), for which heating can be a source of optically significant dilatation (1 mm of aluminum expands by 22 nm when its temperature raises by one Celsius degree). Therefore, more than environmental factors like ambient temperature, the main contributor to delay axis slippage is the exposition to the high power densities associated with our 10 mW average power laser beam. This is especially the case since the laser beam does not hit all the optical elements of the delay line, where the inner mirror is

shielded from visible light by a metallic filter, and the MDM mirror implementation calls for 80% of energy damping in the outer mirror itself. This is confirmed by Figure 3.9, showing a measurement of the collinear delay line status during 4 hours, during which the beam has been turned on at the indicated times with the averaged power required for Attosecond Streaking (AS), *i.e.* 2 mW, then for Attosecond Transient Absorption Spectroscopy (ATAS), *i.e.* 10 mW, and then turned off. Despite the shielding we installed to avoid direct illumination of the optomechanics by the beam, the time axis responds very dynamically, and the disturbance is of the order of the femtosecond.

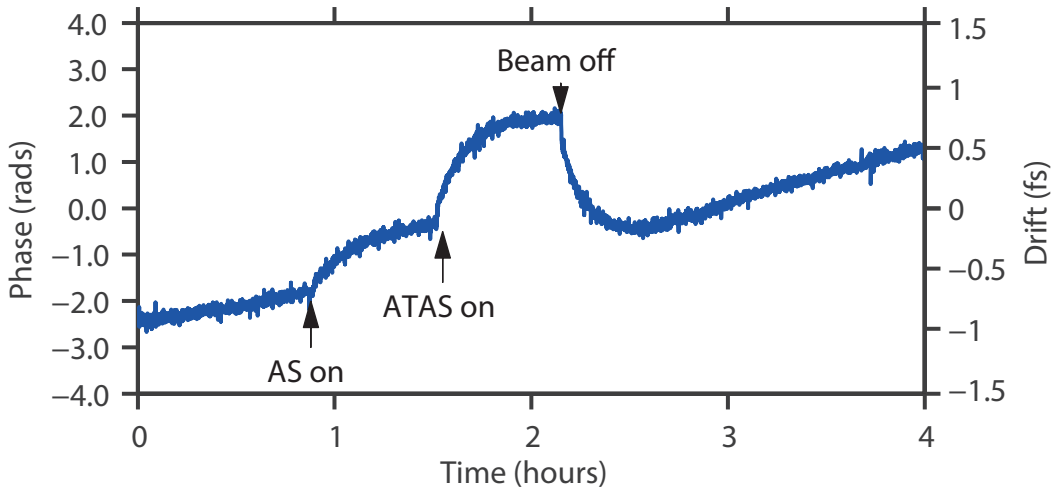


Figure 3.9: Delay (sampling 1 Hz) extracted by the characterization setup with varying shining parameters mimicking the experiment

These spurious effects, which would smear out any subfemtosecond feature in a pump-probe study, have to be counterbalanced. An active continuous feedback loop would slow down the data acquisition process, we therefore opted for the periodic measurement (at time intervals smaller than the drift characteristic time) of the interferometer phase at a reference point. To this end we bring the PZT at a reference position (usually the zero delay point) and average the phase extracted from 10 successive CCD acquisitions. The calibration (Figure 3.8.c.) is then used to account for the shift by adding a constant offset to the PZT position, thus ensuring the correct positioning of the delay axis scan after scan.

Experimental confirmation of setup effectiveness by subfemtosecond feature resolution

The effectiveness of the system can be assessed by back-treatment of experimental data. In the study presented in [3], some aspects of which will be developed in Chapter 4, a synthesized light transient of contrast 2:1, sampled by streaking and used in a Transient Absorption study has demonstrated its ability to temporally confine field ionization to a 700 as time window. This is shown on figure 3.10.b., where the blue dashed line shows the field intensity measured by streaking, and the red line the population of one of the spin

orbit states of Kr^+ measured by ATAS.

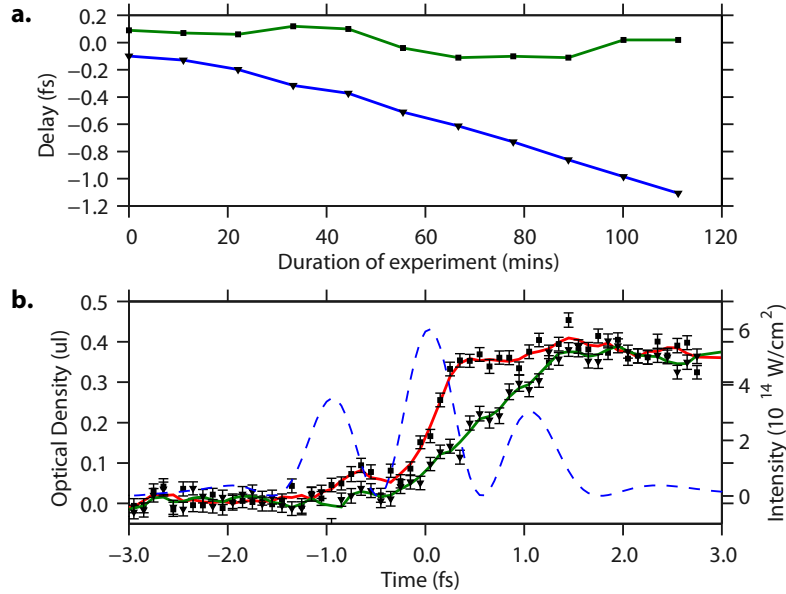


Figure 3.10: A. Blue: cumulative delay correction during the taking of the 11 scans (each point); green: estimated rise time of the ionic line (erf function fit) on two adjacent averaged scans. **B.** Red: Ionization dynamics recorded in the actual experiment, with a rise time of 680 as. Green: the correction imposed by the stabilization setup has been artificially removed before the scans averaging. The rise time is then close to 1.5 fs.

To achieve this result, the temporal superposition of 1 attosecond streaking and 11 Transient Absorption spectrograms was required. The total experiment lasted slightly more than 2 hours, during which the optical power load was changed (streaking to transient absorption transition).

Figure 3.10.a. shows the accumulated delay offset added by the compensation setup during the experiment (blue curve). It amounts to 1.2 fs at the end of the complete procedure. The correctness of the compensation mechanism is demonstrated by the green curve of the same graph, which shows the rise time of 2 aggregated scans fitted with an erf function. This constitutes an absolute clock given by the atomic strong field atomic response, that stays within a ± 100 as band for the complete two hours. A more visual confirmation is given by the green curve of Figure 3.10.b., which shows the data as it would have been collected without our referencing setup. It is not synchronized with the measured field, and shows an ionization rise time of 1.5 fs instead of the measured 680 as.

This technique allows the non invasive referencing of a collinear attosecond pump-probe delay line, based on a Fourier Transform spatial interferometry procedure repeated at periodic intervals during an experiment. This allows compensating for drifts of the delay line imposed by shining the beam itself. The independent clocking provided by the subfemtosecond rise of the ionization of Krypton atoms by a subcycle optical transient proved the efficiency of our strategy, which gives to our setup its full attosecond pump-probe capability. Such a technique can readily be extended to other delay line

geometries and used as a 5 Hz continuous feedback loop if needed by less passively stable setups.

All the experimental results presented in this work will be supported by this technology.

3.4.2 Taking into account spatially induced delays

Field ionization, studied in our Transient Absorption experiments requires field intensities in the several $10^{14} \text{ W.cm}^{-2}$ range. Such intensities are not compatible with streaking, since in this case the IR electric field should not ionize the atom, but only steer the photoelectron produced by the XUV pulse. The waveform has therefore to be characterized with a smaller intensity than the one actually used in the experiment. This intensity reduction is achieved by controlling the opening of an iris located before the experimental chamber. Therefore, spatiotemporal coupling coming from the clipping, or the change of the illuminated section of the pellicle and the double part focusing mirror can distort the waveform.

Another issue that can be encountered when trying to synchronize a transient absorption trace with a streaking measurement is that in some cases, like the the one presented in Chapter 4, the intensity used in the absorption experiment (several $10^{14} \text{ W.cm}^{-2}$) is higher than the intensity compatible with streaking field. Therefore the iris controlling this intensity is opened between these two experiments. This effect has been investigated by recording the cross-correlation trace between the central part of the visible beam, and the portion reflected on the outer mirror, both for transient absorption and streaking iris configurations. The delay has been varied with our collinear interferometer, and the intensity recorded at the focal point of the beams imaged on a CCD camera (averaged over 5×5 pixels covering the central part of the beam). The normalized oscillating term of these cross-correlation traces can be seen on Figure 3.11.

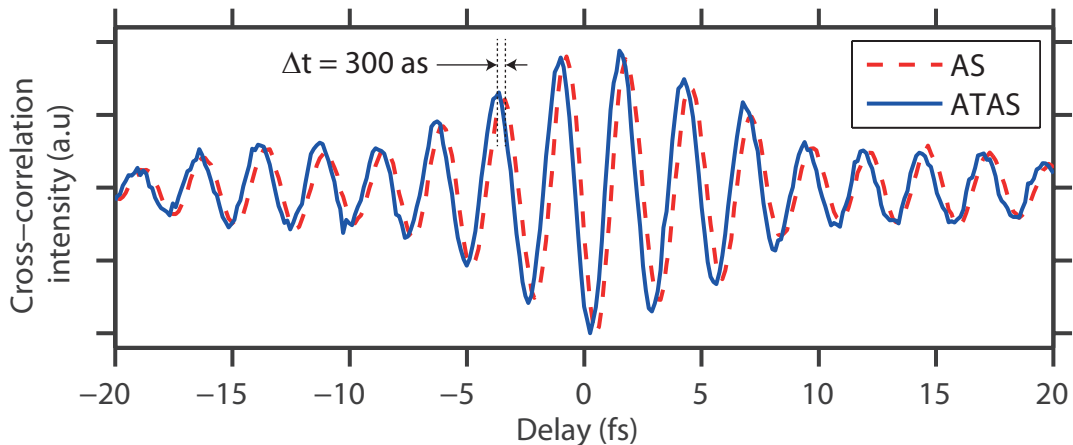


Figure 3.11: Normalized Cross-correlation of the outer and the inner mirror waveforms for two different iris opening conditions: streaking (AS) and transient absorption (TA), showing a spatially induced delay of 300 as

Satisfyingly, the spatially induced delay of 300 as measured on the cross-correlation measurement of Figure 3.11 matches an interpretation based on the geometrically longer

path that a beam reflected far off the center of a spherical mirror of radius r has to undergo compared to a beam reflected in the center [97]:

$$\Delta T(r) = \frac{3 R r^4}{4 c R^4}$$

Thus, for a pulse reflected by an annular portion of a spherical mirror situated between radii r_1 and r_2 , we get a delay (assuming a constant spatial intensity distribution):

$$\Delta T_{r_1}^{r_2} = \frac{\frac{3 R}{4 c} \int_0^{2\pi} \int_{r_1}^{r_2} \frac{r^4}{R^4} r dr d\theta}{\int_0^{2\pi} \int_{r_1}^{r_2} r dr d\theta} = \frac{1 R}{4 c} \frac{1}{R^4} \frac{r_2^6 - r_1^6}{r_2^2 - r_1^2}$$

Therefore, for our mirror with $R=250$ mm, for an inner mirror radius of $r_1 \simeq 1.5$ mm and the streaking beam radius on the mirror to $r_2 \simeq 2.5$ mm, since for the TA configuration we had $r_2 \simeq 8.1$ mm, we obtain then a differential delay of 240 as, which corresponds pretty nicely to the measured delay with the cross-correlations, considering the imprecision of the measurement of the streaking radius and the fact that the mirror is not really at normal incidence. This establishes the validity of this formula which can be used to correct the pump-probe delay axis shift due to spatio-temporal couplings. Further possible developments of this technique are presented in Appendix A.

3.4.3 Dispersion related delays

In this work, experiments in solid state slabs of 120 nm thickness will be presented (see Chapter 6), relying on the attosecond control of the pump-probe delay between two pulses centered at radically different photon energies. 120 nm corresponding to 400 as at the speed of light, it is legitimate to ask what the influence of the medium itself on the pump and the probe pulse will be, and from then how it impacts the pump-probe spectrogram.

As a 0th order calculation, the index of refraction of SiO₂ at 520 nm is 1.5, and slightly less than 1 at 100 eV. Therefore, the attotransient will, in the course of propagation in the medium, be delayed by around 200 as with respect to the attosecond EUV pulse. This should be taken into account.

To get a more precise overview of the phenomenon, a calculation based on Fresnel coefficients has been done, and the propagation of the pulse in the medium taking into account reflection at the SiO₂- vacuum interfaces. The results are presented on Figure 3.12, with a comparison of the effect on the EUV pulse (data for SiO₂ refractive index in the visible range from [98], in the EUV range from [77]). It shows, in a referential moving at the speed of light in vacuum, the evolution of the waveform with position in the SiO₂ slab. The delay of 200 as is indeed to be seen, as well as an intensity variation with propagation, due to thin film effects. The EUV pulse undergoes only absorption, there is no visible effect of dispersion or delaying. This shall be taken into account when analyzing the data.

This chapter has shown how the issues posed by the adaptation of the beamline to the use of attotransients in combination with a broad range of central energies EUV attosecond

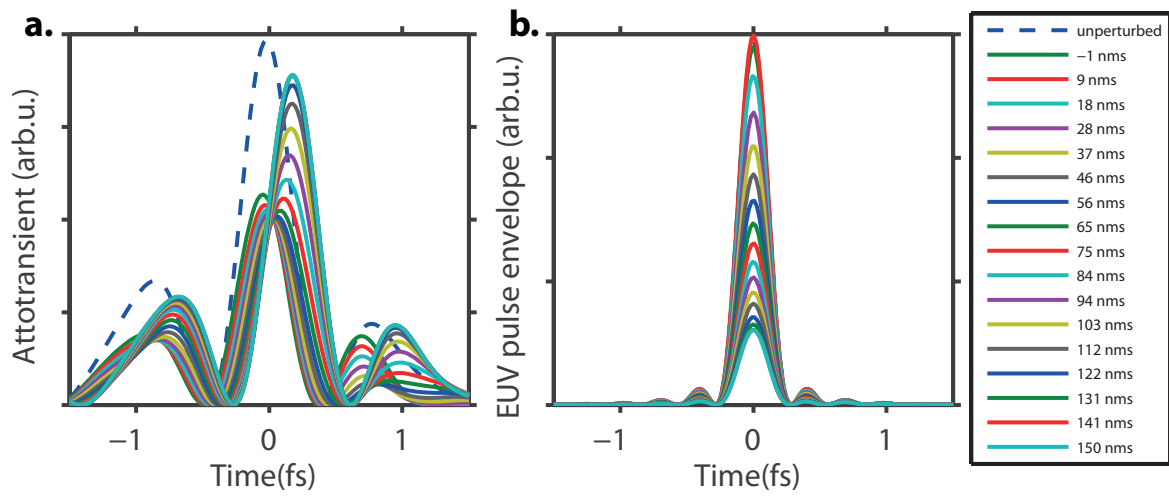


Figure 3.12: Comparison of Propagation in a 120 nm slab of quartz for an attotransient and an EUV pulse

pulses have been addressed, as well as an overview of the techniques and corrections to introduce to extract relevant information about the subfemtosecond dynamics of a system.

4

Polarization effects in Strong Field Ionization

*Un seul être vous manque, et tout est dépeuplé
(One being is missing, and your world becomes desert.)*

– Alphonse de Lamartine

The first demonstration of Attosecond Transient Absorption Spectroscopy (ATAS) [32, 67] has investigated the coherent nature of valence shell ionic wavepacket generation in strong-field ionization, via the detection of beats between two quantum paths including two spin-orbit splitted ionic states generated by field ionization, and leading to the same final state. The period of the measured quantum beats, 6.3 fs, corresponds well to the energy splitting of the spin-orbit states, 0.67 eV. To observe coherence in this context, it was therefore critical to constrain the wavepacket creation, *i.e.* the ionization events, to a window shorter than this period, which was achieved by using a 3.3 fs intensity FWHM pulse. Later on, with the advent of the first generation of light field synthesis, this experiment has been revisited with 2 fs intensity FWHM (half-cycle intensity contrast 2:1) light transients [3], revealing the higher degree of coherence, and allowing the extraction of the absolute phase of the oscillating valence electronic wavepacket.

A careful look has been taken at the delay instances at which the strong visible field and the EUV attosecond pulses overlapped in time, with the goal to resolve the rise of ionic population in real-time via the delay-dependent strength of absorption. However, as will be shown in this chapter, the effect of the strong field is not limited to the ionization of the neutral atom. It also strongly polarizes the ionic states, which has the effect to disturb the absorption process, and leads to intricate lineshape dynamics. This needs to be taken into account to assess the solidity of the real-time ionization reconstruction, and can be exploited to extract useful information on the polarizability of the ionic transitions involved in this process.

This experiment having been presented elsewhere [3, 48], this chapter will mainly focus on the contribution of this work concerning the observation of the polarization of the studied transitions, together with further attempts to extend this approach to double

ionization, and lay down the basics of the modeling of the polarization of a core-shell transition by a synthesized light transient. It is important to note that the transients used for the experiments presented in this chapter were contracted using an earlier generation of light field synthesizer, *i.e.* with only IR, Vis and UV-Vis channels. The addition of the UV channel indeed requires the use of aluminium optics and the spectral shaping MDM mirror, which do not provide enough energy to ionize Krypton atoms.

4.1 Single and double field Ionization of atoms in a subcycle pulse

Ionization of atoms by strong laser fields has been enabled by the development of ultrashort pulses with electric fields reaching strengths comparable to the electrostatic Coulomb field binding the valence electrons to the atom. This section gives a quick review of the relevant phenomena.

4.1.1 Strong field single ionization

Classification of field ionization regimes

The theoretical background relevant to ionization of atoms in an oscillating field has been laid down by Keldysh in 1965 [99, 100]. The basic idea is that the application of an electric field with a strength comparable to the Coulomb field can distort the atomic potential binding an electron, forming a potential barrier through which the electron can tunnel out (see Figure 4.1b.). In an oscillating field, this potential barrier is transiently and alternatively formed on both sides of the atom.

Depending on the ionization potential I_p , the strength E_0 and the oscillation period T_L of the field, several regimes of ionization can be identified and classified by the adiabaticity parameter γ , the so-called Keldysh parameter [99]:

$$\gamma = 2\pi \frac{\sqrt{2m_e I_p}}{eE_0 T_L} = \sqrt{\frac{I_p}{2U_p}} \quad (4.1)$$

Without entering complex quantum mechanical modeling of this problem, described at length in [99, 100], a very simple and naive semi-classical calculation unveils an intuitive interpretation of the Keldysh parameter [101]. The following will be written in atomic units. For an hydrogen atom, with x the spatial dimension over which the laser is polarized, The atomic potential being $V_0(x) = -1/|x|$, and the potential felt by the electron in the presence of an electric field of amplitude E_0 is $V(x) = -1/|x| - E_0 \cdot x$. The potential barrier limits are defined by:

$$-\frac{1}{|x|} - E_0 \cdot x = -I_p \quad (4.2)$$

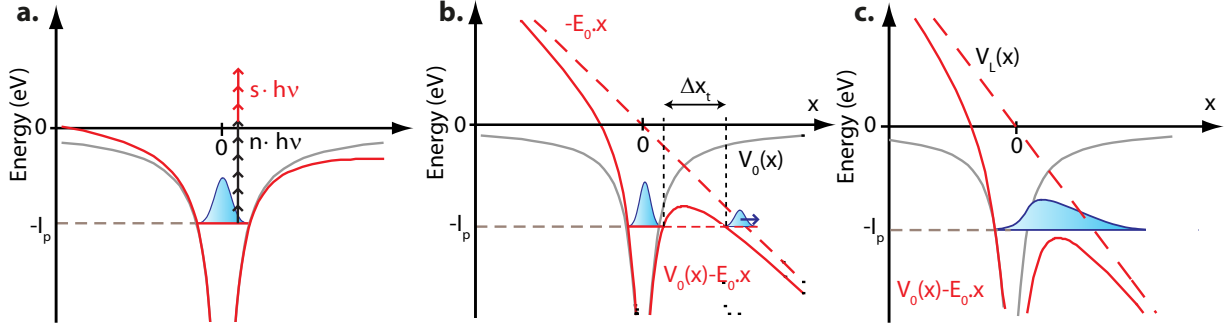


Figure 4.1: Different regimes of field ionization. **a.** For $\gamma \gg 1$, multi-photon ionization. **b.** For $\gamma \ll 1$, tunnel ionization. **b.** For even lower values of γ , the field can suppress the tunneling barrier, it is the barrier suppression regime. Based on [67].

The roots of Equation (4.2) are real only when $E_0 < I_p^2/4$, which is the field E_{BS} above which the barrier is suppressed, and the ionization regime corresponds to Figure 4.1c.. When these roots exist, the distance between them, or barrier size is:

$$\Delta x_t = \frac{I_p}{E_0} \sqrt{1 - \frac{E_0}{E_{BS}}} \simeq \frac{I_p}{E_0} \quad (4.3)$$

The speed of the electron "in the barrier", is a concept of arguable nature, since in this energetically forbidden region, it is an imaginary number, hard to relate to a classical conception of speed. It can however be evaluated to $v \simeq \sqrt{2I_p}$, which yields a "tunneling time" of the order of:

$$\tau_t = \frac{\Delta x}{v} \simeq \sqrt{\frac{I_p}{2E_0^2}} \quad (4.4)$$

The ratio between this semi-classical "tunneling time" and the laser half-period gives the Keldysh parameter, in order of magnitude:

$$\frac{\tau_t}{T_0/2} = \frac{\Delta x}{v} \simeq \sqrt{\frac{2I_p}{T_0^2 E_0^2}} = \frac{1}{\pi} \sqrt{\frac{I_p}{2U_p}} = \frac{\gamma}{\pi} \quad (4.5)$$

We see with this simple considerations that the Keldysh parameter has a very intuitive interpretation: It can be seen as the ratio of the time needed for an electron to tunnel out of the potential barrier at the maximum of the field to the half period of the laser, characteristic time after which the barrier is restored. It is also the square root of the ratio between the ionization potential, the energy that the electron has in the atom, to the ponderomotive energy that it would have, once freed from the atom and oscillating in the field.

From there several regimes of ionization can be defined:

- As shown on Figure 4.1 **a.**, if $\gamma \gg 1$, then the electron does not have enough time to tunnel out of the barrier during a half-cycle, or it gains less energy oscillating in the field than it has in the atom, and ionization cannot occur by tunneling.

Ionization observed in this regime occurs by the so-called multi-photon ionization (MPI) mechanism. The electron absorbs as many photons as necessary to overcome I_p (n in the scheme of Figure 4.1 **a.**), and is set free. If γ becomes much higher than 1, the number of photons absorbed can become higher than the minimum requirement.

- If $\gamma \ll 1$ (Figure 4.1 **b.**), a substantial fraction of the electron can tunnel out during the strong part of a half-cycle. This is the tunneling regime
- At even higher fields the Barrier-Suppression regime starts (see Figure 4.1 **c.**). According to the previous naive calculation, this happens for fields higher than $E_{BS} = I_p^2/4$. For Krypton atoms in discussion in this chapter, the first ionization potential is $I_p^{(II)} = 13.996 \text{ eV}$ [102], and $E_{BS} = 3.3 \text{ V/\AA}$, corresponding to a peak intensity $I_{BS} = 3 \cdot 10^{14} \text{ W.cm}^{-2}$, and the second ionization potential is $I_p^{(III)} = 24.359 \text{ eV}$ [102], and $E_{BS} = 13.7 \text{ V/\AA}$, corresponding to a peak intensity $I_{BS} = 5 \cdot 10^{15} \text{ W.cm}^{-2}$,

Ionization rates

The rates of field ionization have been derived by averaging the DC field rates obtained by Keldysh [99] over a cycle in the quasi-static picture by Ammosov, Delone and Krainov [103], the so-called "ADK" rates. They are widely used in the community to describe field ionization, and have been extended to extract "instantaneous" rates by using the instantaneous rather than the cycle-averaged field strength [100]:

$$\Gamma_{SFI}(t) \propto \left(4 \frac{Z\sqrt{2m_e}I_p^{3/2}}{\hbar e|E(t)|} \right)^{2n^*-1} \exp \left(\frac{4}{3} \frac{Z\sqrt{2m_e}I_p^{3/2}}{\hbar e|E(t)|} \right) \quad (4.6)$$

Here Z is the atomic charge, m_e the electron mass, and $n^* = ZI_p^{1/2}$ with I_p in atomic units. The exponential dependence in field strength, which derives from the tunneling barrier width (see 4.2) is the most noticeable feature of this expression.

Although the application of this formula to a non-cycle averaged field strength is not strictly speaking justified, it has been found to agree well with more evolved calculations for γ below 0.5 [104]. In our experiments, the Keldysh parameter is below 1, it is around 0.6 for the single ionization experiment (peak intensity $10^{15} \text{ W.cm}^{-2}$) and respectively 0.4 and 0.6 for the single and double ionization potential of Kr for the double ionization experiments (peak intensity $8 \cdot 10^{14} \text{ W.cm}^{-2}$). We will therefore use instantaneous rates for the calculations shown here. In the particular case of single ionization of Krypton we used different pre-factors for the exponential of Equation (4.6), coming from a fit of DC rates obtained by precise quantum-mechanical calculations [105]. Readers interested in the most complete analytical treatment of field ionization shall refer to the Yudin-Ivanov formula [106], which includes non-adiabatic effects.

4.1.2 Double ionization

Upon application of a strong enough field, a second electron can be removed from the atom, leading to the formation of the double ion. This double ionization has been studied by different methods, relying mostly on the detection of ions and electrons resulting from this process, and the evolution of their parameters as a function of pulse shape and energy. In the fs regime, early studies [107] has studied the number of single and double He ions generated by a 100 fs pulse of varying intensity in the NIR. Results are shown on Figure 4.2a.. The appearance of a so-called "knee-structure", showing a much higher yield than expected for the double ionization at low intensity has been interpreted as a manifestation of Non-Sequential Double Ionization (NSDI) mechanisms. In sequential ionization, one electron is removed to form the first ion, which is then further ionized to form the second ion, but these two processes are independent, meaning that the photoelectrons are not correlated. On the contrary, in a non-sequential process, the formation of the second ion is linked to the first ionization, and the electrons are correlated. This can be observed using Cold Target Recoil Ion Momentum Spectroscopy (COLTRIMS, [108]), a technique with the ability to record the momentum of the two electrons and the ion, and the result of [109], shown on Figure 4.2b. and c. shows the vanishing of electron correlation at high intensity in Argon.

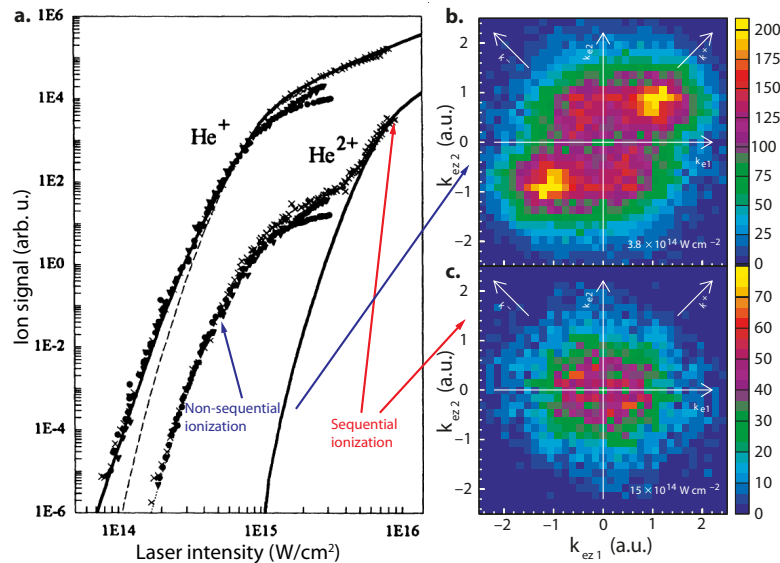


Figure 4.2: Sequential and Non-Sequential double ionization. **a.** In [107], yield of singly and doubly charged He ions generated by a 100 fs pulse of varying intensity in the NIR, displaying a knee structure for He²⁺ (see text for details) **b.-c.** In [109], correlation maps of electrons ejected from Ar atoms while forming a doubly charged ion in non-sequential (**b.**) and sequential (**c.**) double ionization scenarii (see text)

Several mechanisms have been proposed for NSDI, a review of which can be found in [110]. They can be classified in two categories. In one "direct" class the field drives two electrons out of the atomic potential together, called Collective multi electron tunneling [111]. In the second, "indirect" class, the removal of the first electron causes the subsequent

ejection of the second one, be it because the first removed electron, driven by the field, recollides with its parent ion and ejects another electron (recollision impact ionization RII), or excites it enough to have it ionized by the next half-cycle (recollision excitation and subsequent ionization, RESI).

4.1.3 Control of regimes of ionization with the waveform

From the previous discussions, we can understand that a control of the electric field of a waveform such as the one presented in Chapter 1 would give a lot of flexibility to control the ionization processes, which are essential field-driven dynamics, with an exponential nonlinearity in the field, hence a strong sensitivity.

In particular, Figure 4.3a. shows the expected ionization fraction of Krypton atoms as function of time for the pulse that has been used in one of the experiments presented in this chapter, obtained by the resolution of simple rate equations based on ADK-type rates (based on the fitting of more precise data from [105] as discussed above). The pulse is a 2 fs intensity envelope FWHM pulse with a peak intensity of $4.8 \cdot 10^{14}$. As can be seen, the high-contrast should allow the confinement of tunnel ionization to a single half-cycle.

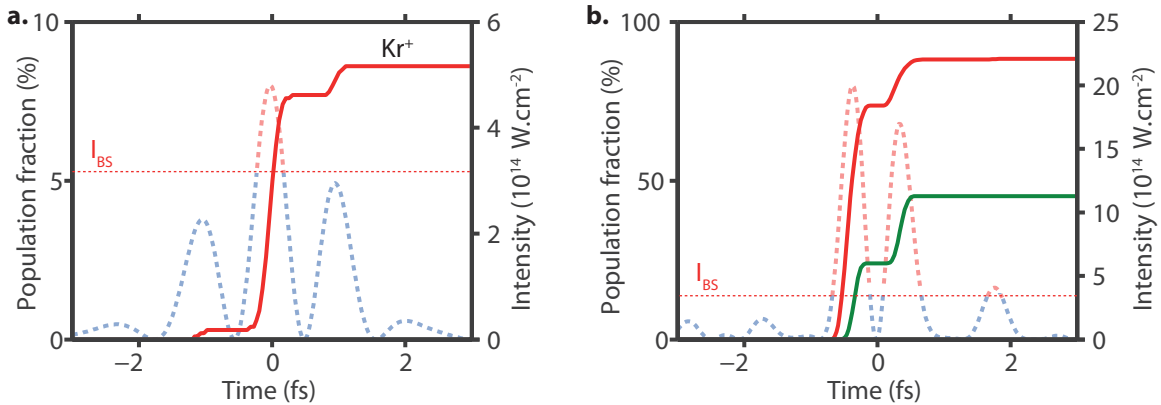


Figure 4.3: Ionization by synthesized pulses in the ADK picture. **a.** The intensity contrast of 2 allows to confine the field ionization of Krypton to a single half-cycle, which is then the only one to go above the Barrier Suppression intensity. **b.** For a double-spike waveform (with DUV channel), the contrast in front of the pre-half-cycle can attain 8:1, allowing to start the generation of Kr^+ and Kr^{++} synchronously, to block indirect double ionization channels before $t = 0$.

In a double-spike waveform (with UV channel, see Chapter 1), the intensity contrast in front of the pre-half-cycle can theoretically attain 8:1. This would allow the generation of Kr^+ and Kr^{++} to start synchronously with sequential or collective tunneling mechanisms, blocking indirect non-sequential double ionization channels before $t = 0$. Figure 4.3 displays a calculation of time-resolved ionic population using ADK rates for the second ionization, and effectively neglecting any non-sequential channel. It shows that there is a regime in which the sequential second ionization channel is open with the same half-cycle as the single ionization channel. Therefore, observation of doubly charged ion at this point

in time would exclude any generation by an indirect non-sequential mechanism. This has been attempted experimentally and will be reported in Section 4.5.

4.2 Real-time observation of strong-field ionization

4.2.1 System description

The schematic energy diagram relevant to this experiment is displayed on Figure 4.4. Kr is an atom with ground state configuration $[\text{Ar}] 3d^{10}4s^24p^6$. Upon exposition to an electric field of the order of the binding Coulomb force exerted by the nucleus and the electronic cloud on a valence electron, one of these electrons can be strong field ionized, thus generating Kr^+ ions in a coherent superposition of ionic states, in the spin-orbit splitted manifolds $4p_{J=3/2}^{-1}$ and $4p_{J=1/2}^{-1}$, separated by 0.67 eV . Under the valence shell containing $4p$ electrons, the first core-shell of Kr atoms is the $3d$ shell. Once an atom is in the $4p^{-1}$ ionic state, transitions are open from the $3d$ shell to the vacancy of the $4p$ shell. 3 transitions are dipole-allowed (they must verify $\Delta J = 0, \pm 1$), $4p_{J=3/2}^{-1} - 3d_{J=5/2}^{-1}$, $4p_{J=3/2}^{-1} - 3d_{J=3/2}^{-1}$ and $4p_{J=1/2}^{-1} - 3d_{J=3/2}^{-1}$.

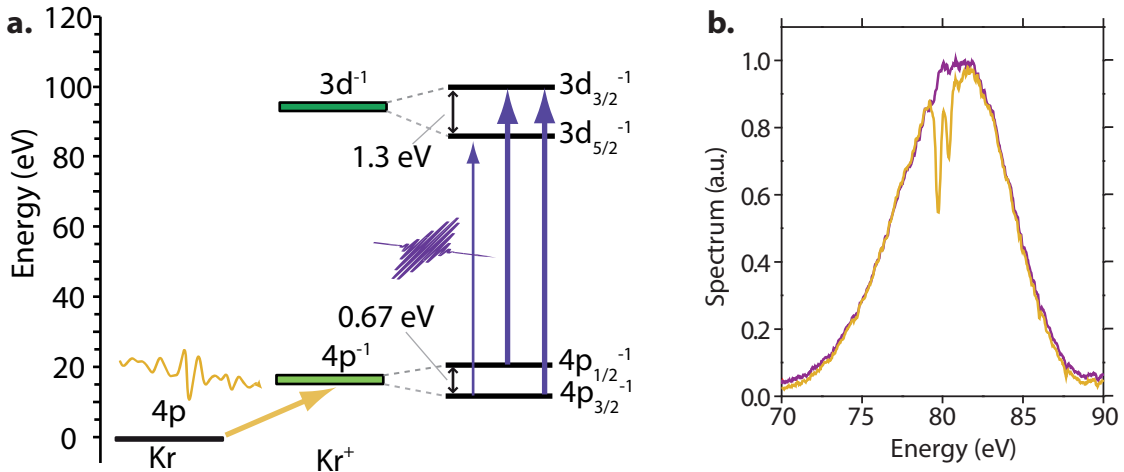


Figure 4.4: **a.** The synthesized transient ionizes a Kr atom, generating an ion in the $4p^{-1}$ manifold, which is then probed by the absorption of photons from the EUV pulse. **b.** Recorded EUV spectra for the EUV pulse preceding (violet) and following (yellow) the ionizing light transient.

4.2.2 Experimental spectrogram

Using the tools described in the previous chapters of this thesis, we have synthesized a 2 fs envelope intensity FWHM, field intensity contrast 2:1 light transient, together with a 160 as EUV pulse, centered at 80 eV . We have set the peak intensity of the transient to $4.8 \cdot 10^{14} \text{ W.cm}^{-2}$, restricting the ionization fraction to 15 %, and thus allowing ionization almost only from the most intense half-cycle of the waveform, as will be shown later on.

The experimental results are summed up on Figure 4.5. The waveform has been sampled by streaking and resynchronized with the transient absorption spectrogram along the principles laid in Chapter 3, thus conferring inherent synchronization between the two types of data.

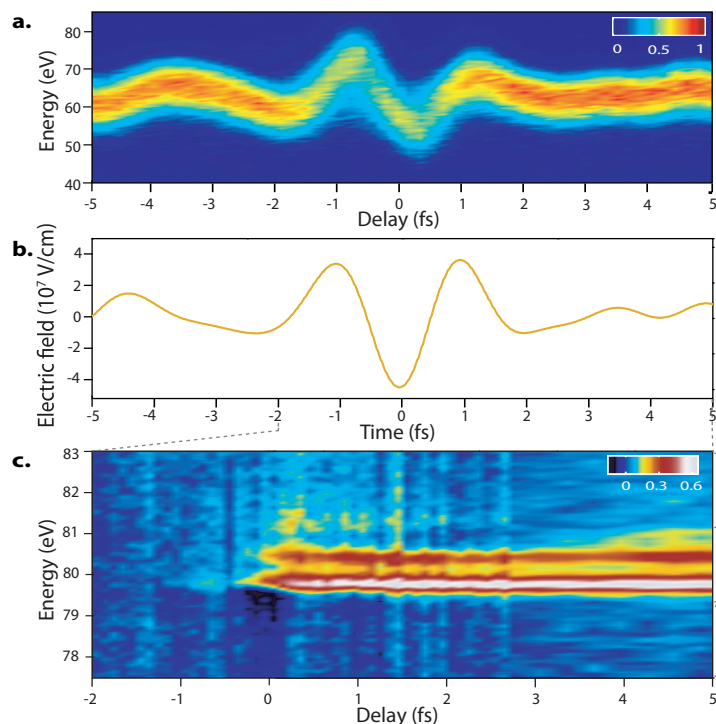


Figure 4.5: **a.** Streaking spectrogram of the pulse used for the transient absorption study of **c.** **b.** Extracted electric field from **a.** along principles exposed in Chapter 1. **c.** Transient absorption spectrogram composed of the averaging of 13 pump-probe scans. Adapted from [3].

The rise of the absorption pattern at the crossing of the 0 delay of the pump-probe axis is clearly to be seen. It is known that the ionizing transient has a duration of 2 fs (intensity FWHM), with an expected subfemtosecond ionization window (see Section 4.1.3), and the coherent oscillations of the generated ionic wavepacket [28, 3, 67] have a period of 6.3 fs. It is therefore reasonable to assume that the coherent evolution of the wavepacket is "frozen" during the ionization, in other words that its influence on the absorption strengths will be limited to a second order effect.

This absorption strength must therefore relate with the production of ions. As the next sections will show however, special care has to be taken to link absorption strength and ionic population.

4.2.3 Effect of the pump pulse on the probing process

To study the coherence of the valence electronic wavepacket [28, 3], successful theoretical approaches have assumed that the visible transient is the pump pulse, whose only effect

is to generate a coherent superposition of ionic states by strong field ionization, and that the EUV pulse merely probes the ionic wavepacket at a time defined by the pump-probe delay [112, 3]. This allows in particular to use the Beer Lambert law (in the short EUV pulse approximation), but it is restricted to positive pump-probe delays, *i.e.* to delays for which EUV pulse attains the sample *after* the visible transient.

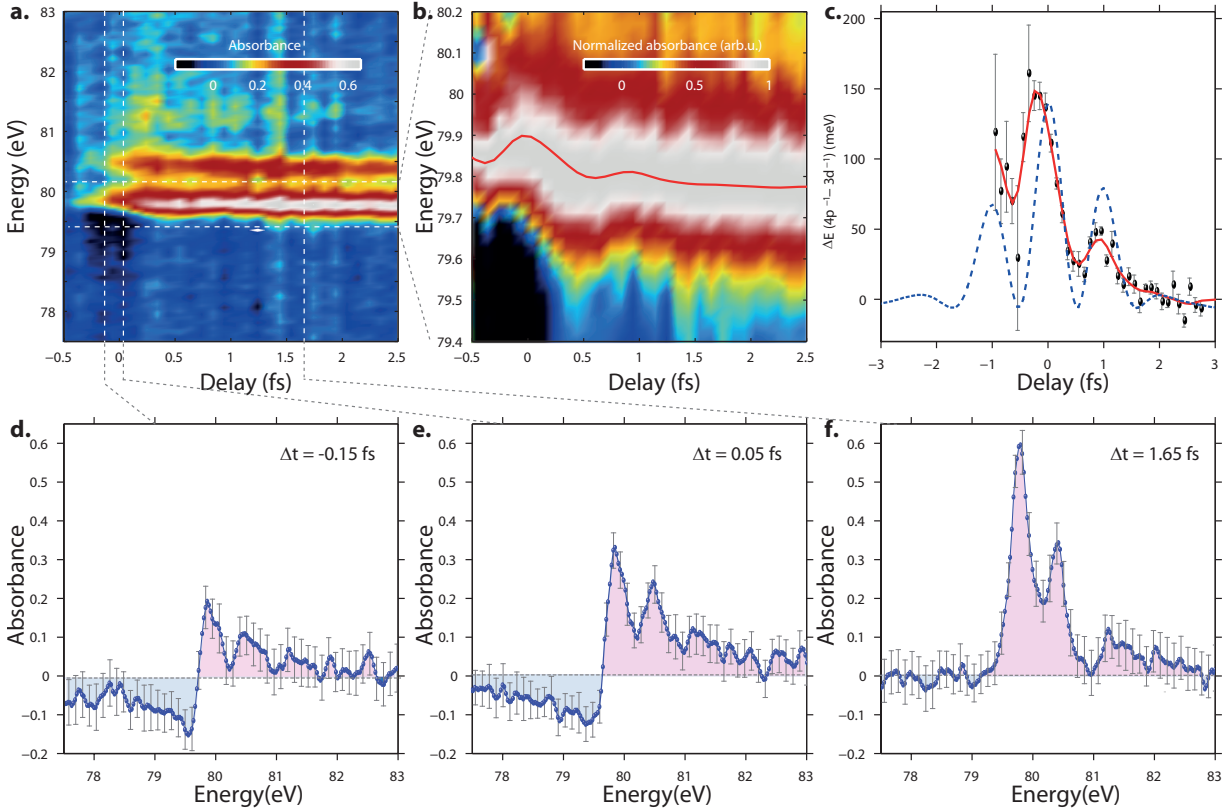


Figure 4.6: Non Lorentzian character of absorption lines in the 0 delay vicinity. **a.** Transient absorption spectrogram already shown on Figure 4.5. **b.** Zoom in on the main ($4p_{J=3/2}^{-1} - 3d_{J=5/2}^{-1}$) absorption line, normalized to its peak, showing the shift of central energy. **c.** Center of mass of the above-mentioned absorption line. **d.-f.** Snapshots of the absorbance profile at 3 pump-probe delays, displaying a broad negative absorption part on the low energy range at low delay. Adapted from [3].

Extending this assumption to the regime of overlapping pump and probe pulses at stake here, one would assume that the absorption lines must keep the Lorentzian shape expected from an exponential dephasing in the picture of the Bloch equations [113, 114, 115]. However, a look at Figure 4.6 will convince the reader that such an affirmation is in that case simplistic. Indeed the lineshapes in the vicinity of 0 delay shows that they display a highly non-Lorentzian behavior, that will be commented later on.

Figure 4.6a. and b. show that the center of mass of the main $4p_{J=3/2}^{-1} - 3d_{J=5/2}^{-1}$ line shifts to high energies in the presence of the field, to a certain extent synchronously with the instantaneous intensity.

The interpretation of the oscillation of the line center seems to point towards the well-

known DC-Stark shift [15]. Indeed, under an imparted electric field $E(t)$ varying with a frequency much lower than the transition frequency ω_0 , a nondegenerate atomic level is expected to follow the electric field adiabatically, $\Delta\omega_0(t) = \alpha/2 \cdot E^2(t)$, with α the polarizability of the level. The observations of Figure 4.6b. would suggest that our lorentzians are barely shifted in central energy by the AC Stark shift.

However an even closer look at the experimental data (see Figure 4.6d.-f) reveals that the center of mass shift is not the only manifestation of strong field influence on the line shape. It is also strongly modified to display a broad negative absorbance at low energies. Shedding this light back to Figure 4.6c., one can also notice that the oscillations are not perfectly in phase with the field, and that the center of mass does not come back to the unperturbed transition energy at the 0-crossings of the field as would be expected from the formula $\Delta\omega_0(t) = \alpha/2 \cdot E^2(t)$.

Therefore, it is to be concluded that the assumption that the transient can be considered as a pump pulse without any effect on the probe (the absorption of an EUV pulse) has to be abandoned. The transient distorts the probing process in a way that is nontrivial when it is temporally overlapping with the probe pulse, and this has to be taken into account for a solid reconstruction of the ionic population. This is the purpose of the next section.

4.3 A simple man's model of polarizability: the 3 levels system

The discussion of the previous paragraph has made us suspect that the AC-Stark shift can be a part of the explanation of the observed non-lorentzian behavior for overlapping pump and probe pulses. In other words, the polarizability of the transition, responding to the strong field, is at stake. To shed more light on this process, we will theoretically consider a simplified version of our experiment incorporating polarization effects phenomenologically. This model describes most of the relevant and observed physics.

4.3.1 Establishment of the model

To estimate the energy shift of a non-degenerate eigenstate $|1\rangle$ of a field-free hamiltonian \hat{H}_0 , coupled to an ensemble of other levels $|i\rangle$ by a constant dipolar term $\hat{\mu} \cdot E$, we can use perturbation theory. In the case of atomic states, the dipole moment has no diagonal elements ($\langle i|\hat{\mu}|i\rangle=0$) and the second order perturbation theory yields:

$$\langle 1|\hat{H}|1\rangle = \langle 1|\hat{H}_0|1\rangle + \sum_{i \neq 1} \frac{\langle 1|\hat{\mu}|i\rangle\langle i|\hat{\mu}|1\rangle}{2(\langle 1|\hat{H}_0|1\rangle - \langle i|\hat{H}_0|i\rangle)} E^2 = \langle 1|\hat{H}_0|1\rangle + \frac{\alpha_1}{2} E^2 \quad (4.7)$$

In this case the modification of the transition frequency between two states $|1\rangle$ and $|2\rangle$ due to polarization of the system by the field *and* the presence of the other levels is

$$\hbar\Delta\omega_{12} = \hbar\Delta\omega_{12}^0 + \left(\frac{\alpha_2 - \alpha_1}{2} \right) E^2 \quad (4.8)$$

We see therefore that the difference of polarizability between ground and excited levels is relevant to our problem.

It is important to mention here that the previous equations are *stricto sensu* only true in the case of a constant field, for which time-independent perturbation theory applies. The dynamic polarizability has to be used for varying-fields, also derivable from second order perturbation theory. This concept is however clear only in the case of quasi monofrequency excitation, and ill-developed in the case of our multioctave fields. In the case of largely nonresonant transitions, as is the case in this chapter, we will take the liberty to apply these formula using a time varying field, *i.e.* make a quasistatic approximation. This is quite arguable, and there is an opportunity for theory studies to clarify this issue.

To go back to our problem and keep the model simple, we will consider only the main EUV transition between $|1\rangle = 4p_{J=3/2}^{-1}$ and $|2\rangle = 3d_{J=5/2}^{-1}$. The polarizability difference between these two states due to their own presence is (numerical data from [116]):

$$\Delta\alpha_{12} = \frac{\langle 1|\hat{\mu}|2\rangle\langle 2|\hat{\mu}|1\rangle}{\langle 2|\hat{H}_0|2\rangle - \langle 1|\hat{H}_0|1\rangle} = \frac{0.345^2}{2.93} = 0.04\text{at. u.} \quad (4.9)$$

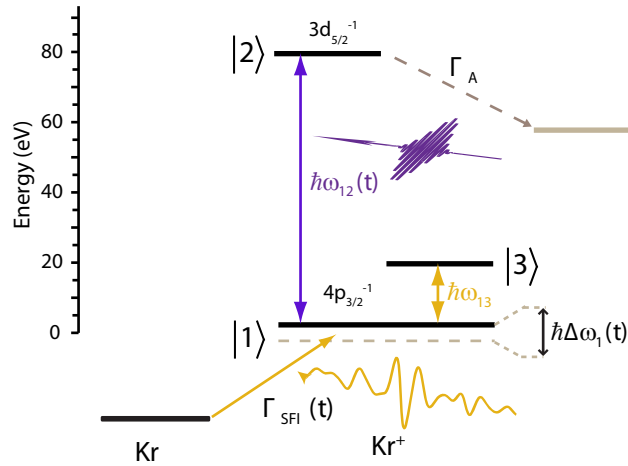


Figure 4.7: Model system for the polarization of EUV transition. The presence of $|3\rangle$ and the transient field polarizes the transition $|1\rangle$ - $|2\rangle$, making the transition energy time-dependent

With the electric field strength at the peak of the waveform, $E = 0.08$ at.u., this would account for a shift of 7.4 meV, much lower than what we have measured (see Figure 4.6). We therefore have to conclude that the presence of other polarizing levels is required. They will be represented in our calculation, again for reasons of simplicity, by the presence of a third state $|3\rangle$, thereafter designed as the "polarizing state". It will be coupled only to the ground state $|1\rangle$, as displayed on Figure 4.7. The idea behind the replacement of the multitude of states actually polarizing both $|1\rangle$ and $|2\rangle$ by a unique state coupled to $|1\rangle$ relies on Equation (4.8), under the condition:

$$\alpha_2 - \alpha_1 = \frac{\langle 1|\hat{\mu}|3\rangle\langle 3|\hat{\mu}|1\rangle}{\langle 3|\hat{H}_0|3\rangle - \langle 1|\hat{H}_0|1\rangle} \quad (4.10)$$

$|3\rangle$ will be placed at an energy of 14 eV. It is quite arbitrarily positioned close to the ionization potential of Kr, what is important is that the transition $|1\rangle$ - $|3\rangle$ is off-resonant for both the transient and the EUV pulses, and that a low population transfer to $|3\rangle$ (typically in the 10^{-4} range in the calculations) is observed. The coupling dipole matrix element $\langle 1|\hat{\mu}|3\rangle$ will be an adjustable parameter. The nature of $|3\rangle$, in other words of the states responsible for polarization of this transitions, is an intriguing question that has been investigated in a joint publication with our collaborators [117], and will be discussed later on Section 4.4.

4.3.2 Atomic response

Bloch equations approach

We will use the reduced density matrix formalism and solve the Von Neumann equation:

$$i\hbar \frac{\partial \rho}{\partial t} = [\hat{H}_0, \rho] - [\hat{\mu}, \rho] \cdot E_{tr}(t) - [\hat{\mu}, \rho] \cdot E_{EUV}(t - \Delta t) + i\hbar \left. \frac{\partial \rho}{\partial t} \right|_{SFI} + i\hbar \left. \frac{\partial \rho}{\partial t} \right|_{relax} \quad (4.11)$$

\hat{H}_0 is the field-free Hamiltonian, $\hat{\mu}$ the dipole matrix, ρ the density matrix

$$\hat{H}_0 = \hbar \begin{pmatrix} \omega_1 & 0 & 0 \\ 0 & \omega_2 & 0 \\ 0 & 0 & \omega_3 \end{pmatrix} \quad \hat{\mu} = \begin{pmatrix} 0 & \mu_{12} & \mu_{13} \\ \mu_{12} & 0 & 0 \\ \mu_{13} & 0 & 0 \end{pmatrix}$$

$E_{tr}(t)$ and $E_{EUV}(t - \Delta t)$ are respectively the transient and EUV pulse electric field, Δt is the EUV-transient delay. In all the calculations presented here we used the electric field measured by streaking for the transient with a peak intensity of $4.8 \cdot 10^{14} \text{W.cm}^{-2}$, and for the EUV a sech pulse with the FWHM of our attosecond pulse, 160 as (extracted by FROG-CRAB).

$i\hbar \left. \frac{\partial \rho}{\partial t} \right|_{SFI}$ describes the strong field ionization, via an electric field dependent feeding rate of the ground state $|1\rangle$: $\Gamma_{SFI}(E_{tr}(t))$, calculated from a fit of calculated static field values [105].

$\left. \frac{\partial \rho}{\partial t} \right|_{relax}$ is a matrix comprising relaxation terms. It takes phenomenologically into account de-excitation and dephasing channels open by to the interaction of the system with the environment that is not described in the hamiltonian (be it the electromagnetic of the free electron continua). The on-diagonal terms are population decay rates, the off-diagonal polarization decay terms.

$$\left. \frac{\partial \rho}{\partial t} \right|_{relax} = \begin{pmatrix} 0 & \Gamma_{12}\rho_{12} & 0 \\ \Gamma_{21}\rho_{21} & \Gamma_{22}\rho_{22} & 0 \\ 0 & 0 & 0 \end{pmatrix} = \begin{pmatrix} 0 & \Gamma_A/2\rho_{12} & 0 \\ \Gamma_A/2\rho_{21} & \Gamma_A\rho_{22} & 0 \\ 0 & 0 & 0 \end{pmatrix}$$

We have considered here that $\Gamma_{22} = \Gamma_A = 1/7.5\text{fs}^{-1}$, and $\Gamma_{12} = \Gamma_A/2$, and that the decay and dephasing rate of elements involving $|3\rangle$ is 0 (they are actually finite in simulations to avoid numerical noise, but it has been checked that they do not play a role in the extracted quantities).

This simplified description does not take relaxation from one state to another into account, which is reasonable in our case since the system decays via an Auger process that produces an entity not described in our system.

Moreover, the inequality $(\Gamma_{ii} + \Gamma_{jj})/2 \leq \Gamma_{ij}$ holds. The physical interpretation of this is rather simple: The polarization of an ensemble of systems can decay for numerous reasons (collisions in a gas, atom dependent Doppler shifts, interactions with the environment). One of these reasons is the decay of the population of the two levels involved. When only this channel is contributing, then the dephasing rate is minimum, and amounts to half of the population decay rate. Indeed coming back to the wavefunction picture, if the amplitude of the wavefunction on state $|i\rangle$ varies like $c_i(t) \propto e^{-\Gamma_i t}$ and for $|j\rangle$ like $c_j(t) \propto e^{-\Gamma_j t}$, then $\rho_{ii}(t) = |c_i(t)|^2 \propto e^{-2\Gamma_i t}$ and $\rho_{ij}(t) = c_i(t)c_j^*(t) \propto e^{-(\Gamma_i + \Gamma_j)t}$, and $\Gamma_{ii} = 2\Gamma_i$, and $(\Gamma_{ii} + \Gamma_{jj})/2 = \Gamma_{ij}$, which is the limiting case.

This yields a system of 9 real coupled differential equations, for the three populations ρ_{ii} , the three real parts and the three imaginary parts of the coherences $\rho_{ij}(i < j)$. The radiating dipole is obtained naturally as $d(t, \Delta t) = \text{Tr}(\hat{\mu}\rho(t, \Delta t)) = 2\text{Re}(\mu_{12}\rho_{12}(t, \Delta t) + \mu_{13}\rho_{13}(t, \Delta t))$. $\rho_{12}(t, \Delta t)$ is the only component with frequency content in the EUV range, and is therefore the coherence which evolution we will focus on.

4.3.3 Macroscopic propagation

The above section has shown how to calculate the ionic dipole response $d(t, \Delta t)$. In the experiment however, we measure the pump-probe delay-dependent absorption as $\alpha(\omega, \Delta t) = -\ln(S_{tr}(\omega, \Delta t)/S_0(\omega))$, with S_{tr} the pump-probe spectrum, and S_0 a reference spectrum, taken typically at delays where no signal is present (*i.e.* when the transient comes long before the EUV pulse). We must therefore consider the macroscopic propagation of the pulse to extract this quantity.

If Beer-Lambert's law can be used, then the absorption is directly linked to the single emitter response, as then, with L the length of the medium and \mathcal{N} the atomic density:

$$\alpha(\omega, \Delta t) = \frac{\omega}{c\epsilon_0} \text{Im} \left(\frac{d(\omega, \Delta t)}{E_{EUV}(\omega, \Delta t) + E_{tr}(\omega)} \right) \cdot \mathcal{N} \cdot L \simeq \left(\frac{d(\omega, \Delta t)}{E_{EUV}(\omega, \Delta t)} \right) \cdot \mathcal{N} \cdot L \quad (4.12)$$

To apply such a law, the *sine qua non* condition is the existence of a linear susceptibility [113], *i.e.* a linear relationship between the dipole response of the emitter $d(\omega)$ and the exciting field $E(\omega)$: $d(\omega) = \chi(\omega) \cdot E(\omega)$. This has been demonstrated in the short pulse approximation [112, 67], in the case of an EUV pulse which comes after the visible pulse, and probes the coherence of the wavepacket. In the case of overlapping pulses, or if the visible pulse comes after the EUV pulse, as will be the case in Chapter 5 and Chapter 6,

the legitimacy of this claim is too be demonstrated and will be addressed in a simple model presented in Chapter 5.

4.3.4 Comparison between model and experimental data

Figure 4.8 shows the results of the calculation presented above, with as input the exact transient field used in the experiment and sampled by streaking, and an EUV pulse of duration 160 as. They are contrasted with the experimental results already displayed on Figure 4.6. As can be seen, most of the features observed are reproduced, like the shift of the center of mass, asynchronous with the field and not going back to 0 (see Figure 4.8 c.), and a negative absorbance on the low energy side (see Figure 4.8 d.-f.). The center of mass shift can actually be seen as a manifestation of the modification of the lineshape.

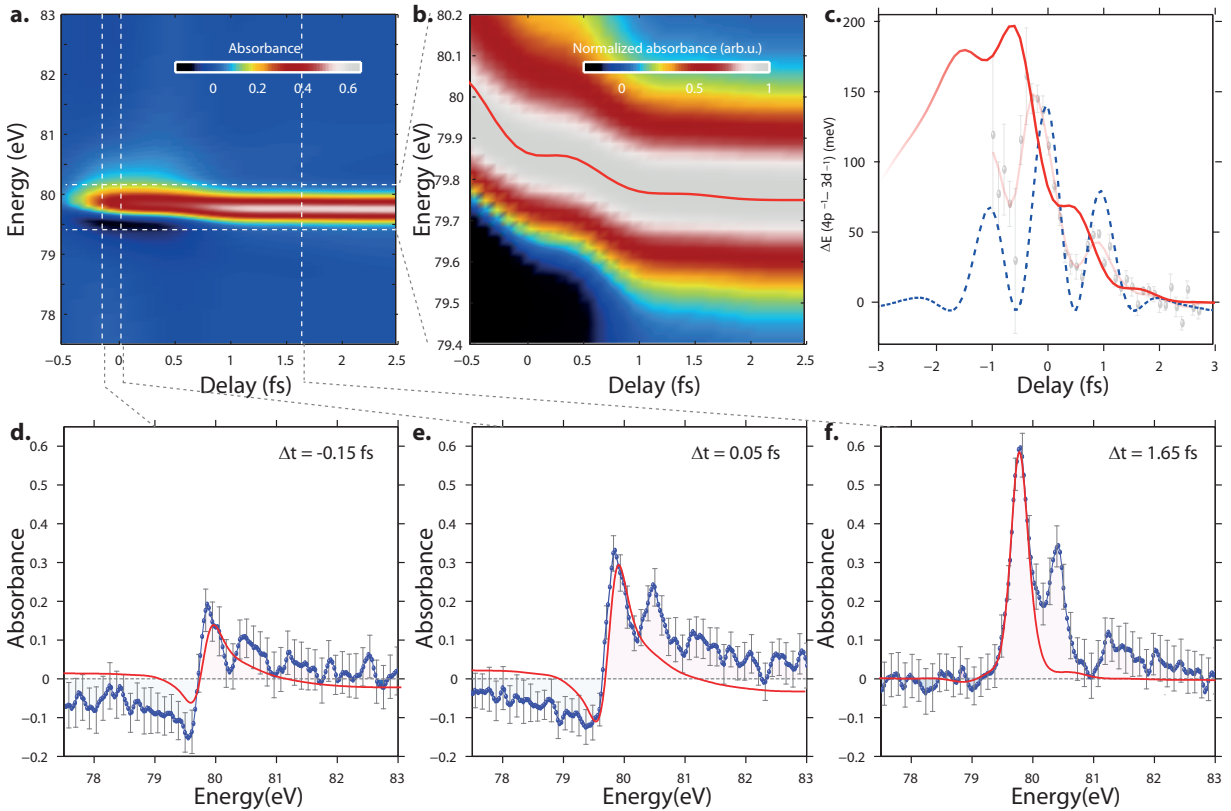


Figure 4.8: Non Lorentzian character of absorption lines in the 0 delay vicinity in the 3 levels description. **a.** Transient absorption spectrogram resulting from the calculations described in the main text **b.** Zoom in on the absorption line, normalized to its peak, showing the shift of central energy. **c.** Center of mass of the above-mentioned absorption line (plain) contrasted with the experiment (transparent in background). **d.-f.** Snapshots of the absorbance profile at 3 pump-probe delays from the simulation (red) and the experiment (transparent in background).

Differences are however still visible, that we have not been able to understand further. The most notable is the very broadband behavior of the negative absorbance shown by

the experiment, but not reproduced by the calculation. This could be due to non-resonant effects, and is still to be explained. We believe however that the most dominant physics is described in the presented picture.

4.3.5 Extraction of instantaneous ionic population and validity study

We have described in the previous sections the way in which the polarizability of the transitions studied modifies the absorption lineshapes, which is more complex than the simple shift of a lorentzian profile that was intuitively expected. However it has been complicated to apply the knowledge gained by this study into a population retrieval procedure, mainly because the shapes are not exactly reproduced by the modelling as discussed above, and because of the presence of several lines. More complex procedures based on FROG type algorithms have also been tried out, without much success.

We have therefore used a naive retrieval procedure, which consisted in fitting each delay instance with an assembly of 3 lorentzians, whose central energies are fit parameters, convoluted with a gaussian $G(\omega)$ of unit area and which width is our spectral resolution (evaluated by the measured linewidth). This yields, from our 3 absorption lines, 3 ionic state populations, $\rho_{3/2,3/2}^{\pm 3/2}(\Delta t)$, $\rho_{3/2,3/2}^{\pm 1/2}(\Delta t)$ and $\rho_{1/2,1/2}^{\pm 1/2}(\Delta t)$. The fitting function is for each delay:

$$A_{fit}(\omega, \Delta t) = -\ln[\exp[-\alpha(\omega, \Delta t)L] \otimes G(\omega)]$$

$$\text{with } \alpha(\omega, \Delta t) \propto \sum_{\text{ionic states}} \rho_{ii}(\Delta t) \frac{\Gamma_A/2}{(\omega - \omega_i(\Delta t))^2 + (\Gamma_A/2)^2} \quad (4.13)$$

We have tested this procedure for our model 3 levels system (with a single transition), for which the "real" population of $|1\rangle$ is known. The result is displayed on Figure 4.9. It shows that such a procedure allows the determination of the population with an accuracy of 10% compared to the density matrix element. Similar tests have been conducted with data from the simulation based on Time-Dependent Configuration Interaction Singles (TDCIS) ran by Stefan Pabst, in the team of Robin Santra in CFEL Hamburg. They have led to similar conclusions, of a 10% accuracy. Details can be found in a joint publication [117].

Armed with this conclusion, we have applied this procedure to the experimental data, which yields graphs of Figure 4.10, and panel **a.** shows clearly that the rise of ionic absorption, and therefore according to our simplified model the rise of population is confined to the strong half-cycle.

This fact is even clearer on Figure 4.10**b.** displaying the extracted ionization rate $\Gamma_{SFI}(t)$, and showing that the ionization window is confined to around 700 as. Our temporal resolution being estimated to 200 as (see Section 3.4.1), we can say that it seems to be broader than expected from our refined ADK model.

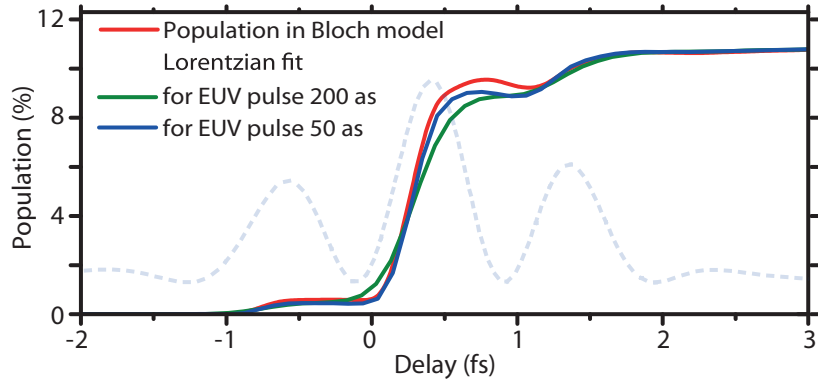


Figure 4.9: Result of the fitting of a moving lorentzian absorption lineshape to synthetic data produced by the resolution of a 3 levels system (details in text), with a 200 as (green) and 50 as (blue) EUV pulse, contrasted with the actual population of state $|1\rangle$

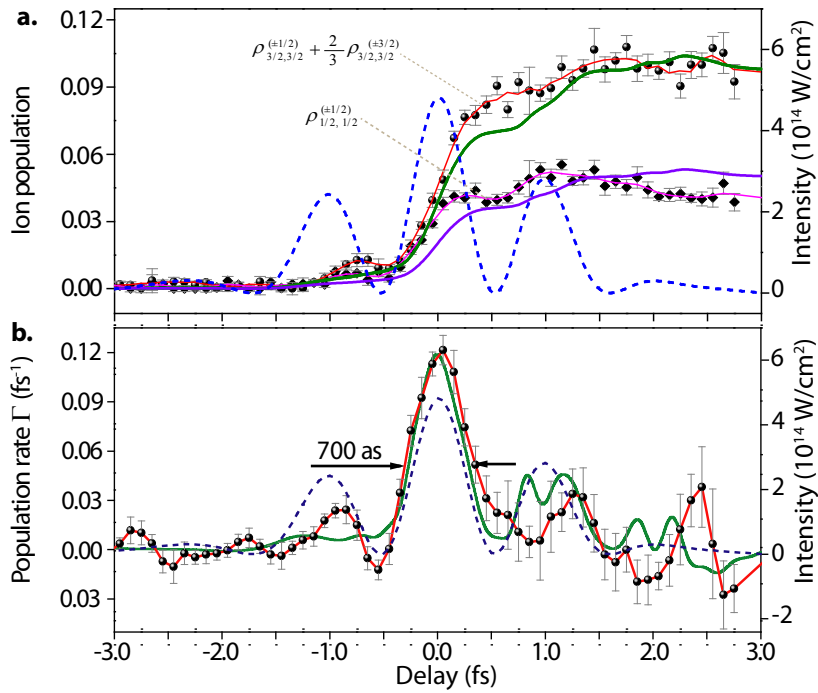


Figure 4.10: **a.** Effective population of the ion ground ($4p_{J=3/2}$, circular dots and red smoothed curve) and excited ($4p_{J=1/2}$, diamond dots and magenta smoothed curve) state manifolds. Green and purple lines are the result of TDSE solving. Details in the main text. **b.** Ionization rate $\Gamma_{SFI}(t)$ in the ground state manifold, calculated from **a.**. Adapted from [3].

4.4 Neutral induced polarizability of ionic Krypton

This section will treat of the content of a paper written in collaboration with the team of Robin Santra, especially Stefan Pabst in CFEL Hamburg [117], and where further details can be found by the curious reader. It addresses the question of the nature of the model state $|3\rangle$, introduced in the first part of this chapter to model the polarizability of the studied transition.

We have investigated the theoretical model solved by our collaborators. It is based on Time-Dependent Configuration Singles (TDCIS, details in [118, 117, 119]) and predicts a phase shift of the dipole, similar to the one exposed earlier in this chapter. We have identified 3 possible sources of phase shift in this model, and alternatively turned the relevant matrix elements off in the calculations to identify the one(s) responsible for our observations.

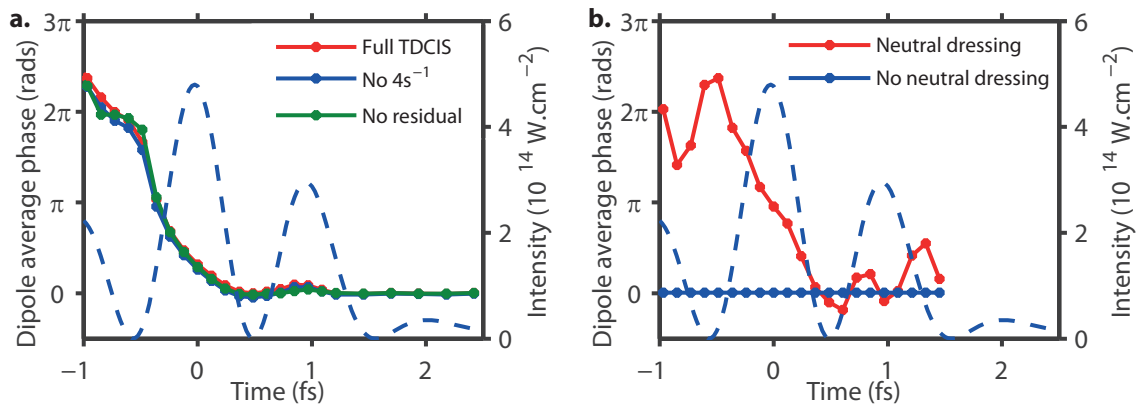


Figure 4.11: Estimations of the averaged phase of the dipole obtained from TDCIS by removing selectively supposed sources of polarizability **a.** Full TDCIS simulation (red), and removing the $4s^{-1}$ manifold (ionic polarizability, blue) and the residual Coulomb interaction (green). **b.** In a simplified model, full TDCIS (red) and turning off the neutral coupling element after the probing step (blue). Adapted from [117].

- **a. The residual Coulomb interaction** is a source of phase shift of the electronic dipole that is not due to the external field, but to the part of the Coulomb interaction that is not taken into account by the mean-field potential used in TDCIS. As can be seen on Figure 4.11a., the removal of this term does not significantly affect the polarizing physics.
- **b. The presence of ionic configurations** coupled to the configurations involved in the EUV transitions by a non zero dipole element, are the most intuitive source of polarizability. The difference of ionic polarizabilities has been calculated by state of the art atomic structure codes (Configuration interaction Singles CIS and Complete Active Space Self-Consistent Field CASSCF in the DALTON quantum chemistry suite), and have a value of around 1 atomic unit [117]. This value is too low to explain the observed phase shift, and it has been confirmed that removing the main

source of ionic polarizability in the TDCIS calculation, the $4s^{-1}$ configurations, does not affect polarizabilities (see Figure 4.11a.). This is therefore not responsible for the observed effect.

- **c. The neutral configuration:** Strong field ionization, in the quantum perspective, is the field driven transfer of a 36 electron system, Krypton, from its ground state, eigenstate of the Hamiltonian, to another eigenstate or superposition of eigenstates of the same 36 electron Hamiltonian, in which an electron is in the continuum and Krypton is singly ionized. There is a non-zero dipole matrix element between the N-electron neutral configuration and the N-electron ionic configurations, which can therefore dress each other by the intermediate of the transient field. Figure 4.11b. shows that turning this coupling off after the EUV pulse impinges on the system removes the phase shift!

This led us to the conclusion that $|3\rangle$, the state responsible for the polarization of the $|1\rangle$ - $|2\rangle$ transition in our simple man model, is not as originally suspected ionic states. The polarizability these are responsible for is too weak and cannot explain the effects observed. In fact, the main source of polarizability is the neutral atom ground state.

4.5 Addressing Double Ionization

4.5.1 System description

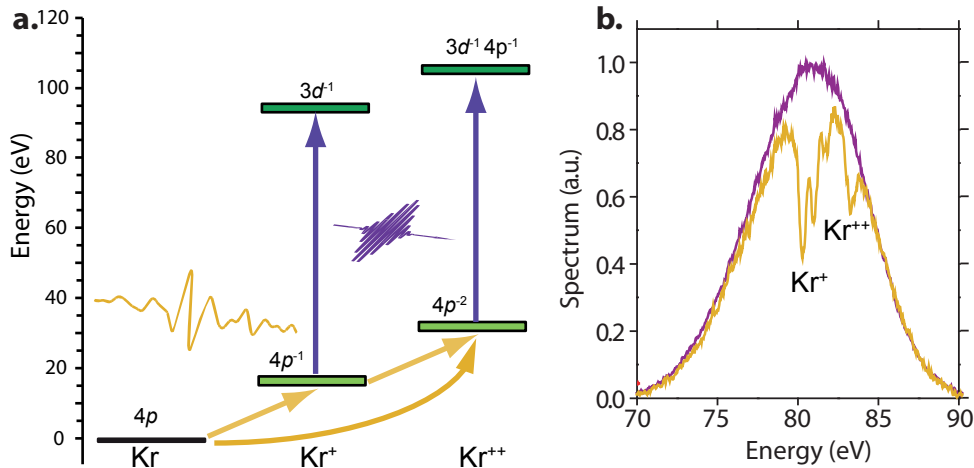


Figure 4.12: **a.** The synthesized transient with high pre-half-cycle contrast ionizes a Kr atom, generating ions in the $4p^{-1}$ and $4p^{-2}$ manifolds, which are then probed by the absorption of photons from the EUV pulse. **b.** Recorded EUV spectra for the EUV pulse preceding (violet) and following (yellow) the ionizing light transient.

As stated in Section 4.1.3, a strong-half cycle of light impinging on an atom which has not previously been exposed to ionizing levels of radiation could in principle be able to generate singly and doubly-charged ions with the same half-cycle, by sequential or

collective tunneling of two electrons. This is what we have investigated, by synthesizing to have a 5:1 pre-half-cycle intensity contrast, *i.e.* a 3 channels compressed pulse with a global phase close to $\pi/2$. It is to be kept in mind that in the current state of technology transients with the spectral content of the 4 channels including DUV are not available with a peak intensity sufficient to field ionize Krypton atoms.

We shun the synthesized pulse on Krypton atoms and probed the presence of both types of ions by monitoring EUV absorption spectra as a function of the pump-probe delay. This can be seen on Figure 4.12, with a spectrum showing the presence of Kr^+ and Kr^{++} , which are absorbing on different spectral ranges.

4.5.2 Experimental results

Experimentally, after synthesizing the pulse, we tuned its intensity up to the point where no Kr^+ ions were visible before the main half-cycle, which is the maximum explorable intensity with our current pre-pulse contrast. A typical pump-probe spectrogram is displayed on Figure 4.13a., with a zoom on the pulse overlap region and an ionic state dependent normalization on b. to enhance visibility.

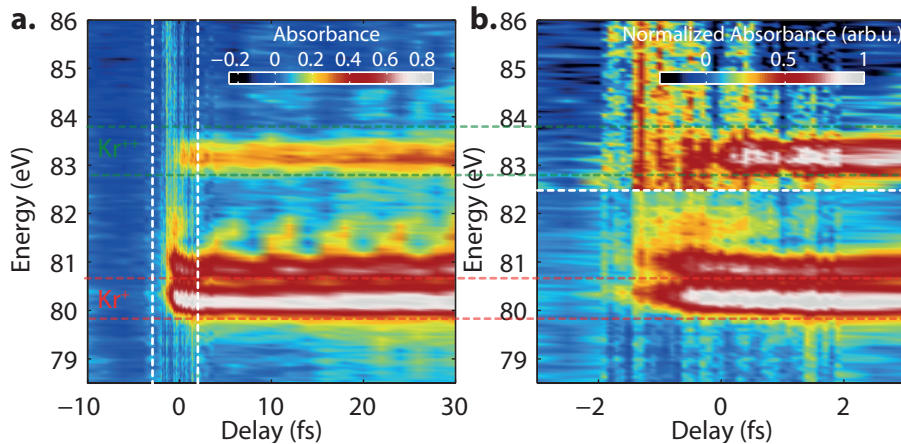


Figure 4.13: Double ionization ATAS Spectrograms **a.** Full spectrogram, resulting of the averaging of 12 spectra per-pump-probe delay, showing the formation of single and double ions of Kr atoms **b.** Close-up on the ionization time window: -3 to 3 fs (white dashed region of panel **a.**).

A calculation based on fitting of the quantum beat pattern [28] of Kr^+ and Kr^{++} absorption strengths suggests that in this experiment, around 50% of the original population has been ionized to Kr^+ , and 2.5% to Kr^{++} .

To extract the population of the singly and doubly charged ions in real-time, we can estimate the pump-probe dependent average optical density in two different spectral bands, containing respectively the main Kr^+ transition $4p_{J=3/2}^{-1} - 3d_{J=5/2}^{-1}$, and the region where Kr^{++} absorbs (see delimitations on Figure 4.13). The result of this crude analysis is shown on Figure 4.14a. and seems to suggest that the two ionic populations are rising synchronously, indicating the regime we were looking for. However an analysis based on the

lorentzian assumption, similar to the one presented in Section 4.3.5, which results are displayed on Figure 4.14b. gives a different picture. It is therefore hard to reach any solid conclusion, and it has been the case for all the scans we have taken. Polarization effects are responsible for this fact, as will be shown in the next subsection.

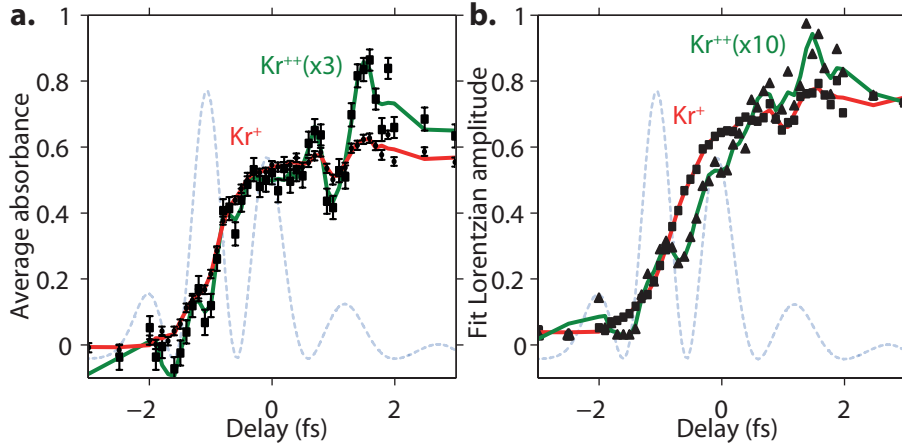


Figure 4.14: Estimations of ionic populations build-ups **a.** Averaged absorbance on a band encompassing the Kr⁺ main absorption line (red, see Figure 4.13), and Kr⁺⁺ absorption features (green, see Figure 4.13) **b.** coefficients of lorentzian fitting of the corresponding features with a methodology similar to the one exposed in Section 4.3.5.

A common feature in all these scans, well noticeable on Figure 4.14a., is the wiggle in the data present at + 1 fs. It has been suggested that this could be a sign of the recollision of a field-extracted electron, in other words to the interference of the EUV pulse and EUV light emitted by the probed process. However of interest, this has not been investigated closer, as we turned to the investigations in atomic Krypton presented in Chapter 5, in order to address polarizability issues in a simpler system.

4.5.3 Polarization effects

A closer look at the absorption cross-section at the overlap of both EUV pulse and transient (Figure 4.15 blue curve) shows that the lineshapes are distorted as was expected from the previous discussion, but also explains why extraction of populations is rendered hard. Indeed, we see that the spectral region where the Kr⁺⁺ absorption features are supposed to show up is contaminated by absorbance from Kr⁺, redistributed by polarization effects. The previously observed broadband negative absorption is also seen.

These facts are hindering our attempts to extract a reasonable population curve out of this data from our current tools, and calls for a more thorough theoretical understanding of the processes at stake.

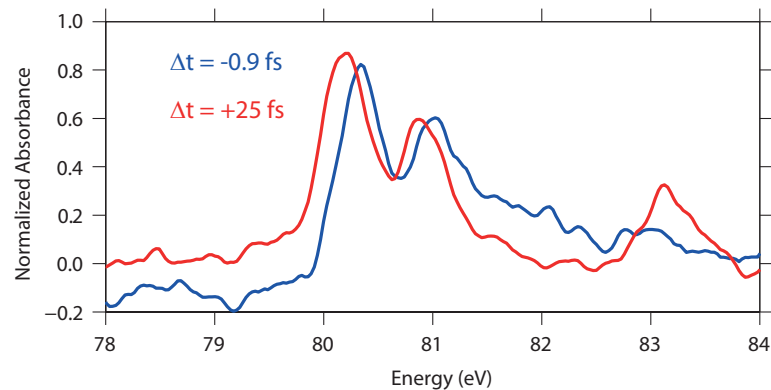


Figure 4.15: Experimental absorption cross-sections at overlap between main first half-cycle and EUV pulse (blue curve), and after the generation (blue curve)

Conclusion

We have investigated strong field single and double ionization by attosecond transient absorption. The obtained spectrograms are the result of the resonant excitation of strong field generated absorbers by an EUV attosecond pulse. The dipole response of this system depends on both the EUV and the strong off-resonance transient field. When the two pulses do not overlap temporally, the response can be derived and coherence properties after ionization can be studied. However, issues arise when trying to investigate the dynamics of the creation of absorbers during the laser pulse. The dipole created by the EUV pulse is then indeed disturbed by the strong transient field. The latter is indeed generating absorbing population through strong field ionization, the studied process (pump), but also changes the internal structure of the ion, by polarizing it, and hence perturbs the probing process. This results in non-lorentzian absorption line shapes in the vicinity of the transient which need to be carefully taken into account, since then a clear separation between pumping and probing steps is not anymore valid.

Once done, in the case of relatively moderate field strength it has been shown that the field ionization rate follows the field, and can be confined to a single half cycle of light by synthesis techniques. We have also at this occasion learned about the polarization of ionic states during the process of strong field ionization, which results mainly from dipole coupling of the N-electron ionic with the N-electron neutral configurations, and not from purely ionic polarizability effects.

However, strong polarization effects have so far impeded our attempts to learn about the temporal dynamics of double ionization processes, which require even higher levels of optical fields.

The mechanism put into light here with Krypton ions in the case of overlap between EUV and visible pulse should be (however with different polarization mechanisms) general and applicable to the neutral atom and more complex systems, where the signal will be present also at delays where the EUV pulse precedes the visible pulse. This part of the pump-probe axis was missing in the experiments presented in this chapter. Indeed, the

absorbers were ions, which do not exist when the EUV pulse hits the atom before the ionizing visible transient. This has triggered our curiosity to explore a new paradigm, for we will consider in the next chapters the EUV pulse as a pump, initiating the absorption process, which will subsequently be probed by the visible transient.

5

Optical dipole gating of Auger decoherence process in Krypton

Perseverance is a great element of success. If you only knock long enough and loud enough at the gate, you are sure to wake up somebody.

– Henry Wadsworth Longfellow

As has been presented at the end of previous chapter, the picture of a strong optical field "pumping" the system to an excited state, *i.e.* , and an EUV pulse probing the instantaneous wavepacket by absorption independently is simplistic in the case of overlapping pulses, or if the optical field impinges the system after the EUV pulse. Indeed the pumping pulse also impacts the probing process, which prevents a reasonably simple interpretation of the results. To investigate the phenomena leading to absorption disturbance more thoroughly, we have studied a simplified system which does not need to be prepared by the optical transient: the neutral Krypton atom. Here the picture is simpler: the pump is the EUV pulse, and the optical transient is the probe. It is able to disturb the decoherence process of the launched electronic dipole. Therefore the notation will be changed with respect to the previous chapter, we will now use $\tau = -\Delta t$ as the pump probe delay, *i.e.* the delay of optical with respect to EUV pulse.

We recorded Attosecond Transient Absorption Spectrograms and developed a formalism based on phase and amplitude gating of the EUV dipole during its dephasing process by the optical field, in order to reconstruct the process with great accuracy.

5.1 The dipole gating paradigm

Basic optics teaches us that absorption and dispersion of an electric field result from its coherent superposition with the field radiated by the macroscopic dipole it has excited in a medium. In the case of the absorption from an EUV pulse shorter than the decay of this dipole, these processes can be separated in two steps: the pulse generates a coherent superposition of ground and excited state, which then oscillates and radiates at its nat-

ural transition frequency. Subject to radiative or non radiative single emitter losses, and macroscopic dephasing sources, the dipole decays.

To understand the effect of the field of the optical transient on this electronic dipole, and therefore the perturbation of the absorption process, we have developed a picture relying on the phase and amplitude gating of this dipole.

5.1.1 The intuitive picture

The absorption of EUV light from the attosecond pulse, which is much shorter than the decay is a 2 steps process. First the EUV pulse creates a coherent superposition of ground and excited states (step 1 on Figure 5.1), and then this coherent superposition oscillates with a $\pi/2$ phase shift compared to the exciting wave, and therefore radiates out of phase with it. The addition of the EUV pulse field and the field radiated by the coherent superposition is responsible for the presence of the absorption line in the spectrum.

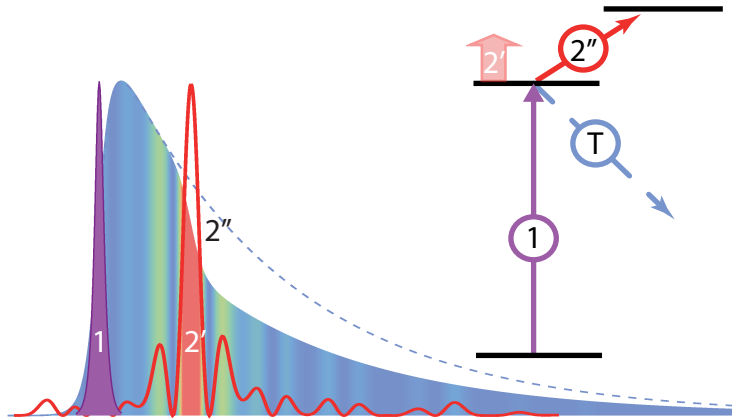


Figure 5.1: Schematic view of the perturbation of the dipole imposed by an attotransient

Following the excitation of this dipole, the application of a delayed comparatively low-frequency pulse, in the form of a delayed attotransient $E_{tr}(t - \tau)$ can modify the behavior of this dipole in two different ways, which will impact absorption and dispersion:

-By polarizing the atom (ground and excited state), it will shift the instantaneous transition frequency as a function of time like $\Delta\omega(t - \tau) = \alpha/2E_{tr}^2(t - \tau)$, and impose a phase shift to the transition dipole, similar to the effect we have seen in Chapter 4. This is represented a step 2' on Figure 5.1.

-The transient can also damp the amplitude of the oscillating dipole, by photoionizing or transferring the electron placed in the excited state to an external state. This is represented a step 2'' on Figure 5.1.

It is important to note that the amount of phase added, or the proportion of dipole damping does not depend on the delay between the EUV pulse and the optical probe, as long as saturation effects can be excluded by an amplitude damping reasonably smaller than 1. In such a configuration, the electronic dipole of a single emitter, shun by an optical field at a controlled delay after an EUV pulse can be expressed in an intuitive way:

$$d(t, \tau) = d^{(0)}(t)A(t - \tau)e^{-i\phi(t-\tau)}$$

$$\text{With } d^{(0)}(t) = i\Theta(t) \exp\left(-i\omega_0 t - \frac{t}{T}\right) \quad (5.1)$$

$d^{(0)}(t)$ is the complex (positive frequency part) dipole in the short EUV pulse approximation, Θ the Heaviside function, T the decay time of the dipole and ω_0 the natural transition frequency. $A(t - \tau)$ and $\phi(t - \tau)$ are respectively the amplitude and phase gates, that are translated through the dipole with the pump probe delay.

5.1.2 Derivation of gating formula from Von Neumann equation

Interestingly a picture of phase and amplitude gating, close to the intuitive thinking developed above can be derived from the simple 3 levels formalism presented in Chapter 4. This links a simple, but quantum perspective with the phenomenological model. To this end, we use a dressed-state approach to fully describe the effect of the polarization of $|1\rangle$ by $|3\rangle$ with a dressed state $|1(t)\rangle$. A quasistatic and a short EUV pulse approximations will be used, and justified as they are made in the derivation. Let us rewrite the Bloch equations Equation (4.11) in the EUV pump optical probe perspective:

$$i\hbar \frac{\partial \rho}{\partial t} = [\hat{H}_0, \rho] - [\hat{\mu}, \rho] \cdot E_{tr}(t - \tau) - [\hat{\mu}, \rho] \cdot E_{EUV}(t) + i\hbar \left. \frac{\partial \rho}{\partial t} \right|_{opt} + i\hbar \left. \frac{\partial \rho}{\partial t} \right|_{relax} \quad (5.2)$$

Here we have added $\left. \frac{\partial \rho}{\partial t} \right|_{opt}$ as a term describing depletion (or construction) of the wavepacket due to the optical field. It is a function of $E_{tr}(t - \tau)$ and it takes the form of time-dependent rate terms $\Gamma_{ij}^{depl}(t - \tau)\rho_{ij}(t)$.

To make the role of the polarization of state $|3\rangle$ clearer we will write 5.2 in the laser dressed state basis. To this end, we diagonalise $\hat{H}_0 - \hat{\mu} \cdot E_{tr}(t - \tau)$ in the subspace formed by $|1\rangle$ and $|3\rangle$. With $M(t - \tau)$ the base-changing matrix, and $\Omega_{ij}^{tr}(t - \tau) = \frac{\mu_{ij} E_{tr}(t - \tau)}{\hbar}$ the instantaneous Rabi frequency between the states $|i\rangle$ and $|j\rangle$:

$$\begin{aligned} \hat{H}_0 - \hat{\mu} \cdot E_{tr}(t) &= \hbar \begin{pmatrix} \omega_1 & -\Omega_{12}^{tr}(t - \tau) & -\Omega_{13}^{tr}(t - \tau) \\ -\Omega_{12}^{tr}(t - \tau) & \omega_2 & 0 \\ -\Omega_{13}^{tr}(t - \tau) & 0 & \omega_3 \end{pmatrix} \\ &= M(t - \tau) \cdot \hbar \begin{pmatrix} \omega_1(t - \tau) & -\tilde{\Omega}^{tr}(t - \tau) & -0 \\ -\tilde{\Omega}_{12}^{tr}(t - \tau) & \omega_2 & -\tilde{\Omega}_{23}^{tr}(t - \tau) \\ 0 & -\tilde{\Omega}_{23}^{tr}(t - \tau) & \omega_3(t - \tau) \end{pmatrix} \cdot M^\dagger(t - \tau) \end{aligned} \quad (5.3)$$

The energy of the adiabatic states $|\tilde{1}(t - \tau)\rangle$ (and $|\tilde{3}(t - \tau)\rangle$), and therefore the probed transition frequency are time dependent in this picture:

$$\omega_{12}(t - \tau) = \omega_2 - \omega_1(t - \tau) = \omega_2 - \omega_1 - \frac{1}{2} \left(\sqrt{\omega_3^2 + 4\Omega_{13}^{tr}(t - \tau)^2} - \omega_3 \right) \quad (5.4)$$

Furthermore we get (from the matrix M):

$$\begin{aligned} |\tilde{1}(t - \tau)\rangle &= a_{11}(t - \tau)|1\rangle + a_{13}(t - \tau)|3\rangle, \\ \text{With: } a_{11}(t) &= \frac{\Omega_{13}^{tr}(t)}{\sqrt{\Omega_{13}^{tr}(t)^2 + \Delta\omega_1(t)^2}} \quad a_{13}(t) = \frac{\Delta\omega_1(t)}{\sqrt{\Omega_{13}^{tr}(t)^2 + \Delta\omega_1(t)^2}} \end{aligned} \quad (5.5)$$

This implies a time dependence of the matrix element $\tilde{\mu}_{12}(t - \tau) = \langle \tilde{1}(t - \tau) | \hat{\mu} | 2 \rangle = a_{11}(t - \tau)\mu_{12}$. We can rewrite Equation (5.2) in this base by multiplying it left with $M(t - \tau)$ and right with $M^\dagger(t - \tau)$. The equation of evolution of $\tilde{\rho}_{12}(t)$ in this new base is:

$$\begin{aligned} \left(i \frac{d}{dt} - \omega_{12} + i \frac{\Gamma_{Aug}}{2} - \Delta\omega_{12}(t - \tau) + i\Gamma_{12}^{depl}(t - \tau) \right) \tilde{\rho}_{12} + f(t) \\ = - \frac{E_{EUV}(t)}{\hbar} \tilde{\mu}_{12}(t - \tau) (\tilde{\rho}_{22}(t) - \tilde{\rho}_{11}(t)) \end{aligned} \quad (5.6)$$

$f(t)$ is a term depending on derivatives of M and M^\dagger . In this situation, a quasistatic approximation can be made and f neglected, because M varies with the time scale of E_{tr} , which is much slower than the natural oscillation period of the coherence $2\pi/\omega_{12}$.

In the short EUV pulse approximation, $E_{EUV}(t) = A\delta(t)$, and neglecting the population of $|2\rangle$, the solution of the above equation is:

$$\tilde{\rho}_{12}(t, \tau) = A\tilde{\mu}_{12}(-\tau)\tilde{\rho}_{11}(0)\chi_{12}(t, \tau) \quad (5.7)$$

With χ_{12} the delay dependent response function:

$$\begin{aligned} \chi_{12}(t, \tau) &= \frac{i}{\hbar} \Theta(t) \exp \left(-\frac{\Gamma_{Aug}}{2} t - i\omega_{12} t \right) \\ &\quad \cdot \exp \left(-\int_0^t \Gamma_{12}^{depl}(t' - \tau) dt' - i \int_0^t \Delta\omega_{12}(t' - \tau) dt' \right) \end{aligned} \quad (5.8)$$

We see that if the transient field is set to zero, $\Delta\omega_{12}(t) = 0$, and $\Gamma_{12}^{depl}(t) = 0$, and we get the nonperturbed linear response function:

$$\chi_{12}^0(t) = \frac{i}{\hbar} \Theta(t) \exp \left(-\frac{\Gamma_{Aug}}{2} t - i\omega_{12} t \right) \quad (5.9)$$

Let us define $r(t) = \int_{-\infty}^t \Gamma_{12}^{depl}(t') dt'$ and $\phi(t) = \int_{-\infty}^t \Delta\omega_{12}(t') dt'$. Then we can calculate the analytical (positive frequency part) dipole, using the trace, which is base independent.

$$\begin{aligned}
d_{12}(t, \tau) &= \text{Tr}(\hat{\mu}\tilde{\rho}(t, \tau)) \\
&\simeq \tilde{\mu}_{12}(t - \tau)\tilde{\rho}_{12}(t, \tau) \\
&= A\mu_{12}^2 a_{11}(0)^2 \rho_{11}(0) \chi_{12}^0(t) \\
&\quad \cdot a_{11}(-\tau) \exp(r(-\tau) + i\phi(-\tau)) \\
&\quad \cdot a_{11}(t - \tau) \exp(-r(t - \tau) - i\phi(t - \tau))
\end{aligned} \tag{5.10}$$

If the pump probe delay is longer than the duration of the transient $\tau > T_{tr}$, we have $a_{11}(-\tau) \exp(r(-\tau) + i\phi(-\tau)) = 1$. Then the modification induced to the electronic dipole is indeed reduced to the translation of an amplitude and phase gate on the electronic dipole, which was postulated from phenomenological considerations in the previous section :

$$G(t - \tau) = a_{11}(t - \tau) \exp(-r(t - \tau) - i\phi(t - \tau)) \tag{5.11}$$

It is to be noted that in the dressed states base, there will also be a component d_{23} of the dipole. It will however be short lived and weak since $\tilde{\mu}_{23} \neq 0$ only during the transient. Moreover, it cannot affect the response on the EUV spectral range if $|3\rangle$ is away from $|1\rangle$ by more than the energy span of the EUV. In the case of closer levels, and short lifetime excitations (in the range of the transient duration), this term has to be considered in the dipole emission. This question goes beyond the scope of this work, and will not be considered further.

Based on Equation (5.10), it is possible to derive an expression similar to the one used in Frequency Resolved Optical Gating for the Complete reconstruction of Attosecond Bursts (FROG-CRAB) [55], and in principle to apply a principal component generalized projections algorithm (PGCPA) [120] to extract both the phase and amplitude gate, and the gated dipole as a function of time. This derivation is developed in Appendix B. Our few attempts to use it have failed in the case of decoherence times longer than the optical pulse. This is due to the slight difference in mathematical formulation with a FROG expression. Moreover, tests on perfect numerical data have revealed that the method is not sensitive enough to allow the PGCPA algorithm to converge towards satisfying pump and gate fields. It is however a quite general concept which could be investigated further as an extension of the work presented here.

5.1.3 Macroscopic propagation

As seen in Section 4.3.3, to apply the Beer-Lambert law (Equation (4.12)), the *sine qua non* condition is the existence of a linear susceptibility [113], *i.e.* a linear relation between the dipole response of the emitter $d(\omega)$ and the exciting field $E(\omega)$: $d(\omega) = \chi(\omega) \cdot E(\omega)$. This has been demonstrated in the short pulse approximation [112, 67], in the case of an EUV pulse which comes after the visible pulse, and probes the coherence of the wavepacket. When the visible pulse overlaps or comes after the EUV pulse, in the simplified framework developed in the previous section, it has been shown with Equation (5.10), which amounts

to $d_{12}(\omega, \tau) = E_{EUV}(\omega) \cdot \chi_{12}(\omega, \tau)$. This allows us to use the Beer Lambert law. A more systematic demonstration goes beyond the scope of this study.

5.1.4 Associated model functions for the lineshape

Equation (5.1) and Equation (5.10) have shown that for the case of an EUV transition between two states $|1\rangle$ and $|i\rangle$, dressed by an attotransient, under some hypotheses we can write a generalized response function, dependent on the delay τ between the EUV and the optical attosecond pulses:

$$\chi_{1i}(t, \tau) \propto i\Theta(t)A(t - \tau)\exp\left(-\frac{t}{T_{1i}} - i\omega_{1i}t - i\phi(t - \tau)\right) \quad (5.12)$$

The absorption lineshape is readily obtained from this form using the Beer Lambert law (Equation (4.12)), as soon as the amplitude and phase gate are specified. In our experiments we used two types of approach, the instantaneous and the field based gates.

Instantaneous gate

If the attotransient can be considered as much shorter than T_{1i} , it is reasonable to assume the loss of amplitude and the phase shift to be instantaneous: $A(t - \tau) = 1 - r \Theta(t - \tau)$ and $\phi(t - \tau) = \phi_0 \Theta(t - \tau)$. In that case there is a simple analytic expression for $\chi_{1i}(\omega, \tau)$, thus for $\alpha_{1i}(\omega, \tau)$:

$$\begin{aligned} \chi_{1i}(\omega, \tau) &\propto \int_{-\infty}^{\infty} \chi_{1i}(t, \tau) e^{i\omega t} dt \\ \chi_{1i}(\omega, \tau) &\propto i \int_0^{\tau} e^{-\frac{t}{T_{1i}} - i(\omega_{1i} - \omega)t} + i(1 - r) \int_{\tau}^{\infty} e^{-\frac{t}{T_{1i}} - i(\omega_{1i} - \omega)t - i\phi_0} dt \\ \chi_{1i}(\omega, \tau) &\propto \frac{-1}{(\omega - \omega_{1i}) + \frac{i}{T_{1i}}} \left(1 - e^{(i(\omega - \omega_{1i}) - 1/T_{1i})\tau} (1 - (1 - r)e^{i\phi_0})\right) \\ \chi_{1i}(\omega, \tau) &= \chi_{1i}^{(0)}(\omega) \left(1 - e^{(i(\omega - \omega_{1i}) - 1/T_{1i})\tau} (1 - (1 - r)e^{i\phi_0})\right) \end{aligned} \quad (5.13)$$

In this form, the physics governing the lineshape change is easy to grasp: the dipole decays unperturbed until $t = \tau$, the point in time when its phase and amplitude are changed abruptly by an infinitely fast optical field. The lineshape results from the coherent sum of the unperturbed part and the perturbed part of the dipole, as shown on Figure 5.2.

It is possible to get a more intuitive understanding of the role of phase and amplitude. The absorption contribution from the unperturbed part of the dipole looks like a cardinal sine function, with a period $1/\tau$. Indeed, it is generated by a truncated exponential function. The absorption from the perturbed part of the dipole is asymmetric when the phase is not 0 or π , and its amplitude is modulated by the amplitude factor. Thus, the highest the amplitude depletion factor, the more the absorption lineshape will look like a

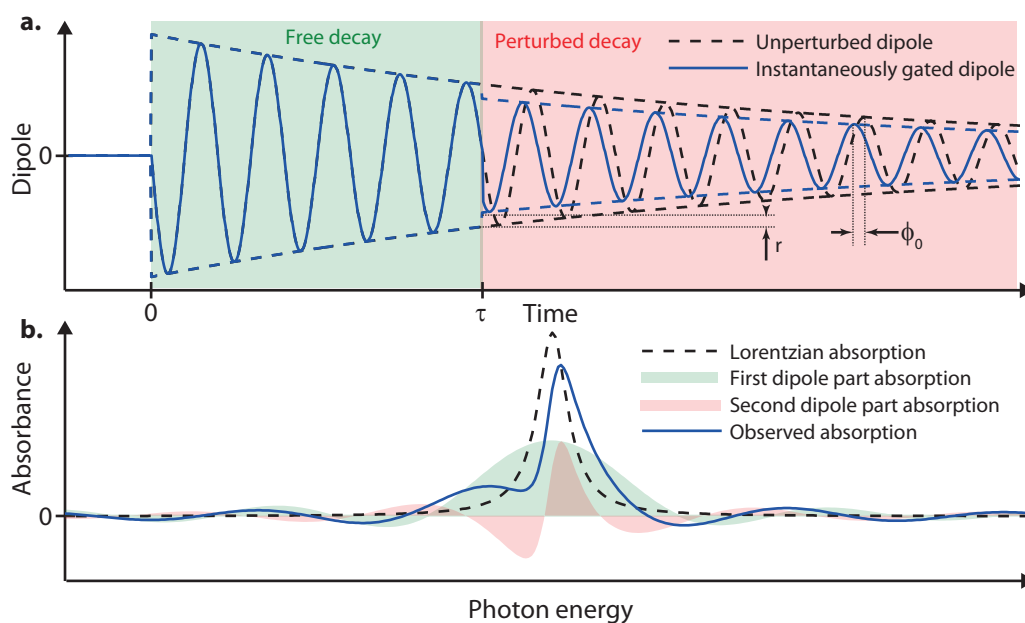


Figure 5.2: The gating process and its influence on the absorption for $r = 0.2$ and $\phi_0 = \pi/4$. **a.** Until $t = \tau$, the dipole decays in an identical fashion with the perturbation-free dipole, and then with a phase ϕ_0 and an amplitude drop of a fraction r . **b.** The first part of the dipole, unperturbed, is responsible for absorption pictured by the green area. The second, perturbed part for the absorption represented by the red area. The net absorption lineshape is the blue curve, the sum of both contributions.

sinc function. The delay is of course an important parameter, since the highest it is, the closest to the original lorentzian the lineshape will be.

Figure 5.3a. shows a pump-probe delay map of the absorption lineshapes calculated with Equation (5.13) and the parameters used for Figure 5.2. Figure 5.3b. displays the difference between these and the lorentzian lineshape, or differential absorption. The axes are labeled in units of T for the delay and ω_0 for the photon energy. The spectral oscillations coming from the first unperturbed part of the dipole with period $1/\tau$ are well visible. As intuitively expected, the perturbation dies out for $\tau > T$, so these maps carry indication of the dephasing time T on the pump-probe axis.

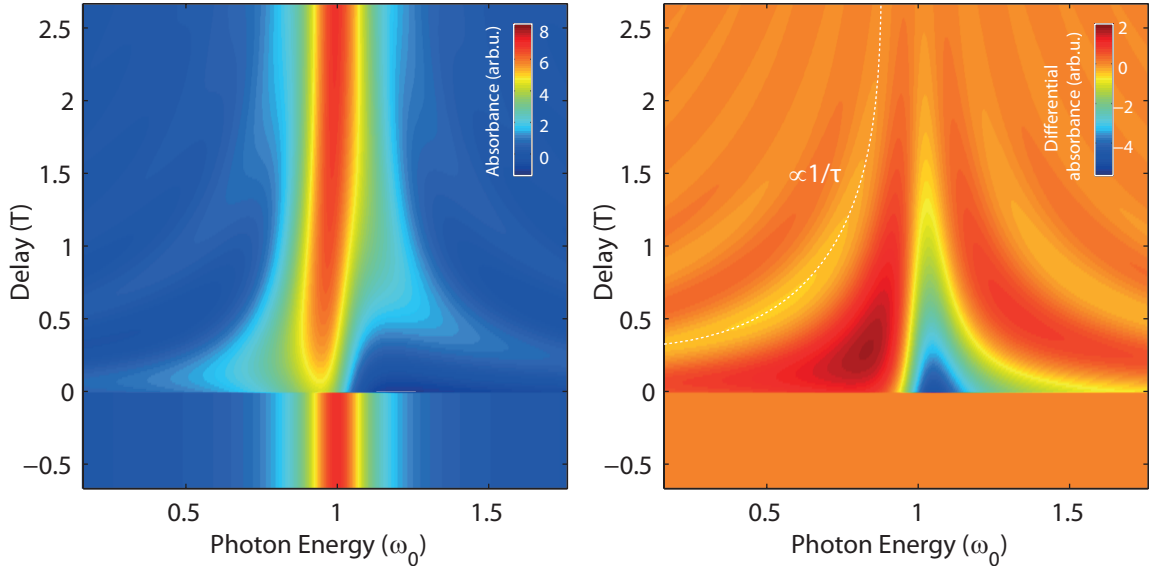


Figure 5.3: Absorption lineshapes pump-probe delay maps for $r = 0.2$ and $\phi_0 = \pi/4$. **a.** Absorbance map and **b.** Differential absorbance map. The axes are in unit of T and ω_0 .

Optical field-based gate

Since the field of the transient $E_{tr}(t)$ is measured directly via streaking in our experiments, and the pump-probe axis carefully locked as described in Chapter 3, we also have the opportunity to assume a field dependence for the amplitude and phase gates, and use it to calculate the lineshape. In this case, the formula is not analytical anymore, but surely more realistic when the decay time of the dipole approaches the transient duration. We can, for the sake of the present discussion, assume that the instantaneous frequency shift is quadratic in field (as is the case for the Stark shift), and that so is the the amplitude depletion rate, corresponding to a linear photoionization (This corresponds to our experimental conditions, as discussed later in Section 5.2.1, but could be adapted to other contexts):

$$\phi(t - \tau) = \int_0^t dt' \frac{\alpha}{2} E_{tr}^2(t' - \tau) \quad (5.14)$$

$$\text{and } A(t - \tau) = 1 - \exp\left(-\int_0^t dt' \gamma E_{tr}^2(t' - \tau)\right) \quad (5.15)$$

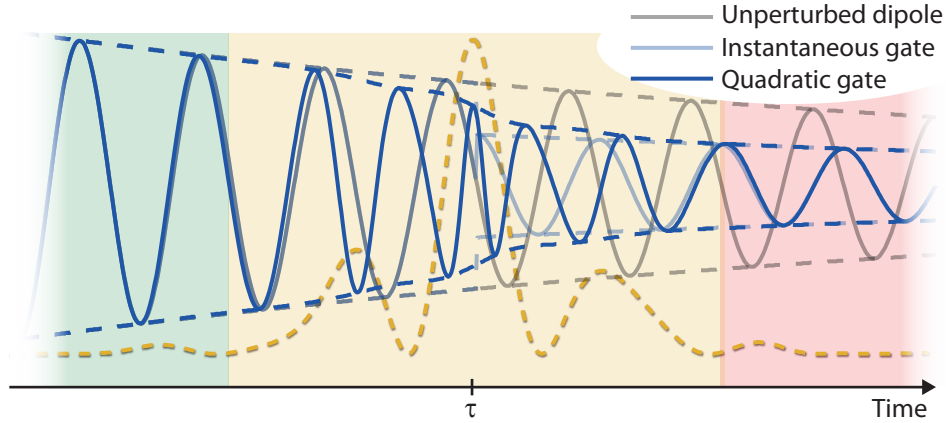


Figure 5.4: Schematic temporal evolution of the dipole for the two different kinds of gates.

Figure 5.4 shows the difference between the dipoles in the two cases. The difference between lineshapes calculated from Equation (5.13) and Equation (5.14) is only sensible close to delay $\tau = 0$ and if the dipole decoherence time is close to the transient main half-cycle duration. Indeed then, the part of the dipole that is radiated *during the probe pulse* is significant compared to the unperturbed and fully perturbed dipole before and after the probe. Equation (5.14) is best suited to study the sensitivity of the lineshapes to the decoherence time T . Figure 5.5 shows pump-probe absorption maps calculated for variable decoherence times, calculated with the electric field sampled in the experiment.

As can be seen on the left panels **a.** and **d.**, when the decoherence time is smaller than the half-period of the field, the lineshape change is merely a shift in energy, and is confined to the overlap between EUV pulse and transient field. It is somewhat intuitive, since then during the complete process of absorption, the frequency of the transition is shifted by the quadratic Stark shift. Of course in this regime, the information about decoherence time does not exist anymore on the pump-probe delay axis. The absorption line center of mass is then exactly mapping the field intensity. For decoherence times of the order of the field sensitive structure on the pump-probe axis is still visible, but smearing out, and it is completely lost in the other extreme at high T (panels **c.** and **f.**).

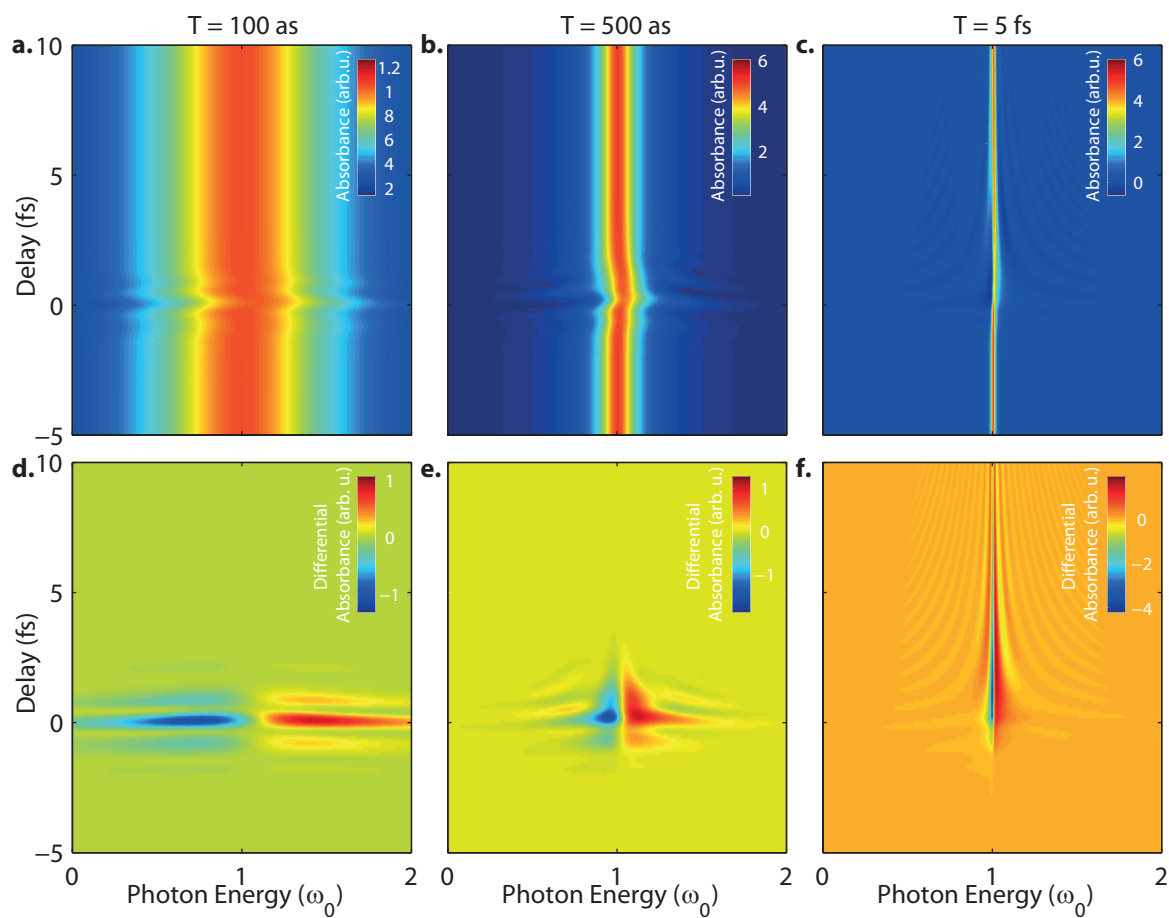


Figure 5.5: Absorbance (a.-c.) and Differential absorbance (d.-f.) pump-probe delay maps for $T = 100$ as (left), $T = 500$ as (center) and $T = 5$ fs (right)

5.2 Dipole gating measurement in Krypton

To verify the concepts developed in the previous sections, we have calculated and measured Attosecond Transient Absorption Spectrograms of $3d - np$ edge in Kr atoms. The dipole excited in these transitions decays mainly because of the Auger filling of the 3d hole, which time constant has already been measured by various techniques, in the spectral and time domain. Its time-domain investigation in an all-photonic fashion remains however unexplored, and is, given its timescale, an object of choice for the first demonstration and benchmarking of our technique.

5.2.1 The $3d - np$ absorption edge of Krypton

Spectroscopic description

In Chapter 4, the EUV transitions considered consisted of a transition between $3d$ core-shell levels and a vacancy of the $4p$ shell generated by field ionization. In neutral Krypton, the $4p$ shell is full and these transitions are not possible anymore. We have used EUV pulses centered at 93 eV with a bandwidth of more than 12 eV . At these photon energies above the third ionization threshold of Krypton ($13.99 + 24.36 + 36.95 = 75.3 \text{ eV}$), the possible induced transitions from the ground state configuration $|1\rangle = [\text{Ar}]4s^24p^6$ are:

- Photoionization of one or several (up to three $4p$) $4s$ and/or $4p$ electrons. constitutes the constant nonresonant absorption background.
- Resonant transfer of a $3d$ electron to a np ($n > 4$) or a $n'f$ ($n' > 3$) shell. According to ref. [121], confirmed by calculations with the COWAN atomic structure code [122], only the np transitions have a significant contribution in this energy range, the transitions will then be $1 \rightarrow 3d^{-1}np^1$. They are divided into two series due to the spin orbit splitting of the $3d^{-1}$ states of the relevant configurations of Krypton.
- Above the $3d$ ionization threshold, one of these electron can be directly photoionized. Once again there are two ionization thresholds due to the spin-orbit splitting of the states of the $3d^{-1}$ configuration of Krypton II.

On the graph of Figure 5.6, the measured transient free absorption spectrum is shown (red) together with the expected resonant absorption cross-section extracted from the atomic structure code COWAN [122] (dashed and dotted for the 2 spin-orbit manifolds, blue for the total). The energy axis of the COWAN calculation is shifted by $+0.8 \text{ eV}$ to match the energy of the first transition to the value measured in reference [121] and convoluted with our estimated spectral resolution of 195 meV . The TDCIS energy axis is untouched, but the cross-section convoluted with the experimental resolution. The experimental energy scale has been calibrated using the position of the first and second lines of the trace with reported data of the litterature. The dilatation factor compared to what would be expected from the grating equation is around 1.4, which corresponds to usual values seen in previous experiments.

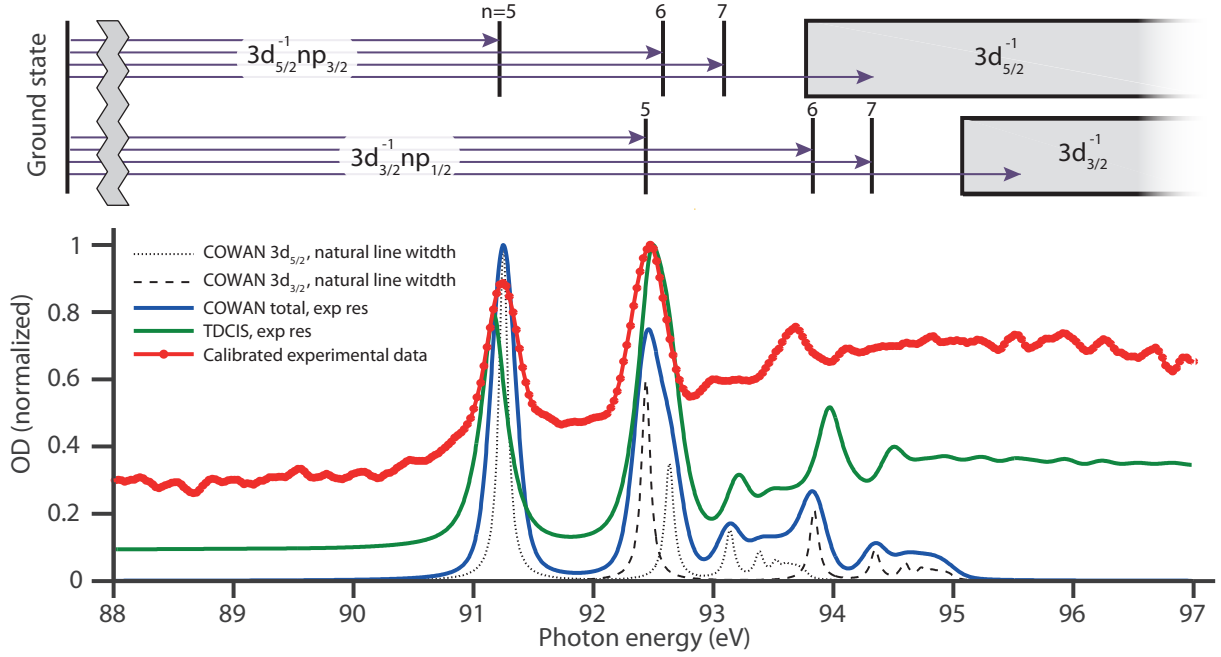


Figure 5.6: Experimental, TDCIS and COWAN calculated absorption cross sections (configurations up to $15p$ taken into account for COWAN)

Electronic dynamics induced in the $3d - np$ edge

The absorption, resonant or non-resonant, of an EUV photon by a $3d$ electron leaves a hole in the core-shell of Krypton. This state is unstable and decays naturally via Auger processes, which are more likely to happen at that energy than the emission of an EUV fluorescence photon [123].

The time constant associated with the filling of the hole was obtained first in the spectral domain by several methods: measuring the linewidth of the resonance peaks in high resolution Electron Energy Loss Spectroscopy, [124], in X-Ray Absorption Spectroscopy [125] and of the linewidth of Auger lines in Auger Electron Spectroscopy [126]. All these methods are spectral, and show a linewidth of between 79 meV and 88 meV , corresponding to a time constant of the Auger decay $\tau_A = \hbar/\Gamma_A$ between 6.7 and 8.3 fs (see Table 5.1). The first and only pump-probe measurement of this decay time has used the technique of the streak camera [1], exploiting the fact that the direct photoelectron and the Auger electron have a different temporal structure and are therefore affected by the streaking field in a different way. They have extracted a decay time of $7.9^{+1.0}_{-0.9} \text{ fs}$.

The initial Auger decay leads in a cascaded way to the first, second and third ions of Krypton. The time constants of these cascades have been measured by ion charge state chronoscopy [127, 128], but the initial time constant of around 8 fs could not be extracted by these measurements, which use too long pulses. We propose to use our dipole gating technique, which presumably has subfemtosecond resolution, to investigate these phenomena.

Transition	EELS [124]	XAS [125]	AES [126]	Streak camera[1]
$3d_{5/2}^{-1} - 5p_{3/2}$	7.9 ± 0.4 fs	7.9 ± 0.1 fs		
$3d_{5/2}^{-1} - 6p_{3/2}$		8.3 ± 0.2 fs		
$3d_{5/2}^{-1}$			7.5 ± 0.4 fs	$7.9_{-0.9}^{+1.0}$ fs
$3d_{3/2}^{-1} - 5p_{1/2}$		7.9 ± 0.2 fs		
$3d_{3/2}^{-1} - 6p_{1/2}$	6.7 ± 0.8 fs	7.8 ± 0.3 fs		
$3d_{3/2}^{-1}$			7.5 ± 0.4 fs	$7.9_{-0.9}^{+1.0}$ fs

Table 5.1: Existing measurements of Kr 3d hole Auger decay time constants. EELS, XAS and XPS are spectral methods, and streak camera is a time domain measurement.

Susceptibility to gating experiments

The susceptibility of the $3d - 5p$ transition to a strong optical field has been studied at the FLASH Self Amplified Stimulated Emission Free Electron Laser (SASE-FEL) by Auger Photoelectron Spectroscopy by shining 200 fsEUV pulses (the central frequency of which was scanned through the transition) on Kr atoms under illumination by a 350-700 fsInfrared pulse [129]. It has been recognized that Auger photoelectron lines are shifted and broadened respectively due to ponderomotive shift and two-photon ionization from the $5p$ state. However with pulses much longer than the process at stake, as well as intensity and envelope fluctuating in nature [25], any time-resolved perspective was smeared out.

With our well controlled short pulses, we set to the exploration of this dynamics in a time-resolved fashion. The phase perturbation term can be attributed to the Stark shift of the np levels (the $3d$ state is quite deep and as such moderately polarizable). Concerning the amplitude term, the $3d_{5/2}^{-1}5p_{3/2}$ state lies at an energy of 91.25 eV from the ground state, and the $3d_{5/2}^{-1}$ continuum starts at 93.8 eV ([121]). Therefore the ionization potential is 2.65 eV. A substantial amount of our transient spectrum (spanning from 1.1 eV to 4.6 eV), is then able to single photon ionize the $5p$ electron, and a Keldysh parameter $\gamma = 2.4$ supports this idea. However at the same time, the associated barrier suppression intensity is $4 \cdot 10^{11}$ W.cm⁻² and is well below our transient intensity, so it appears that the transient would field ionize it very easily. This is a manifestation of the fact that the Keldysh theory is ill-adapted to low ionization potentials. Indeed, since the tunneling intensity varies like I_p and the Barrier suppression intensity like I_p^2 , at low I_p the former is lower than the later. We will however assume that the ionization rate is quadratic in field, *i.e.* that the ionizing mechanism is mainly linear.

5.2.2 Reconstruction of a numerical experiment

Numerical experiment

To test the idea of the gating presented above, we confronted it with a state-of-the-art simulation of the system, and we ran a calculation based on Time-Dependent Configuration Interaction Singles ([118, 117, 119]), using the field actually sampled by streaking in the

experiment.

In this code, the finite lifetime of the $3d$ hole is emulated by adding an imaginary part to the energy of the relevant orbitals. It is therefore a parameter put by hand in the calculation.

The resolution of the spectrometer later achieved in the experiment (220 meV) is taken into account by convoluting the computed spectra with a unitary Gaussian function. The resulting spectrogram, calculated with the field measured in the experiment and a peak intensity of 10^{13}W.cm^{-2} is displayed on Section 5.2.2. In panel **a.**, the absorbance is calculated by referencing the pump-probe spectra $S(\omega, \tau)$ to the incoming spectrum of the EUV pulse, $S^0(\omega)$, it is the real absorbance of the "sample". The represented quantity is then $-\ln(S(\omega, \tau)/S^0(\omega))$. In panel **b.**, the differential absorbance is displayed, meaning that the reference spectrum is calculated without perturbation from the attotransient $S^{Kr}(\omega)$. The represented quantity is then $-\ln(S(\omega, \tau)/S^{Kr}(\omega))$, and it highlights the perturbation due to the attotransient.

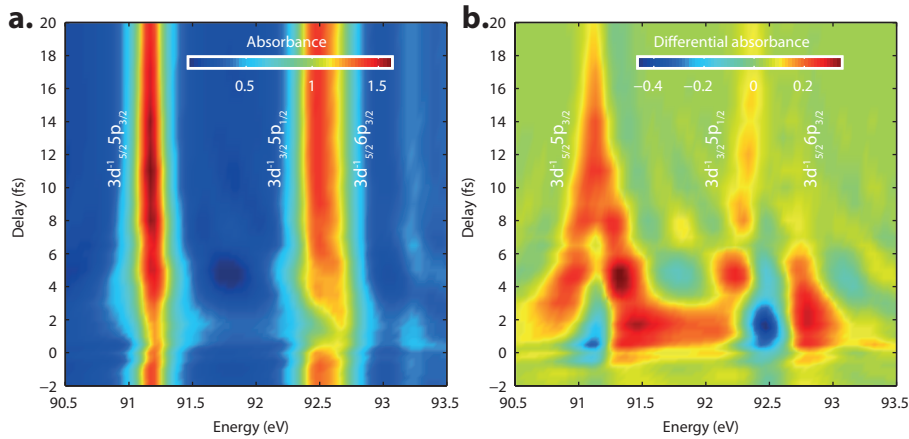


Figure 5.7: Numerical spectrogram calculated by TDCIS **a.** In the direct absorbance representation and **b.** in the differential absorbance representation.

Reconstruction of the experiment using model functions

We will apply the formalism deployed in the beginning of this chapter to fit the experiment with the introduced model functions. In order to make the fit rely on less adjustable parameters, we determine the position and the strength of the transitions by fitting a field free absorption cross-section with an arctangent background (commonly used to fit nonresonant absorption edges [130, 131, 132]), with an assembly of N lorentzians, N depending on the number of considered transitions. The profile is then convoluted with a unitary gaussian of which the width is fitted, to determine the resolution. The result is displayed on Figure 5.8. With $N = 6$, we consider the two spin-orbit manifolds up to $3d - 7p$, with $N = 4$ only up to $3d - 6p$, and $N = 3$ even neglects accounting for the $3d_{3/2} - 6p_{1/2}$, which is comparatively lower in signal.

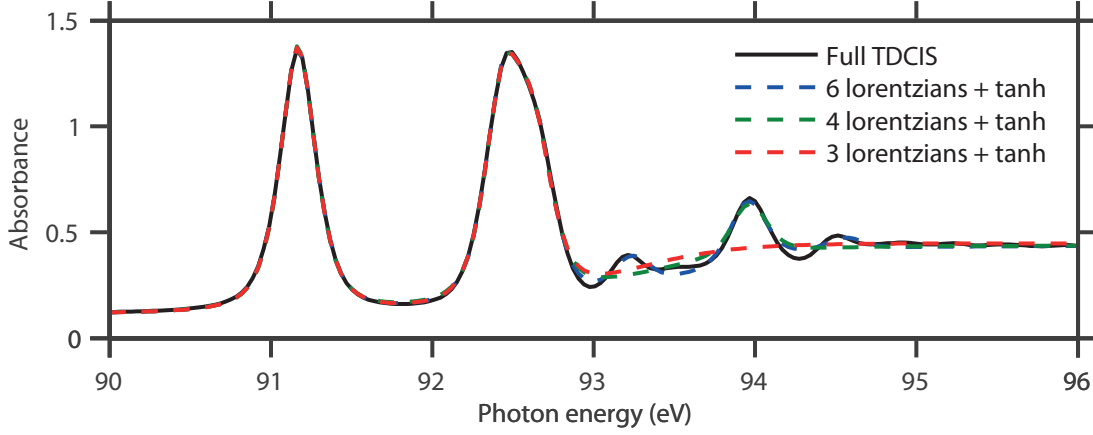


Figure 5.8: Fit of the field free optical density of TDCIS calculation

This procedure yields the central energies of the transitions $\hbar\omega_0^i$, as well as the dipole strength D^i (with $d^i(t, \tau) = D^i \chi^i(t, \tau)$), together with the "experimental" resolution. The fitted parameters are quite robust to the fitting conditions.

The differential absorption spectrogram highlighting the changes operated by the probe pulse resulting from this calculation is shown on Figure 5.9.a. and Figure 5.10.a..

The full differential absorbance map is then fitted using the lineshape expressions presented in Section 5.1.4, with as free parameters for each transition the phase and amplitude parameters (respectively ϕ_0^i and r^i or α^i and γ^i for the instantaneous and field-based gates), as well as the decay time of the $3d$ hole $\tau_A = T/2$. The result of these fittings, incorporating the 3 main transitions ($3d_{5/2} - 5p_{3/2}$, $3d_{3/2} - 5p_{1/2}$ and $3d_{5/2} - 6p_{3/2}$,) is shown respectively on Figure 5.9 and Figure 5.10 for the instantaneous and the field based gates.

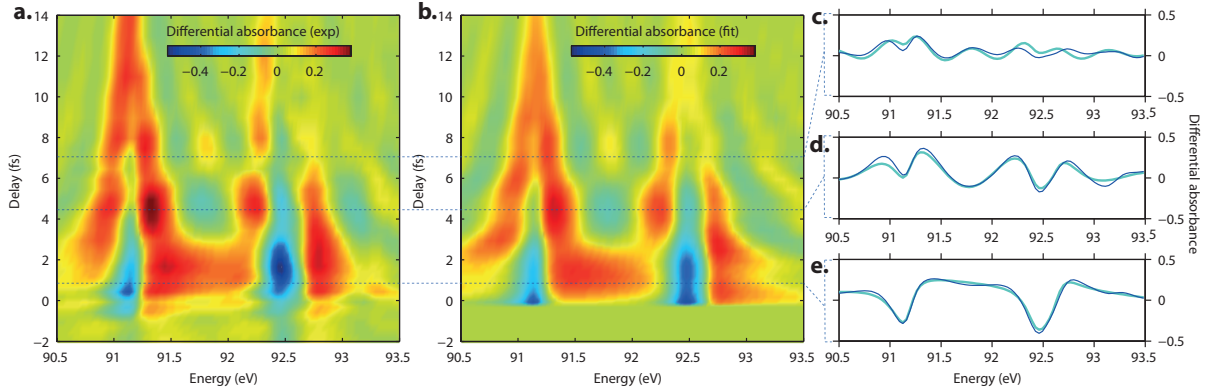


Figure 5.9: Fit of the TDCIS spectrogram with instantaneous gate. **a.** Numeric differential absorption spectrogram. **b.** Fitting of the spectrogram using the instantaneous gating model (see text) **c.d.e.** Comparison between calculated (dark blue) and fitted (light blue) cross-sections at 3 different pump-probe delays (c, 0.8 fs, d, 4.4 fs and e, 7 fs).

The agreement with the numerical data is striking, and the results of the fitting are summarized in Table 5.2, together with 95% confidence intervals.

To ease the comparison between the two fits, the phases ϕ_0 retrieved in the case of

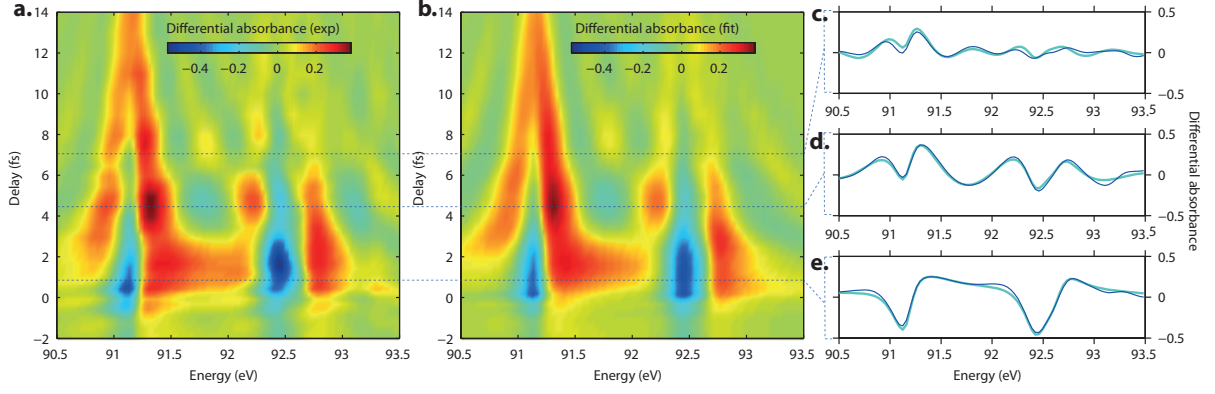


Figure 5.10: Fit of the TDCIS spectrogram with field-based gate. **a.** Numeric differential absorption spectrogram. **b.** Fitting of the spectrogram using the field based gating model (see text) **c.d.e.** Comparison between calculated (dark blue) and fitted (light blue) cross-sections at 3 different pump-probe delays (c, 0.8 fs, d, 4.4 fs and e, 7 fs).

transition	Instantaneous gate model			Field based gate model		
	$5p_{3/2}$	$5p_{1/2}$	$6p_{3/2}$	$5p_{3/2}$	$5p_{1/2}$	$6p_{3/2}$
τ_A (fs)	8.01 ± 0.25	5.04 ± 0.25	16.2 ± 14	7.06 ± 0.1	4.7 ± 0.1	30 ± 20
ϕ_0 (π mrad)	61 ± 2	-3.1 ± 5	65 ± 5			
α (at. u.)	1000 ± 2	-50 ± 5	1000 ± 10	920 ± 10	340 ± 4	880 ± 10
Depletion r	$33\% \pm 1\%$	$37\% \pm 1\%$	$0\% \pm 5\%$	$51\% \pm 2\%$	$58\% \pm 2\%$	$0\% \pm 5\%$

Table 5.2: Results of the fitting of the TDCIS spectrogram using our two different methods. See text for details.

the instantaneous gate have been converted to polarizability, assuming they have been imparted by a quadratic energy shift caused by a half-cycle of light of 400 as intensity FWHM duration and correct peak intensity (see procedure in Appendix C). The field based approach gives field induced decoherence values around 2 times higher than the instantaneous gate approach. This is actually coherent, since in the field based model this depletion is the depletion due to the full pulse, 50% of which intensity is located in the main half cycle. Intuitively, the instantaneous gate model only captures the depletion due to the central half-cycle. The two models therefore give very comparable values, validating the use of the instantaneous gate for this class of decoherence times, although of course the agreement around pump-probe delay 0 is better in the field gate based approach.

Since the two highest lines are spectrally overlapping, the fitting algorithm runs into difficulties to resolve individual values for each of them, which results in numerical values far from reasonable expectation and large confidence intervals. The reconstruction values are however quite accurate for the main transition, falling close to the value of τ_A used as input in the code, 7.5 fs. The depletion factor is almost twice higher for the field based gate, which can be explained by the fact that 50% of the energy of the waveform is confined in the main half-cycle, and that therefore 50% of the depletion is expected to happen within this window of time. The instantaneous gate model then only reconstructs this "instantaneous" depletion .

Our intuitive picture of gating, even in its very simple form of instantaneous gating, is therefore able to reconstruct the numerical experiment to a very satisfying level, and yields the constants that have been introduced in the calculation, both concerning the decay time of the dipole and the associated polarizability of the main transition, as well as the field-induced decoherence seen on the calculated dipole.

Effect of a longer probe pulse

We calculated pump-probe maps with generated with a longer pulse (5 fs) to see the qualitative difference made by the use of a single half-cycle of light. We attempted a fitting with the instantaneous gate, to show the discrepancy generated. The results are displayed on Figure 5.11.

The temporal dynamics displayed on the trace looks is not as rich in spectral oscillations, and seems more field related than in the previous study, as oscillations can be seen along pump-probe axis. Their period is half the period of the field, which reminds of the dynamics seen experimentally in Chapter 4, and in [3, 133], and attributed to the AC-Stark shift. The reconstruction is however not possible with the instantaneous gate model, as was expected for a pulse with a duration approaching the decay time to be reconstructed. To be sensitive to the dynamics of the dipole and not of the pulse, the decoherence time must therefore be safely above the pulse duration.

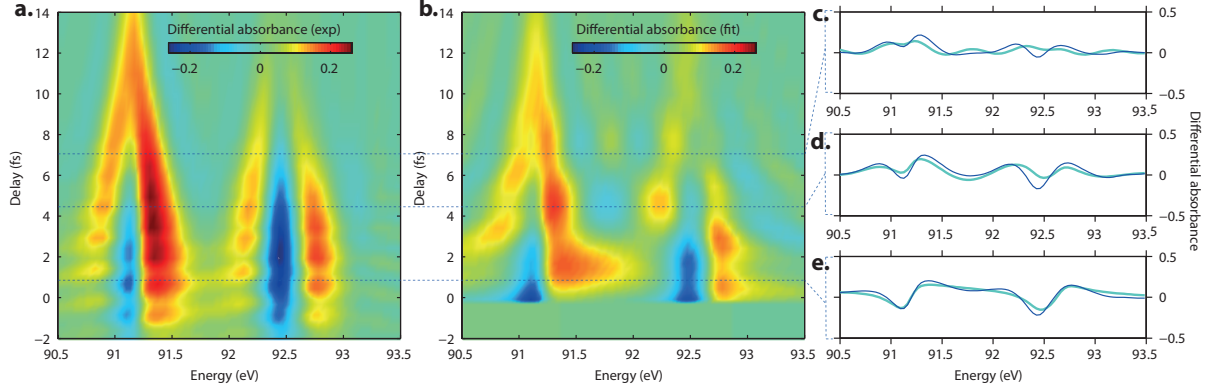


Figure 5.11: Fit of a TDCIS spectrogram computed with a 5 fspulse with instantaneous gate. **a.** Numeric differential absorption spectrogram. **b.** Fitting using the instantaneous gating model **c.d.e.** Comparison between calculated (dark blue) and fitted (light blue) cross-sections at 3 different pump-probe delays (c, 0.8 fs, d, 4.4 fs and e, 7 fs).

5.2.3 Experimental reconstruction and extraction of physical quantities

We investigated the validity of our approach experimentally, where more factors enter the problem. Especially spatial effects, be it propagation in the gas, or integration in the focal plane, could be of importance and blur the picture presented above. To this end, we have used the pump-probes setup described in Chapter 3, and shun 90 mbars of Kr atoms in a gas tube with a 200 as FWHM EUV pulses centered at 93 eV and a 400 as field FWHM optical attosecond transient of peak intensity $2 \cdot 10^{13} \text{W} \cdot \text{cm}^{-2}$, with a relative delay controlled with a 25 as accuracy. No effect of gas pressure on linewidths has been observed. The resulting delay-dependent spectrum is measured around 1m downstream in a commercial McPherson EUV spectrometer, after filtering out the visible radiation with a 100 nm thick Zr film and steering and refocusing the beam with our double Rhodium based reflector. The pump-probe absorbance data is represented on Section 5.2.3 in two different ways. In panel **a.**, the absorbance is calculated by referencing the pump-probe spectra $S(\omega, \tau)$ to a spectrum measured without Kr atoms in the target, $S^0(\omega)$. The represented quantity is then $-\ln(S(\omega, \tau)/S^0(\omega))$. In panel **b.**, the differential absorbance is displayed, meaning that the reference spectrum is taken with Kr atoms in the target, but without perturbation from the attotransient $S^{Kr}(\omega)$. Usually this spectrum is recorded by averaging spectra at 3 large different negative delays. The represented quantity is then $-\ln(S(\omega, \tau)/S^{Kr}(\omega))$.

Here again, the field free cross-section has been fitted first, to extract line positions and amplitudes.

The spectrogram displayed on Figure 5.13.a. is the result of the averaging of 30 spectra at each of the 67 delay steps. It has been fitted with the instantaneous gate model, which result is displayed on Figure 5.13.b.. The field-based gate approach can also be implemented with similar results, but will not be shown here. It is worth mentioning that here, since the two transitions $3d_{3/2} - 5p_{1/2}$ and $3d_{5/2} - 6p_{3/2}$ are spectrally overlapping, we used only one dipole to describe them both, which has the advantage to give more reliable

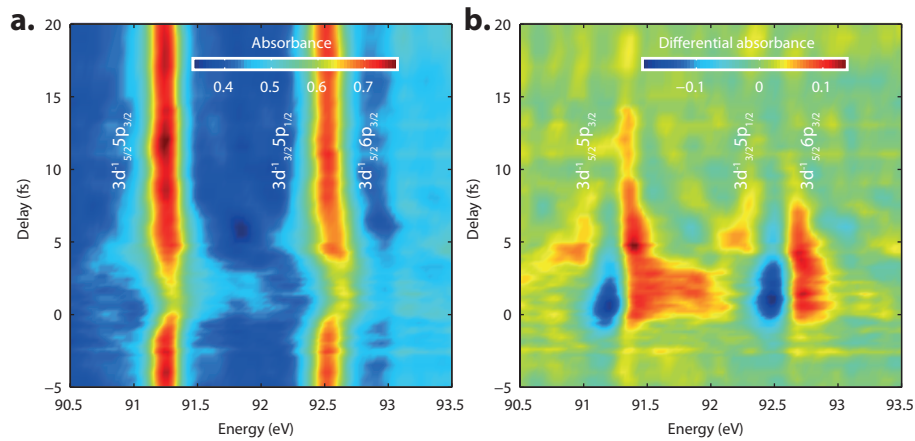


Figure 5.12: Experimental spectrogram resulting from the averaging of 30 spectra per pump-probe delay point **a**. In the direct absorbance representation **b**. In the differential absorbance representation

fitting values.

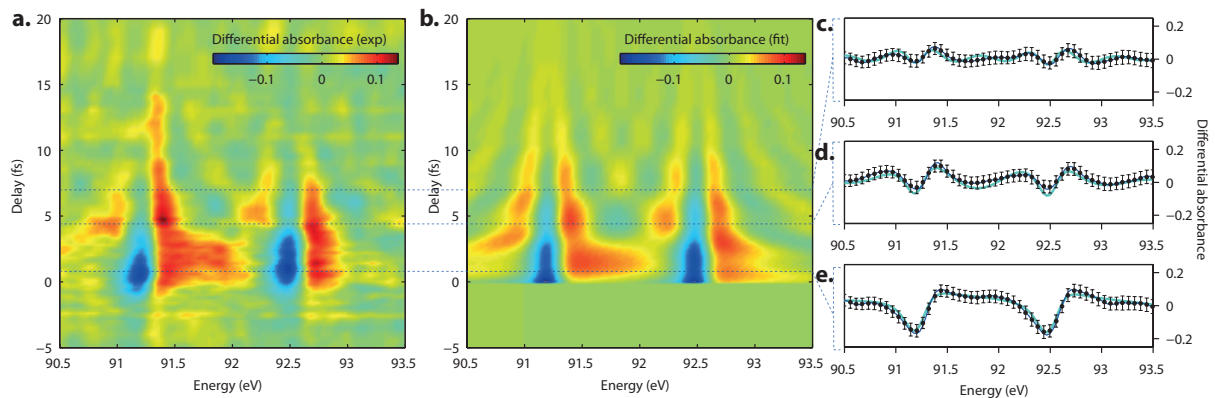


Figure 5.13: Fit of the Experimental spectrogram with instantaneous gate. **a**. Differential absorption spectrogram. **b**. Fitting of the spectrogram using the instantaneous gating model (see text) **c.d.e**. Comparison between calculated (dark blue) and fitted (light blue) cross-sections at 3 different pump-probe delays (**c**, 0.8 fs, **d**, 4.4 fs and **e**, 7 fs). The error bars represent the standard error of the measurement.

Also in the case of the experiment, the agreement between data and fitting is very good, and leads us to the conclusion that our simple model indeed has the potential to fully describe our experiment. The precise results of the fitting are reported in Table 5.3. Here again the errors indicated correspond to the 95 % confidence interval of the fitting procedure, calculated incorporating the experimental statistical error, except in the case of polarizability, a 10% uncertainty in peak intensity is reported on the result as well and dominates.

The reconstructed values are close to the literature values for the Auger decay time, and constitute a quite unprecedented measurement of dynamic polarizability of these transi-

	Instantaneous gate	
transition	$5p_{3/2}$	$5p_{1/2}$ & $6p_{3/2}$
τ_A (fs)	9.8 ± 0.5	7.7 ± 0.5
ϕ_0 (π mrad)	170 ± 6	210 ± 10
α (at. u.)	1300 ± 150	1600 ± 150
Depletion r	$45\% \pm 1\%$	$44\% \pm 1\%$

Table 5.3: Results of the fitting of the experimental spectrogram.

tions and of the field induced decoherence. These properties are inaccessible by standard one-photon X-ray absorption spectroscopy, and indeed require a pulse shorter than the decay to be accessed.

5.2.4 Behavior at higher field intensities

In the experiment presented in the above section, we have been careful to leave the intensity low enough to stay in a regime where our model describes the physics accurately, *i.e.* where the visible pulse is only disturbing the dipole in the presented fashion. At higher field intensities, several issues are faced, which are illustrated on Figure 5.14. The panel **a.** shows a pump-probe spectrogram taken at an intensity of $9 \cdot 10^{13} \text{W.cm}^{-2}$. It is noticeable that the background level of absorbance is evolving. Thus, the optical density at 85 eV, well below the transitions, is 0.3 at negative delays, when it rises to 0.6 at positive delays. It is also visible on resonance (see green curve of panel **c.**). This is a sign that the optical pulse starts to ionize the atom. Indeed in the ion, the triple ionization threshold is $24.36 + 36.95 + 52.5 = 113.8 \text{ eV}$, and therefore above our spectrum, when it is only 75.3 eV in the neutral atom. As a result, this channel closes when the optical pulse comes before the EUV pulse and ionizes the atom, leading to lower absorption at negative pump-probe delays. This prevents the efficient use of our fitting algorithm in the region of the zero delay.

The oscillations at 91 eV around $\tau = 0$ in the spectrogram of Figure 5.14.**a.** are also to be noticed, they are highlighted on the plot of Figure 5.14.**b.**, showing the integrated absorbance around the main transition, together with the field intensity $E_{tr}(t)$ sampled by streaking before the experiment. The oscillations are in phase with $E^2(-\tau)$, which could be a good indication that they are caused by the $a_{11}(-\tau)$ term of Equation (5.10).

Another effect that is harmful for the reconstruction, is the complete disappearance of the line structure around the zero delay, to be seen on Figure 5.14.**c.**. It could be described by our model functions for high depletion, but the signal to noise ratio becomes very unfavorable for good detection.

It is to be mentioned that the accuracy of the reconstruction also decreases greatly with increasing intensity in TDCIS simulations, possibly linked with effects such as population oscillations (Rabi flopping), not taken into account in the phenomenological model. This could guide a possible extension of the model, which has not been pursued in the context of this study, after the goal of decoherence time extraction had been reached.

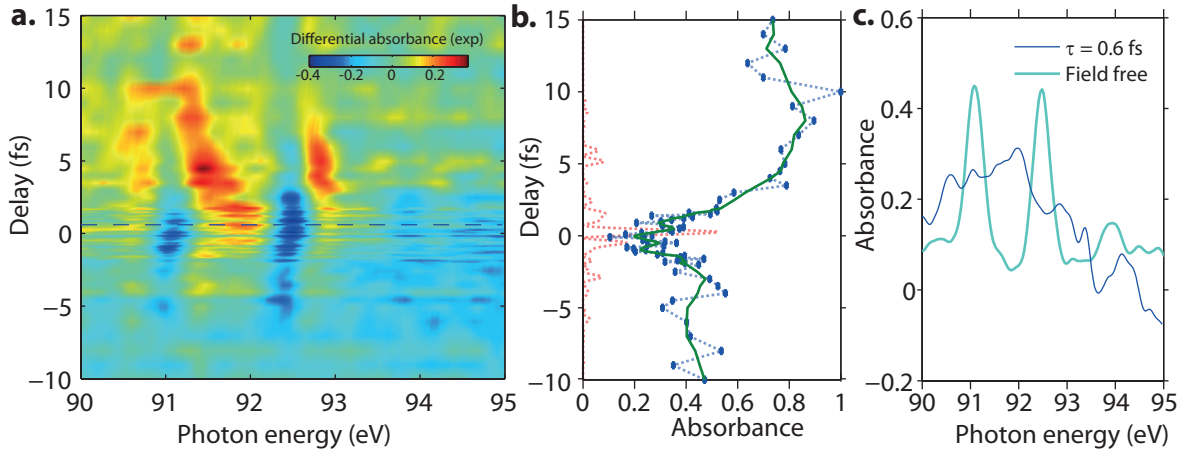


Figure 5.14: Behavior at high intensity **a.** Differential absorbance spectrogram, showing lower background at $\tau < 0$ due to ionization **b.** integrated absorbance on a 0.5eV spectral band around the main resonance (dashed blue) and its smoothed version (3 points averaging, green). **c.** Comparison between the absorbance field free (light blue) and one of the most disturbed delay instance ($\tau = 0.6\text{ fs}$) cross-sections.

Conclusion

We have shown with the numerical and the experimental approaches presented in this chapter that we understand the perturbation of the EUV absorption by an attotransient well enough to model it with simple model functions making use of the picture of the gating of the electronic dipole by the short field, in the limit of an intensity avoiding Rabi flopping. We have thus demonstrated an EUV pump-optical probe scheme, and reconstructed a dipole decay time of around 16 fs, compatible with previous measurements by other techniques, together with the polarizability of the system, and a measurement of the field-induced decay ratio.

The next step is the application of this technique to systems where the decay time of the dipole requires our ultimate temporal resolution, which we believe to be subfemtosecond. At the photons energies which we can attain, atomic systems do not, in general, display this kind of decay times, which can however be found in the absorption edges of solids. The extension of our EUV pump-optical probe to the $L_{2,3}$ edge of SiO_2 will be treated in the next chapter.

6

Attosecond nonlinear X-Ray Absorption Near-Edge Spectroscopy

In theory, there is no difference between theory and practice

– Attributed to multiple people

Having demonstrated our EUV pump-optical probe technique on the $3d - np$ edge of Krypton atoms, we have applied it to the study of the $L_{2,3}$ absorption edge structure of SiO_2 , which is well known from synchrotron studies [134] to display resonant-like structures with bandwidths indicating subfemtosecond dynamics. It is therefore quite adapted to our scheme. The first part of this chapter will remind some aspects of conventional X-Ray absorption spectroscopy and specific facts about the exact system we are considering. It will be followed by the presentation of our pump-probe study, which revealed nonlinear properties of the studied system, inaccessible by single photon transitions.

6.1 The $L_{2,3}$ absorption edge of Silicon dioxide

6.1.1 X-Ray Absorption spectroscopy

This section will review the principles of conventional X-Ray Absorption Spectroscopy (XAS) that are relevant to our studies. The reader curious to learn more about this technique is redirected to this excellent review [135].

As can be seen on Figure 6.1a., the X-Ray absorption spectrum of an element (in this particular case Pb) is a succession of edges. As soon as the photon energy is higher than the binding energy of a filled deep-shell orbital, it can photoionize it in the case of a gas, or promote it to a conduction band in the case of a solid. Traditionally, the edges are labelled according to the quantum numbers of the excited electron: K for $n=1$, L for $n=2$, M for $n=3...$ The edges have then subdivisions. The L edge for example is separated into L_1 , resulting from excitation of a 2s electron, L_2 and L_3 from the excitation of a 2p electron, are separated by spin-orbit interaction.

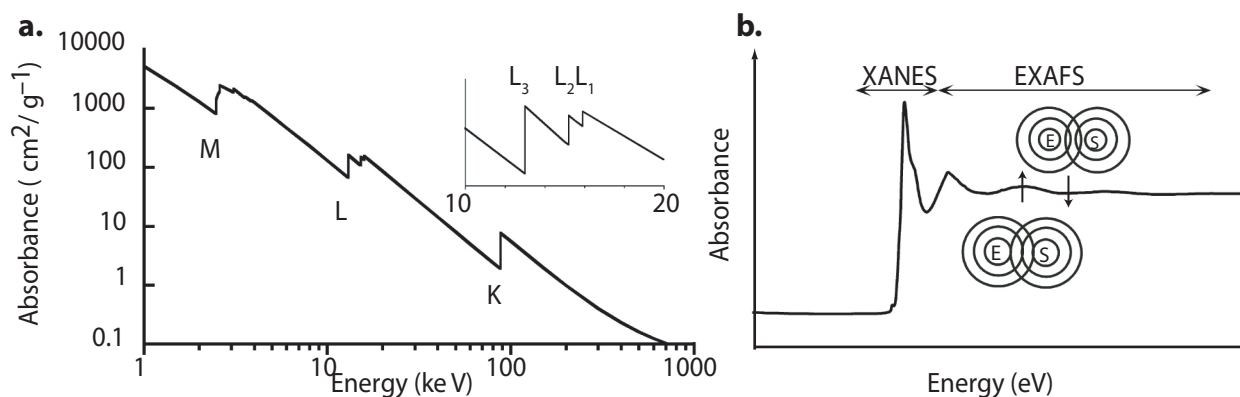


Figure 6.1: Principles of X-Ray Absorption spectroscopy **a.** X-Ray Absorption spectrum for Pb (see text for explanation) **b.** Zoom on an absorption edge, XANES-EXAFS distinction, and emitter/scatterer picture. Adapted from [135].

A closer look at an absorption edge, shown on Figure 6.1**b.**, reveals the separation of an edge in two zones, the X-Ray Near Edge Structure (XANES) (reviewed in [136]), often displaying one or several spikes (called white lines in reference to the unimpressed zones that these were leaving on photographic films originally used in XAS), and the Extended X-ray Absorption Fine Structure (EXAFS). The frontier between these two regimes is quite arbitrarily usually placed 20-30 eV above the edge. It relies on the fact that the physics governing EXAFS is quite intuitive to understand and was explained in the early days of XAS [137]. Indeed, it often displays spectral oscillations, that can be related to the scattering of the photoelectron generated on an emitter atom E by a scatterer S (see scheme on Figure 6.1**b.**). Depending on the kinetic energy of the photoelectron $\hbar\omega - E_{edge}$, the interference between direct and scattered electronic wavepacket are constructive or destructive, leading to oscillations in the absorption spectrum. These oscillations can be analytically fitted by numerous available models (see *e.g.* [137]) to yield interesting information about the environment of the ionized atom, such as the bond lengths.

The previous description relies on the fact that at relatively high photoelectron energies, the mean free path of the photoelectron is such that only one scattering event is significant. However, closer to the edge, the photoelectron has a very low kinetic energy, and a long mean-free path, which means that multi-scattering will play a dominant role and prevents the intuitive interpretation of the spectra as is the case in EXAFS. Therefore, XANES spectra are used mainly for qualitative analysis, *e.g.* about oxidation stage, a parameter for which the position of the edge is very sensitive [138], or for identification of components, by fitting with a library of reference spectra.

6.1.2 The near Si $L_{2,3}$ edge structure of Silicon dioxide

Experimental characterization

The Silicon $L_{2,3}$ edge has first been measured in amorphous Silicon samples [139, 140]. Due to the extreme sensitivity of XANES to the local atomic environment it takes a more peculiar shape in silicon oxides, which has been first observed few years later in [134]. The impact of the exact nature of the sample (deposition method, stoichiometry, amorphicity...) being so high, we have sent the very samples we used in our experiments, *i.e.* evaporated films of SiO_2 of thickness 120 nm to a synchrotron where its absorption spectrum has been measured around the silicon $L_{2,3}$ edge, with a resolution of 0.05 eV , and an energy axis calibrated within 0.02 eV from known gas transitions (source: Physikalisch-Technische Bundesanstalt). The result is displayed on Figure 6.2, together with the spectrum measured at our beamline with a 200 as pulse centered on 107 eV . This spectrum has been calibrated using the lanthanum edge present in our EUV mirror (see Section 3.3.1), and the position the strongest resonance taken from the synchrotron measurement. Using a fitting procedure of the former with the later convoluted by a unitary gaussian, our experimental resolution has been estimated to be 450 meV (the grating used in these experiments had 600 grooves/mm and did not give the highest achievable resolution as in the case of Chapter 5, in order to get a better signal to noise ratio).

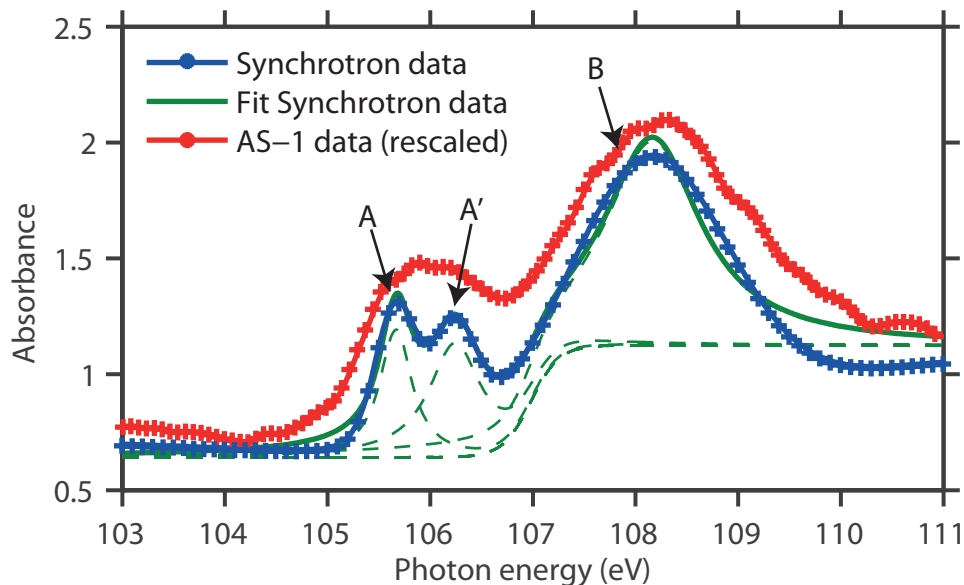


Figure 6.2: XANES spectrum of Si $L_{2,3}$ edge, taken in a high resolution beamline at PTB (blue) and its fit with an arctangent function and 3 lorentzians (green). Superimposed is the absorption measured with our setup, rescaled for visibility (red).

3 resonances are clearly identified in the close vicinity of the edge, they are labelled A, A' and B. According to the literature (calculation [141], measurement in silane gas [142] and in SiO_2 [143]), A and A' are due to the spin-orbit splitting of the $2p$ hole configurations, quite

universally measured between 0.6 eV and 0.7 eV, which corresponds to our observation. As suggested in [136], we have fitted the synchrotron profile with 3 lorentzians and an arctangent background [130]. The fitted bandwidths of the 3 resonances are respectively 0.37 eV, 0.62 eV and 1.13 eV, leading to estimated decay time of dipoles of 3.6 fs, 2.2 fs and 1.1 fs. It is to be noted however that this fitting is quite sensitive to boundary conditions on the fitting parameters, thus making its interpretation somehow doubtful.

Theoretical considerations

From a quantum mechanical point of view, the rate of transitions from a core-shell band $|i\rangle$, composed of states $|i, \vec{k}\rangle$, to a continuum of states $|f, \vec{k}\rangle$ with the density of empty states (DOS) D is governed by the Fermi golden rule, *i.e.* in the case of a continuous excitation at frequency ω :

$$\theta_{i\vec{k},f,\vec{k}'} = \frac{2\pi}{\hbar} \delta(\vec{k} - \vec{k}') \left| \langle i, \vec{k} | -\mu \cdot E(\omega) | f, \vec{k}' \rangle \right|^2 D(\omega_{f\vec{k}'} = \omega_{i\vec{k}} + \omega) \quad (6.1)$$

The $\delta(\vec{k} - \vec{k}')$ term comes from momentum conservation and states that only vertical transitions are allowed. Assuming exponential decays with rates $\Gamma_{i\vec{k},f,\vec{k}'}$, and non saturation of the transitions, we can therefore write the absorption cross-section for the edge $|i\rangle$ as:

$$\begin{aligned} \sigma^i(\omega) &\propto \int_{f\vec{k}} \theta_{i\vec{k},f,\vec{k}} \frac{\frac{\Gamma_{i\vec{k},f,\vec{k}}}{2}}{\left(\frac{\Gamma_{i\vec{k},f,\vec{k}}}{2}\right)^2 + (\omega - (\omega_{f\vec{k}} - \omega_{i\vec{k}}))^2} d^3\vec{k} \\ &\propto \frac{2\pi}{\hbar} \int_{f\vec{k}} \left| \langle i\vec{k} | \mu | f\vec{k} \rangle \right|^2 D(\omega_{f\vec{k}} = \omega + \omega_{i\vec{k}}) \frac{\frac{\Gamma_{i\vec{k},f,\vec{k}}}{2}}{\left(\frac{\Gamma_{i\vec{k},f,\vec{k}}}{2}\right)^2 + (\omega - (\omega_{f\vec{k}} - \omega_{i\vec{k}}))^2} d^3\vec{k} \end{aligned} \quad (6.2)$$

As for a core hole, the dispersion of the band is quite low and practically $\omega_{i,\vec{k}}$ does not depend on \vec{k} , it is tempting to consider the edge profile as a replica of the density of empty states, *i.e.* as a probe of the conduction band structure. There are certain limits to this idea, which will be developed in the next subsections.

XANES as a probe of symmetry specific DOS

From Equation (6.2), it is obvious that the accessible density of states is filtered by the matrix elements $|\langle i\vec{k} | \mu | f\vec{k} \rangle|^2$. Since in most cases the quadrupolar interaction is negligible, the selection rules hold, and the dipole matrix element projects the DOS on the symmetries allowed from the initial state.

In the case of the silicon XANES in SiO₂, which concerns us here, in the L_{2,3} XANES, an electron from the 2*p* core orbital of an Si atom is excited, and therefore it can access only the partial DOS that possesses *s* or a *d* symmetry, referenced to the Si atom. To access the partial Si *p*-DOS, Si-K edge XANES must be recorded. This edge is located

around 1840 eV ([144]). The fair comparison between these two measurements is however a challenging task, first experimentally because a source covering this broad range of photon energies, with a perfectly calibrated response has to be available. But also quite some difficulties arise from the fact that the $L_{2,3}$ and the K edge refer to a different hole:

- The first one is the energy scale difference. The L edge $\sigma^{2p}(\omega)$ is located around 100 eV, the K edge $\sigma^{1s}(\omega)$ around 1.84 keV [144]. Placing these two spectra on a common energy scale requires an external measurement that extracts $\hbar(\omega_{2p} - \omega_{1s})$. The most direct method is the energy measurement of $K\alpha$ X-ray fluorescence photons emitted by a $2p$ electron decaying into a hole of the $1s$ shell. These are by-products emitted during K edge XANES measurements. Once this quantity measured, $\sigma^{2p}(\omega)$ and $\sigma^{1s}(\omega - (\omega_{2p} - \omega_{1s}))$ have a common energy scale. The absolute energy scaling can then be accessed by a measurement of the $2p$ electron binding energy by X-ray Photoelectron Spectroscopy (XPS, [145]).
- The dipole matrix elements and dephasing rates have to be calculated to compare both DOS on fair absolute scales. To yield the actual DOS, the XANES spectrum must be corrected for the energy dependent dipole matrix element variation [146].
- Another difficulty, more conceptual, is that the p -DOS existing in the presence of the $2p$ hole, invisible in the $L_{2,3}$ edge XANES, might be different from the one existing in the presence of the $1s$ hole, probed by the K edge XANES. In other words, the presence of the hole in a core-shell could modify the hamiltonian, and therefore the final states $|f\rangle$ could be dependent of the hole. This is indeed the case as will be shown in the next subsection, and is not an easy obstacle to overcome.

XANES and Core-hole DOS

In the picture of the XANES profile being a replica of the empty DOS, the presence of sharp resonance-like features in the XANES profile of Figure 6.2 can seem rather unintuitive. This would be linked to a bandstructure made of narrow isolated bands, which above the bandgap of a dielectric is unusual. Indeed, the band structure of quartz, calculated by Density Functional Theory (DFT) using the Wien2k software package [147] (calculation Nick Karpowicz) is shown on Figure 6.3 **a.**, and the associated DOS, the blue curve on the **b.** panel, does not display sharp features. Resonances are rather intuitively associated with the presence of bound states, which hints towards their interpretation.

Theoretical works [148] show that the inclusion of a core hole in a DFT calculation is *required* to theoretically reproduce the Electron Energy Loss Spectrum (EELS, also subject to the same selection rules) of the $L_{2,3}$ edge of SiO_2 . In other words, the removal of the electron in the core-shell changes the spatial potential in the solid, by adding a positive charge. The core states being deep in energy, their inter-atomic coupling is weak and this charge can be considered as localized on a single Si atom. This localized term in the potential changes the DOS, and in particular provokes the appearance of silicon like bound states at the bottom of the band structure, as shown schematically on Figure 6.3 **c.**

This has the effect to break the degeneracy of the bands, hence their high number in **c.** It decreases the bandgap by dragging an isolated band to lower energies (it is stabilized by the attraction of the positive charge). This isolated band, responsible for the $A+A'$ absorption feature, is often referred to as an exciton, because it lied in the bandgap of the undisturbed material. The localized charge also gives the quantum states a marked atomic character (represented by the circles, coding for the overlap of the wavefunction with the Si atomic orbital database).

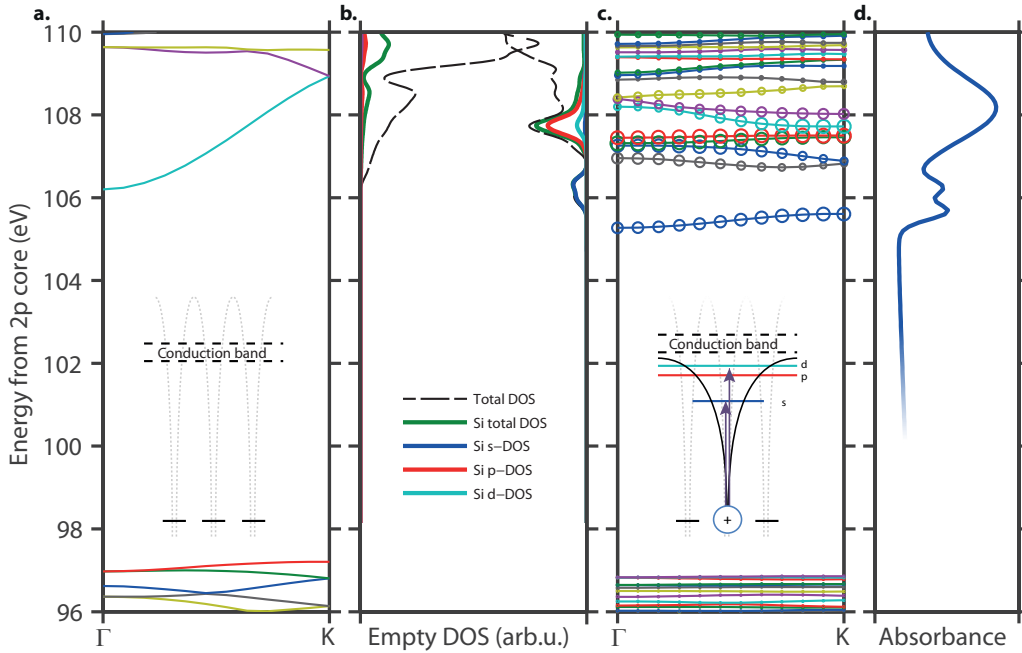


Figure 6.3: Modification of the band structure by the core-hole. **a.** DFT calculation (Wien2k) of the bandstructure of SiO_2 . The scheme shows an the unperturbed conduction band of a dielectric. **b.** DOS calculated by DFT with (left) and without (right) inclusion of the core-hole. See text for comments. **c.** DFT calculation (Wien2k) of the bandstructure of a supercell of $2 \times 2 \times 1$ SiO_2 unit cells, with a hole in the $2p$ orbital of the central Si atom. The circles represent the atomic character of the states. The scheme represents the formation of the core-hole dressed conduction band (see text). **d.** Absorbance

These effects are also visible on the calculated DOS on panel **b.** In the case of normal SiO_2 (left side), the Si DOS (green) has the same shape as the total DOS (black). This means that all the states are delocalized between Silicon and Oxygen atoms. On the contrary when the hole is present (right side), the total DOS is composed only of Si DOS below 108 eV, the excitonic states are localized on the positively charged silicon atom. These states have a strong atomic character, as can be seen from the momentum specific DOS, also plotted.

The part of this newly formed hole dressed DOS that has s or a d symmetry is therefore probed by XANES or EELNES. Looking at the corresponding curves on the DOS graphs of the right side of panel **b.**, the resonance-like structure is clearly visible. At higher photon

energies though, the states become more delocalized again, and the part of this DOS that has the correct symmetry is accessed by absorption. The picture of the scattered photoelectron used in EXAFS then becomes accurate. The transition from localized to delocalized states is not linear with energy though, as localized states exist also at higher energies. It is worth mentioning also that this scheme of dressing by the core-hole and creation of localized states is also valid for the valence bands, and present in the DFT data, although not presented here.

About linewidths in XANES

The linewidths observed in the resonant features of the XANES profile have the result of several effects, different in nature, revealed by inspecting Equation (6.2). This expression shows that the profile is the result of the superposition of an infinity of Lorentzians, for each transition $|i, \vec{k}\rangle$ to $|f, \vec{k}\rangle$, weighted by the DOS and the corresponding matrix element.

The variation of this weight with energy is the first effect. It has been covered in the previous section about core-hole effects, and the appearance of spikes in the bottom of the band attributed to the core hole potential.

This spectral profile is further affected by the presence of a significant energy dependent broadening of the individual Lorentzians. We have seen in the previous chapters that the dephasing rate of a coherent superposition of two states is the average of the decay rate of the initial and the final state, plus additional dephasing terms *i.e.* $\Gamma_{if} = (\Gamma_i + \Gamma_f)/2 + \Gamma_{ext,if}$.

In our case, the decay rate of the initial state is the same for all the transitions. Indeed the $2p$ hole of silicon is filled by an Auger process that can be considered as independent of the final state of the electron, with a characteristic time on the order of 10 fs (linewidths of 60 meV have been measured in the $L_{2,3}$ of silane gas SiH_4 [142]).

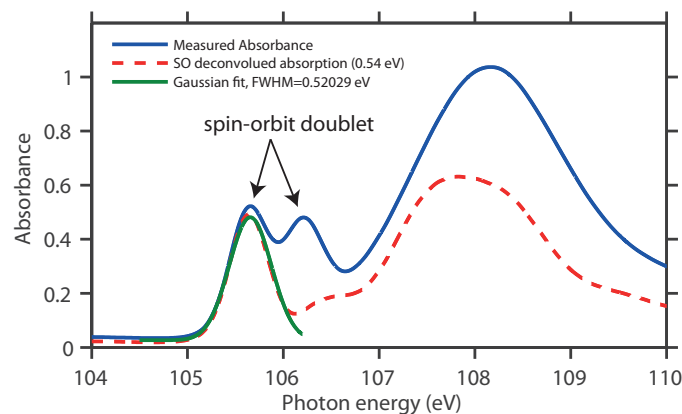


Figure 6.4: EUV absorbance (blue), spin orbit deconvoluted absorbance (dashed red) and Gaussian fit of core-exciton spike (green)

The other part is the finite lifetime of the final electron state, and is investigated at length in [143]. It can be either due to homogeneous factors (the states decay), or to the amorphicity of the sample, which makes the environment of each center slightly different

form the others, and adds an inhomogeneous broadening factor $\Gamma_{ext,if}$. Unlike the core-hole lifetime, these factors are dependent on the kinetic energy of the electron, *i.e.* $\hbar\omega - E_{edge}$, and therefore energy dependent, leading to different lifetimes for the resonances present in the spectrum. We applied the procedure described in [149] to estimate the so-called coherence length, or short range order of our samples. We deconvoluted the spin-orbit doublet with a double Dirac function with a weight of 1:0.7 and a spacing of 0.54 eV, and estimated the FWHM of the feature, 0.52 eV (see Figure 6.4). According to [149], the associated coherence length of our samples is above 20 angstrom, *i.e.* more than 4 unit cells. In other words they do not impact the XANES profile and our samples can therefore be considered as crystalline for this process, which is also confirmed by comparison with [144], which associates the presence of a distinguishable spin-orbit doublet A+A' with crystallinity.

6.2 Dipole gating measurement of the $L_{2,3}$ edge of SiO_2

Experiment

We have shun an attosecond EUV pulse centered at 105 eV with a bandwidth of 14 eV, followed by a delay-controlled attotransient with intensity contrast between main and secondary half-cycle 3:1 on a 125 nm thick film of fused silica (same coating batch as the one tested at the synchrotron and presented in the previous section). We have thus recorded the dipole gating spectrogram, presented in Figure 6.5 in the absorbance (a.) and differential absorbance (b.) frameworks.

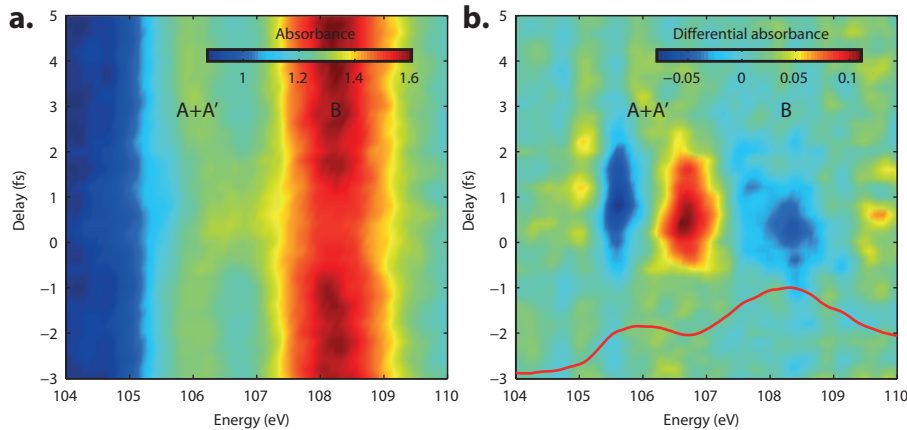


Figure 6.5: Dipole gating spectrogram of the SiO_2 $L_{2,3}$, represented in the direct (a.) and differential (b.) absorbance picture. As a guide for the eye the field free absorbance is represented on b. (red line)

The spectra have been averaged and normalized to the number of EUV counts, and smoothed with a Butterworth filter of cutoff energy 350 meV, below the spectral resolution

of the measurement. They have also been smoothed in the delay dimension with a 2 points Savitsky-Golay filter.

Without going to further analysis, a few interesting facts are already noticeable with bare eye. It is in a first place clear that the A and A' resonances are distorted over a longer delay range than B. A closer observation also reveals that these two groups of resonances are affected in a different way by the transient field. While A and A' are primarily shifted to higher energies, B is mostly damped, and does not shift much. These facts will be put into a more quantitative light in the following sections.

Hints on temporal resolution

To investigate the temporal resolution of our technique, on Figure 6.6 the average absolute differential density for resonances A and A' is plotted. The field sampled by streaking before this experiment is also represented. There we see that the rising time is subfemtosecond, which substantiates the picture of an attosecond pump-probe measurement.

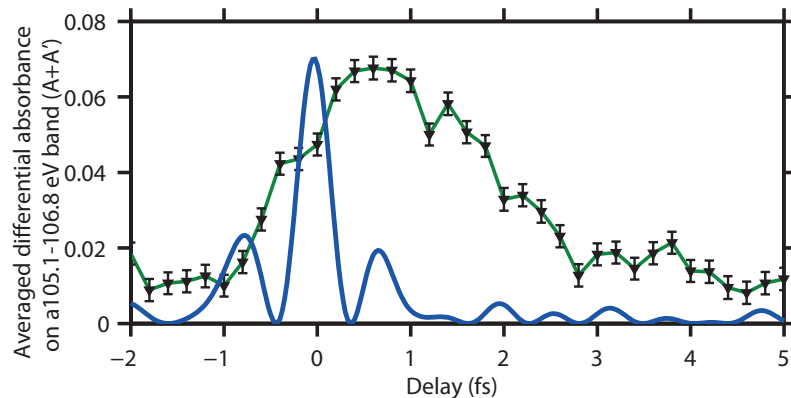


Figure 6.6: Absolute value of the differential absorbance, averaged on a band encompassing the A and A' features. The field intensity used in the experiment is plotted in blue. Error bars represent the statistical standard error of this quantity.

6.2.1 Dipole gating modeling

We applied the fitting procedure already described in Chapter 5, with 3 transitions, A, A' and B, which values of amplitude and energy are taken from the fit of the synchrotron cross-section. The result is summarized on Figure 6.7 and Table 6.1 in the by now familiar format.

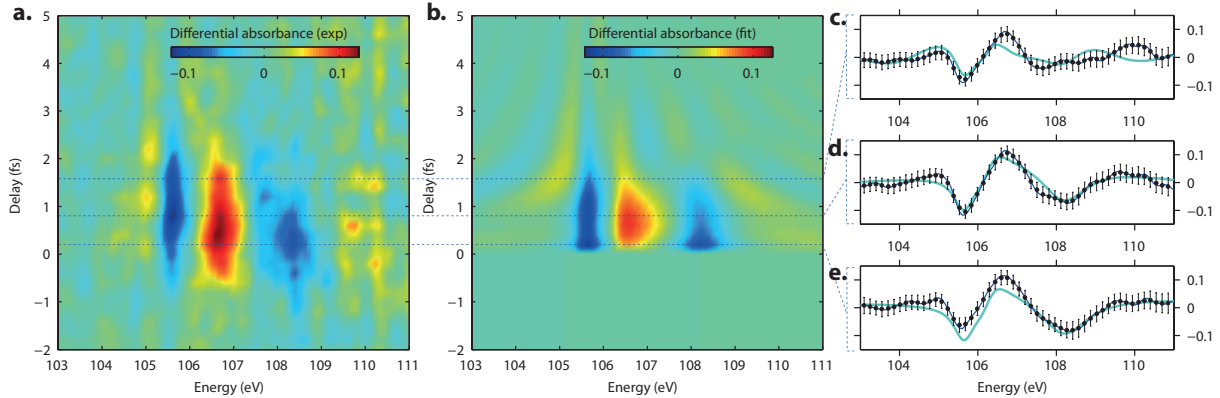


Figure 6.7: Fit of the spectrogram with instantaneous gate. **a.** Differential absorption spectrogram. **b.** Fitting of the spectrogram using the instantaneous gating model (see text) **c.d.e.** Comparison between calculated (dark blue) and fitted (light blue) cross-sections at 3 different pump-probe delays (**c.**, 0.2 fs, **d.**, 0.8 fs and **e.**, 1.6 fs).

The agreement between measurement and fit is not as good as in the case of Krypton, studied in the previous chapter. The reasons for this discrepancy mainly relies on the picture used for modeling, probably slightly too simple for the full description of a solid.

Indeed, the model of isolated lorentzian transitions is arguable. Since by nature in a solid the states are not well defined in energy but spread in an energy band, a broadening due to the band structure could be at play, and it would not lead to a lorentzian profile, or to an exponential decay, assumed by our modeling. However, attempts to fit such a nonexponential decay have revealed themselves unconvincing, the impact of a modification of a decay law on the goodness of the reconstruction being insignificant, numerically speaking.

transition	Instantaneous gate		
	A	A'	B
T_d (fs)	6.2 ± 1	3.2 ± 1	0.9 ± 0.1
ϕ_0 (π mrad)	31 ± 9	56 ± 14	-7 ± 5
α (at. u.)	105 ± 30	190 ± 50	-23 ± 16
Depletion r	$22\% \pm 2\%$	$0\% \pm 2\%$	$20\% \pm 3\%$

Table 6.1: Results of the fitting of the spectrogram. See text for details.

The parameters extracted by the fitting procedure are reported in Table 6.1. The decoherence time fitted correspond to the bandwidths observed, although they are a longer

for A and A'. As was the case for the two overlapping transitions on Krypton, the fitting has troubles to resolve A and A'. It is however clear that the sign of the polarizability is opposite for A and A' on one side, and B on the other side. The polarizability of B is furthermore quite low, reflecting the fact that, as had been seen from the trace, the resonance position is not so much shifted but rather damped. In other words, the corresponding dipole is more subject to amplitude than phase gating.

6.3 Nonlinear spectroscopy of SiO₂ core-hole excitonic system

6.3.1 *p* and *s, d* DOS in the core-hole system

As stated in the previous section, allowed EUV transitions from the Si *2p* core shell can address only the *s* or *d* DOS. The Si-*p* DOS is spectroscopically invisible in the Si L_{2,3}edge and has to be extracted from the Si K edge XANES, and various techniques have to be employed to compare these. It is however to be expected that the *1s* and the *2p* holes impact the DOS in a slightly different way, so that the *p*-DOS probed by Si K edge XANES is different than the *p*-DOS present, but unprobed in Si L edge XANES. Although this effect is expected to be of low magnitude (the *2p* and *1s* holes are both quite small compared to the unit cell and should therefore produce similar disturbances on the DOS), it calls for a technique sensitive to the *p*-DOS from the conventional L-edge XANES.

Our pump-probe scheme is especially suited to this purpose. Indeed, since dipolar transitions between (*s* or *d*) and (*p*) states are allowed, once the EUV pulse has populated the *s* and *d* DOS, the optical transient is able to act on them via coupling to the *p* DOS. The careful investigation of the effect of this coupling on the pump-probe XANES shall carry information about the "invisible" *p*-DOS, and on the coupling (dipole matrix elements) that link it to the *s* and *d* DOS.

Figure 6.8a. shows again the momentum specific Si-DOS extracted from DFT of the core-hole SiO₂ supercell, but including the valence bands, referenced from the *2p* hole energy. As can be seen, the atomic like DOS (solid blue, red and cyan curves) are very spiked, supporting the picture of bound states created in the potential of the hole localized positive charge. The *p*-DOS of the conduction band is overlapping with the *d*-DOS around 108 eV (most probably these states have are hybrids of *p* and *d* character orbitals). In the valence band, the *p*-DOS is located around 93 eV.

Taking advantage of the bound character of the states (localized DOS) involved in our experiment, we propose to model it using a few level system, as shown on Figure 6.8b.. The goal is to reproduce the experimental data in a simple formalism, understand if our method is sensitive to the parameters of the "hidden" *p* DOS and if we can retrieve them, although they are spectroscopically inaccessible in XANES.

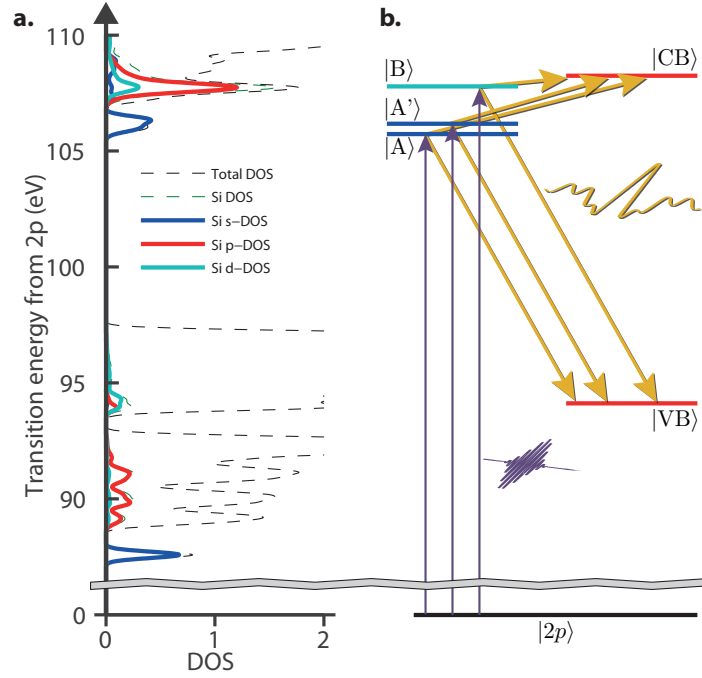


Figure 6.8: Modeling as a 6 levels system. **a.** DOS with Si-atomic like characters marked **b.** Proposed equivalent system for modeling of our experiment.

6.3.2 Reconstruction of the process in a 6 levels modeling

Model description

We propose to model our experiment with a 6 levels system, as shown on Figure 6.8b.. The ground state $|2p\rangle$ represents the $2p$ state of Si from which the electron is taken, $|A\rangle$, $|A'\rangle$ and $|B\rangle$ are the s and d like states respectively responsible for the, A, A' and B absorption features. Then $|VB\rangle$ and $|CB\rangle$ the spiked p -DOS of respectively the valence and the conduction bands, uncoupled to $|2p\rangle$, but to which $|A\rangle$, $|A'\rangle$ and $|B\rangle$ are linked by a non-zero dipole matrix element. The relevant matrices are therefore:

$$\hat{H}_0 = \begin{pmatrix} E_{2p} & 0 & 0 & 0 & 0 & 0 \\ 0 & E_A & 0 & 0 & 0 & 0 \\ 0 & 0 & E_{A'} & 0 & 0 & 0 \\ 0 & 0 & 0 & E_B & 0 & 0 \\ 0 & 0 & 0 & 0 & E_{VB} & 0 \\ 0 & 0 & 0 & 0 & 0 & E_{CB} \end{pmatrix} \quad (6.3)$$

$$\hat{\mu} = \begin{pmatrix} 0 & \mu_{2p,A} & \mu_{2p,A'} & \mu_{2p,B} & 0 & 0 \\ \mu_{2p,A}^* & 0 & 0 & 0 & \mu_{VB,A} & \mu_{CB,A} \\ \mu_{2p,A'}^* & 0 & 0 & 0 & \mu_{VB,A'} & \mu_{CB,A'} \\ \mu_{2p,B}^* & 0 & 0 & 0 & \mu_{VB,B} & \mu_{CB,B} \\ 0 & \mu_{VB,A}^* & \mu_{VB,A'}^* & \mu_{VB,B}^* & 0 & 0 \\ 0 & \mu_{CB,A}^* & \mu_{CB,A'}^* & \mu_{CB,B}^* & 0 & 0 \end{pmatrix} \quad (6.4)$$

$$\hat{\Gamma} = \begin{pmatrix} 0 & \Gamma_{2p,A} & \Gamma_{2p,A'} & \Gamma_{2p,B} & \Gamma_{2p,VB} & \Gamma_{2p,CB} \\ \Gamma_{2p,A} & \Gamma_{A,A} & 0 & 0 & \Gamma_{VB,A} & \Gamma_{CB,A} \\ \Gamma_{2p,A'} & 0 & \Gamma_{A',A'} & 0 & \Gamma_{VB,A'} & \Gamma_{CB,A'} \\ \Gamma_{2p,B} & 0 & 0 & \Gamma_{B,B} & \Gamma_{VB,B} & \Gamma_{CB,B} \\ \Gamma_{2p,VB} & \Gamma_{VB,A} & \Gamma_{VB,A'} & \Gamma_{VB,B} & \Gamma_{VB,VB} & \Gamma_{VB,CB} \\ \Gamma_{2p,CB} & \Gamma_{CB,A} & \Gamma_{CB,A'} & \Gamma_{CB,B} & \Gamma_{VB,CB} & \Gamma_{CB,CB} \end{pmatrix} \quad (6.5)$$

The quantities written in light blue are accessible by conventional XANES spectroscopy, in red they relate to the p -DOS and are therefore unknown, and in beige, the dephasing rates of the direct EUV transitions can be estimated from the width of the spectral features, but we are interested to reconstruct them also in the time domain. Quantities in black do not play a role in the physics of our experiment, being population decay constants. The dephasing times displayed in red, relating to transitions between excited states have also been found to have no impact on the calculation and fixed to 0.1 fs. In the regime in which we work, this is rather intuitive, because these transitions do not occur on our spectral range.

Reconstruction of experimental data

We developed a fitting procedure, in which we fit the full calculated pump-probe map using the Von Neumann formalism and assuming Beer-Lambert law for the propagation to the experimental data. The fields used in the simulation are the very waveform extracted from streaking before the absorption data has been recorded, and a 200 as EUV pulse centered on 105 eV, mimicking our EUV pulse. The fitting parameters are exactly the red and beige quantities (except, as explained the red dephasing times). The dipole matrix elements are assumed to be real numbers, which proved sufficient for the description of the system. The result of this fit is shown on Figure 6.9. The agreement is better than with the dipole gating model, which tells us that more delicate effects are at play in this trace, that are not sufficiently described by the simple picture we used earlier. Coherent population transfer within the A, A', B system through the conduction and the valence band states could be an example. They are captured by our 6 levels calculation. Although the dispersion related delay of 200 as (see Section 3.4.3) has been taken into account, there seems to be more signal in the negative delay range in our experiment than in the reconstruction....

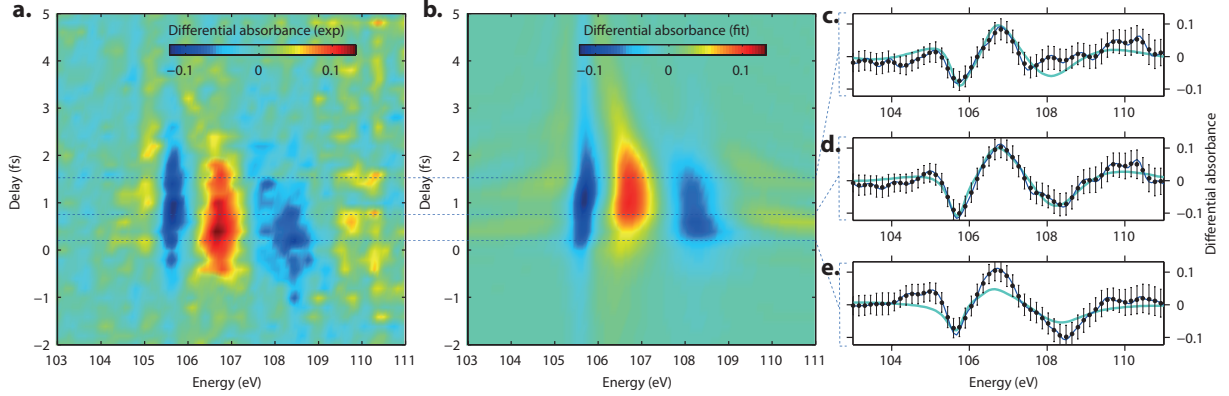


Figure 6.9: Fit of the spectrogram with our undetermined 6 levels system. **a.** Differential absorption spectrogram. **b.** Fitting of the spectrogram using the 6 levels model (see text) **c.d.e.** Comparison between calculated (dark blue) and fitted (light blue) cross-sections at 3 different pump-probe delays (**c.**, 0.2 fs, **d.**, 0.8 fs and **e.**, 1.6 fs).

Numerical results

The complete reconstructed dephasing times are $\Gamma_{2p,A}^{-1} = 2.2 \pm 0.3$ fs and $\Gamma_{2p,B}^{-1} = 750 \pm 60$ as (with 95 % confidence intervals). They are compatible with the times reconstructed with our simple dipole gating model in Section 6.2.1, although a bit shorter, probably due to pulse durations effects not taken well into account in the instantaneous gating model used earlier. However $\Gamma_{2p,A}$ is not correctly reconstructed, the fitting algorithm being stuck at the highest allowed value. This did not impact the robustness of the other values, and can be attributed to a lack of spectral resolution.

Moreover, the reconstructed position of the Si p-DOS of the conduction band is $E_{CB} = 109.8 \pm 0.8 eV$, This is rather close to the position predicted by DFT, as can be seen on Figure 6.8 and constitutes the first measurement of nonlinear properties in the context of XANES measurements. The retrieved position of the valence band state is $E_{VB} = 11.7 \pm 4 eV$. This is somewhat surprising and will be commented later on.

The dipole matrix elements are also reconstructed with a good accuracy by our procedure. We extract the following matrix (values in atomic units). As explained above, blue elements are obtained by the fitting of the static cross-section, while red elements are extracted from the reconstruction of the full spectrogram.

$$\hat{\mu} = \begin{pmatrix} 0 & 0.027 & 0.021 & 0.094 & 0 & 0 \\ 0.027 & 0 & 0 & 0 & 7 \pm 0.6 & 0.7 \pm 0.2 \\ 0.021 & 0 & 0 & 0 & 13.9 \pm 0.6 & 1.4 \pm 0.3 \\ 0.094 & 0 & 0 & 0 & -1.6 \pm 0.4 & 1.5 \pm 0.1 \\ 0 & 7 \pm 0.6 & 13.9 \pm 0.6 & -1.6 \pm 0.4 & 0 & 0 \\ 0 & 0.7 \pm 0.2 & 1.4 \pm 0.3 & 1.5 \pm 0.1 & 0 & 0 \end{pmatrix} \quad (6.6)$$

A few interesting points can be noted. First, the magnitude of these matrix elements.

Then the sign of the CB state. The VB state is far away and mostly polarizes in a nonresonant way, mostly the exciton.

It is not corresponding to the position of an actual DOS in the DFT calculation, and its determination by the algorithm is not very specific. The reason for this is the fact that this level being strongly off-resonantly coupled to the A, A' and B states, it mostly modifies them by Stark shifting them. The relevant physical quantity is then the polarizability $\alpha = \mu^2/\Delta E$, and a change in energy can be compensated by a change in matrix element. Thus the relevant quantity concerning the valence band DOS is:

$$\alpha_{A,VB} = \frac{7^2}{95eV/1Ry} = 14 \text{at. u.} \quad (6.7)$$

It is important to state here that the quantities retrieved describe fundamental properties of the system, and are not pulse dependent. Therefore they can be used to predict the result of a different experiment. We tested it with the intensity variation of our differential absorbance signal.

6.3.3 Intensity scaling

We have conducted a detailed study of the scaling of the perturbation with the intensity of the driving transient. To this end, we have selected 5 pump-probe delays, and measured spectra for different values of the optical field intensity. Intensity was then calibrated using the procedure described in Section 3.1.1. The results are displayed on Figure 6.10. Panel **a.** shows the pump-probe trace, **b.-f.** the intensity scaling of the differential absorbance respectively at delays +3 fs, +1.5 fs, +0.5 fs, 0 fs and -5 fs. It is noticeable that at +1.5 fs, the effect of the transient on B is quite low, when the effect on A+A' is still quite marked, confirming the different decoherence time of these two groups of transitions. To represent the scaling law, we have calculated and plotted on panel **g.** the average of the absolute differential absorbance on a spectral band containing features A and A', for the 5 studied pump-probe delays. The linear scaling with intensity is thus made clear, confirming the picture of a quadratic perturbation of the EUV induced dipole by the visible field.

We could perform a simulation of this intensity variation using the fitted values of energy, dipole matrix and dephasing times, and obtained the data of Figure 6.11. It is quite comparable to the experiment, except for the signal at $\tau = 0$ fs, stronger in the experiment than in the simulation. The linear intensity dependence of the differential absorbance (panel **g.**) is also reproduced, although some saturation effect is displayed towards 10^{14} W.cm⁻² that is not seen in the experiment.

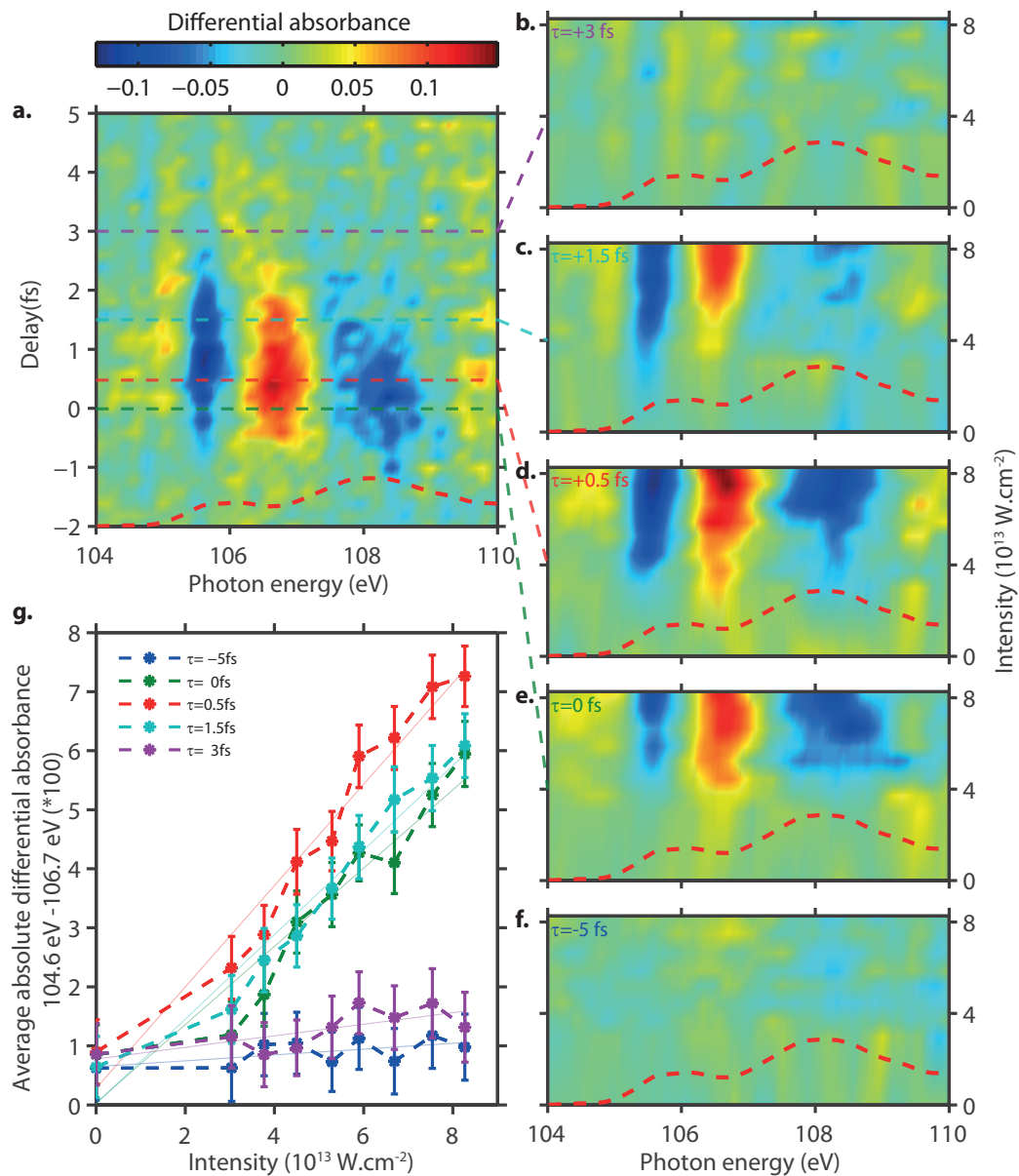


Figure 6.10: Intensity scaling of NLXANES. **a.** NLXANES pump-probe spectrum of Si $L_{2,3}$ edge. **b.-f.** intensity scaling of the differential XANES spectrum at respectively +3 fs, +1.5 fs, +0.5 fs, 0 fs and -5 fs. (measurements taken in a set different from panel **a.**). **g.** Scaling with intensity of the average absolute differential absorbance over the A and A' features at different pump-probe delays.

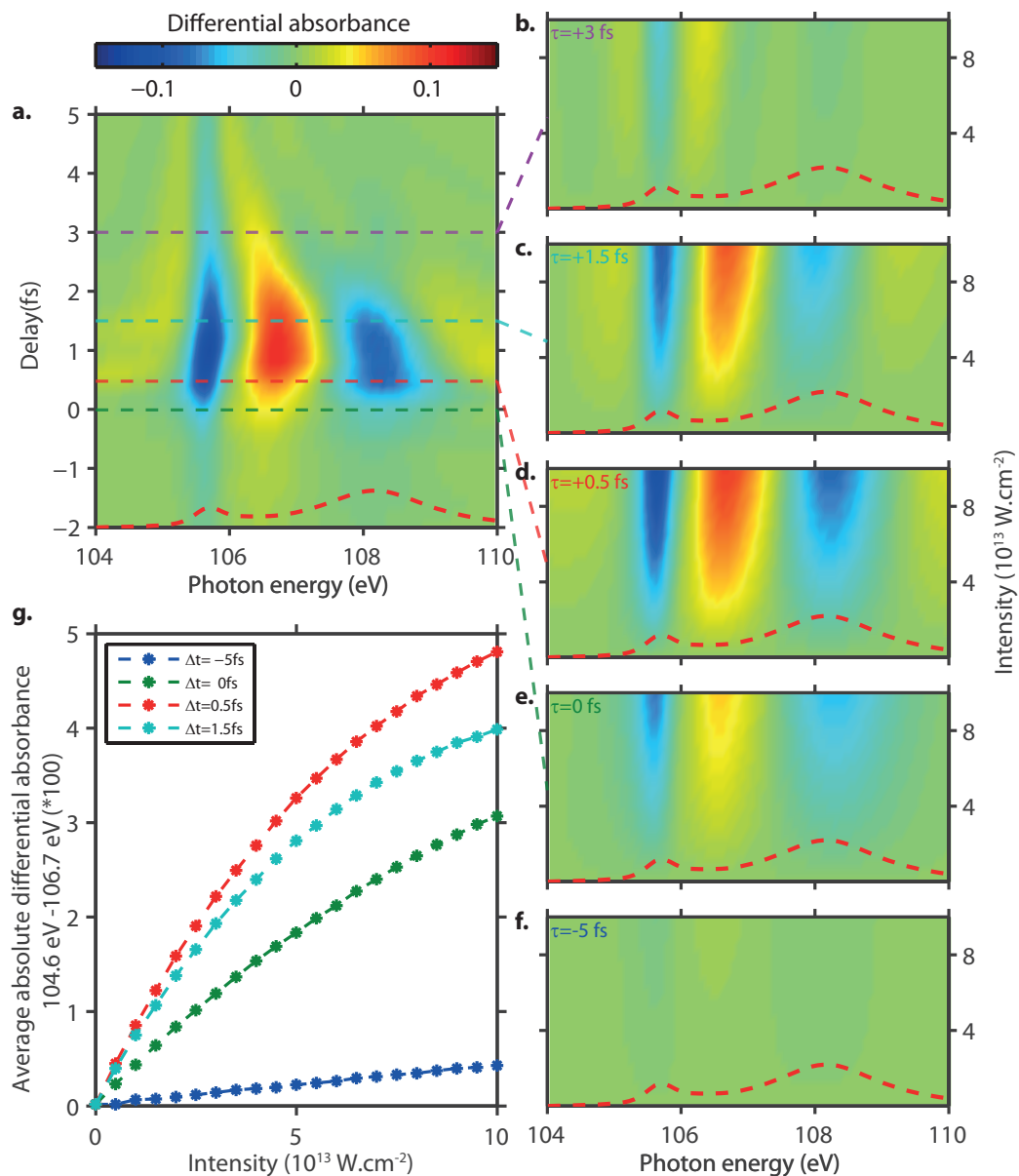


Figure 6.11: Intensity scaling of NLXANES calculated using the 6 levels model with the parameters fitted in the previous section. **a.** NLXANES pump probe spectrum of Si L_{2,3} edge. **b.-f.** intensity scaling of the differential XANES spectrum at respectively +3 fs, +1.5 fs, +0.5 fs, 0 fs and -5 fs. **g.** Scaling with intensity of the average absolute differential absorbance over the A and A' features at different pump-probe delays.

Conclusion

We have demonstrated here the direct tracing in the time domain of sub- and few femtosecond decoherence times of an EUV absorption edge in fused silica, using the concept of phase and amplitude gating of an electronic dipole presented and benchmarked in Chapter 5. Going deeper into the physics of the studied system and the localized nature of the associated density of states, we proposed a modeling based on a few level hydrogenic system, which reproduced the experimental data to an extremely good level. This technique also allowed the reconstruction, (*i.e.* in our modeling the energy position) of the part of the density of states that is not accessible by conventional time-integrated spectroscopy and usually has to be retrieved by other techniques, as well as the coupling dipole matrix elements between the different DOS, shedding light on the nonlinear behavior of transitions involved in XANES spectroscopy.

7

Conclusions and outlooks

To infinity, and beyond!

– Buzz Lightyear, space ranger

In this work, I presented the first attosecond EUV - attosecond visible pump-probe scheme. Based on the perturbation of the absorption of EUV by the application of a visible transient perturbing the states involved, it has been inspired by the first observation of the instantaneous Stark shift in an experiment addressing probing of Strong Field Ionization in real-time (Chapter 4).

Having understood this phenomenon, we then applied this scheme to the resonant $3d - np$ edge of Krypton atoms. The intuitive model of amplitude and phase gating developed at this occasion has allowed us to resolve the decoherence time of these resonances in the time domain, successfully benchmarking our approach with a system already studied in the time and frequency domain, and giving a handy tool to describe perturbation of a multilevel system by a superoctave continuum in a the time-based approach, when frequency-based concepts are ill-adapted. Other quantities related to the nonlinear behavior of the addressed excited states, namely polarizability and the percentage of field induced ionization have also been efficiently reconstructed.

We then turned to a more complex object of study, the $L_{2,3}$ edge of SiO_2 . Linewidths discernible in these resonances hint towards sub and few femtoseconds decoherence times, which challenged the limits of our technique. The application of our gating reconstruction technique has indeed allowed us to retrieve these dephasing times for the first time in a time-resolved approach, together again with other nontrivial properties of the EUV transitions. Going further into the modeling allowed us to get a deeper understanding of the coupling schemes involved, using a simple few level formalism. The ability of this model to reconstruct the experimental data, and to predict its intensity dependence is a strong hint to confirm the excitonic nature of core-shell excitations in solids. It also allowed us to get access to the position of momentum specific density of states which are transition forbidden by dipole selection rules in XANES, and to the strength of the couplings involved.

The tools developed in the framework of this thesis have a very broad range of potential applications in the advancement of attosecond science. Though they cannot replace modern

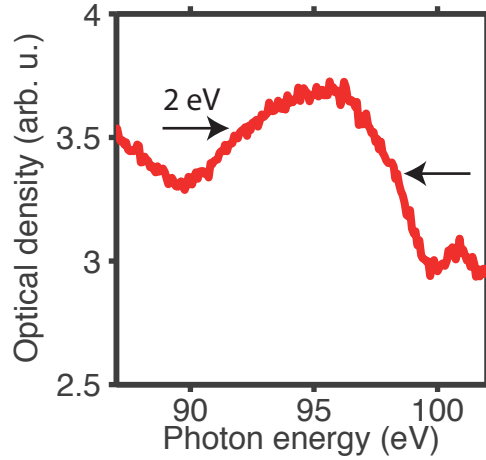


Figure 7.1: Resonant $3p$ absorption in ZnO

advanced *ab initio* calculations, they provide experimentalists a quick and intuitive tool to interpret their experiments. Thus, the modeling tools would be of big help for the interpretation of time-resolved ionization studies similar to the ones presented in Chapter 4, for which, as we have seen, polarization effects have to be included to allow a correct interpretation. The development of more advanced retrieval methods, possibly based on Appendix B would be of additional use.

Further implementations of this pump-probe scheme with unprecedented temporal resolution could also be made in different systems whose bandwidths also hint towards sub-femtosecond dynamics, such as the transitions from the $3p$ subshell of zinc in ZnO. The 2 eV bandwidth indeed suggests a 350 as decoherence time, slightly under our resolution limit. Thin (15 nm) ZnO slabs have been tried in the lab (see Figure 7.1a.), but although some signal was recorded, due to a huge nonresonant absorption background, further improvements in signal to noise ratio would be required to address this system efficiently.

Furthermore, our work in SiO₂ granted us an advanced knowledge of EUV absorption perturbation by visible fields. This information about the system is not pulse shape dependent, and can therefore be used to design experiments in which the attotransient opens an ultrafast absorption window for an EUV light which spectrum overlaps with the A and A' resonances, thus realizing an attosecond EUV switch that could be of interest to the XFEL or synchrotron community.

Doors are also open on the theoretical side. Indeed our picture of coupled excitonic DOS, although reproducing the experiments to an extended degree could be profitably challenged by full *ab-initio* calculations, relying on Time-Dependent Density Functional Theory (TDDFT) for example.

On a separate notice, in the course of the SiO₂ experiments, it has been noticed that the samples used in absorption spectroscopy actually gave a significant yield of photoelectrons, which could be recorded by the time-of flight spectrometer. A software infrastructure has been designed to record simultaneously pump-probe absorption and photoelectron signals,

and Figure 7.2 shows the spectrogram recorded together with the absorption data analyzed in Chapter 6. A clear streaking structure is seen, that could actually be used to ensure the stability of the experimental conditions during the recording of the data. These electrons actually coming from the valence band of SiO_2 , they could actually also be of use to extract information in conjunction to the absorption pump-probe spectrum, something which we have not looked into by lack of time.

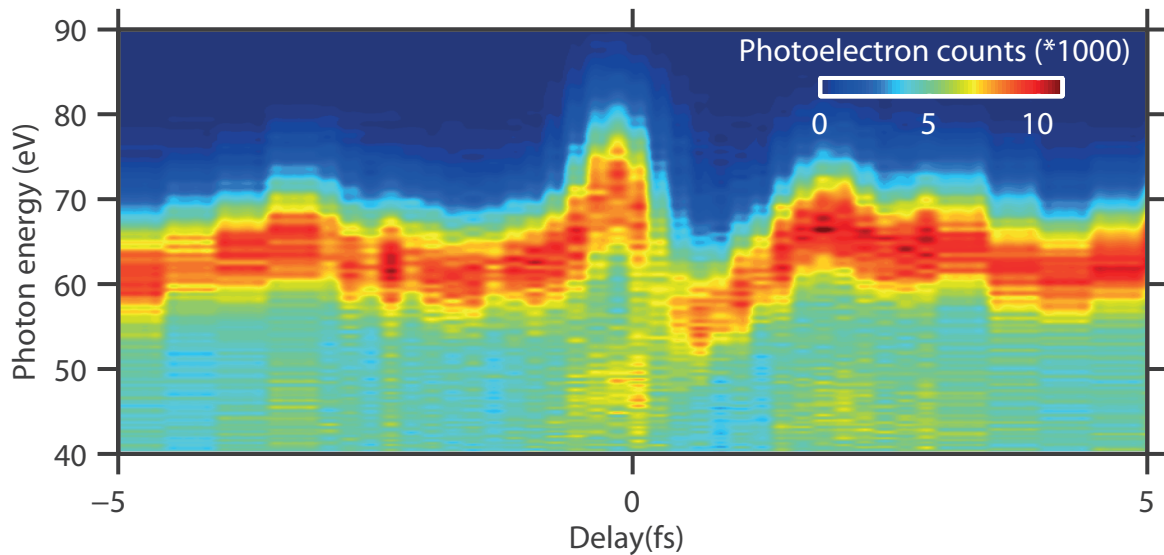


Figure 7.2: Streaking spectrogram from SiO_2 surface recorded in synchronization with the data presented in Chapter 6

This photoelectron signals have inspired the master project of A. Jain [150], who investigated the capability of such a tool to resolve spatio-temporal dynamics on the nanoscale for metal-dielectric structures. Further is to come on this side as well.

Appendix A

Going further in exploiting the cross-correlation concept

The goal of the present note is to go further than the approach presented in Chapter 3 to extract the iris opening induced delay, and show the procedure to follow in order to fully deduce the waveform at an iris opening different from the one at which the streaking measurement was performed.

The streaking waveform is known from the streaking measurement. We will use its cross-correlation with the inner mirror waveform, and the cross-correlation of the transient absorption waveform with the inner mirror waveform to extract a "transfer function" which will describe the relationship between transient absorption and streaking waveforms, and allow us to reconstruct this transient absorption waveform which otherwise remains unknown.

A.1 Definitions

Let us first define correctly the objects that we will consider in the following text:

The time t is understood as the time axis associated with the piezo position x ($t = 2(x - x_0)/c$).

What we call waveform is the temporal electric field arising from light reflected respectively by the inner mirror ($E_{in}(t)$), the outer mirror with streaking opening ($E_{st}(t)$) and the outer mirror with transient absorption opening ($E_{TA}(t)$), in the plane imaged by the camera, averaged over the points of the spatial profile taken to calculate the autocorrelation (5×5 pixels on the camera, i.e an area of $22\mu\text{m}^2$ in the actual beam profile).

A.2 Principle

The streaking/inner mirror cross-correlation $S_{st/in}(t)$ can be written as follows:

$$\begin{aligned}
S_{st/in}(t) &= \int (E_{in}(t') + E_{st}(t' - t))^2 dt' \\
&= \int (E_{in}(t')^2 + E_{st}(t')^2) dt' + 2 \int E_{in}(t') E_{st}(t' - t) dt' \\
&= \int (E_{in}(t')^2 + E_{st}(t')^2) dt' + 2E_{st}(-t) \otimes E_{in}(t)
\end{aligned}$$

Here \otimes represents the convolution product. Figure (A.1) shows the oscillating term of the cross correlations of streaking and transient absorption.

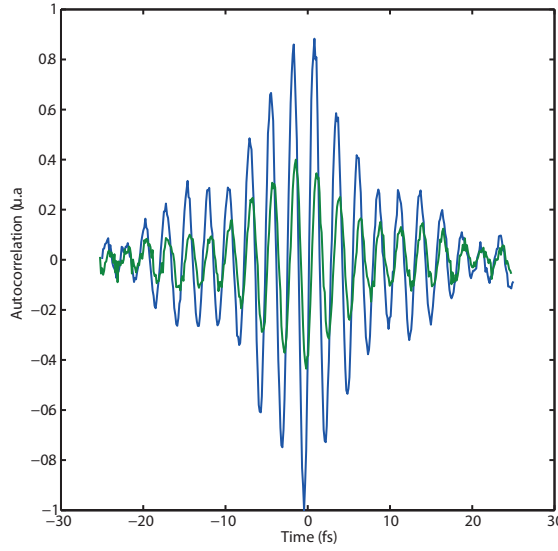


Figure A.1: Streaking (blue) and transient absorption (green) cross-correlations

Taking the Inverse Fourier Transform of the cross correlation trace gives us, according to known properties of Fourier analysis:

$$\begin{aligned}
\mathcal{F}^{-1}[S_{st/in}(t)] &= \delta(\omega) \times \int (E_{in}(t')^2 + E_{st}(t')^2) dt' \\
&\quad + 2E_{st}^*(\omega) E_{in}(\omega)
\end{aligned}$$

The above expression shows that simple filtering in the frequency domain (actually removing the value at zero frequency) allows to extract the term that is of importance for us:

$$f_{st/in}(\omega) = 2E_{st}^*(\omega) E_{in}(\omega)$$

We also get from the other crosscorrelation (with evident notations) $f_{TA/in}(\omega)$. Then we define the streaking to transient absorption transfer function:

$$H_{st/TA}(\omega) = \frac{f_{TA/in}^*(\omega)}{f_{st/in}^*(\omega)}$$

The work is then almost done, since we can get the transient absorption waveform spectral amplitude from the measured streaking waveform spectral amplitude with:

$$E_{TA}(\omega) = E_{st}(\omega) \times H_{st/TA}(\omega)$$

The waveform is then deduced by simple Fourier Transform back in the time domain.

A.3 Influence of the transmission system

If the transmission of the light from the image plane to the CCD camera used for the measurement is linear (lens, mirrors, window and even propagation effects), then the extracted transfer function is independent of this transmission, as long as the signal to noise ratio is sufficient to have appreciable signal on the complete spectrum. Indeed, the linear transmission then enables us to write for the waveforms *on the detector*:

$$E_{st}^{det}(\omega) = E_{st}(\omega) \cdot G_{trans}(\omega)$$

And therefore:

$$H_{st/TA}^{det}(\omega) = \left(\frac{f_{TA/in}^{det}(\omega)}{f_{st/in}^{det}(\omega)} \right)^* = \left(\frac{f_{TA/in}(\omega)}{f_{st/in}(\omega)} \right)^* \times \left(\frac{G_{trans}^2(\omega)}{G_{trans}^2(\omega)} \right)^* = H_{st/TA}(\omega)$$

The transfer function being independent of this linear transmission and the streaking waveform measured inside the chamber, the calculation of the transient absorption waveform is not affected. Only restriction is that the transfer function $G_{trans}(\omega)$ should allow the transmission of all the frequency components of the waveform, which was not the case during our first experimental investigation.

A.4 Spatio-temporal characterization

All the presented formalism can be applied at different spatial positions in the focal plane, allowing the extraction of the spatio-temporal variations of the field.

Appendix B

EUV Dipole FROG

The object of this appendix is to explain the derivation of a FROG-CRAB [55] type expression, which would be subject to the use of a PGCPA algorithm to retrieve amplitude and phase gate, as well as dipole in function of time from our dipole optical gating traces. According to [55], if a pump-probe spectrogramm (function of ω and τ) can be written as:

$$S(\omega, \tau) = \left| \int_{-\infty}^{+\infty} dt G(t) E(t - \tau) e^{i\omega t} \right|^2 \quad (\text{B.1})$$

With G the gate, and E the field, then the PGCPA [120] algorithm can be used to extract efficiently gate and field. We can derive such an expression for our dipole gating method from Equation (5.10):

$$\begin{aligned} d_{12}(t, \tau) = & A\mu_{12}^2 a_{11}(0)^2 \rho_{11}(0) \\ & \cdot a_{11}(-\tau) \exp(r(-\tau) + i\phi(-\tau)) \\ & \chi_{12}^0(t) \cdot a_{11}(t - \tau) \exp(-r(t - \tau) - i\phi(t - \tau)) \end{aligned} \quad (\text{B.2})$$

We then get:

$$\begin{aligned} d_{12}(\omega, \tau) = & A\mu_{12}^2 a_{11}(0)^2 \rho_{11}(0) \\ & \cdot a_{11}(-\tau) \exp(r(-\tau) + i\phi(-\tau)) \\ & \int_{-\infty}^{+\infty} dt \chi_{12}^0(t) \cdot a_{11}(t - \tau) \exp(-r(t - \tau) - i\phi(t - \tau)) e^{i\omega t} \end{aligned} \quad (\text{B.3})$$

Let us remind that this expression had been obtained with an EUV pulse $E_{EUV}(t) = A\delta(t)$, we therefore get, applying the Lambert Beer law and using $G(t) = a_{11}(t) \exp(r(t) + i\phi(t))$:

$$\begin{aligned}
\sigma(\omega, \tau) &= \frac{\omega}{c\epsilon_0} \text{Im} \left(\frac{d(\omega, \tau)}{E_{EUV}(\omega)} \right) \cdot \mathcal{N} \cdot L \\
&= \frac{\omega}{c\epsilon_0} \cdot \mathcal{N} \cdot L \mu_{12}^2 a_{11}(0)^2 \rho_{11}(0) \\
&\quad \cdot \text{Im} \left(G(-\tau) \int_{-\infty}^{+\infty} dt \chi_{12}^0(t) \cdot G(t - \tau) e^{i\omega t} \right)
\end{aligned} \tag{B.4}$$

This is not yet written in the fashion of Equation (B.1), because of the term $G(-\tau)$ and of the use of the imaginary part and not the absolute value squared. The later problem can however be tackled relatively easily, using the fact that $f(t) = \chi_{12}^0(t) \cdot G(t - \tau)$ respects the causality principle (for $t < 0$, t a real number, $f(t) = 0$). Therefore its Fourier Transform verifies Kramers-Kronig relationships, and:

$$\text{Re}(f(\omega)) = \frac{1}{\pi} \int_{\mathbb{R}} \frac{\text{Im}(f(\xi))}{\xi - \omega} d\xi \tag{B.5}$$

Therefore we can easily calculate, from the absorption cross-section, a quantity $S(\omega, \tau)$ that writes:

$$\begin{aligned}
S(\omega, \tau) &= \left(\frac{\sigma(\omega, \tau)}{\omega} \right)^2 + \left(\frac{1}{\pi} \int_{\mathbb{R}} \frac{\sigma(\xi, \tau)/\xi}{\xi - \omega} d\xi \right)^2 \\
&= \left(\frac{1}{c\epsilon_0} \cdot \mathcal{N} \cdot L \mu_{12}^2 a_{11}(0)^2 \rho_{11}(0) \right)^2 \\
&\quad \cdot \left| G(-\tau) \int_{-\infty}^{+\infty} dt \chi_{12}^0(t) \cdot G(t - \tau) e^{i\omega t} \right|^2
\end{aligned} \tag{B.6}$$

We thus see that in the case of not too strong perturbation, or if the gate is very short so that most of the cases $G(-\tau) \simeq 1$, $S(\omega, \tau)$ is of the type of Equation (B.1), and a PGCPA algorithm can be used to retrieve field free dipole $\chi_{12}^0(t)$ as well as phase and amplitude gate $G(t)$. Unfortunately the attempts we have made to use this technique have been hindered by a poor retrieval. The small changes applied by the gate to the dipole were indeed not significant enough to allow good retrieval. It could however be revisited, and tried with either gate or dipole being fixed, so that it does not work in blind (two unknown functions) mode anymore, and information about the gate and the dipole can be extracted, knowing the other one.

Appendix C

Linking polarizability and phase in the instantaneous gate model

The instantaneous phase of an oscillating dipole is:

$$\phi(t - \tau) = \int_0^t dt' \Delta\omega_{ge_i}(t' - \tau) \quad (\text{C.1})$$

We know that for a Stark Shifted dipole, with α the polarizability of the transition,

$$\Delta\omega_{ge_i}(t' - \tau) = \frac{\alpha E^2(t - \tau)}{2\hbar} = \frac{\alpha I(t - \tau)}{2\hbar\epsilon_0 c} \quad (\text{C.2})$$

The atomic unit of polarizability is:

$$\alpha_0 = \frac{(ea_0)^2}{E_0} = \frac{(5.291 \cdot 10^{-11} \cdot 1.602 \cdot 10^{-19})^2}{4.3597 \cdot 10^{-18}} = 1.6438 \cdot 10^{-41} \text{m}^2 \cdot \text{C}^2 \cdot \text{J}^{-1} \quad (\text{C.3})$$

Combining the previous formulas we get:

$$\phi(t - \tau) = \alpha(\text{at. u.}) \cdot \frac{0.0933}{2} \cdot \int_0^t dt' I(t' - \tau) (\text{W.cm}^{-2}) \quad (\text{C.4})$$

Therefore for a half-cycle of peak intensity I_0 in W.cm^{-2} and FWHM duration 400 as, the link between phase accumulated and polarizability is:

$$\begin{aligned} \phi_0 &= \alpha(\text{at. u.}) \cdot I_0 (\text{W.cm}^{-2}) \cdot \frac{0.0933}{2} \cdot \frac{1}{2} \cdot 400 \cdot 10^{-18} \\ &= \alpha(\text{at. u.}) \cdot I_0 (\text{W.cm}^{-2}) \cdot 9.33 \cdot 10^{-18} \end{aligned} \quad (\text{C.5})$$

Appendix D

Data Archiving

The experimental raw data, evaluation files, and original figures can be found on the Data Archive Server of the Laboratory for Attosecond Physics at the Max Planck Institute of Quantum Optics:

`/afs/rzg/mpq/lap/publication_archive`

The list below contains paths to all the relevant files given with respect to the root folder of the thesis.

For all the streaking data, the raw data is located in the folder Streaking Data. The analysis (field extraction, channels extractions,...) is done using the Labview program LFS.vi, according to the guidelines given in the document LFS_userguide.docx. The Lewenstein HHG and ADK calculations are also done using the appropriated module of this software. The *.wfs file can be loaded by the LFS.vi and the field extracted.

For all the transient absorption data, the raw data is located in the folder APSS Data, sorted by day. The data is then treated by the Labview program Analyzer_APSS.vi, found in the same folder. Using this program according to the guidelines found in the document Analyzer_APSS_userguide.docx and with the averaging parameter file pointed to here yields the treated data, which is pointed to in the following pages. To apply the various map fitting procedures described in the text, the relevant fitting module of the software has to be used according to guidelines, or the fitting file pointed to here loaded with the relevant function.

The folder of each figures contains then treated data and Matlab plotting routine, as described in the following. To generate the figures the routine was applied, and it has been reworked via Adobe Illustartor. The given figure path is the adobe illustrator file, that has been converted to pdf for inclusion in the document.

Figure 1.1

- ▶ Routine `chapter01/Principle/onefspulse.m`
- ▶ Figure `chapter01/Principle/1fs.ai`

Figure 1.2

Field from the streaking of the 21st of December 2012, scan 10, Fourier limit. 5 cms or 10 cms of air dispersion added by LFS.vi.

- ▶ Data `chapter01/5cmair/Data`
- ▶ Routine `chapter01/5cmair/10cmsair.m`
- ▶ Figure `chapter01/5cmair/10cms.ai`

Figure 1.3

- ▶ Routine `chapter01/Phi_g/Phig.m`
- ▶ Figure `chapter01/Phi_g/Phig.ai`

Figure 1.4

- ▶ Figure `chapter01/LaserSystem/LaserSystem.ai`

Figure 1.5

- ▶ Data `chapter01/Broadening/Data`
- ▶ Routine `chapter01/Broadening/FigBroadening.m`
- ▶ Figure `chapter01/Broadening/Broadening.ai`

Figure 1.6

- ▶ Data `chapter01/Wizzler`
- ▶ Routine `chapter01/Wizzler/FigWizzler.m`
- ▶ Figure `chapter01/Wizzler/SRSI.ai`

Figure 1.7

- ▶ Data b. `chapter01/Fiber/Spectrum_fiber.opj`
`chapter01/Fiber/20140612-15h0000-AmpSpec.txt`
- ▶ Figure `chapter01/Fiber/Fiber.ai`

Figure 1.8

- ▶ Data See archiving Theses/2013/Hassan Mohammed
- ▶ Figure `chapter01/Synthesizer/Synthesizer.ai`

Figure 1.9

The streakings considered are scan 3 and 4 of the 22nd of February 2013.

- ▶ Data `chapter01/Streaking/Data`
- ▶ Routine `chapter01/Streaking/StreakingFig.m`
- ▶ Figure `chapter01/Streaking/Streaking.ai`

Figure 2.1

4 fs pulse obtained from frequency filtering of the field extracted from the streaking of the 22nd of December 2012, scan10, Fourier limited, to keep a 540 nm central wavelength. Lewenstein calculations done with LFS, trajectory with the Matlab routine

- ▶ Data `chapter02/HHG TransientFigure/Data`
- ▶ Routine `chapter02/HHG TransientFigure/Fig4fs.m`
- ▶ Figure `chapter02/HHG TransientFigure/HHGTransient4fs.ai`

Figure 2.2

1 fs pulse obtained from the field extracted from the streaking of the 22nd of December 2012, scan10, Fourier limited, and global phase change applied by LFS.vi. Lewenstein calculations done with LFS, trajectory with the Matlab routine. The routine has to be ran for the two global phase settings

- ▶ Data `chapter02/HHG TransientFigure/Data`
- ▶ Routine `chapter02/HHG TransientFigure/Fig1fs.m`
- ▶ Figure `chapter02/HHG TransientFigure/HHGTransient1fs.ai`

Figure 2.3

Run this routine after the previous ones (Fig1fs.m or Fig4fs.m).

- ▶ Routine `chapter02/HHG TransientFigure/Traj_cutoff.m`
- ▶ Figure `chapter02/HHG TransientFigure/Cutoffs.ai`

Figure 2.4

- ▶ Data `chapter02/SpectraTransient/Data`
- ▶ Routine `chapter02/SpectraTransient/FigSpectra.m`
- ▶ Figure `chapter02/SpectraTransient/SpectraTransient.ai`

Figure 2.5

The streakings are scan 19 and 21 from the 11th of August 2010, treated by the LFS software.

- ▶ Data `chapter02/EUVdelays/Data`
- ▶ Routine `chapter02/EUVdelays/PlotFigCompOrig.m`
- ▶ Figure `chapter02/EUVdelays/CompWF1.ai`

Figure 2.6

Lewenstein calculations from LFS, trajectory calculation in the routine.

- ▶ Data `chapter02/EUVdelays/Data`
- ▶ Routine `chapter02/EUVdelays/PlotLewenstein_Traj.m`
- ▶ Figure `chapter02/EUVdelays/EUV_Lewensteins.ai`

Figure 2.7

- ▶ Data chapter02/EUVdelays/Data
- ▶ Routine chapter02/EUVdelays/PlotFigCompShifted.m
- ▶ Figure chapter02/EUVdelays/CompWFSync.ai

Figure 2.8

- ▶ Data chapter02/keV/fields1248_I1E16cep05 (1).OPJ
- ▶ Figure chapter02/keVs/FracIon.ai

Figure 2.9

- ▶ Data chapter02/keV/fields1248_I1E16cep05 (1).OPJ
- ▶ Figure chapter02/keVs/Generation.ai

Figure 2.10

- ▶ Data chapter02/keV/fields1248_I1E16cep05 (1).OPJ
- ▶ Figure chapter02/keVs/RisephotonEnergy.ai

Figure 2.11

- ▶ Data chapter02/keV/nsp(t)_80%cutoff.OPJ
- ▶ Figure chapter02/keVs/AsPulses.ai

Figure 3.1

- ▶ Figure chapter03/Setup/beamline.ai

Figure 3.2

Raw data is measurement of the full beam profile in the focus as function of iris opening, and treated in Fullmatlab.mat

- ▶ Data chapter03/IntensityScaling/Data
- ▶ Routine chapter03/IntensityScaling/script_full.m
- ▶ Figure chapter03/IntensityScaling/IntensityScaling.ai

Figure 3.3

Before modification measured on the 17th of April 2012, after on the 18th of June 2012.

- ▶ Data chapter03/ReductionAngle/Data
- ▶ Routine chapter03/ReductionAngle/treatment.m
- ▶ Figure chapter03/ReductionAngle/ProfilesChannels.ai

Figure 3.4

- ▶ Data `chapter03/XUVMultilayers/Data`
- ▶ Routine `chapter03/XUVMultilayers/XUVMultilayers.m`
- ▶ Figure `chapter03/XUVMultilayers/XUVMultilayers.ai`

Figure 3.5

- ▶ Data `chapter03/ReflectivityRhodium/Data`
- ▶ Routine `chapter03/ReflectivityRhodium/Reflectivities.m`
- ▶ Figure `chapter03/ReflectivityRhodium/DoubleRhReflector.ai`

Figure 3.6

- ▶ Data `chapter03/EfficiencyMcPherson/Data`
- ▶ Origin file `chapter03/EfficiencyMcPherson/EfficiencyMcPh.opj`
- ▶ Figure `chapter03/EfficiencyMcPherson/McPherson_efficiency.ai`

Figure 3.7

- ▶ Data `chapter03/InterfSetup/DataCCD/Fringes2D.txt`
- ▶ Routine `chapter03/InterfSetup/PlotFringes.m`
- ▶ Figure `chapter03/InterfSetup/Setup3d_2.ai`

Figure 3.8

- ▶ Data `chapter03/Extraction+calib/Data`
- ▶ Routine `chapter03/Extraction+calib/PlotNumerics.m`
- ▶ Figure `chapter03/Extraction+calib/dataNumerics.ai`

Figure 3.9

- ▶ Data `chapter03/Stability/Data/201307314pm.txt`
- ▶ Routine `chapter03/Stability/PlotDataLT2.m`
- ▶ Figure `chapter03/Stability/DataLT2.ai`

Figure 3.10

- ▶ Data `chapter03/DataScience/Data`
- ▶ Routine `chapter03/DataScience/PlotDataScience.m`
- ▶ Figure `chapter03/DataScience/DataScience.ai`

Figure 3.11

- ▶ Data `chapter03/Crossco/Data/matlab_ws.mat`
- ▶ Routine `chapter03/DataScience/PlotGraph.m`

► Figure `chapter03/DataScience/CrossCo.ai`

Figure 3.12

Calculation done in the Labview vi `PropagFresnel_slab.vi`.

► Calculated Data `chapter03/PropagationFresnel/DataForPlot`
 ► Dispersion Data `chapter03/PropagationFresnel/MediaDispersions Folder`
 ► Calculation `chapter03/PropagationFresnel/PropagFresnel_slab.vi`
 ► Calculation `chapter03/PropagationFresnel/Plot.m`
 ► Figure `chapter03/PropagationFresnel/PropagFresnel.ai`

Figure 4.1

► Figure `chapter04/Ionization/Ionization_regimes.ai`

Figure 4.2

► Figure `chapter04/DoubleIonization/Double_ionization.ai`

Figure 4.3

Calculation done in the Labview LFS.vi, ionization tab, and data saved in the figure folder, compiled with `FigADK.m`

► Data `chapter04/ADKIonization/Single`
`chapter04/ADKIonization/DoubleLow`
 ► Routine `chapter04/ADKIonization/FigADK.m`
 ► Figure `chapter04/ADKIonization/ADK.ai`

Figure 4.4

► Figure `chapter04/Energydiagram/KrIonIIEnergyDiag.ai`

Figure 4.5

Adapted from [3], data and routines to be found in the relevant archive folder.

► Figure `chapter04/ATASKrII/ATASKrII.ai`

Figure 4.6

Adapted from [3], data and routines to be found in the relevant archive folder.

► Figure `chapter04/COMKrII/COMKrII.ai`

Figure 4.7

► Figure `chapter04/3levelsScheme/3levScheme.ai`

Figure 4.8

Adapted from [3], calculation routines found in the relevant archive folder.

- ▶ Data `chapter04/3levels_ATAS/MapSFI_SOM`
- ▶ Routine `chapter04/3levels_ATAS/Plot.m`
- ▶ Figure `chapter04/3levels_ATAS/3levelsATAS.ai`

Figure 4.9

Adapted from [3], calculation routines found in the relevant archive folder.

- ▶ Figure `chapter04/ValidityLor/ValidityLor.ai`

Figure 4.10

Adapted from [3], data and routines found in the relevant archive folder.

- ▶ Figure `chapter04/IonizationGate/IonGate.ai`

Figure 4.11

Data from collaboration with S. Pabst. For the simulation code contact him directly.

- ▶ Data `chapter04/NeutralPol`
- ▶ Routine `chapter04/NeutralPol/FigNeutralPol.m`
- ▶ Figure `chapter04/NeutralPol/NeutralPol.ai`

Figure 4.12

- ▶ Figure `chapter04/Energydiagram/KrIonII+IIIEnergyDiag.ai`

Figure 4.13

- ▶ Data `chapter04/DoubleIon/Data170612_2`
- ▶ Routine `chapter04/DoubleIon/PLOT.m`
- ▶ Figure `chapter04/DoubleIon/KrIIDI_spectrograms.ai`

Figure 4.14

- ▶ Data `chapter04/DoubleIon/Data170612_2`
- ▶ Routine `chapter04/DoubleIon/PLOT.m`
- ▶ Figure `chapter04/DoubleIon/KrIIDI_Pops2.pdf`

Figure 4.15

- ▶ Data `chapter04/DoubleIon/Data170612_2`
- ▶ Routine `chapter04/DoubleIon/PLOT.m`

► Figure `chapter04/DoubleIon/KrIII_Pol2.pdf`

Figure 5.1

► Figure `chapter05/Gating/GatingIntuitive2.ai`

Figure 5.2

► Figure `chapter05/Gating/GatingInst.ai`

Figure 5.2

► Routine `chapter05/Gating/Gating.m`

► Figure `chapter05/Gating/GatingInst.ai`

Figure 5.3

► Routine `chapter05/Gating/Gating.m`

► Figure `chapter05/Gating/Maps_Inst_Axes.ai`

Figure 5.4

► Routine `chapter05/Gating/GatingInstVSField.m`

► Figure `chapter05/Gating/InstVSField2.ai`

Figure 5.5

► Routine `chapter05/Gating/GatingFieldVaryingT.m`

► Figure `chapter05/Gating/Maps_FieldGateVariableT.ai`

Figure 5.6

► Data measured `chapter05/KrAbs/Kr Energy diagram`

► Data COWAN `chapter05/KrAbs/KrI3d9_np.spec`

► Data TDCIS `chapter05/KrAbs/res.cs-xuv.MB.dat`

► Routine `chapter05/KrAbs/KrAbsorption.m`

► Figure `chapter05/KrAbs/KrAbs_alt2.ai`

Figure 5.7

► Data TDCIS `chapter05/TDCISspectrogram/TDCIS_Res220meV`

► Routine `chapter05/TDCISspectrogram/PLOTKrTDCISSpectrogram.m`

► Figure `chapter05/TDCISspectrogram/KrTDCIS.ai`

Figure 5.8

- ▶ Data fit `chapter05/ODFreeKrStefan`
- ▶ Fitting Routine In the main analyzer VI
- ▶ Plotting Routine `chapter05/ODFreeKrStefan/FigResolutionStefan.m`
- ▶ Figure `chapter05/ODFreeKrStefan/Resolution.ai`

Figure 5.9

- ▶ Raw data In the raw data folder, Stefan1E13
- ▶ Data fit `chapter05/Fits/TDCIS/Stefan1E13forplotting`
- ▶ Fitting Routine In the main analyzer VI
- ▶ Plotting Routine `chapter05/Fits/TDCIS/PLOTStefanFitForFigure.m`
- ▶ Figure `chapter05/Fits/TDCIS/TDCIS_Inst.ai`

Figure 5.10

- ▶ Raw data In the raw data folder, Stefan1E13
- ▶ Data fit `chapter05/Fits/TDCIS/3taus_BG0145_fullwindow.mat`
- ▶ Fitting Routine `chapter05/Fits/TDCIS/AttoTemporalGatingnorm_full.m`
- ▶ Plotting Routine `chapter05/Fits/TDCIS/PLOTStefanFitForFigure.m`
- ▶ Figure `chapter05/Fits/TDCIS/TDCIS_FieldGate.ai`

Figure 5.11

- ▶ Raw data In the raw data folder, Stefan1E13Long
- ▶ Data fit `chapter05/Fits/TDCISLongPulse/Fit3lines`
- ▶ Fitting Routine In the main analyzer VI
- ▶ Plotting Routine `chapter05/Fits/TDCISLongPulse/PLOTStefanFitForFigure.m`
- ▶ Figure `chapter05/Fits/TDCISLongPulse/TDCIS_LongPulse.ai`

Figure 5.12

- ▶ Raw Data In the raw data folder, 20140219
- ▶ Data plot `chapter05/ExperimentalSpectrogram/20140219`
- ▶ Plotting Routine `chapter05/ExperimentalSpectrogram/PLOTKrExpSpectrogram.m`
- ▶ Figure `chapter05/ExperimentalSpectrogram/Kr_spectrogram.ai`

Figure 5.13

- ▶ Raw data In the raw data folder, 20140219
- ▶ Data fit `chapter05/Fits/Experiment/Fit2Plot_20140219`
- ▶ Fitting Routine In the main analyzer VI
- ▶ Plotting Routine `chapter05/Fits/Experiment/PLOTKrFitForFigure.m`
- ▶ Figure `chapter05/Fits/Experiment/Exp_Inst.ai`

Figure 5.14

- ▶ Raw data In the raw data folder, 20130320
- ▶ Plotting Routine chapter05/HighIntensity/Plot.m
- ▶ Figure chapter05/HighIntensity/HighIntScandiff2.ai

Figure 6.1

- ▶ Figure chapter06/XAS/Principle.ai

Figure 6.2

- ▶ Data AS-1 chapter06/Synchrotron/Fits/OD20140515_3
- ▶ Data Synchrotron chapter06/Synchrotron
- ▶ Fitting routine chapter06/Synchrotron/VIsFit/FitSynchrotron.vi
- ▶ Plotting routine chapter06/Synchrotron/Extraction.m
- ▶ Figure chapter06/Synchrotron/XANESSio2.ai

Figure 6.3

- ▶ Data Wien2k chapter06/SiO2bandstructure/BandStructureSiO2_Data
- ▶ Figure chapter06/SiO2bandstructure/BandStructureDOS.ai

Figure 6.4

- ▶ Data Synchrotron chapter06/Synchrotron
- ▶ Fitting routine chapter06/Synchrotron/Extraction.m
- ▶ Figure chapter06/Synchrotron/Cristallinity.ai

Figure 6.5

- ▶ Data chapter06/SiO2Spectrogram/20140515_3
- ▶ Plotting routine chapter06/SiO2Spectrogram/PL0TSiO2Spectrogram.m
- ▶ Figure chapter06/SiO2Spectrogram/SiO2.ai

Figure 6.6

- ▶ Data chapter06/SiO2Spectrogram/20140515_3
- ▶ Plotting routine chapter06/SiO2Spectrogram/PL0TSiO2Spectrogram.m
- ▶ Figure chapter06/SiO2Spectrogram/RiseTime.pdf

Figure 6.7

- ▶ Data chapter06/SiO2Spectrogram/20140515_3_Fit3linesFromSynchFitThesis
- ▶ Plotting routine chapter06/FitSiO2Inst/PL0TSiO2FitForFigure.m
- ▶ Figure chapter06/FitSiO2Inst/SiO2FitInst.ai

Figure 6.8

- ▶ Data Wien2k `chapter06/SiO2bandstructure/BandStructureSiO2_Data`
- ▶ Plotting routine `chapter06/FitSiO2Inst/PlotBandStructure.m`
- ▶ Figure `chapter06/SiO2bandstructure/BandStructureSiO2_Data/Model6levels.ai`

Figure 6.9

- ▶ Fit Data `chapter06/FitAPSSSiO2Nlevels/6levelsfullfinal`
- ▶ Plotting routine `chapter06/FitAPSSSiO2Nlevels/PLOTFigures.m`
- ▶ Figure `chapter06/FitAPSSSiO2Nlevels/6levelsfullfinal.ai`

Figure 6.10

- ▶ Data `chapter06/IntensityScaling/20140518`
- ▶ Plotting routine `chapter06/IntensityScaling/DataExtractPlot.m`
- ▶ Figure `chapter06/IntensityScaling/scaling.ai`

Figure 6.11

- ▶ Calculation `chapter06/IntensityScalingNlevelsfit/Nlevels.vi`
- ▶ Data `chapter06/IntensityScalingNlevelsfit/6levelsFinal`
- ▶ Plotting routine `chapter06/IntensityScalingNlevelsfit/DataExtractPlot.m`
- ▶ Figure `chapter06/IntensityScalingNlevelsfit/scaling.ai`

Bibliography

- [1] M. Drescher, M. Hentschel, R. Kienberger, M. Uiberacker, V. Yakovlev, A. Scrinzi, T. Westerwalbesloh, U. Kleineberg, and F. Krausz. Time-resolved atomic inner-shell spectroscopy. *Nature*, 419:803, 2002.
- [2] E. Goulielmakis, M. Uiberacker, R. Kienberger, A. Baltuska, V. Yakovlev, A. Scrinzi, T. Westerwalbesloh, U. Kleineberg, U. Heinzmann, M. Drescher, and F. Krausz. Direct measurement of light waves. *Science*, 305(5688):1267–1269, 2004. URL: <http://www.sciencemag.org/content/305/5688/1267.abstract>, arXiv:<http://www.sciencemag.org/content/305/5688/1267.full.pdf>.
- [3] A. Wirth, M. T. Hassan, I. Grguraš, J. Gagnon, A. Moulet, T. T. Luu, S. Pabst, R. Santra, Z. A. Alahmed, A. M. Azzeer, V. S. Yakovlev, V. Pervak, F. Krausz, and E. Goulielmakis. Synthesized light transients. *Science*, 334(6053):195–200, 2011. URL: <http://www.sciencemag.org/content/334/6053/195.abstract>, arXiv:<http://www.sciencemag.org/content/334/6053/195.full.pdf>.
- [4] M. T. Hassan, T. T. Luu, A. Moulet, O. Raskazovskaya, P. Zhokhov, M. Garg, N. Karpowicz, A. M. Zheltikov, V. Pervak, F. Krausz, and E. Goulielmakis. Attosecond optical control of bound electrons. *in preparation*, 2015.
- [5] W. H. Wollaston. A method of examining refractive and dispersive powers, by prismatic reflection. *Philosophical Transactions of the Royal Society of London*, 92:365–380, 1802. URL: <http://rstl.royalsocietypublishing.org/content/92/365.short>, arXiv:<http://rstl.royalsocietypublishing.org/content/92/365.full.pdf+html>.
- [6] J. Fraunhofer. Bestimmung des brechungs- und des farbenzerstreungs-vermögens verschiedener glasarten, in bezug auf die vervollkommnung achromatischer fernrhre. *Denkschriften der Mnch. Akademie der Wissenschaften*, 5(197), 1817.
- [7] L. Foucault. *L’Institut, (1re section); Socit Philomatique de Paris. Extraits des procs verbaux des sances pendant l’anne 1849*, 17(44):16–20, 1849.
- [8] G. Kirchhoff. Ueber die fraunhofer’schen linien. *Annalen der Physik*, 185(1):148–150, 1860. URL: <http://dx.doi.org/10.1002/andp.18601850115>.
- [9] T. H. Maiman. Stimulated optical radiation in ruby. *Nature*, 187:493–494, 1960.
- [10] F. J. McClung and R. W. Hellwarth. Giant optical pulsations from ruby. *Appl. Opt.*, 1(S1):103–105, Jan 1962. URL: <http://ao.osa.org/abstract.cfm?URI=ao-1-101-103>.

- [11] A. J. DeMaria, D. A. Stetser, and H. Heynau. Self modelocking of lasers with saturable absorbers. *Applied Physics Letters*, 8(7):174–176, 1966. URL: <http://scitation.aip.org/content/aip/journal/apl/8/7/10.1063/1.1754541>.
- [12] T. W. Hänsch, I. S. Shahin, and A. L. Schawlow. High-resolution saturation spectroscopy of the sodium d lines with a pulsed tunable dye laser. *Phys. Rev. Lett.*, 27:707–710, Sep 1971. URL: <http://link.aps.org/doi/10.1103/PhysRevLett.27.707>.
- [13] T. W. Hänsch, S. A. Lee, R. Wallenstein, and C. Wieman. Doppler-free two-photon spectroscopy of hydrogen $1s - 2s$. *Phys. Rev. Lett.*, 34:307–309, 1975. URL: <http://link.aps.org/doi/10.1103/PhysRevLett.34.307>.
- [14] M. Niering, R. Holzwarth, J. Reichert, P. Pokasov, T. Udem, M. Weitz, T. W. Hänsch, P. Lemonde, G. Santarelli, M. Abgrall, P. Laurent, C. Salomon, and A. Clairon. Measurement of the hydrogen $1S-2S$ transition frequency by phase coherent comparison with a microwave cesium fountain clock. *Phys. Rev. Lett.*, 84:5496–5499, Jun 2000. URL: <http://link.aps.org/doi/10.1103/PhysRevLett.84.5496>.
- [15] S. H. Autler and C. H. Townes. Stark effect in rapidly varying fields. *Phys. Rev.*, 100:703–722, Oct 1955. URL: <http://link.aps.org/doi/10.1103/PhysRev.100.703>.
- [16] G. Porter. Flash photolysis and spectroscopy. a new method for the study of free radical reactions. *Proceedings of the Royal Society of London. Series A. Mathematical and Physical Sciences*, 200(1061):284–300, 1950. URL: <http://rspa.royalsocietypublishing.org/content/200/1061/284.abstract>, arXiv:<http://rspa.royalsocietypublishing.org/content/200/1061/284.full.pdf+html>.
- [17] R. G. W. Norrish and G. Porter. Spectroscopic studies of the hydrogen-oxygen explosion initiated by the flash photolysis of nitrogen dioxide. *Proceedings of the Royal Society of London. Series A. Mathematical and Physical Sciences*, 210(1103):439–460, 1952. URL: <http://rspa.royalsocietypublishing.org/content/210/1103/439.abstract>, arXiv:<http://rspa.royalsocietypublishing.org/content/210/1103/439.full.pdf+html>.
- [18] M. Eigen, G. Kurtze, and K. Tamm. Zum reaktionmechanismus der ultraschallabsorption in wssrigen elektrolytungen. *Z. Elektrochem. Ber. Bunsenges. Phys. Chem.*, 57(103), 1953.
- [19] M. Dantus, M. J. Rosker, and A. H. Zewail. Realtime femtosecond probing of transition states in chemical reactions. *The Journal of Chemical Physics*, 87(4):2395–2397, 1987. URL: <http://scitation.aip.org/content/aip/journal/jcp/87/4/10.1063/1.453122>.

- [20] T. S. Rose, M. J. Rosker, and A. H. Zewail. Femtosecond realtime observation of wave packet oscillations (resonance) in dissociation reactions. *The Journal of Chemical Physics*, 88(10):6672–6673, 1988. URL: <http://scitation.aip.org/content/aip/journal/jcp/88/10/10.1063/1.454408>.
- [21] C. Pellegrini. The history of x-ray free-electron lasers. *The European Physical Journal H*, 37(5):659–708, 2012. URL: <http://dx.doi.org/10.1140/epjh/e2012-20064-5>.
- [22] A. A. Sorokin, S. V. Bobashev, T. Feigl, K. Tiedtke, H. Wabnitz, and M. Richter. Photoelectric effect at ultrahigh intensities. *Phys. Rev. Lett.*, 99:213002, Nov 2007. URL: <http://link.aps.org/doi/10.1103/PhysRevLett.99.213002>.
- [23] L. Young, E. P. Kanter, B. Krässig, Y. Li, A. M. March, S. T. Pratt, R. Santra, S. H. Southworth, N. Rohringer, L. F. DiMauro, G. Doumy, C. A. Roedig, N. Berrah, L. Fang, M. Hoener, P. H. Bucksbaum, J. P. Cryan, S. Ghimire, J. M. Glowina, D. A. Reis, J. D. Bozek, C. Bostedt, and M. Messerschmidt. Femtosecond electronic response of atoms to ultra-intense x-rays. *Nature*, 466(7302):56–61, 07 2010. URL: <http://dx.doi.org/10.1038/nature09177>.
- [24] M. Meyer, D. Cubaynes, V. Richardson, J. T. Costello, P. Radcliffe, W. B. Li, S. Düsterer, S. Fritzsche, A. Mihelic, K. G. Papamihail, and P. Lambropoulos. Two-photon excitation and relaxation of the $3d-4d$ resonance in atomic kr. *Phys. Rev. Lett.*, 104:213001, May 2010. URL: <http://link.aps.org/doi/10.1103/PhysRevLett.104.213001>.
- [25] E. Saldin, E. Schneidmiller, and M. Yurkov. Statistical properties of radiation from {VUV} and x-ray free electron laser. *Optics Communications*, 148(46):383 – 403, 1998. URL: <http://www.sciencedirect.com/science/article/pii/S0030401897006706>.
- [26] M. Hentschel, R. Kienberger, C. Spielmann, G. A. Reider, N. Milosevic, T. Brabec, P. Corkum, U. Heinzmann, M. Drescher, and F. Krausz. Attosecond metrology. *Nature*, 414(6863):509–513, nov 2001. URL: <http://dx.doi.org/10.1038/35107000>.
- [27] P. Tzallas, D. Charalambidis, N. A. Papadogiannis, K. Witte, and G. D. Tsakiris. Direct observation of attosecond light bunching. *Nature*, 426:267–271, 2003.
- [28] E. Goulielmakis, Z.-H. Loh, A. Wirth, R. Santra, N. Rohringer, V. S. Yakovlev, S. Zherebtsov, T. Pfeifer, A. M. Azzeer, M. Kling, S. Leone, and F. Krausz. Real-time observation of valence electron motion. *Nature*, 466:739743, 2010.
- [29] C. Ott, A. Kaldun, P. Raith, K. Meyer, M. Laux, J. Evers, C. H. Keitel, C. H. Greene, and T. Pfeifer. Lorentz meets fano in spectral line shapes: A universal phase and its laser control. *Science*, 340(6133):716–720, 2013. URL: <http://www.sciencemag.org/content/340/6133/716.abstract>, arXiv:<http://www.sciencemag.org/content/340/6133/716.full.pdf>.

- [30] M. Schultze, E. M. Bothschafter, A. Sommer, S. Holzner, W. Schweinberger, M. Fiess, M. Hofstetter, R. Kienberger, V. Apalkov, V. S. Yakovlev, M. I. Stockman, and F. Krausz. Controlling dielectrics with the electric field of light. *Nature*, 493(7430):75–78, 01 2013. URL: <http://dx.doi.org/10.1038/nature11720>.
- [31] C. A. Schmuttenmaer. Exploring dynamics in the far-infrared with terahertz spectroscopy. *Chemical Reviews*, 104(4):1759–1780, 2004. PMID: 15080711. URL: <http://pubs.acs.org/doi/abs/10.1021/cr020685g>, arXiv:<http://pubs.acs.org/doi/pdf/10.1021/cr020685g>.
- [32] E. Goulielmakis, M. Schultze, M. Hofstetter, V. S. Yakovlev, J. Gagnon, M. Uiberacker, A. L. Aquila, E. M. Gullikson, D. T. Attwood, R. Kienberger, F. Krausz, and U. Kleineberg. Single-cycle nonlinear optics. *Science*, 320(5883):1614–1617, 2008.
- [33] S. E. Harris and A. V. Sokolov. Subfemtosecond pulse generation by molecular modulation. *Phys. Rev. Lett.*, 81:2894–2897, Oct 1998. URL: <http://link.aps.org/doi/10.1103/PhysRevLett.81.2894>.
- [34] H.-S. Chan, Z.-M. Hsieh, W.-H. Liang, A. H. Kung, C.-K. Lee, C.-J. Lai, R.-P. Pan, and L.-H. Peng. Synthesis and measurement of ultrafast waveforms from five discrete optical harmonics. *Science*, 331(6021):1165–1168, 2011. URL: <http://www.sciencemag.org/content/331/6021/1165.abstract>, arXiv:<http://www.sciencemag.org/content/331/6021/1165.full.pdf>.
- [35] S.-W. Huang, G. Cirimi, J. Moses, K.-H. Hong, S. Bhardwaj, J. R. Birge, L.-J. Chen, E. Li, B. J. Eggleton, G. Cerullo, and F. X. Kartner. High-energy pulse synthesis with sub-cycle waveform control for strong-field physics. *Nat Photon*, 5(8):475–479, August 2011. URL: <http://dx.doi.org/10.1038/nphoton.2011.140>.
- [36] C. Manzoni, S.-W. Huang, G. Cirimi, P. Farinello, J. Moses, F. X. Kärtner, and G. Cerullo. Coherent synthesis of ultra-broadband optical parametric amplifiers. *Opt. Lett.*, 37(11):1880–1882, Jun 2012. URL: <http://ol.osa.org/abstract.cfm?URI=ol-37-11-1880>.
- [37] M. Nisoli, S. D. Silvestri, O. Svelto, R. Szipöcs, K. Ferencz, C. Spielmann, S. Sartania, and F. Krausz. Compression of high-energy laser pulses below 5 fs. *Opt. Lett.*, 22(8):522–524, Apr 1997. URL: <http://ol.osa.org/abstract.cfm?URI=ol-22-8-522>.
- [38] D. Strickland and G. Mourou. Compression of amplified chirped optical pulses. *Optics Communications*, 56(3):219 – 221, 1985. URL: <http://www.sciencedirect.com/science/article/pii/0030401885901208>.
- [39] T. Fuji, J. Rauschenberger, C. Gohle, A. Apolonski, T. Udem, V. S. Yakovlev, G. Tempea, T. W. Hensch, and F. Krausz. Attosecond control of optical waveforms. *New Journal of Physics*, 7(1):116, 2005. URL: <http://stacks.iop.org/1367-2630/7/i=1/a=116>.

- [40] P. Tournois. Acousto-optic programmable dispersive filter for adaptive compensation of group delay time dispersion in laser systems. *Optics Communications*, 140(46):245–249, August 1997. URL: <http://www.sciencedirect.com/science/article/pii/S0030401897001533>.
- [41] F. Verluise, V. Laude, J.-P. Huignard, P. Tournois, and A. Migus. Arbitrary dispersion control of ultrashort optical pulses with acoustic waves. *J. Opt. Soc. Am. B*, 17(1):138–145, Jan 2000. URL: <http://josab.osa.org/abstract.cfm?URI=josab-17-1-138>.
- [42] D. F. Hotz. Gain narrowing in a laser amplifier. *Appl. Opt.*, 4(5):527–530, May 1965. URL: <http://ao.osa.org/abstract.cfm?URI=ao-4-5-527>.
- [43] T. Brabec and F. Krausz. Intense few-cycle laser fields: Frontiers of nonlinear optics. *Review of Modern Physics*, 72:545–591, 2000.
- [44] A. M. Zheltikov. Let there be white light: supercontinuum generation by ultrashort laser pulses. *Physics-Uspekhi*, 49(6):605, 2006. URL: <http://stacks.iop.org/1063-7869/49/i=6/a=R04>.
- [45] A. M. Weiner. *Ultrafast Optics*. Wiley, New Jersey, 2009.
- [46] T. Oksenhendler, S. Coudreau, N. Forget, V. Crozatier, S. Grabielle, R. Herzog, O. Gobert, and D. Kaplan. Self-referenced spectral interferometry. *Applied Physics B*, 99(1-2):7–12, 2010. URL: <http://dx.doi.org/10.1007/s00340-010-3916-y>.
- [47] A. Moulet, S. Grabielle, C. Cornaggia, N. Forget, and T. Oksenhendler. Single-shot, high-dynamic-range measurement of sub-15 fs pulses by self-referenced spectral interferometry. *Opt. Lett.*, 35(22):3856–3858, Nov 2010. URL: <http://ol.osa.org/abstract.cfm?URI=ol-35-22-3856>.
- [48] M. T. Hassan. *Synthesis and Control of Attosecond Light Transients*. PhD thesis, Ludwig-Maximilians-Universität, München, 2011.
- [49] R. Szipöcs, C. Spielmann, F. Krausz, and K. Ferencz. Chirped multilayer coatings for broadband dispersion control in femtosecond lasers. *Opt. Lett.*, 19(3):201–203, Feb 1994. URL: <http://ol.osa.org/abstract.cfm?URI=ol-19-3-201>.
- [50] V. Pervak, A. Tikhonravov, M. Trubetskov, S. Naumov, F. Krausz, and A. Apolonski. 1.5-octave chirped mirror for pulse compression down to sub-3 fs. *Applied Physics B*, 87(1):5–12, 2007. URL: <http://dx.doi.org/10.1007/s00340-006-2467-8>.
- [51] M. T. Hassan, A. Wirth, I. Grguraš, A. Moulet, T. T. Luu, J. Gagnon, V. Pervak, and E. Goulielmakis. Invited article: Attosecond photonics: Synthesis and control of light transients. *Review of Scientific Instruments*, 83(11):111301, 2012. URL: <http://link.aip.org/link/?RSI/83/111301/1>.

- [52] M. Schultze, A. Wirth, I. Grguras, M. Uiberacker, T. Uphues, A. Verhoef, J. Gagnon, M. Hofstetter, U. Kleineberg, E. Goulielmakis, and F. Krausz. State-of-the-art attosecond metrology. *Journal of Electron Spectroscopy and Related Phenomena*, 184(36):68 – 77, 2011. Advances in Vacuum Ultraviolet and X-ray Physics The 37th International Conference on Vacuum Ultraviolet and X-ray Physics (VUVX2010). URL: <http://www.sciencedirect.com/science/article/pii/S0368204811000090>.
- [53] J. Itatani, F. Quéré, G. L. Yudin, M. Y. Ivanov, F. Krausz, and P. B. Corkum. Attosecond streak camera. *Phys. Rev. Lett.*, 88:173903, 2002.
- [54] M. Kitzler, N. Milosevic, A. Scrinzi, F. Krausz, and T. Brabec. Quantum theory of attosecond xuv pulse measurement by laser dressed photoionization. *Phys. Rev. Lett.*, 88:173904, Apr 2002. URL: <http://link.aps.org/doi/10.1103/PhysRevLett.88.173904>.
- [55] Y. Mairesse and F. Quéré. Frequency-resolved optical gating for complete reconstruction of attosecond bursts. *Phys. Rev. A*, 71(1):011401, Jan 2005.
- [56] J. Gagnon, E. Goulielmakis, and V. Yakovlev. The accurate frog characterization of attosecond pulses from streaking measurements. *Applied Physics B*, 92(1):25–32, 2008. URL: <http://dx.doi.org/10.1007/s00340-008-3063-x>.
- [57] V. S. Yakovlev, J. Gagnon, N. Karpowicz, and F. Krausz. Attosecond streaking enables the measurement of quantum phase. *Phys. Rev. Lett.*, 105:073001, Aug 2010. URL: <http://link.aps.org/doi/10.1103/PhysRevLett.105.073001>.
- [58] V. Vénierard, R. Taïeb, and A. Maquet. Phase dependence of ($N + 1$)-color (N greater than 1) ir-uv photoionization of atoms with higher harmonics. *Phys. Rev. A*, 54:721–728, Jul 1996.
- [59] P. M. Paul, E. S. Toma, P. Breger, G. Mullot, F. Augé, P. Balcou, H. G. Muller, and P. Agostini. Observation of a train of attosecond pulses from high harmonic generation. *Science*, 292(5522):1689–1692, 2001. URL: <http://www.sciencemag.org/content/292/5522/1689.abstract>, arXiv:<http://www.sciencemag.org/content/292/5522/1689.full.pdf>.
- [60] H. G. Muller. Reconstruction of attosecond harmonic beating by interference of two-photon transitions. *Appl. Phys. B*, 74:S17–S21, 2002.
- [61] J. Gagnon and V. Yakovlev. The direct evaluation of attosecond chirp from a streaking measurement. *Applied Physics B*, 103(2):303–309, 2011. URL: <http://dx.doi.org/10.1007/s00340-010-4358-2>.
- [62] T. T. Luu. ?? PhD thesis, Ludwig-Maximilians-Universität, München, 2014.

- [63] T. T. L. et. al. ?? ??, ??:??, ?? submitted.
- [64] M. Ferray, A. L'Huillier, X. F. Li, L. A. Lompre, G. Mainfray, and C. Manus. Multiple-harmonic conversion of 1064 nm radiation in rare gases. *Journal of Physics B: Atomic, Molecular and Optical Physics*, 21(3):L31, 1988. URL: <http://stacks.iop.org/0953-4075/21/i=3/a=001>.
- [65] X. F. Li, A. L'Huillier, M. Ferray, L. A. Lompré, and G. Mainfray. Multiple-harmonic generation in rare gases at high laser intensity. *Phys. Rev. A*, 39:5751–5761, Jun 1989. URL: <http://link.aps.org/doi/10.1103/PhysRevA.39.5751>.
- [66] R. W. Boyd. *Nonlinear Optics, Third Edition*. Academic Press, Elsevier, 2008.
- [67] A. Wirth. *Attosecond Transient Absorption Spectroscopy*. PhD thesis, Ludwig-Maximilians-Universität, München, 2011.
- [68] F. Krausz and M. Ivanov. Attosecond physics. *Rev. Mod. Phys.*, 81:163–234, Feb 2009. URL: <http://link.aps.org/doi/10.1103/RevModPhys.81.163>.
- [69] F. Brunel. Harmonic generation due to plasma effects in a gas undergoing multi-photon ionization in the high-intensity limit. *J. Opt. Soc. Am. B*, 7(4):521–526, Apr 1990. URL: <http://josab.osa.org/abstract.cfm?URI=josab-7-4-521>.
- [70] P. B. Corkum. Plasma perspective on strong field multiphoton ionization. *Phys. Rev. Lett.*, 71:1994, 1993.
- [71] P. Ehrenfest. Bemerkung ber die angenherte gltigkeit der klassischen mechanik innerhalb der quantenmechanik. *Zeitschrift fr Physik*, 45(7-8):455–457, 1927. URL: <http://dx.doi.org/10.1007/BF01329203>.
- [72] M. Lewenstein, P. Balcou, M. Y. Ivanov, A. L'Huillier, and P. B. Corkum. Theory of high-harmonic generation by low-frequency laser fields. *Phys. Rev. A*, 49:2117–2132, 1994.
- [73] P. Antoine, A. L'Huillier, M. Lewenstein, P. Salières, and B. Carré. Theory of high-order harmonic generation by an elliptically polarized laser field. *Phys. Rev. A*, 53:1725–1745, Mar 1996. URL: <http://link.aps.org/doi/10.1103/PhysRevA.53.1725>.
- [74] M. Y. Ivanov, T. Brabec, and N. Burnett. Coulomb corrections and polarization effects in high-intensity high-harmonic emission. *Phys. Rev. A*, 54:742–745, Jul 1996. URL: <http://link.aps.org/doi/10.1103/PhysRevA.54.742>.
- [75] A. Scrinzi, M. Geissler, and T. Brabec. Ionization above the coulomb barrier. *Phys. Rev. Lett.*, 83:706–709, Jul 1999. URL: <http://link.aps.org/doi/10.1103/PhysRevLett.83.706>.

- [76] A. Scrinzi. *Private communication to Dr. Tosa.*
- [77] B. Henke, E. Gullikson, and J. Davis. X-ray interactions: Photoabsorption, scattering, transmission, and reflection at $e = 50\text{--}30,000$ eV, $z = 1\text{--}92$. *Atomic Data and Nuclear Data Tables*, 54(2):181 – 342, 1993. URL: <http://www.sciencedirect.com/science/article/pii/S0092640X83710132>.
- [78] I. J. Sola, E. Mevel, L. Elouga, E. Constant, V. Strelkov, L. Poletto, P. Villoresi, E. Benedetti, J.-P. Caumes, S. Stagira, C. Vozzi, G. Sansone, and M. Nisoli. Controlling attosecond electron dynamics by phase-stabilized polarization gating. *Nat Phys*, 2(5):319–322, May 2006. URL: <http://dx.doi.org/10.1038/nphys281>.
- [79] X. Feng, S. Gilbertson, H. Mashiko, H. Wang, S. D. Khan, M. Chini, Y. Wu, K. Zhao, and Z. Chang. Generation of isolated attosecond pulses with 20 to 28 femtosecond lasers. *Phys. Rev. Lett.*, 103:183901, Oct 2009. URL: <http://link.aps.org/doi/10.1103/PhysRevLett.103.183901>.
- [80] T. Pfeifer, A. Jullien, M. J. Abel, P. M. Nagel, L. Gallmann, D. M. Neumark, and S. R. Leone. Generating coherent broadband continuum soft-x-ray radiation by attosecond ionization gating. *Opt. Express*, 15(25):17120–17128, Dec 2007. URL: <http://www.opticsexpress.org/abstract.cfm?URI=oe-15-25-17120>.
- [81] G. Sansone, L. Poletto, and M. Nisoli. High-energy attosecond light sources. *Nat Photon*, 5(11):655–663, November 2011. URL: <http://dx.doi.org/10.1038/nphoton.2011.167>.
- [82] T. Popmintchev, M.-C. Chen, D. Popmintchev, P. Arpin, S. Brown, S. Aliauskas, G. Andriukaitis, T. Baliunas, O. D. Mcke, A. Pugzlys, A. Baltuka, B. Shim, S. E. Schrauth, A. Gaeta, C. Hernandez-Garcia, L. Plaja, A. Becker, A. Jaron-Becker, M. M. Murnane, and H. C. Kapteyn. Bright coherent ultrahigh harmonics in the keV x-ray regime from mid-infrared femtosecond lasers. *Science*, 336(6086):1287–1291, 2012. URL: <http://www.sciencemag.org/content/336/6086/1287.abstract>, arXiv: <http://www.sciencemag.org/content/336/6086/1287.full.pdf>.
- [83] L. E. Chipperfield, J. S. Robinson, J. W. G. Tisch, and J. P. Marangos. Ideal waveform to generate the maximum possible electron recollision energy for any given oscillation period. *Phys. Rev. Lett.*, 102:063003, Feb 2009. URL: <http://link.aps.org/doi/10.1103/PhysRevLett.102.063003>.
- [84] V. Tosa, C. Altucci, K. Kovacs, M. Negro, S. Stagira, C. Vozzi, and C. Velotta. Isolated attosecond pulse generation by two-mid-ir laser fields. *Selected Topics in Quantum Electronics, IEEE Journal of*, 18(1):239–247, Jan 2012.
- [85] E. Constant, D. Garzella, P. Breger, E. Mével, C. Dorrer, C. Le Blanc, F. Salin, and P. Agostini. Optimizing high harmonic generation in absorbing gases: Model and

- experiment. *Phys. Rev. Lett.*, 82:1668–1671, Feb 1999. URL: <http://link.aps.org/doi/10.1103/PhysRevLett.82.1668>.
- [86] F. Trager. *Springer Handbook of Lasers and Optics*. Springer New York, 2007. URL: <http://link.springer.com/referencework/10.1007/978-0-387-30420-5>.
- [87] W. R. Hunter. Optical constants of metals in the extreme ultraviolet. i. a modified critical-angle technique for measuring the index of refraction of metals in the extreme ultraviolet. *J. Opt. Soc. Am.*, 54(1):15–18, Jan 1964. URL: <http://www.opticsinfobase.org/abstract.cfm?URI=josa-54-1-15>.
- [88] L. A. S. A. Corporation). Vacuum ultraviolet reflection filter.
- [89] A.-S. Morlens, P. Balcou, P. Zeitoun, C. Valentin, V. Laude, and S. Kazamias. Compression of attosecond harmonic pulses by extreme-ultraviolet chirped mirrors. *Opt. Lett.*, 30(12):1554–1556, Jun 2005. URL: <http://ol.osa.org/abstract.cfm?URI=ol-30-12-1554>.
- [90] A. Wonisch, U. Neuhäusler, N. M. Kabachnik, T. Uphues, M. Uiberacker, V. Yakovlev, F. Krausz, M. Drescher, U. Kleineberg, and U. Heinzmann. Design, fabrication, and analysis of chirped multilayer mirrors for reflection of extreme-ultraviolet attosecond pulses. *Appl. Opt.*, 45(17):4147–4156, Jun 2006. URL: <http://ao.osa.org/abstract.cfm?URI=ao-45-17-4147>.
- [91] M. Suman, G. Monaco, M.-G. Pelizzo, D. L. Windt, and P. Nicolosi. Realization and characterization of an xuvmultilayer coating for attosecond pulses. *Opt. Express*, 17(10):7922–7932, May 2009. URL: <http://www.opticsexpress.org/abstract.cfm?URI=oe-17-10-7922>.
- [92] M. Hofstetter, M. Schultze, M. Fieß, B. Dennhardt, A. Guggenmos, J. Gagnon, V. S. Yakovlev, E. Goulielmakis, R. Kienberger, E. M. Gullikson, F. Krausz, and U. Kleineberg. Attosecond dispersion control by extreme ultraviolet multilayer mirrors. *Opt. Express*, 19(3):1767–1776, Jan 2011. URL: <http://www.opticsexpress.org/abstract.cfm?URI=oe-19-3-1767>.
- [93] M. Hofstetter, A. Aquila, M. Schultze, A. Guggenmos, S. Yang, E. Gullikson, M. Huth, B. Nickel, J. Gagnon, V. S. Yakovlev, E. Goulielmakis, F. Krausz, and U. Kleineberg. Lanthanummolybdenum multilayer mirrors for attosecond pulses between 80 and 130eV. *New Journal of Physics*, 13(6):063038, 2011. URL: <http://stacks.iop.org/1367-2630/13/i=6/a=063038>.
- [94] A. Guggenmos, R. Rauhut, M. Hofstetter, S. Hertrich, B. Nickel, J. Schmidt, E. M. Gullikson, M. Seibald, W. Schnick, and U. Kleineberg. Aperiodic crsc multilayer mirrors for attosecond water window pulses. *Opt. Express*, 21(19):21728–21740, Sep 2013. URL: <http://www.opticsexpress.org/abstract.cfm?URI=oe-21-19-21728>.

- [95] M. Fiess, M. Schultze, E. Goulielmakis, B. Dennhardt, J. Gagnon, M. Hofstetter, R. Kienberger, and F. Krausz. Versatile apparatus for attosecond metrology and spectroscopy. *Review of Scientific Instruments*, 81(9):093103, 2010. URL: <http://link.aip.org/link/?RSI/81/093103/1>.
- [96] C. Palmer. *Diffraction Grating Handbook, ed. 7*. Richardson Gratings, Newport Corporation, Rochester, NY, 2014.
- [97] J.-C. Diels and W. Rudolph. *Ultrashort Laser Pulse Phenomenon: Fundamentals, techniques and applications on a femtosecond time scale*. Academic Press, 2007.
- [98] I. H. MALITSON. Interspecimen comparison of the refractive index of fused silica. *J. Opt. Soc. Am.*, 55(10):1205–1208, Oct 1965. URL: <http://www.opticsinfobase.org/abstract.cfm?URI=josa-55-10-1205>.
- [99] L. Keldysh. Ionization in the field of a strong electromagnetic wave. *Soviet Physics JETP*, 20:1307, 1965.
- [100] V. S. Popov. Tunnel and multiphoton ionization of atoms and ions in a strong laser field (keldysh theory). *Physics-Uspekhi*, 47(9):855, 2004. URL: <http://stacks.iop.org/1063-7869/47/i=9/a=R01>.
- [101] P. Salières. Harmoniques d’ordre élevé et impulsions attosecondes. In *Réseau CNRS Femto Ecole des Houches 2009*, 2009. URL: http://reseau-femto.cnrs.fr/IMG/pdf/Houches2009_cours12-17.pdf.
- [102] A. Kramida, Yu. Ralchenko, J. Reader, and and NIST ASD Team. NIST Atomic Spectra Database (ver. 5.1), [Online]. Available: <http://physics.nist.gov/asd> [2014, July 31]. National Institute of Standards and Technology, Gaithersburg, MD., 2013.
- [103] M. V. Ammosov, N. B. Delone, and V. P. Krainov. Tunnel ionization of complex atoms and of atomic ions in an alternating electromagnetic field. *JETP*, 64:1191, 1986.
- [104] E. E. Serebryannikov, A. J. Verhoef, A. Mitrofanov, A. Baltuška, and A. M. Zheltikov. Signatures of attosecond electron tunneling dynamics in the evolution of intense few-cycle light pulses. *Phys. Rev. A*, 80:053809, Nov 2009. URL: <http://link.aps.org/doi/10.1103/PhysRevA.80.053809>.
- [105] R. Santra, R. W. Dunford, and L. Young. Spin-orbit effect on strong-field ionization of krypton. *Phys. Rev. A*, 74:043403, Oct 2006. URL: <http://link.aps.org/doi/10.1103/PhysRevA.74.043403>.
- [106] G. L. Yudin and M. Y. Ivanov. Nonadiabatic tunnel ionization: Looking inside a laser cycle. *Phys. Rev. A*, 64:013409, Jun 2001. URL: <http://link.aps.org/doi/10.1103/PhysRevA.64.013409>.

- [107] B. Walker, B. Sheehy, L. F. DiMauro, P. Agostini, K. J. Schafer, and K. C. Kulander. Precision measurement of strong field double ionization of helium. *Phys. Rev. Lett.*, 73:1227–1230, Aug 1994. URL: <http://link.aps.org/doi/10.1103/PhysRevLett.73.1227>.
- [108] R. Dörner, V. Mergel, O. Jagutzki, L. Spielberger, J. Ullrich, R. Moshhammer, and H. Schmidt-Böcking. Cold target recoil ion momentum spectroscopy: a momentum microscope to view atomic collision dynamics. *Physics Reports*, 330(23):95–192, June 2000. URL: <http://www.sciencedirect.com/science/article/pii/S037015739900109X>.
- [109] T. Weber, H. Giessen, M. Weckenbrock, G. Urbasch, A. Staudte, L. Spielberger, O. Jagutzki, V. Mergel, M. Vollmer, and R. Dorner. Correlated electron emission in multiphoton double ionization. *Nature*, 405(6787):658–661, June 2000. URL: <http://dx.doi.org/10.1038/35015033>.
- [110] W. Becker, X. Liu, P. J. Ho, and J. H. Eberly. Theories of photoelectron correlation in laser-driven multiple atomic ionization. *Rev. Mod. Phys.*, 84:1011–1043, Jul 2012. URL: <http://link.aps.org/doi/10.1103/RevModPhys.84.1011>.
- [111] U. Eichmann, M. Dörr, H. Maeda, W. Becker, and W. Sandner. Collective multielectron tunneling ionization in strong fields. *Phys. Rev. Lett.*, 84:3550–3553, Apr 2000. URL: <http://link.aps.org/doi/10.1103/PhysRevLett.84.3550>.
- [112] R. Santra, V. S. Yakovlev, T. Pfeifer, and Z.-H. Loh. Theory of attosecond transient absorption spectroscopy of strong-field-generated ions. *Phys. Rev. A*, 83:033405, Mar 2011. URL: <http://link.aps.org/doi/10.1103/PhysRevA.83.033405>.
- [113] M. Joffre. *Optique non-linéaire en régimes continu et femtoseconde*. 2014. URL: <https://www.enseignement.polytechnique.fr/profs/physique/Manuel.Joffre/onl/cours.pdf>.
- [114] P. Hamm. *Principles of Nonlinear Optical Spectroscopy: A Practical Approach, or Mukamel for Dummies*. 2005. URL: <http://www.mit.p.lodz.pl/evu/lectures/Hamm.pdf>.
- [115] S. Mukamel. *Principles of Nonlinear Optical Spectroscopy*. 1999.
- [116] R. Santra. Internal communication.
- [117] S. Pabst, A. Sytcheva, A. Moulet, A. Wirth, E. Goulielmakis, and R. Santra. Theory of attosecond transient-absorption spectroscopy of krypton for overlapping pump and probe pulses. *Physical Review A*, 86(6):063411, 2012.
- [118] L. Greenman, P. J. Ho, S. Pabst, E. Kamarchik, D. A. Mazziotti, and R. Santra. Implementation of the time-dependent configuration-interaction singles method for

- atomic strong-field processes. *Phys. Rev. A*, 82:023406, Aug 2010. URL: <http://link.aps.org/doi/10.1103/PhysRevA.82.023406>.
- [119] S. Pabst, L. Greenman, D. A. Mazziotti, and R. Santra. Impact of multichannel and multipole effects on the cooper minimum in the high-order-harmonic spectrum of argon. *Phys. Rev. A*, 85:023411, Feb 2012. URL: <http://link.aps.org/doi/10.1103/PhysRevA.85.023411>.
- [120] D. Kane. Real-time measurement of ultrashort laser pulses using principal component generalized projections. *Selected Topics in Quantum Electronics, IEEE Journal of*, 4(2):278–284, Mar 1998.
- [121] K. Codling and R. P. Madden. Optically observed inner shell electron excitation in neutral kr and xe. *Phys. Rev. Lett.*, 12:106–108, Jan 1964. URL: <http://link.aps.org/doi/10.1103/PhysRevLett.12.106>.
- [122] R. Cowan. *The Theory of Atomic Structure and Spectra*. Los Alamos Series in Basic and Applied Sciences. University of California Press, 1981. URL: <https://www.tcd.ie/Physics/people/Cormac.McGuinness/Cowan/>.
- [123] M. O. Krause. Atomic radiative and radiationless yields for k and l shells. *Journal of Physical and Chemical Reference Data*, 8(2):307–327, 1979. URL: <http://scitation.aip.org/content/aip/journal/jpcrd/8/2/10.1063/1.555594>.
- [124] G. C. King, M. Tronc, F. H. Read, and R. C. Bradford. An investigation of the structure near the l 2,3 edges of argon, the m 4,5 edges of krypton and the n 4,5 edges of xenon, using electron impact with high resolution. *Journal of Physics B: Atomic and Molecular Physics*, 10(12):2479, 1977. URL: <http://stacks.iop.org/0022-3700/10/i=12/a=026>.
- [125] O.-P. Sairanen, A. Kivimäki, E. Nömmiste, H. Aksela, and S. Aksela. High-resolution pre-edge structure in the inner-shell ionization threshold region of rare gases xe, kr, and ar. *Phys. Rev. A*, 54:2834–2839, Oct 1996. URL: <http://link.aps.org/doi/10.1103/PhysRevA.54.2834>.
- [126] M. Jurvansuu, A. Kivimäki, and S. Aksela. Inherent lifetime widths of ar $2p^{-1}$, kr $3d^{-1}$, xe $3d^{-1}$, and xe $4d^{-1}$ states. *Phys. Rev. A*, 64:012502, Jun 2001. URL: <http://link.aps.org/doi/10.1103/PhysRevA.64.012502>.
- [127] T. Uphues, M. Schultze, M. F. Kling, M. Uiberacker, S. Hendel, U. Heinzmann, N. M. Kabachnik, and M. Drescher. Ion-charge-state chronoscopy of cascaded atomic auger decay. *New Journal of Physics*, 10(2):025009, 2008. URL: <http://stacks.iop.org/1367-2630/10/i=2/a=025009>.
- [128] A. J. Verhoef, A. V. Mitrofanov, X. T. Nguyen, M. Krikunova, S. Fritzsche, N. M. Kabachnik, M. Drescher, and A. Baltuka. Time-and-energy-resolved measurement

- of auger cascades following kr 3d excitation by attosecond pulses. *New Journal of Physics*, 13(11):113003, 2011. URL: <http://stacks.iop.org/1367-2630/13/i=11/a=113003>.
- [129] T. Mazza, K. G. Papamihail, P. Radcliffe, W. B. Li, T. J. Kelly, J. T. Costello, S. Dsterer, P. Lambropoulos, and M. Meyer. Controlling core hole relaxation dynamics via intense optical fields. *Journal of Physics B: Atomic, Molecular and Optical Physics*, 45(14):141001, 2012. URL: <http://stacks.iop.org/0953-4075/45/i=14/a=141001>.
- [130] F. K. Richtmyer, S. W. Barnes, and E. Ramberg. The widths of the l -series lines and of the energy levels of au(79). *Phys. Rev.*, 46:843–860, Nov 1934. URL: <http://link.aps.org/doi/10.1103/PhysRev.46.843>.
- [131] L. G. Parratt. X-ray resonance absorption lines in the argon k spectrum. *Phys. Rev.*, 56:295–297, Aug 1939. URL: <http://link.aps.org/doi/10.1103/PhysRev.56.295>.
- [132] M. J. Bedzyk and G. Materlik. Electron-energy-loss x-ray absorption spectroscopy: A nondestructive structural-depth microprobe. *Phys. Rev. B*, 32:4228–4231, Sep 1985. URL: <http://link.aps.org/doi/10.1103/PhysRevB.32.4228>.
- [133] M. Chini, B. Zhao, H. Wang, Y. Cheng, S. X. Hu, and Z. Chang. Subcycle ac stark shift of helium excited states probed with isolated attosecond pulses. *Phys. Rev. Lett.*, 109:073601, Aug 2012.
- [134] F. C. Brown, R. Z. Bachrach, and M. Skibowski. $L_{2,3}$ threshold spectra of doped silicon and silicon compounds. *Phys. Rev. B*, 15:4781–4788, May 1977. URL: <http://link.aps.org/doi/10.1103/PhysRevB.15.4781>.
- [135] J. Penner-Hahn. 2.13 - x-ray absorption spectroscopy. In J. A. McCleverty and T. J. Meyer, editors, *Comprehensive Coordination Chemistry {II}*, pages 159 – 186. Pergamon, Oxford, 2003. URL: <http://www.sciencedirect.com/science/article/pii/B008043748601063X>.
- [136] G. S. Henderson, F. M. de Groot, and B. J. Moulton. X-ray absorption near-edge structure (xanes) spectroscopy. *Reviews in Mineralogy and Geochemistry*, 78(1):75–138, 2014. URL: <http://ring.geoscienceworld.org/content/78/1/75.short>, arXiv:<http://ring.geoscienceworld.org/content/78/1/75.full.pdf+html>.
- [137] E. A. Stern, D. E. Sayers, and F. W. Lytle. Extended x-ray-absorption fine-structure technique. iii. determination of physical parameters. *Phys. Rev. B*, 11:4836–4846, Jun 1975. URL: <http://link.aps.org/doi/10.1103/PhysRevB.11.4836>.
- [138] J. A. Kirby, D. B. Goodin, T. Wydrzynski, A. S. Robertson, and M. P. Klein. State of manganese in the photosynthetic apparatus. 2. x-ray absorption edge studies on

- manganese in photosynthetic membrane. *Journal of the American Chemical Society*, 103(18):5537–5542, 1981. URL: <http://pubs.acs.org/doi/abs/10.1021/ja00408a043>, arXiv:<http://pubs.acs.org/doi/pdf/10.1021/ja00408a043>.
- [139] C. Gähwiller and F. C. Brown. Photoabsorption near the $L_{II,III}$ edge of silicon and aluminum. *Phys. Rev. B*, 2:1918–1925, Sep 1970. URL: <http://link.aps.org/doi/10.1103/PhysRevB.2.1918>.
- [140] F. C. Brown, R. Z. Bachrach, and M. Skibowski. $L_{2,3}$ threshold spectra of doped silicon and silicon compounds. *Phys. Rev. B*, 15:4781–4788, May 1977. URL: <http://link.aps.org/doi/10.1103/PhysRevB.15.4781>.
- [141] F. Herman and S. Skillman. *Atomic structure calculations*. Prentice-Hall, 1963.
- [142] W. Hayes and F. C. Brown. Absorption by some molecular gases in the extreme ultraviolet. *Phys. Rev. A*, 6:21–30, Jul 1972. URL: <http://link.aps.org/doi/10.1103/PhysRevA.6.21>.
- [143] G. R. Harp, Z.-L. Han, and B. P. Tonner. Spatially-resolved x-ray absorption near-edge spectroscopy of silicon in thin silicon-oxide films. *Physica Scripta*, 1990(T31):23, 1990. URL: <http://stacks.iop.org/1402-4896/1990/i=T31/a=003>.
- [144] D. Li, G. M. Bancroft, M. Kasrai, M. E. Fleet, R. A. Secco, X. H. Feng, K. H. Tan, and B. X. Yang. X-ray absorption spectroscopy of silicon dioxide (sio 2) polymorphs; the structural characterization of opal. *American Mineralogist*, 79(7-8):622–632, 1994. URL: <http://ammin.geoscienceworld.org/content/79/7-8/622.short>.
- [145] C. D. Wagner, D. E. Passoja, H. F. Hillery, T. G. Kinisky, H. A. Six, W. T. Jansen, and J. A. Taylor. Auger and photoelectron line energy relationships in aluminum-oxygen and siliconoxygen compounds. *Journal of Vacuum Science and Technology*, 21(4):933–944, 1982. URL: <http://scitation.aip.org/content/avs/journal/jvst/21/4/10.1116/1.571870>.
- [146] X. Weng, P. Rez, and O. F. Sankey. Pseudo-atomic-orbital band theory applied to electron-energy-loss near-edge structures. *Phys. Rev. B*, 40:5694–5704, Sep 1989. URL: <http://link.aps.org/doi/10.1103/PhysRevB.40.5694>.
- [147] P. Blaha, K. Schwarz, G. Madsen, D. Kvasnicka, and J. Luitz. Wien2k, an augmented plane wave + local orbitals program for calculating crystal properties. (*Karlheinz Schwarz, Techn. Universitt Wien, Austria*), ISBN 3-9501031-1-2, 2001. URL: <http://www.wien2k.at/>.
- [148] G. Duscher, R. Buczko, S. Pennycook, and S. Pantelides. Core-hole effects on energy-loss near-edge structure. *Ultramicroscopy*, 86(34):355 – 362, 2001. International Symposium on Spectroscopy of Materials. URL: <http://www.sciencedirect.com/science/article/pii/S0304399100001261>.

-
- [149] G. R. Harp, D. K. Saldin, and B. P. Tonner. Finite-size effects and short-range crystalline order in si and sio2 studied by x-ray absorption fine structure spectroscopy. *Journal of Physics: Condensed Matter*, 5(31):5377, 1993. URL: <http://stacks.iop.org/0953-8984/5/i=31/a=003>.
- [150] A. Jain. Route to attosecond nanoscopy, 2014.

Acknowledgements

The perilous exercise of acknowledgements carries so much risk of forgetting someone that it is almost paralyzing. I tried my best and I trust those who should be there but are not to know it, forgive me and claim their well-deserved apology beer as soon as possible.

I want to start by thanking my supervisor Dr. Eleftherios Goulielmakis. His thorough experience, deep drive and the motivation he brings in to make things happen have been key elements in making this work happen. Special thanks also go to Professor Ferenc Krausz for having managed to gather so much expertise in such good conditions to explore the frontiers of ultrafast science in his division.

I also of course want to express my deepest gratitude to the attoelectronics team: Trung who is always "ok!" and so wise, Julien for memorable evenings in the lab, filled with Quebec hunting stories and music of good to arguable level, Manish our Indian prince, Arohi for her invaluable touch of good mood and laughter, Adrian who taught me a lot, Mohammed for his good mood and strong will, Till, and the newcomers in the team, Harschit and Minje, as well as the summer and werkstudents.

Without first-class external collaborators, this work would not have happened, and I also thank them deeply: Stefan Pabst from the Center for Free Electron Laser science in Hamburg, Valer Tosa from the National Institute for R & D of Isotopic and Molecular Technologies in Romania, Alexander Guggenmos from Prof. Kleineberg group, Vlad Yakovlev, Nick Karpowicz are but some of these.

The environment of the MPQ has been a great one colleague-wise, both for scientific and more coffe-break related issues, and other colleagues of the Krausz group cannot be spared: Nick, well of science, Hani whose laugh filled the corridors so efficiently, Wolfgang and his Plätzchen, Michael, Sabine, Lisa, Annka, Daniel, Olga, the 3 Alex's, Tim, Agustin, Justin, Vlad, Stan, Markus, the 2 Christophs, Sandro, Antonin and so many more.

The support of our team of technicians, Hr. Böswald, Tobias Kleinhenz, Hr. Fischer, Hr. Haas and Hr. Horn, and the great team of the workshop led by Tom and Michael have been a key ingredient in the success of this work, as well as the Einkauf team which processed the numerous orders necessary to the realization of the complicated experiments carried, the complete Verwaltung of the institute (especially Frau Wild, so irreplaceable), and the cafeteria team, especially Christine.

Outside of the institute the supports have also been legion. I have the great luck to be part of a family which is available any time, be it for support, advice, last minute moving help and numerous other small things that are so important. I thank them all, papa, maman, Pauline, Margaux, and all the uncles, aunts and cousins, especially Chloé.

I would not have made it through these 4 years without the presence and support of so many friends that I cannot possibly name them all here. Without pretending to be exhaustive then I thank Thomas who managed to come to Munich 14 times in 4 years, and his wonderful Macha of course, Hubert who was never far, Sixte always ready to spend

punctos with me, Solène, my partner in crime, all the great roomies of the Hortensienstrasse 2, who made Munich a home in no time, especially Ste and Fra. Last but not least Lima, Michael, Béné, Henri, Gilles, Antonin, Lara, Quentin, Marie, Julien, Mathieu, Thibault, Doudou, Gautier, Tim, Djé, and all those whose name should be there and will recognize themselves. The skydiving friends would be too long to name but shared holidays and weekends for our common passion.

Very special thoughts go of course to Karoline, who has managed to support me these last 2 years, through tough and happier moments. Fruits in the morning, 5:30 AM wake up calls for (her) sport sessions, intense bathroom cleaning sessions, epic summitings and boarisch crash courses are but small elements of the balance she brought me when I most needed it, and I hope she will go on doing so.

Curriculum Vitae

Antoine Moulet

Nationality: French
Date of Birth: 26.03.1987
Place of Birth: Verdun (France)

Education and Training

- 2010 – 2014 PhD candidate at the Ludwig-Maximilians-Universität Munich in the group of Prof. F. Krausz, team of Dr. E. Goulielmakis at the Max Planck Institute of Quantum Optics, Garching bei München
- 2009 – 2010 Masters 2 in Quantum Physics (with grade very good) at the Ecole Normale Supérieure, Paris.
- 2006 – 2009 Studies at the Ecole Polytechnique, Palaiseau. Class 2006 valedictorian (on 500 students).
- 2004 – 2006 Preparatory classes at Lycée Louis le Grand, Paris
- 2001 – 2004 Lycée Henri Poincaré, Nancy. Baccalaureate in Science with the highest grade

Professional Experiences

- 2009 – 2010 Fastlite, development engineer. Developed a femtosecond laser pulses measurement device.
- 2009 Capasso group, Harvard University, research internship: Coupling of optical antennas and plasmonic waveguides.
- 2008 – 2009 Lycée Louis-le-grand, Paris, teaching assistant in Physics for undergraduates.
- 2006 – 2007 17th Paratrooper Engineering Regiment, Montauban (a French military unit specialized in military engineering). Served as an army officer.

Awards and scholarships

- 2010 – 2013 Marie Curie ATTOFEL initial training network fellow
- 2005 International Chemistry Olympiads, Taipei, Taiwan (competitive exam between 300 students from around 100 countries) Was awarded a silver medal.
- 2004 Concours general (concourse rewarding French best scientific students) 2nd prize in Biology.

Publications

Authored or co-authored seven publications in peer-reviewed journals, and ten contributions to international scientific conferences.